Published for SISSA by Springer

Received: October 17, 2017
Accepted: November 3, 2017
Published: December 12, 2017

Measurement of the Drell-Yan triple-differential cross section in pp collisions at $\sqrt{s} = 8$ TeV

The ATLAS collaboration

E-mail: atlas.publications@cern.ch

Abstract: This paper presents a measurement of the triple-differential cross section for the Drell-Yan process $Z/\gamma^* \to \ell^+\ell^-$ where ℓ is an electron or a muon. The measurement is performed for invariant masses of the lepton pairs, $m_{\ell\ell}$, between 46 and 200 GeV using a sample of 20.2 fb^{-1} of pp collisions data at a centre-of-mass energy of $\sqrt{s} = 8$ TeV collected by the ATLAS detector at the LHC in 2012. The data are presented in bins of invariant mass, absolute dilepton rapidity, $|y_{\ell\ell}|$, and the angular variable $\cos\theta^*$ between the outgoing lepton and the incoming quark in the Collins-Soper frame. The measurements are performed in the range $|y_{\ell\ell}| < 2.4$ in the muon channel, and extended to $|y_{\ell\ell}| < 3.6$ in the electron channel. The cross sections are used to determine the Z boson forward-backward asymmetry as a function of $|y_{\ell\ell}|$ and $m_{\ell\ell}$. The measurements achieve high-precision, below the percent level in the pole region, excluding the uncertainty in the integrated luminosity, and are in agreement with predictions. These precision data are sensitive to the parton distribution functions and the effective weak mixing angle.

Keywords: Hadron-Hadron scattering (experiments)

ArXiv ePrint: 1710.05167

Open Access, Copyright CERN,
for the benefit of the ATLAS Collaboration.
Article funded by SCOAP^3.

https://doi.org/10.1007/JHEP12(2017)059

JHEP12(2017)059

source: https://doi.org/10.7892/boris.114221 | downloaded: 12.10.2024

Contents

1 Introduction **1**

2 ATLAS detector **4**

3 Simulated event samples **4**

4 Event selection **6**
- 4.1 Central rapidity electron channel 6
- 4.2 High rapidity electron channel 7
- 4.3 Central rapidity muon channel 7
- 4.4 Measurement bins 8

5 Background estimation **9**
- 5.1 Fake lepton background estimation in the central rapidity electron channel 9
- 5.2 Fake lepton background estimation in the high rapidity electron channel 10
- 5.3 Fake lepton background estimation in the central rapidity muon channel 10
- 5.4 Top quark and electroweak backgrounds 11

6 Cross-section measurement **11**

7 Measurement uncertainties **17**
- 7.1 Statistical uncertainties 17
- 7.2 Systematic uncertainties 17
- 7.3 Central and high rapidity electron channels 17
  - 7.3.1 Energy scale and resolution 18
  - 7.3.2 Reconstruction and identification efficiencies 18
  - 7.3.3 Trigger efficiency 18
  - 7.3.4 Charge misidentification 19
  - 7.3.5 Multijet background 19
- 7.4 High rapidity electron channel 19
- 7.5 Central rapidity muon channel 20
  - 7.5.1 Momentum scale and resolution 20
  - 7.5.2 Reconstruction efficiency 21
  - 7.5.3 Trigger efficiency 21
  - 7.5.4 Isolation and impact parameter efficiency 21
  - 7.5.5 Multijet background 22
- 7.6 Systematic uncertainties common to all channels 22
  - 7.6.1 Top, diboson, W+jet, $Z/\gamma^* \to \tau\tau$, and photon-induced background normalisation 22
  - 7.6.2 Unfolding bias 23
  - 7.6.3 MC modelling 23
  - 7.6.4 PDF uncertainty 24
  - 7.6.5 Luminosity 24
- 7.7 Summary of measurement uncertainties 24

JHEP12(2017)059

8 Results **28**
8.1 Combination of the central rapidity electron and muon channels 28
8.2 Compatibility tests and integrated measurements 29
8.2.1 Compatibility of the central and high rapidity measurements 29
8.2.2 Compatibility with published data 30
8.2.3 Integrated cross sections 30
8.3 Triple-differential cross sections 33
8.4 Forward-backward asymmetry 43

9 Conclusion **46**

A Data tables **47**
A.1 Integrated cross-section tables 47
A.2 Triple-differential cross-section tables 49
A.3 Forward-backward asymmetry tables 55

The ATLAS collaboration **62**

1 Introduction

In the Drell-Yan process [1, 2] $q\bar{q} \to Z/\gamma^* \to \ell^+\ell^-$, parity violation in the neutral weak coupling of the mediator to fermions induces a forward-backward asymmetry, A_{FB}, in the decay angle distribution of the outgoing lepton (ℓ^-) relative to the incoming quark direction as measured in the dilepton rest frame. This decay angle depends on the sine of the weak mixing angle, $\sin^2\theta_{\mathrm{W}}$, which enters in the fermionic vector couplings to the Z boson. At leading order in electroweak (EW) theory it is given by $\sin^2\theta_{\mathrm{W}} = 1 - m_W^2/m_Z^2$, where m_W and m_Z are the W and Z boson masses, respectively. Higher-order loop corrections modify this relation depending on the renormalisation scheme used, and so experimental measurements are often given in terms of the sine of the effective weak mixing angle, $\sin^2\theta^{\mathrm{eff}}$ [3]. High-precision cross-section measurements sensitive to the asymmetry, and therefore to the effective weak mixing angle, provide a testing ground for EW theory and could offer some insight into physics beyond the Standard Model (SM).

Previous measurements by ATLAS and CMS of the Drell-Yan (DY) process include measurements of fiducial cross sections [4–7], and one-dimensional differential cross sections as a function of rapidity [8, 9], transverse momentum [9–12], and invariant mass [13–15]. Double-differential cross-section measurements as a function of invariant mass and either rapidity or transverse momentum [16–21] have also been published, as well as Z boson polarisation coefficients [22, 23] and the forward-backward asymmetry [24, 25]. Extraction of the effective weak mixing angle in leptonic Z boson decays, $\sin^2\theta^{\mathrm{eff}}_{\mathrm{lept}}$, from A_{FB} measurements has been performed by ATLAS using $5\,\mathrm{fb}^{-1}$ of proton-proton collision data at $\sqrt{s} = 7$ TeV [24] — a result in which the largest contribution to the uncertainty was due to limited knowledge of the parton distribution functions (PDFs) of the proton.

JHEP12(2017)059

A complete description of the Drell-Yan cross section to all orders in quantum chromodynamics (QCD) depends on five kinematic variables of the Born-level leptons, namely $m_{\ell\ell}$, the invariant mass of the lepton pair; $y_{\ell\ell}$, the rapidity of the dilepton system; θ and ϕ, the lepton decay angles in the rest frame of the two incident quarks; and $p_{\mathrm{T},Z}$, the transverse momentum of the vector boson. In this paper, measurements of the triple-differential Drell-Yan cross section, $\mathrm{d}^3\sigma/\mathrm{d}m_{\ell\ell}\mathrm{d}|y_{\ell\ell}|\mathrm{d}\cos\theta^*$, are reported as a function of $m_{\ell\ell}$, $|y_{\ell\ell}|$, and $\cos\theta^*$, where the lepton decay angle is defined in the Collins-Soper (CS) reference frame [26]. These cross-section measurements are designed to be simultaneously sensitive to $\sin^2\theta^{\mathrm{eff}}_{\mathrm{lept}}$ and to the PDFs, therefore allowing a coherent determination of both. A simultaneous extraction has the potential to reduce the PDF-induced uncertainty in the extracted value of the effective weak mixing angle.

At leading order (LO) in perturbative electroweak and QCD theory, the Drell-Yan triple-differential cross section can be written as

$$\frac{\mathrm{d}^3\sigma}{\mathrm{d}m_{\ell\ell}\mathrm{d}y_{\ell\ell}\mathrm{d}\cos\theta^*} = \frac{\pi\alpha^2}{3m_{\ell\ell}s}\sum_q P_q\left[f_q(x_1,Q^2)f_{\bar{q}}(x_2,Q^2)+(q\leftrightarrow\bar{q})\right], \tag{1.1}$$

where s is the squared proton-proton (pp) centre-of-mass energy; the incoming parton momentum fractions are $x_{1,2} = (m_{\ell\ell}/\sqrt{s})\mathrm{e}^{\pm y_{\ell\ell}}$; and $f_q(x_1,Q^2)$ are the PDFs for parton flavour q. Here, Q^2 is the four-momentum transfer squared and is set to the dilepton centre-of-mass energy, $m_{\ell\ell}$, which is equal to the partonic centre-of-mass energy. The $q\leftrightarrow\bar{q}$ term accounts for the case in which the parent protons of the q and $\bar{q}$ are interchanged. The function P_q in equation (1.1) is given by

$$\begin{aligned} P_q = {} & e_\ell^2 e_q^2(1+\cos^2\theta^*) \\ & + e_\ell e_q \frac{2m_{\ell\ell}^2(m_{\ell\ell}^2-m_Z^2)}{\sin^2\theta_{\mathrm{W}}\cos^2\theta_{\mathrm{W}}\left[(m_{\ell\ell}^2-m_Z^2)^2+\Gamma_Z^2 m_Z^2\right]}\left[v_\ell v_q(1+\cos^2\theta^*)+2a_\ell a_q\cos\theta^*\right] \\ & + \frac{m_{\ell\ell}^4}{\sin^4\theta_{\mathrm{W}}\cos^4\theta_{\mathrm{W}}\left[(m_{\ell\ell}^2-m_Z^2)^2+\Gamma_Z^2 m_Z^2\right]}\left[(a_\ell^2+v_\ell^2)(a_q^2+v_q^2)(1+\cos^2\theta^*)+8a_\ell v_\ell a_q v_q\cos\theta^*\right]. \end{aligned} \tag{1.2}$$

In this relation m_Z and Γ_Z are the Z boson mass and width, respectively; e_ℓ and e_q are the lepton and quark electric charges; and $v_\ell = -\frac{1}{4}+\sin^2\theta_{\mathrm{W}}$, $a_\ell = -\frac{1}{4}$, $v_q = \frac{1}{2}I_q^3 - e_q\sin^2\theta_{\mathrm{W}}$, and $a_q = \frac{1}{2}I_q^3$ are the vector and axial-vector lepton and quark couplings, respectively where I_q^3 is the third component of the weak isospin.

The first term in equation (1.2) corresponds to pure virtual photon, γ^*, exchange in the scattering process, the second corresponds to the interference of γ^* and Z exchange, and the last term corresponds to pure Z exchange. Thus the DY invariant mass spectrum is characterized by a $1/m_{\ell\ell}^2$ fall-off from γ^* exchange contribution, an $m_{\ell\ell}$-dependent Breit-Wigner peaking at the mass of the Z boson, and a Z/γ^* interference contribution which changes sign from negative to positive as $m_{\ell\ell}$ increases across the m_Z threshold.

The terms which are linear in $\cos\theta^*$ induce the forward-backward asymmetry. The largest contribution comes from the interference term, except at $m_{\ell\ell} = m_Z$ where the interference term is zero, and only the Z exchange term contributes to the asymmetry. The resulting asymmetry is, however, numerically small due to the small value of v_ℓ. The

JHEP12(2017)059

net effect is an asymmetry which is negative for $m_{\ell\ell} < m_Z$ and increases, becoming positive for $m_{\ell\ell} > m_Z$. The point of zero asymmetry occurs slightly below $m_{\ell\ell} = m_Z$.

The forward-backward asymmetry varies with $|y_{\ell\ell}|$. The incoming quark direction can only be determined probabilistically: for increasing $|y_{\ell\ell}|$ the momentum fraction of one parton reaches larger x where the valence quark PDFs dominate because the valence quarks typically carry more momentum than the antiquarks. Therefore, the Z/γ^* is more likely to be boosted in the quark direction. Conversely, at small boson rapidity, $|y_{\ell\ell}| \sim 0$, it becomes almost impossible to identify the direction of the quark since the quark and antiquark have nearly equal momenta.

The sensitivity of the cross section to the PDFs arises primarily from its dependence on $y_{\ell\ell}$ (and therefore x_1 and x_2) in equation (1.1). Further sensitivity is gained by analysing the cross section in the $m_{\ell\ell}$ dimension, since in the Z resonance peak the partons couple through the weak interaction and off-peak the electric couplings to the γ^* dominate. Therefore, the relative contributions of up-type and down-type quarks vary with $m_{\ell\ell}$. Finally, the $\cos\theta^*$ dependence of the cross section provides sensitivity to terms containing $a_\ell a_q$ and $v_\ell v_q a_\ell a_q$ in equation (1.2). Three different combinations of couplings to the incident quarks contribute to the LO cross section. The magnitude of the asymmetry is proportional to the valence quark PDFs and offers direct sensitivity to the corresponding PDF component.

The full five-dimensional cross section can also be decomposed into harmonic polynomials for the lepton decay angle scattering amplitudes and their corresponding coefficients A_{0-7} [22]. Higher-order QCD corrections to the LO $q\bar{q}$ process involve $qg + \bar{q}g$ terms at next-to-leading order (NLO), and gg terms at next-to-next-to-leading order (NNLO). These higher-order terms modify the decay angle dependence of the cross section. Measuring the $|\cos\theta^*|$ distribution provides additional sensitivity to the gluon versus sea-quark PDFs and is related to the measurements of the angular coefficients as a function of the Z boson transverse momentum [22, 23].

Initial-state QCD radiation can introduce a non-zero transverse momentum for the final-state lepton pair, leading to quark directions which may no longer be aligned with the incident proton directions. Hence, in this paper, the decay angle is measured in the CS reference frame [26] in which the decay angle is measured from an axis symmetric with respect to the two incoming partons. The decay angle in the CS frame (θ^*) is given by

$$\cos\theta^* = \frac{p_{\mathrm{z},\ell\ell}}{m_{\ell\ell}|p_{\mathrm{z},\ell\ell}|}\frac{p_1^+ p_2^- - p_1^- p_2^+}{\sqrt{m_{\ell\ell}^2 + p_{\mathrm{T},\ell\ell}^2}}\,,$$

where $p_i^\pm = E_i \pm p_{\mathrm{z},i}$ and $i = 1$ corresponds to the negatively-charged lepton and $i = 2$ to the positively-charged antilepton. Here, E and p_z are the energy and longitudinal z-components of the leptonic four-momentum, respectively; $p_{\mathrm{z},\ell\ell}$ is the dilepton z-component of the momentum; and $p_{\mathrm{T},\ell\ell}$ the dilepton transverse momentum.

The triple-differential cross sections are measured using $20.2\,\mathrm{fb}^{-1}$ of pp collision data at $\sqrt{s} = 8$ TeV. The measurements are performed in the electron and muon decay channels for $|y_{\ell\ell}| < 2.4$. The electron channel analysis is extended to high rapidity in the region $1.2 < |y_{\ell\ell}| < 3.6$. The measured cross sections cover the kinematic range $46 < m_{\ell\ell} <$

JHEP12(2017)059

200 GeV, $0 < |y_{\ell\ell}| < 3.6$, and $-1 < \cos\theta^* < +1$. For convenience the notation

$$\mathrm{d}^3\sigma \equiv \frac{\mathrm{d}^3\sigma}{\mathrm{d}m_{\ell\ell}\mathrm{d}|y_{\ell\ell}|\mathrm{d}\cos\theta^*}$$

is used. The cross sections are classified as either *forward* ($\cos\theta^* > 0$) or *backward* ($\cos\theta^* < 0$) and used to obtain an experimental measurement of A_{FB} differentially in $m_{\ell\ell}$ and $|y_{\ell\ell}|$:

$$A_{\mathrm{FB}} = \frac{\mathrm{d}^3\sigma(\cos\theta^* > 0) - \mathrm{d}^3\sigma(\cos\theta^* < 0)}{\mathrm{d}^3\sigma(\cos\theta^* > 0) + \mathrm{d}^3\sigma(\cos\theta^* < 0)} \,. \tag{1.3}$$

2 ATLAS detector

The ATLAS detector [27] consists of an inner tracking detector (ID) surrounded by a thin superconducting solenoid, electromagnetic and hadronic calorimeters, and a muon spectrometer (MS). Charged particles in the pseudorapidity[1] range $|\eta| < 2.5$ are reconstructed with the ID, which consists of layers of silicon pixel and microstrip detectors and a straw-tube transition-radiation tracker having a coverage of $|\eta| < 2.0$. The ID is immersed in a 2 T magnetic field provided by the solenoid. The latter is surrounded by a hermetic calorimeter that covers $|\eta| < 4.9$ and provides three-dimensional reconstruction of particle showers. The electromagnetic calorimeter is a liquid-argon sampling calorimeter, which uses lead absorbers for $|\eta| < 3.2$. The hadronic sampling calorimeter uses plastic scintillator tiles as the active material and steel absorbers in the region $|\eta| < 1.7$. In the region $1.5 < |\eta| < 3.2$, liquid argon is used as the active material, with copper absorbers. A forward calorimeter covers the range $3.2 < |\eta| < 4.9$ which also uses liquid argon as the active material, and copper and tungsten absorbers for the EM and hadronic sections of the subdetector, respectively.

Outside the calorimeters, air-core toroids supply the magnetic field for the MS. There, three layers of precision chambers allow the accurate measurement of muon track curvature in the region $|\eta| < 2.7$. The majority of these precision chambers is composed of drift tubes, while cathode-strip chambers provide coverage in the inner layers of the forward region $2.0 < |\eta| < 2.7$. The muon trigger in the range $|\eta| < 2.4$ uses resistive-plate chambers in the central region and thin-gap chambers in the forward region. A three-level trigger system [28] selects events to be recorded for offline analysis.

3 Simulated event samples

Monte Carlo (MC) simulation samples are used to model the expected signal and background yields, with the exception of certain data-driven background estimates. The MC samples are normalised using the highest-order cross-section predictions available in perturbation theory.

[1] ATLAS uses a right-handed coordinate system with its origin at the nominal interaction point in the centre of the detector and the z-axis along the beam pipe. The x-axis points from the interaction point to the centre of the LHC ring, and the y-axis points upward. Cylindrical coordinates (r, ϕ) are used in the transverse plane, ϕ being the azimuthal angle around the beam pipe. The pseudorapidity is defined in terms of the polar angle θ as $\eta = -\ln\tan(\theta/2)$.

JHEP12(2017)059

The DY process was generated at NLO using Powheg-Box (referred to as Powheg in the following) [29–32] and the CT10 PDF set [33], with Pythia 8 [34] to model parton showering, hadronisation, and the underlying event (UEPS). The $Z/\gamma^* \to \ell^+\ell^-$ differential cross section as a function of mass has been calculated at NNLO in perturbative QCD (pQCD) using FEWZ 3.1 [35–37] with the MSTW2008NNLO PDF set [38]. The renormalisation, μ_r, and factorisation, μ_f, scales were both set equal to $m_{\ell\ell}$. The calculation includes NLO EW corrections beyond final-state photon radiation (FSR) using the G_μ EW scheme [39]. A mass-dependent K-factor used to scale the $Z/\gamma^* \to \ell^+\ell^-$ MC sample is obtained from the ratio of the calculated total NNLO pQCD cross section with the additional EW corrections, to the total cross section from the Powheg sample. This one-dimensional (and therefore partial) NNLO K-factor is found to vary from 1.035 at the lowest invariant mass values considered in this analysis to 1.025 at the highest. This factor also improves the modelling of the Z boson lineshape. The DY production of τ pairs was modelled using Powheg in the same way as the signal simulation.

The scattering amplitude coefficients describing the distributions of lepton decay angles are known to be not accurately modelled in Powheg particularly A_0 at low $p_{\mathrm{T},Z}$ [22]. For this reason, the signal MC events are reweighted as a function of $p_{\mathrm{T},Z}$ and $y_{\ell\ell}$ to improve their modelling. These weights were calculated using the cross-section calculator DYNNLO [40].

The photon-induced process, $\gamma\gamma \to \ell\ell$, is simulated at LO using Pythia 8 and the MRST2004qed PDF set [41]. The expected yield for this process also accounts for NLO QED/EW corrections from references [42, 43], which decrease the yield by approximately 30%.

The production of top quark pairs with prompt isolated leptons from electroweak boson decays constitutes a dominant background. It is estimated at NLO in QCD using Powheg and the CT10 PDF set, with Pythia 6 [44] for UEPS. The $t\bar{t}$ sample is normalized using a cross section calculated at NNLO in QCD including resummation effects [45–50]. Small compared to the $t\bar{t}$ contribution, single-top production in association with a W boson (Wt) is also modelled by Powheg and the CT10 PDF set, with Pythia 6 for UEPS. Both the $t\bar{t}$ and Wt contributions are summed and collectively referred to as the top quark background.

Further small background contributions are due to diboson (WW, WZ and ZZ) production with decays to final states with at least two leptons. The diboson processes were generated at LO with Herwig, using the CTEQ6L1 PDF set [51]. The samples are scaled to NLO calculations [52, 53] or to ATLAS measurements as described in reference [17]. Additionally, the background arising from W boson production in association with jets (W+jets) is studied with MC samples generated with Powheg under identical conditions as the DY signal samples.

All MC samples used in the analysis include the effects of QED FSR, multiple interactions per bunch crossing ("pile-up"), and detector simulation. QED FSR was simulated using Photos [54], while the effects of pile-up were accounted for by overlaying simulated minimum-bias events [55] generated with Pythia8 [34]. The interactions of particles with the detector were modelled using a full ATLAS detector simulation [55] based on Geant4 [56]. Finally, several corrections are applied to the simulated samples, ac-

JHEP12(2017)059

Process	Generator	Parton shower & underlying event	Generator PDF	Model parameters ("Tune")
$Z/\gamma^* \to \ell\ell$	Powheg v1(r1556)	Pythia 8.162	CT10	AU2 [62]
$Z/\gamma^* \to \tau\tau$	Powheg v1(r1556)	Pythia 8.162	CT10	AU2
$\gamma\gamma \to \ell\ell$	Pythia 8.170	Pythia 8.170	MRST2004qed	4C [63]
$t\bar{t}$	Powheg v1(r1556)	Pythia 6.427.2	CT10	AUET2 [64]
Wt	Powheg v1(r1556)	Pythia 6.427.2	CT10	AUET2
Diboson	Herwig 6.520	Herwig 6.520	CTEQ6L1	AUET2
$W \to \ell\nu$	Powheg v1(r1556)	Pythia 8.162	CT10	AU2

Table 1. Overview of the Monte Carlo samples used in this analysis.

counting for differences between data and simulation in the lepton trigger, reconstruction, identification, and isolation efficiencies as well as lepton resolution and muon momentum scale [57–61, 61]. The electron energy scale corrections are applied to the data.

An overview of the simulated event samples is given in table 1.

4 Event selection

Events are required to have been recorded during stable beam condition periods and must pass detector and data-quality requirements. This corresponds to an integrated luminosity of 20.2 fb^{-1} for the muon channel. Small losses in the data processing chain lead to an integrated luminosity of 20.1 fb^{-1} for the electron channel. Due to differences in the detector response to electrons and muons the selection is optimised separately for each channel and is described in the following.

4.1 Central rapidity electron channel

The electron data were collected using a dilepton trigger which uses calorimetric and tracking information to identify compact electromagnetic energy depositions. Identification algorithms use calorimeter shower shape information and the energy deposited in the vicinity of the electron candidates to find candidate electron pairs with a minimum transverse energy of 12 GeV for both the leading and subleading electron.

Electrons are reconstructed by clustering energy deposits in the electromagnetic calorimeter using a sliding-window algorithm. These clusters are then matched to tracks reconstructed in the inner detector. The calorimeter provides the energy measurement and the track is used to determine the angular information of the electron trajectory. An energy scale correction determined from $Z \to e^+e^-$, $W \to e\nu$, and $J/\psi \to e^+e^-$ decays [57] is applied to data. Central electron candidates are required to have $|\eta^e| < 2.4$. Furthermore, candidates reconstructed within the transition region between the barrel and endcap calorimeters, $1.37 < |\eta^e| < 1.52$, are excluded from the measurement. Each candidate is required to satisfy the "medium" electron identification [58, 59] criteria, based on calorimetric shower shapes and track parameters. To ensure the selected electrons are on the efficiency plateau of the trigger, electrons are required to have $E_{\text{T}}^e > 20$ GeV. Candidate events are

JHEP12(2017)059

required to have exactly one pair of oppositely-charged electrons and their invariant mass is required to be in the range $46 < m_{ee} < 200\,\text{GeV}$.

4.2 High rapidity electron channel

In this channel, the rapidity range of the measurement is extended by selecting one central electron and one forward electron. Forward electrons are defined as having pseudorapidities in the range $2.5 < |\eta^e| < 4.9$, reconstructed by the endcap or forward calorimeters. The data were collected using two single-electron triggers in the central calorimeter region with $E_{\text{T}}^e > 24\,\text{GeV}$ or $E_{\text{T}}^e > 60\,\text{GeV}$. The lower-threshold trigger has additional criteria for the shower shape and energy deposited in the vicinity of the electron candidate. The reconstructed central electrons are required to have $E_{\text{T}}^e > 25\,\text{GeV}$, $|\eta^e| < 2.4$, and must satisfy the "tight" identification criteria. Electrons in the calorimeter transition regions $1.37 < |\eta^e| < 1.52$ are rejected. Leptons produced in the Drell-Yan process are expected to be well isolated from other particles not associated with the lepton. This provides a good discriminant against the multijet background arising from the semileptonic decays of heavy quarks or hadrons faking electrons. The track isolation is defined as the scalar sum of the transverse momenta, $\sum p_{\text{T}}$, of the additional tracks contained in a cone of size $\Delta R = \sqrt{(\Delta\phi)^2 + (\Delta\eta)^2} = 0.2$ around the electron (omitting the contribution from the electron track). Central electrons are required to have a track isolation less than 14% of E_{T}^e.

The forward electron is required to satisfy "tight" identification criteria, $E_{\text{T}}^e > 20\,\text{GeV}$, and $2.5 < |\eta^e| < 4.9$, excluding the transition region between the endcap and forward calorimeters, $3.00 < |\eta^e| < 3.35$. Due to insufficient accuracy in the modelling of the material in front of the endcap calorimeter, forward electrons in the region $2.70 < |\eta^e| < 2.80$ are also rejected.

A dedicated calibration procedure is performed for the forward electrons. Energy scale and Gaussian resolution corrections are derived in bins of η^e by comparing the peak position and the width of the m_{ee} distributions in data and simulation. The scale and resolution corrections are the values that bring the peak regions, $80 < m_{ee} < 100\,\text{GeV}$, of the data and simulation into the best agreement.

No isolation criteria are applied to the forward electron and due to the absence of tracking information in the forward region, no charge requirements are placed on the selected electron pair. Lastly, events in the high rapidity electron channel are required to have exactly one central-forward pair of electrons with an invariant mass in the range $66 < m_{ee} < 150\,\text{GeV}$. Events with more than one possible central-forward pair are not used in this measurement channel.

4.3 Central rapidity muon channel

Candidate events in the muon channel were collected using two sets of triggers with the set of triggers used depending on the p_{T}^μ of the muon with the larger transverse momentum. For $p_{\text{T}}^\mu > 25\,\text{GeV}$, two single-muon triggers are used, with transverse momentum thresholds of 24 GeV and 36 GeV. The low-threshold trigger requires the muon to be isolated. This combination of triggers collected the majority of the events in the data sample. For $p_{\text{T}}^\mu <$

JHEP12(2017)059

25 GeV, a dimuon trigger is used which requires two muons with transverse momentum thresholds of 18 GeV for one muon and 8 GeV for the other.

Muons are identified by tracks reconstructed in the muon spectrometer matched to tracks reconstructed in the inner detector, and are required to have $p_{\mathrm{T}}^{\mu} > 20\,\mathrm{GeV}$ and $|\eta^{\mu}| < 2.4$. Additionally, they must satisfy identification criteria based on the number of hits in the inner detector and muon spectrometer, and on the consistency between the charge and momentum measurements in both systems [60]. Backgrounds from multijet events are efficiently suppressed by imposing an isolation condition requiring that the sum of the transverse momentum, $\sum p_{\mathrm{T}}$, of the tracks contained in a cone of size $\Delta R = 0.2$ around the muon (omitting the contribution from the muon track) to be less than 10% of p_{T}^{μ}. A small contribution of cosmic muons is removed by requiring the magnitude of the longitudinal impact parameter with respect to the primary interaction vertex z_0 to be less than 10 mm. Events are selected if they contain exactly two oppositely-charged muons satisfying the isolation and impact parameter requirements. Finally, the dilepton invariant mass must be in the range $46 < m_{\mu\mu} < 200\,\mathrm{GeV}$.

In order to minimise the influence of residual misalignments between the ID and MS, muon kinematic variables are measured using the ID only. A small residual η^{μ}- and charge-dependent bias in the muon momentum was observed, most likely arising from residual rotational misalignments of the inner detector. Such ID misalignments bias the measurement of the muon track sagitta and have an opposite effect on the momentum of positively- and negatively-charged muons. Hence, the reconstructed invariant mass or rapidity of muon pairs are not affected, in contrast to measurements of $\cos\theta^*$ which are charge-dependent. These residual inner detector misalignments are corrected for based on two methods, one which uses $Z \to \mu^+\mu^-$ events, and another using $Z \to e^+e^-$ events as described in reference [65]. Together with a χ^2 minimisation technique, the dimuon data sample is used to determine the corrections binned finely, which are however insensitive to the η-independent component of the track curvature bias. This bias is corrected for using dielectron data by comparing the ratio of the calorimeter energy to the track momentum for electrons and positrons.

4.4 Measurement bins

The measurement bins are chosen by taking into consideration several competing demands on the analysis such as its sensitivity to the underlying physics, the statistical precision in each bin, and detector resolution effects particularly in the $m_{\ell\ell}$ dimension. The binning must also match those used in recent ATLAS cross section measurements [13, 18].

The measurement is performed in seven bins of $m_{\ell\ell}$ from 46 GeV to 200 GeV with edges set at 66, 80, 91, 102, 116, and 150 GeV; 12 equidistant bins of $|y_{\ell\ell}|$ from 0 to 2.4; and bins of $\cos\theta^*$ from -1 to $+1$, separated at -0.7, -0.4, 0.0, $+0.4$, $+0.7$ giving 6 bins. In total, 504 measurement bins are used for the central rapidity electron and muon channel measurements.

For the high rapidity electron channel the measurement is restricted to the 5 invariant mass bins in the region $66 < m_{\ell\ell} < 150\,\mathrm{GeV}$. The $|y_{\ell\ell}|$ region measured in this channel ranges from 1.2 to 3.6 in 5 bins with boundaries at 1.6, 2.0, 2.4, 2.8. The $\cos\theta^*$ binning is

JHEP12(2017)059

identical to the binning of the central analyses. A total of 150 measurement bins is used in this channel.

5 Background estimation

The background from processes with two isolated final-state leptons of the same flavour is estimated using MC simulation. The processes with non-negligible contributions are $Z/\gamma^* \to \tau\tau$, diboson (WW, WZ and ZZ), and photon-induced dilepton production — together termed the *electroweak* background sources. The top quark background arising from $t\bar{t}$ and Wt production is also estimated using MC simulation. The samples used for these estimates are listed in table 1.

Background contributions from events where at least one final state jet satisfies the electron or muon selection criteria, hereafter referred to as the *fake lepton* background, are determined using a combination of data-driven methods and MC simulation. By far the largest contribution to the fake lepton background comes from light- and heavy-flavour multijet production, referred to as the *multijet* background, which is determined from data. Descriptions on the fake background estimations used in each of the three channels are given in the following subsections.

5.1 Fake lepton background estimation in the central rapidity electron channel

To separate the signal from the multijet background, the analysis relies on the electron relative transverse energy isolation distribution (I^e). This is a good discriminant for the multijet contribution, which has larger values of I^e than the signal process. It is defined as the ratio of the summed calorimetric transverse energy contained in a cone of size $\Delta R = 0.2$ around the electron to the electron transverse energy: $I^e = \sum E_{\mathrm{T}}(\Delta R = 0.2)/E_{\mathrm{T}}^e$. The smaller of the I^e values of the two electron candidates is chosen to represent each event, as it was found to provide optimal discrimination.

The multijet fraction is then estimated from data by fitting this distribution using a template method. The background template is selected with inverted electron identification requirements and the signal, electroweak, and W+jet templates are taken from simulation. The non-isolated sample where the smaller I^e of the two electrons exceeds a certain value is found to be dominated by multijet background and is used to adjust the normalization of the background template, taking into account the small signal contamination. Since the multijet background is not expected to exhibit any parity violating effects and the $\cos\theta^*$ background templates in data were found not to show any asymmetry about $\cos\theta^* = 0$, the method is symmetrised in bins of $|\cos\theta^*|$, resulting in a doubling of the sample sizes and therefore more stable results.

The multijet contribution is found to be largest at low m_{ee} and also at large $|\cos\theta^*|$ for $|y_{ee}| \sim 0$, where it reaches 15% of the expected number of signal events. In the pole region, $80 < m_{ee} < 102\,\mathrm{GeV}$, the contribution is less than 0.1%.

The contribution of W+jet production to the fake lepton background is estimated from MC simulation. It is small compared to the multijet background for all kinematic regions, and therefore does not introduce any significant charge asymmetry.

JHEP12(2017)059

5.2 Fake lepton background estimation in the high rapidity electron channel

The multijet background in the high rapidity electron channel is estimated using a template method similar to the one used in the central electron channel with, however, some small adjustments. The isolation variable is used for the normalisation of the multijet background only for the mass bins in the range $80 < m_{ee} < 102\,\text{GeV}$. The size of the isolation cone in this case is increased to $\Delta R = 0.3$, which was found to improve the stability of the fits. For the off-peak mass bins, the transverse energy of the forward electron is used as an alternative discriminating variable, where the multijet background contributes mostly at low E_{T}. This decreases the statistical uncertainty of the estimation and reduces its dependence on the W+jet background modelling, as discussed below.

The multijet background is the dominant contribution to the background in this measurement channel and is typically about 5–10% of the expected signal, but increases rapidly at large $|\cos\theta^*|$. It can be as large as 30–60% in some bins at large $|y_{ee}|$ where the $|A_{\text{FB}}|$ is large and the signal cross section is suppressed, i.e. $\cos\theta^* < 0$ for $m_{ee} > m_Z$.

The W+jet background is estimated using MC simulation. As was the case in the central electron analysis, it is found to be small under the peak of the Z resonance. It is found to be more significant off peak, reaching 30% of the fake lepton background.

5.3 Fake lepton background estimation in the central rapidity muon channel

The multijet background remaining after event selection in the muon channel is largely due to heavy-flavour b- and c-quark decays, and is estimated in two steps. First, the shape as a function of $|y_{\mu\mu}|$ and $|\cos\theta^*|$ is estimated in each $m_{\mu\mu}$ bin. Next its overall normalisation is then determined in each invariant mass region.

Three orthogonal control regions with inverted muon isolation requirements defined by $I^\mu = \sum p_{\text{T}}(\Delta R = 0.2)/p^\mu_{\text{T}} > 0.1$, and/or inverted muon pair charge requirements are used to determine the multijet background. In each control region the contamination from signal and electroweak background is subtracted using simulation.

A comparison of the shape of the I^μ distributions for muons in events with same-charge and opposite-charge muon pairs shows a small linear deviation from unity of up to +10% when extrapolated into the isolated signal region $I^\mu < 0.1$. This is found to be independent of $m_{\mu\mu}$, and is accounted for in the extrapolation. The $|y_{\mu\mu}|$ and $|\cos\theta^*|$ dependence of the background in each $m_{\mu\mu}$ bin is obtained in the multijet enriched data control region in which pairs of same-charge and opposite-charge muons satisfy $I^\mu > 0.1$. Finally, the resulting $|y_{\mu\mu}|$ and $|\cos\theta^*|$ spectra are normalised in the signal region using the constraint that the yield ratio of opposite-charge to same-charge muon pairs is similar in the isolated and non-isolated control regions.

This method does not account for a potential W+jets background contribution. This component is estimated from simulation and found to be negligible.

The estimated fake lepton background contribution in the muon channel is everywhere smaller than its contribution in the central electron channel, and never more than 5% of the expected signal yield.

JHEP12(2017)059

5.4 Top quark and electroweak backgrounds

These sources of background arise from QCD and EW processes in which two prompt isolated leptons are produced. Their contributions are estimated using MC simulation.

Background events from top quark processes increase with $m_{\ell\ell}$ and are typically below 2% of the expected signal yields. The contribution is largest at the extremes of $\cos\theta^*$ where it can reach 10–20% of the expected signal in the central channels. At high rapidity, this background source is typically below 5% everywhere.

The diboson background increases with invariant mass and reaches about 6% of the expected signal yield at large $|\cos\theta^*|$ in both the central electron and muon channels. In the high rapidity electron channel it reaches about 3% at moderate $|y_{\ell\ell}|$.

The background from $Z \to \tau\tau$ is significant only at low $m_{\ell\ell}$, where it can reach 7% in the central rapidity channels and 3% in the high rapidity channel.

Photon-induced production of dilepton pairs gives a small background contribution of 2% or less in all channels. However, for large values of $m_{\ell\ell}$, this contribution can reach about 5%.

6 Cross-section measurement

As defined in section 4.4, the binning scheme used for the triple-differential measurements consists of 504 bins for the central rapidity electron and muon channels, and 150 bins in the high rapidity electron channel. The Drell-Yan cross section is measured in the central rapidity channels within the fiducial region defined by $p_{\mathrm{T}}^{\ell} > 20\,\mathrm{GeV}$, $|\eta^{\ell}| < 2.4$, and $46 < m_{\ell\ell} < 200\,\mathrm{GeV}$. In the high rapidity electron channel the fiducial region of the measurement is defined by $p_{\mathrm{T}}^{\ell} > 25\,\mathrm{GeV}$ and $|\eta^{\ell}| < 2.4$ for the central electron, $p_{\mathrm{T}}^{\ell} > 20\,\mathrm{GeV}$ and $2.5 < |\eta^{\ell}| < 4.9$ for the forward electron, and $66 < m_{\ell\ell} < 150\,\mathrm{GeV}$.

The cross-section results are first unfolded to the "dressed"-level, defined at the particle-level using leptons after FSR recombined with radiated photons within a cone of $\Delta R = 0.1$. The unfolded data are then corrected to the Born-level, before final-state QED radiation at the particle-level, using a correction factor obtained from the Powheg MC sample. This procedure neglects the bin migrations between the dressed- and Born-level kinematics, an approximation which was verified to have a negligible impact on the central values and uncertainties of the results presented in this paper.

The triple-differential cross section is calculated as

$$\left.\frac{\mathrm{d}^3\sigma}{\mathrm{d}m_{\ell\ell}\,\mathrm{d}|y_{\ell\ell}|\,\mathrm{d}\cos\theta^*}\right|_{l,m,n} = \mathcal{M}_{ijk}^{lmn} \cdot \frac{N_{ijk}^{\mathrm{data}} - N_{ijk}^{\mathrm{bkg}}}{\mathcal{L}_{\mathrm{int}}} \frac{1}{\Delta_{m_{\ell\ell}} \cdot 2\Delta_{|y_{\ell\ell}|} \cdot \Delta_{\cos\theta^*}} \,, \tag{6.1}$$

where i, j, k are the bin indices for reconstructed final-state kinematics; l, m, n are the bin indices for the generator-level kinematics; and $\mathcal{L}_{\mathrm{int}}$ is the integrated luminosity of the data set. Quantity N^{data} is the number of candidate signal events observed in a given bin of width $\Delta_{m_{\ell\ell}}$, $\Delta_{|y_{\ell\ell}|}$, and $\Delta_{\cos\theta^*}$, while N^{bkg} is the number of background events in the same bin. The factor of two in the denominator accounts for the modulus in the rapidity bin

JHEP12(2017)059

width. Integrated single- and double-differential cross sections are measured by summing over the corresponding indices of equation (6.1).

The factor $\mathcal{M}$ is the inverted response matrix and takes into account the efficiency of the signal selection and bin migration effects. It gives the probability that a selected event reconstructed in some measurement bin was originally generated in a given fiducial (generator-level) bin. The factor $\mathcal{M}$ is obtained from the Drell-Yan signal samples after correcting for differences in the reconstruction, identification, trigger, and isolation efficiencies between data and simulation, as well as for momentum scale and resolution mismodelling effects. It also accounts for events originally outside of the fiducial selection that migrate into the reconstructed event sample. Finally, $\mathcal{M}$ also includes extrapolations over the regions that are excluded from the electron selection ($1.37 < |\eta^e| < 1.52$, $2.70 < |\eta^e| < 2.80$, and $3.00 < |\eta^e| < 3.35$).

The quality of the simulation and its ability to describe the data are checked in figures 1–4, comparing data and prediction for the $y_{\ell\ell}$, $\cos\theta^*$, and $m_{\ell\ell}$ distributions in selected regions of the measured kinematic range, as indicated in the figure captions. The expected number of events is calculated as the sum of expected signal and background yields. Acceptable agreement is found in all channels, given that the simulation is only accurate to NLO for the observables shown in figures 1–3, and to NNLO accuracy for the $m_{\ell\ell}$ distribution shown in figure 4.

The background-subtracted data are unfolded to fiducial cross sections using the inverse of the response matrix obtained using an iterative Bayesian unfolding method [66] in which the prior is improved at each iteration. When using such methods the statistical and systematic uncertainties (discussed in section 7) increase with each unfolding iteration, while the residual bias from the initial prior decreases. A balance between these two competing effects must be struck when deciding on the number of iterations to be used to unfold the measurement. Only small changes to the prior are expected, however, since the lineshape of the Z boson resonance and the PDFs are known to high-precision. Moreover, the prior (Powheg) is enhanced using QCD and EW corrections and describes the data within experimental uncertainties. An optimum was found using two iterations in this analysis.

Finally, measurement bins which are predicted by signal MC simulation to have fewer than 25 signal events are expected to have large statistical uncertainties and therefore these bins are removed from the analysis. Approximately 50 bins are discarded in each of the central electron and muon channels. They typically lie at large $|y_{\ell\ell}|$ and large $|\cos\theta^*|$. In the high rapidity electron channel, 27 bins are removed, all corresponding to small $|\cos\theta^*|$. In all cases the discarded bins correspond to ones for which the signal prediction at LO in QCD is consistent with zero.

JHEP12(2017)059

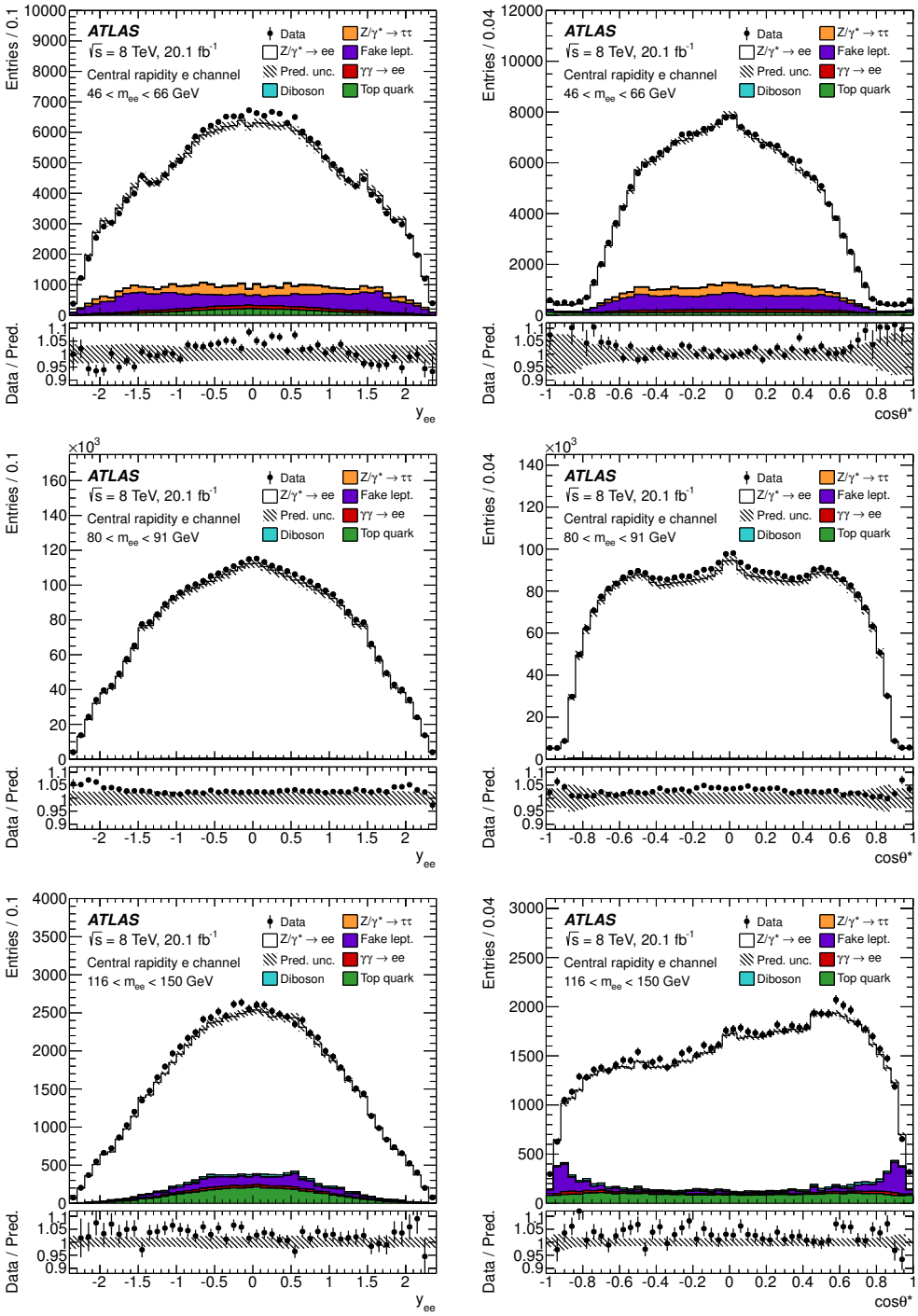

Figure 1. Distributions of dilepton rapidity (left) and $\cos\theta^*$ (right) in the central rapidity electron channel for m_{ee} bins 46–66 GeV (top row), 80–91 GeV (middle), and 116–150 GeV (bottom). The data (solid markers) and the prediction (stacked histogram) are shown after event selection. The lower panels in each plot show the ratio of data to prediction. The error bars represent the data statistical uncertainty while the hatched band represents the systematic uncertainty in the prediction.

JHEP12(2017)059

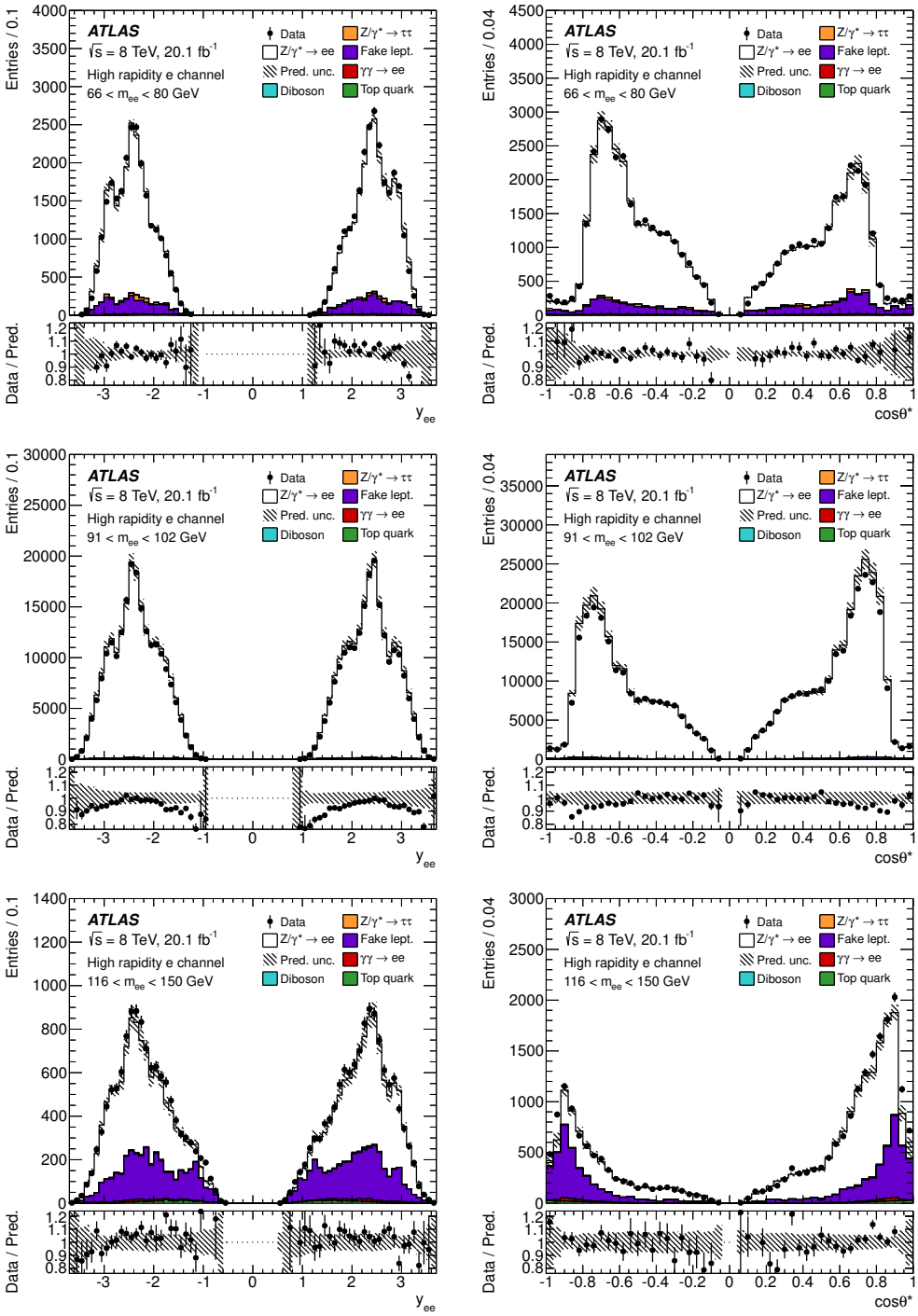

Figure 2. Distributions of dilepton rapidity (left) and $\cos\theta^*$ (right) in the high rapidity electron channel for m_{ee} bins 66–80 GeV (top row), 91–102 GeV (middle), and 116–150 GeV (bottom). The data (solid markers) and the prediction (stacked histogram) are shown after event selection. The lower panels in each plot show the ratio of data to prediction. The error bars represent the data statistical uncertainty while the hatched band represents the systematic uncertainty in the prediction.

JHEP12(2017)059

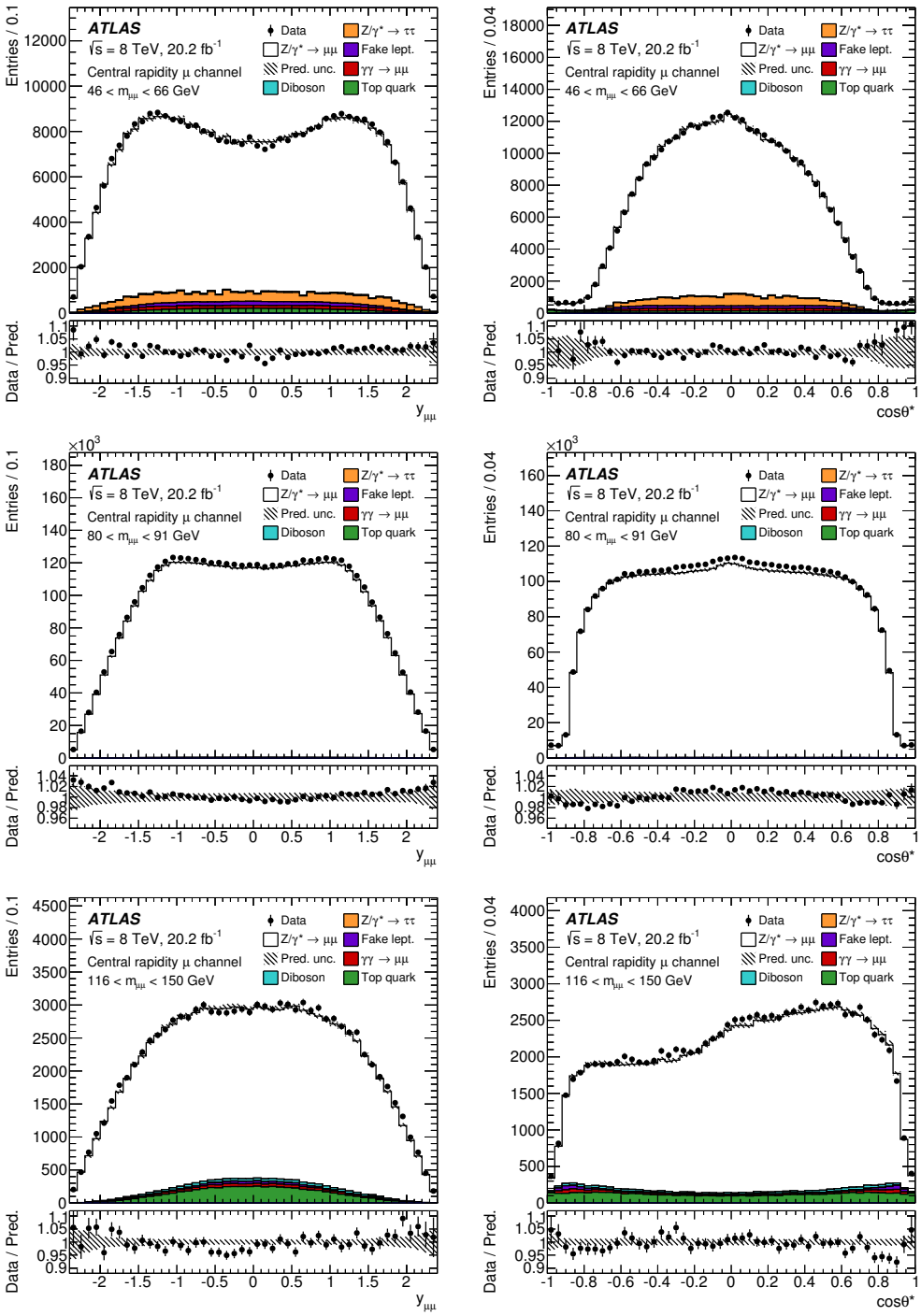

Figure 3. Distributions of dilepton rapidity (left) and $\cos\theta^*$ (right) in the central rapidity muon channel for $m_{\mu\mu}$ bins 46–66 GeV (top row), 80–91 GeV (middle), and 116–150 GeV (bottom). The data (solid markers) and the prediction (stacked histogram) are shown after event selection. The lower panels in each plot show the ratio of data to prediction. The error bars represent the data statistical uncertainty while the hatched band represents the systematic uncertainty in the prediction.

JHEP12(2017)059

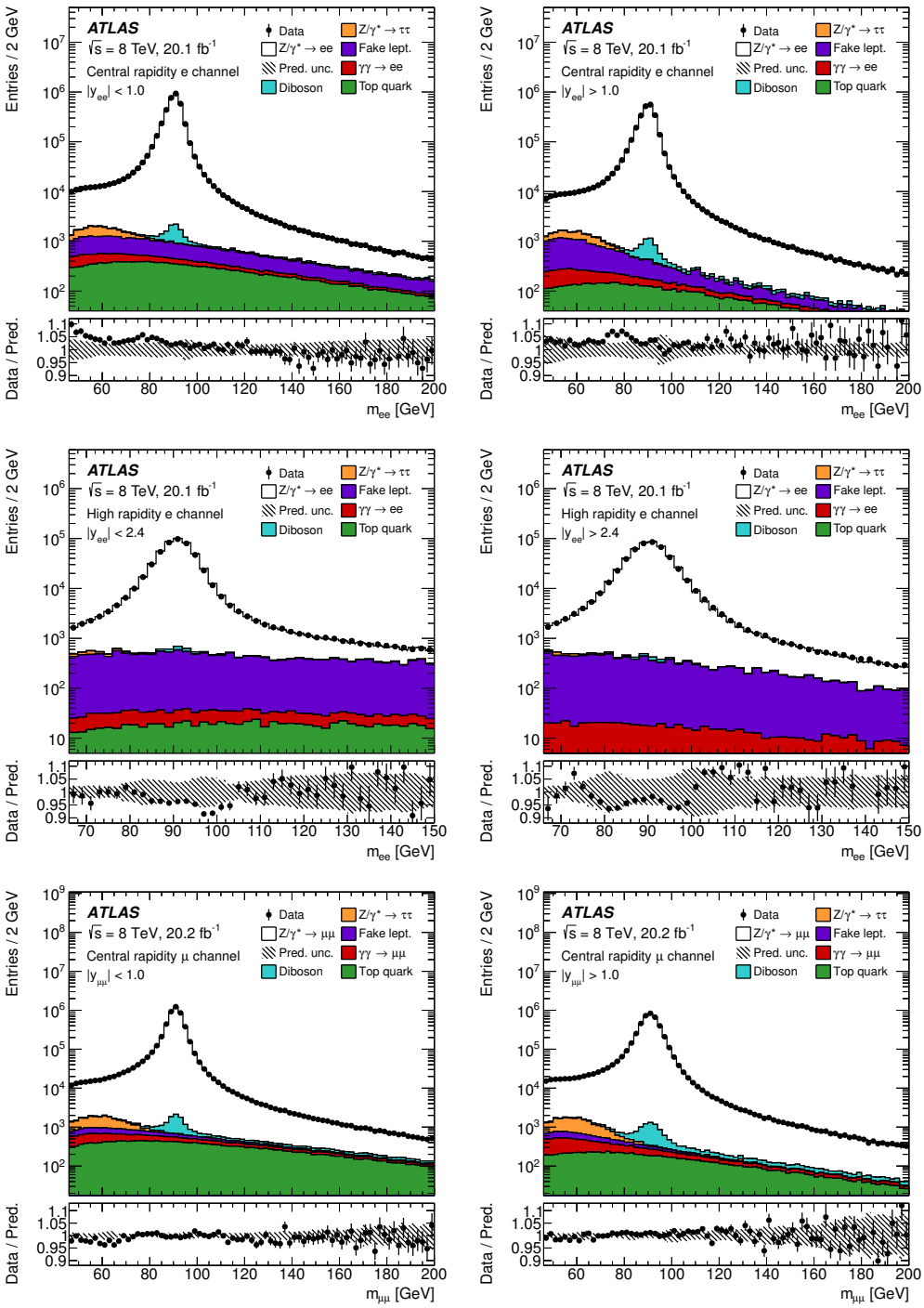

Figure 4. Distributions of invariant mass for all three measurements: the central rapidity electron (top row), the high rapidity electron channel (middle), and the central rapidity muon (bottom) channels. For the central measurements, the distributions are plotted for $|y_{\ell\ell}| < 1.0$ (left) and $|y_{\ell\ell}| > 1.0$ (right) while for the high rapidity measurement, regions $|y_{ee}| < 2.4$ (left) and $|y_{ee}| > 2.4$ (right) are shown. The data (solid markers) and the prediction (stacked histogram) are shown after event selection. The lower panels in each plot show the ratio of data to prediction. The error bars represent the data statistical uncertainty while the hatched band represents the systematic uncertainty in the prediction.

JHEP12(2017)059

7 Measurement uncertainties

The uncertainties in the measurements are discussed separately starting with the sources relevant to both electron channels, then the sources only appearing in the high rapidity electron channel. Next, sources of uncertainty specific to the muon channel are given followed by the sources common to all three measurements. Uncertainties due to statistical sources from both the data and MC samples, the modelling of the energy and momentum response to leptons, lepton selection efficiencies, background subtraction, and theoretical uncertainties are covered in this section. Each source is classified as being correlated or uncorrelated between measurement bins in a single channel. The sources are propagated using one of three techniques: the bootstrap method [67], the pseudo-experiment method, or the offset method.

7.1 Statistical uncertainties

The impact of the statistical uncertainty in the number of events in the data and MC simulations on the cross-section measurement is quantified using the bootstrap method, a statistical resampling technique in which each event is reweighted with a random number drawn from a Poisson distribution with a mean of unity. This reweighting procedure is done 1000 times producing 1000 replicas of the measurement. All replicas are then unfolded and the uncertainty is taken as the standard deviation of the measured cross sections. In the case of the signal MC sample the bootstrap replicas are used to produce an ensemble of 1000 response matrices which are used to unfold the measurement. The standard deviation of the unfolded cross sections is used as the signal MC statistical uncertainty.

7.2 Systematic uncertainties

The pseudo-experiment method is used for correction factors determined in bins of lepton kinematics, typically η and transverse energy/momentum. These correction factors have statistical and systematic uncertainties which are fluctuated randomly using 1000 pseudo-experiments according to a Gaussian distribution whose mean and standard deviation are set to the value and uncertainty of the correction factor, respectively. For correlated sources, a single set of varied correction factors is used for all measurement bins, whereas for uncorrelated sources the random shifts are applied separately for each bin. The uncertainties are propagated via the unfolding procedure yielding 1000 cross-section results which are used to determine a covariance matrix.

In the offset method the correction factor values from each source are coherently shifted upwards and downwards by one standard deviation and the measurement is remade using the varied values. The uncertainty is taken as half the difference between the two unfolded measurements.

7.3 Central and high rapidity electron channels

The systematic uncertainties in the cross section that are unique to the electron channels are dominated by the uncertainties in the electron energy scale, and the electron reconstruction and identification efficiency uncertainties. In addition, a large contribution to the

JHEP12(2017)059

uncertainty arises from the electron energy resolution uncertainty in the two neighbouring m_{ee} bins at the Z-peak, $80 < m_{ee} < 91$ GeV and $91 < m_{ee} < 102$ GeV.

7.3.1 Energy scale and resolution

The electron energy scale and resolution and their corresponding uncertainties are determined using $Z \to e^+e^-$, $W \to e\nu$, and $J/\psi \to e^+e^-$ decays. The uncertainty in the energy scale is separated into a statistical component and 14 uncorrelated systematic sources. Some of these sources are split into fine η^e bins, while others are coarsely binned into barrel and endcap regions as described in reference [57]. These sources are found to be strongly anti-correlated between the regions $m_{ee} < m_Z$ and $m_{ee} > m_Z$. The statistical uncertainty in the energy scale is found to be negligible. Adding the effects of the 14 sources of uncertainty in the energy scale in quadrature after propagating to the measured cross sections, the combined uncertainty is 1–2% for the mass bins $80 < m_{ee} < 91$ GeV and $91 < m_{ee} < 102$ GeV, but is less than 1% at low and high m_{ee}. However, in the integrated m_{ee} cross-section measurement the effect of these sources is strongly reduced as a result of the anti-correlation between these two m_{ee} bins.

The uncertainty in the energy resolution is separated into seven uncorrelated systematic sources which are propagated to the cross-section measurements individually. This combined uncertainty is typically 0.1–0.5% except in the invariant mass regions neighbouring the Z-peak where it reaches 1%.

7.3.2 Reconstruction and identification efficiencies

The reconstruction and identification efficiencies of electrons are determined from data using various tag-and-probe methods in Z and J/ψ decays, following the prescription in reference [58] with certain improvements and adjustments for the 2012 conditions [68]. The uncertainties arise from variations in the tag-and-probe selection and the background subtraction methods. The correlated systematic uncertainty is taken from the RMS of all variations, separately for the reconstruction and identification efficiency sources, and propagated using the pseudo-experiment method.

The influence of the identification efficiency uncertainty is found to be 0.2–0.4% increasing for larger $|\cos\theta^*|$, and up to 2% at low m_{ee}. The reconstruction efficiency uncertainty translates into a variation of the measured cross section which is generally below 0.2% but as large as 0.4% at low m_{ee}.

7.3.3 Trigger efficiency

The trigger efficiency is measured in both the data and MC simulation using a tag-and-probe method in $Z \to e^+e^-$ decays and is composed of a statistical uncorrelated component which is small, and a correlated piece which is propagated using the pseudo-experiment method. The resulting uncertainty in the cross section amounts to approximately 0.5% at low m_{ee} but decreases to approximately 0.1% for $m_{ee} > 116$ GeV.

JHEP12(2017)059

7.3.4 Charge misidentification

The electron charge is determined from the sign of the curvature of the associated ID track. Bremsstrahlung radiation and subsequent conversion of the radiated photons can lead to misidentification of the charge. This is measured in Z boson decays in which one lepton has an incorrectly reconstructed charge. Such events are selected by requiring the electron pair to possess the same electric charge and an invariant mass to be near m_Z, consistent with a Z boson decay. The resulting correlated uncertainty is propagated with the offset method and found to be less than 0.2% everywhere.

7.3.5 Multijet background

Uncertainties in the multijet estimation arise from the sample size used in the method, the subtracted signal and EW contamination, the shape of the multijet distribution, and the range of the isolation distribution used. The subtracted top quark and diboson contamination is varied coherently within the theoretical cross-section uncertainties. The subtracted signal contamination is varied by ±5%. The shape of the multijet distribution is varied by relaxing the same-sign charge requirement in the case of the central electron channel, and using the transverse energy E_{T}^{e} of the forward electron as an alternative discriminant in the high rapidity electron channel. The range of the isolation distribution used is varied by ±15%.

The variations made to account for systematic uncertainties in the method lead to changes in the estimated multijet yield in the central electron channel. The variations in the multijet yields range from about 10% at low m_{ee} and $\cos\theta^* \sim 0$, to more than 100% in regions where the nominal multijet yield is small, e.g. at large $|\cos\theta^*|$ and high m_{ee}.

The uncorrelated statistical component is propagated to the measured cross sections with the bootstrap replica method. The remaining two correlated components are propagated with the offset method, which when summed in quadrature amount to a measurement uncertainty of less than 0.1% of the cross section, except at low m_{ee} and large $|\cos\theta^*|$ where it grows to almost 1% in the central electron channel.

In the high rapidity channel the multijet yields range from 15% to more than 100% due to systematic uncertainties in the method. At small $\cos\theta^*$ and high invariant masses where the signal contribution is suppressed, the expected multijet background can be very large, as noted in section 5.2. Here, the systematic uncertainty in the multijet background is 20–70% depending on $|y_{ee}|$, resulting in a measurement uncertainty of 30% or greater when propagated to the triple-differential cross section.

7.4 High rapidity electron channel

The high rapidity electron analysis differs from the central electron channel measurement by requiring one electron to be in the forward region $2.5 < |\eta^e| < 4.9$ where there is no tracking system, which leads to larger background contamination. This is compensated for by the addition of an isolation requirement on the central electron, and more restrictive identification requirements (see section 4.2) on the central and forward electrons. The technique used to calibrate the forward calorimeters is also different, and the impact of

JHEP12(2017)059

potential charge misidentification is different. Since the charge can be measured only for the central electron, the impact of misidentification is to swap the sign of $\cos\theta^*$. Each of these leads to additional sources of systematic uncertainty which are discussed in the following.

The energy scale and resolution corrections for forward electrons lead to correlated sources of uncertainty propagated using the offset method. They arise from changes in the event selection used to perform the calibration as well as variations of the methodology. The influence of the scale uncertainty on the measurement is about 1% but can reach 5% at high $|\cos\theta^*|$. The resolution uncertainty amounts to 0.1–0.3% increasing to 3–5% at large $|\cos\theta^*|$ and off-peak mass bins.

The uncertainty in the cross-section measurement due to the identification efficiency of forward electrons is considered to be correlated across the measurement bins and is estimated using the pseudo-experiment method. It amounts to about 1% uncertainty in the cross section.

The efficiency of the isolation selection for central electrons is derived using a tag-and-probe method in central $Z \to e^+e^-$ decays and is well described by the simulation. The resulting uncertainty in the cross section is negligible.

To verify that the modelling of the W+jet background does not affect the estimation of the total fake lepton background in the high rapidity channel, its normalisation is varied by 60% (as motivated by reference [18]) and the fit of the multijet background is repeated. Since the shape of the E_{T} distribution is similar for the W+jet and multijet backgrounds, the total fake lepton background remains almost invariant for the off-peak regions while for the peak mass bins the variation is small compared to the multijet background uncertainty.

7.5 Central rapidity muon channel

Uncertainties related to the muon momentum scale and resolution, and the efficiencies of the muon trigger, reconstruction, and isolation and impact parameter selections are all studied using $Z \to \mu^+\mu^-$ events, and in some cases $J/\psi \to \mu^+\mu^-$ events are also used. The efficiencies are determined using a tag-and-probe method. The largest contributions to the systematic uncertainty in the measurements typically arise from the reconstruction efficiency and isolation efficiency modelling, and from the muon momentum scale calibration.

7.5.1 Momentum scale and resolution

Corrections to the muon momentum scale and resolution are obtained from fits to the $Z \to \mu^+\mu^-$ and $J/\psi \to \mu^+\mu^-$ lineshapes with scale and resolution parameters derived in local detector regions [60]. These sources are separated into 12 correlated components for the resolution in fine η^μ bins and one correlated component for the momentum scale. Uncertainties in the momentum scale arising from the methodology, and uncertainties in the ID material simulation, muon angle reconstruction, and alignment are propagated using the offset method. They result in a systematic uncertainty correlated in η^μ bins of the measured cross sections of typically 0.3%, increasing for larger $|y_{\mu\mu}|$, $|\cos\theta^*|$, and $m_{\mu\mu}$

JHEP12(2017)059

to 2%. The correlated resolution uncertainty has a small influence on the measurement and is also propagated with the offset method.

The influence of residual misalignments is estimated from two sources. The first arises from the statistical uncertainty of the alignment corrections derived using $Z \to \mu^+\mu^-$ data and is considered uncorrelated. This component is propagated to the cross section using the pseudo-experiment method, and is separated into 84 uncorrelated components. The second source accounts for biases in the correction method, and is defined as the difference between the corrections derived for data and simulation in bins of η^μ. This uncertainty is separated into 40 correlated components. After propagating this correlated source to the cross section using the pseudo-experiment method, the resulting uncertainty is found to be about 0.2%, increasing significantly with $|\cos\theta^*|$ at large $|y_{\mu\mu}|$.

7.5.2 Reconstruction efficiency

The uncertainty due to the muon reconstruction efficiency is parameterised as a function of η^μ and p_{T}^μ [60] and is decomposed into correlated and uncorrelated parts. The uncertainty is propagated to the cross section using the offset and pseudo-experiment methods for the correlated and uncorrelated components, respectively. The correlated component has an uncertainty of 0.1%, which corresponds to an uncertainty in the measured cross section of 0.2–0.4%.

7.5.3 Trigger efficiency

The efficiency corrections for single-muon and dimuon triggers are obtained using the tag-and-probe method as described in reference [61]. They are parameterised in terms of muon pseudorapidity η^μ, azimuthal angle ϕ^μ, and electric charge. The correlated uncertainty components arise from the background contamination, a possible residual dependence on muon p_{T}^μ, and an uncertainty based on the event topology, which are propagated using the offset method. The uncorrelated statistical uncertainty is propagated to the cross section using the pseudo-experiment method. Events selected with the single-muon triggers ($p_{\mathrm{T}}^\mu > 25\,\mathrm{GeV}$) cover most of the kinematic range of the measurement, whereas the dimuon triggers supplement the selection at low $m_{\mu\mu}$ and have somewhat larger uncertainties. This translates into a correlated uncertainty in the measured cross section which is typically 0.1% where the single-muon triggers are used, and can reach 0.6% at large $|\cos\theta^*|$ in the lowest $m_{\mu\mu}$ bin.

7.5.4 Isolation and impact parameter efficiency

Muon isolation and impact parameter selection efficiencies give rise to additional systematic uncertainties and are estimated together. The sources considered include the remaining background contamination, the residual variation in η^μ, and a possible bias from the event topology estimated by varying the azimuthal opening angle between the two muons used in the tag-and-probe method. The resulting correlated cross-section uncertainty determined with the pseudo-experiment method is found to be typically 0.2%, rising to 0.5% at high $m_{\mu\mu}$.

JHEP12(2017)059

7.5.5 Multijet background

The uncertainty in the multijet background estimate comes from several sources. The uncorrelated statistical uncertainty of the control regions is propagated using the bootstrap replica method and can be significant, in particular from the isolated same-charge control sample. The subtracted top quark and diboson contamination in the control regions is varied coherently within the theoretical cross-section uncertainties given in section 3. The subtracted signal contamination is varied by ±5%. The correlated uncertainty in the shape of the $|y_{\mu\mu}|$ and $|\cos\theta^*|$ spectra is determined from the RMS of these distributions in five regions of increasing non-isolation of the muon pairs obtained from the control regions. The final contribution comes from the fit extrapolation of the background estimate into the signal region and is assessed by varying the range of the fit. Systematic components lead to changes in the multijet yields of 15% to 30% of the expected signal contribution. This is largest in the regions of large $|\cos\theta^*|$. The variations can be up to 60% for large $|\cos\theta^*|$ and large $|y_{\ell\ell}|$.

Both the shape and extrapolation uncertainties are propagated to the cross section using the offset method and dominate the total uncertainty. The combined uncertainty in the background estimate when propagated to the cross-section measurement is below 0.1% in all measurement bins except in the lowest $m_{\mu\mu}$ bin where it reaches 1% at large $|\cos\theta^*|$ and small $|y_{\mu\mu}|$.

7.6 Systematic uncertainties common to all channels

The systematic uncertainties common to all three channels are derived using identical methods. With the exception of the statistical uncertainties arising from the MC samples used, which are uncorrelated between the measurement channels, common systematic uncertainties are assumed to be fully correlated between the channels. The dominant common uncertainty is the uncertainty in the luminosity measurement.

7.6.1 Top, diboson, W+jet, $Z/\gamma^* \to \tau\tau$, and photon-induced background normalisation

The normalisation uncertainties considered for these background sources arise from variations in the PDFs, α_S, and the QCD scales used in the theoretical predictions. The normalisation uncertainty in the top quark background, which is dominated by $t\bar{t}$ production, is taken to be 6% following the PDF4LHC prescription [69]. The uncertainty includes scale and α_S variations and also takes into account the uncertainty in the top-quark mass. Diboson (WW, WZ and ZZ) production is another important background source for which the normalisation uncertainties are about 10%. See reference [17] for additional information on the normalisation uncertainties of the various Monte Carlo samples used.

The background contributions from W+jet processes are assigned a normalisation uncertainty of 5% for the central rapidity measurements. For the high rapidity electron channel, where W+jet is a dominant background, a variation of 60% is considered (see section 7.4).

The background contribution from $Z/\gamma^* \to \tau\tau$ decays is assigned a normalisation uncertainty of 5%. The photon-induced background is assigned an uncertainty of 40%,

JHEP12(2017)059

derived by calculating the photon-induced contribution in a constituent and a current mass scheme for the quark [41], and taking the magnitude of the difference between either scheme and their average [13]. In all cases the normalisation uncertainties are propagated to the final cross sections using the offset method.

7.6.2 Unfolding bias

The simulation used as an initial prior in the unfolding process could lead to a potential bias in the measured cross sections. This potential bias is quantified by varying the predictions within theoretical uncertainties. The PDF bias is probed using signal MC events reweighted to each of the 26 different eigenvector variations of the CT10 PDF set in the determination of $\mathcal{M}$. For each variation the change in the unfolded cross section is found to be much smaller than the change in the predicted cross section using each eigenvector PDF set. Changing the PDF set can alter the predicted cross section by up to a few percent but the influence on the unfolded result is less than 0.1%. Furthermore, the change in the unfolded result, using one to five iterations of unfolding, is much smaller than the total uncertainty in the data. This study is repeated by reweighting the signal MC events to different values of the scattering amplitude coefficient $A_4 = \frac{8}{3}A_{\mathrm{FB}}$, which is proportional to $\sin^2\theta_W$. A variation of ± 0.01 is used, corresponding to a maximum change of 0.5% in the cross-section prior, which results in a change in the unfolded cross section of less than 0.1%. These studies show that potential biases are small for five iterations or less.

A potential overestimate or underestimate of the statistical and systematic uncertainties of the measurement due to the chosen number of unfolding iterations is also studied. Tests of the statistical uncertainty are performed using pseudo-data generated using an alternative PDF. Ultimately, two unfolding iterations are used for the final cross-section determination. This number has a negligible bias due to the initial prior and produces a negligible bias in the data statistical and systematic uncertainties.

7.6.3 MC modelling

The Z boson p_{T} distribution is not well modelled in MC simulation and could influence the measurement. The potential bias is estimated by reweighting the signal MC events to the observed data spectrum at reconstruction-level. This reweighted MC sample is used to unfold the cross section and the difference to the nominal measurement is taken as the uncertainty, which is typically below 0.1%, rising to about 1% at large $|\cos\theta^*|$ and large $|y_{\ell\ell}|$.

Adjustments to the reweighting of the scattering amplitude coefficients in the Powheg MC sample are found to have negligible impact on the measured cross sections.

The MC simulations used for modelling the underlying event and parton shower processes are not explicitly studied here, but are only expected to influence this measurement via the lepton isolation selection efficiencies. Studies presented in reference [18] indicate that such effects are small.

JHEP12(2017)059

7.6.4 PDF uncertainty

As discussed in section 6, the response matrix $\mathcal{M}$ also includes a small acceptance interpolation from the measured region to the fiducial region. These acceptance corrections differ in each of the three measurement channels due to $\eta^{e,\mu}$ gaps in the detector. The corrections are 5–10% but can be larger in certain bins of the triple-differential cross-section measurement. The PDF uncertainties due to these acceptance corrections are estimated using the CT10 PDF eigenvector set at 68% confidence level. They are found to be small, with uncertainties on the order of 0.1% or below for most cross-section measurement bins in the electron channel. In the high rapidity electron channel the uncertainty is also found to be small, except at large $|\cos\theta^*|$ where it can reach 0.6%. The uncertainty evaluated in the muon channel is found to be about 0.5% at low $m_{\mu\mu}$, negligible for $m_{\mu\mu}$ at m_Z, and reaches 0.6% for large $|\cos\theta^*|$ and large $|y_{\mu\mu}|$.

7.6.5 Luminosity

The uncertainty in the integrated luminosity is 1.9%, which is derived following the methodology detailed in reference [70]. This is fully correlated across all measurement bins and analysis channels.

7.7 Summary of measurement uncertainties

Tables 2–4 present the contributions of the individual uncertainties discussed above for each channel in selected analysis bins. The influence of the experimental systematic uncertainties on the measurements of $\mathrm{d}^3\sigma$ can be divided into three regions of $m_{\ell\ell}$ — below the resonance peak, on the peak region, and above the resonance. In the electron channels, the largest measurement uncertainties arise from background and efficiency correction uncertainties at low and high $m_{\ell\ell}$. In the peak region the uncertainty is dominated by the energy scale sources. The muon channel precision is limited by the background uncertainty at low $m_{\ell\ell}$, and by both the momentum scale and misalignment uncertainties in the peak region. At larger invariant mass the uncertainties related to the muon reconstruction and isolation efficiency also become important.

JHEP12(2017)059

Bin	m_{ee} [GeV]	$\lvert y_{ee}\rvert$	$\cos\theta^*$	$\delta^{\rm stat}_{\rm unc}$ [%]	$\delta^{\rm sig}_{\rm unc}$ [%]	$\delta^{\rm bkg}_{\rm unc}$ [%]	$\delta^{\rm mj}_{\rm unc}$ [%]	$\delta^{\rm bkg}_{\rm cor}$ [%]	$\delta^{\rm mj}_{\rm cor}$ [%]	$\delta^{\rm scl}_{\rm cor}$ [%]	$\delta^{\rm res}_{\rm cor}$ [%]	$\delta^{\rm rec}_{\rm cor}$ [%]	$\delta^{\rm id}_{\rm cor}$ [%]	$\delta^{\rm trig}_{\rm cor}$ [%]	$\delta^{\rm qmid}_{\rm cor}$ [%]	$\delta^{\rm kfac}_{\rm cor}$ [%]	$\delta^{\rm zpt}_{\rm cor}$ [%]	$\delta^{\rm pdf}_{\rm cor}$ [%]	$\delta^{\rm tot}$ [%]
1	46, 66	0.0, 0.2	−1.0, −0.7	6.7	2.4	3.4	3.1	1.9	5.2	0.5	0.7	0.5	2.5	0.7	0.2	0.0	0.9	0.2	10.6
2	46, 66	0.0, 0.2	−0.7, −0.4	2.3	0.8	1.2	0.9	1.1	2.0	0.2	0.2	0.5	2.7	0.9	0.0	0.0	0.0	0.1	4.7
3	46, 66	0.0, 0.2	−0.4, 0.0	1.4	0.5	0.9	0.4	0.9	0.9	0.3	0.1	0.3	1.9	0.3	0.0	0.0	0.0	0.0	2.9
4	46, 66	0.0, 0.2	0.0, +0.4	1.4	0.5	0.8	0.5	0.9	0.9	0.3	0.1	0.3	1.9	0.3	0.0	0.0	0.0	0.1	3.0
5	46, 66	0.0, 0.2	+0.4, +0.7	2.2	0.8	0.9	0.9	1.1	2.0	0.2	0.1	0.5	2.6	0.8	0.0	0.0	0.0	0.1	4.5
6	46, 66	0.0, 0.2	+0.7, +1.0	6.7	2.3	4.8	3.1	1.8	4.9	0.9	0.5	0.5	2.6	0.7	0.1	0.0	0.9	0.2	10.9
79	66, 80	0.2, 0.4	−1.0, −0.7	2.7	1.3	0.5	0.7	0.5	1.6	1.5	1.1	0.6	3.7	1.2	0.1	0.0	0.3	0.2	5.6
80	66, 80	0.2, 0.4	−0.7, −0.4	1.3	0.6	0.4	0.3	0.3	0.3	0.4	0.4	0.3	1.7	0.4	0.1	0.0	0.0	0.0	2.5
81	66, 80	0.2, 0.4	−0.4, 0.0	1.3	0.4	0.4	0.3	0.3	0.1	0.3	0.1	0.1	0.7	0.2	0.0	0.0	0.0	0.0	1.6
82	66, 80	0.2, 0.4	0.0, +0.4	1.2	0.5	0.3	0.4	0.3	0.1	0.3	0.1	0.1	0.7	0.2	0.1	0.0	0.0	0.0	1.7
83	66, 80	0.2, 0.4	+0.4, +0.7	1.4	0.6	0.3	0.3	0.3	0.3	0.6	0.2	0.3	1.7	0.4	0.1	0.0	0.1	0.0	2.6
84	66, 80	0.2, 0.4	+0.7, +1.0	2.7	1.4	0.4	0.7	0.4	1.6	2.8	1.0	0.6	3.8	1.2	0.2	0.0	0.3	0.1	6.1
157	80, 91	0.4, 0.6	−1.0, −0.7	0.6	0.3	0.0	0.1	0.0	0.1	1.4	0.3	0.3	3.2	0.4	0.1	0.0	0.0	0.1	3.6
158	80, 91	0.4, 0.6	−0.7, −0.4	0.4	0.2	0.0	0.0	0.0	0.0	1.0	0.1	0.1	0.5	0.2	0.1	0.0	0.1	0.0	1.2
159	80, 91	0.4, 0.6	−0.4, 0.0	0.4	0.1	0.0	0.0	0.0	0.0	1.0	0.1	0.0	0.3	0.1	0.1	0.0	0.0	0.0	1.1
160	80, 91	0.4, 0.6	0.0, +0.4	0.4	0.1	0.0	0.0	0.0	0.0	1.0	0.0	0.0	0.3	0.1	0.1	0.0	0.0	0.0	1.2
161	80, 91	0.4, 0.6	+0.4, +0.7	0.4	0.2	0.0	0.0	0.0	0.0	1.0	0.1	0.1	0.5	0.2	0.1	0.0	0.1	0.0	1.2
162	80, 91	0.4, 0.6	+0.7, +1.0	0.6	0.3	0.0	0.0	0.0	0.1	1.6	0.2	0.3	3.2	0.4	0.1	0.0	0.0	0.1	3.7
235	91, 102	0.6, 0.8	−1.0, −0.7	0.5	0.2	0.0	0.1	0.0	0.0	2.1	0.2	0.3	2.6	0.5	0.0	0.0	0.2	0.0	3.5
236	91, 102	0.6, 0.8	−0.7, −0.4	0.4	0.2	0.0	0.0	0.0	0.0	1.3	0.0	0.1	0.5	0.2	0.0	0.0	0.1	0.0	1.5
237	91, 102	0.6, 0.8	−0.4, 0.0	0.4	0.1	0.0	0.0	0.0	0.0	1.0	0.1	0.0	0.2	0.1	0.0	0.0	0.0	0.0	1.1
238	91, 102	0.6, 0.8	0.0, +0.4	0.3	0.1	0.0	0.0	0.0	0.0	1.0	0.0	0.0	0.2	0.1	0.0	0.0	0.0	0.0	1.1
239	91, 102	0.6, 0.8	+0.4, +0.7	0.4	0.2	0.0	0.0	0.0	0.0	1.2	0.0	0.1	0.5	0.2	0.0	0.0	0.1	0.0	1.4
240	91, 102	0.6, 0.8	+0.7, +1.0	0.5	0.2	0.0	0.1	0.0	0.1	2.1	0.1	0.3	2.6	0.5	0.0	0.0	0.2	0.0	3.4
313	102, 116	0.8, 1.0	−1.0, −0.7	2.8	1.2	0.6	0.8	0.5	0.7	2.1	0.9	0.2	1.4	0.3	0.1	0.0	0.1	0.0	4.3
314	102, 116	0.8, 1.0	−0.7, −0.4	2.6	1.2	0.2	0.5	0.2	0.9	2.3	1.0	0.0	0.4	0.2	0.0	0.0	0.1	0.1	4.0
315	102, 116	0.8, 1.0	−0.4, 0.0	2.0	0.8	1.6	0.3	0.2	0.2	1.0	0.3	0.1	0.3	0.1	0.1	0.0	0.0	0.0	2.9
316	102, 116	0.8, 1.0	0.0, +0.4	1.8	0.7	0.1	0.2	0.2	0.1	0.9	0.5	0.1	0.3	0.1	0.0	0.0	0.1	0.1	2.2
317	102, 116	0.8, 1.0	+0.4, +0.7	2.3	1.0	0.5	0.4	0.2	0.7	1.7	1.3	0.0	0.4	0.2	0.1	0.0	0.0	0.1	3.5
318	102, 116	0.8, 1.0	+0.7, +1.0	2.3	1.0	0.2	0.6	0.3	0.6	2.1	0.6	0.2	1.4	0.3	0.0	0.0	0.0	0.1	3.8
391	116, 150	1.0, 1.2	−1.0, −0.7	4.8	1.0	2.8	1.8	1.3	5.1	0.2	0.4	0.1	0.4	0.2	0.1	0.0	0.0	0.1	8.0
392	116, 150	1.0, 1.2	−0.7, −0.4	3.5	0.9	0.4	0.7	0.7	0.6	0.6	0.1	0.1	0.3	0.2	0.1	0.0	0.2	0.1	3.9
393	116, 150	1.0, 1.2	−0.4, 0.0	3.1	0.8	1.3	0.4	0.5	0.8	0.6	0.1	0.1	0.4	0.2	0.1	0.0	0.0	0.2	3.7
394	116, 150	1.0, 1.2	0.0, +0.4	3.0	0.8	0.6	0.5	0.4	0.9	0.6	0.2	0.1	0.4	0.2	0.1	0.0	0.1	0.0	3.5
395	116, 150	1.0, 1.2	+0.4, +0.7	2.8	0.7	0.5	0.5	0.5	0.4	0.6	0.4	0.1	0.3	0.2	0.1	0.0	0.1	0.1	3.2
396	116, 150	1.0, 1.2	+0.7, +1.0	3.7	0.8	2.2	1.1	0.8	3.4	0.4	0.2	0.1	0.4	0.2	0.1	0.0	0.0	0.1	5.7
469	150, 200	1.2, 1.4	−1.0, −0.7	11.9	1.4	2.0	3.6	2.2	1.5	0.4	0.3	0.1	0.5	0.3	0.1	0.0	0.0	0.2	12.9
470	150, 200	1.2, 1.4	−0.7, −0.4	6.6	0.8	1.0	5.9	1.6	0.9	0.9	0.2	0.1	0.5	0.3	0.1	0.0	0.0	0.1	9.2
471	150, 200	1.2, 1.4	−0.4, 0.0	6.6	1.0	3.1	1.9	1.0	0.4	1.0	0.1	0.2	0.6	0.3	0.2	0.0	0.0	0.1	7.8
472	150, 200	1.2, 1.4	0.0, +0.4	5.3	0.9	0.8	0.9	0.6	0.2	0.6	0.2	0.2	0.6	0.3	0.2	0.0	0.1	0.0	5.6
473	150, 200	1.2, 1.4	+0.4, +0.7	4.4	0.6	0.5	1.9	0.7	0.4	0.9	0.2	0.1	0.5	0.3	0.1	0.0	0.0	0.0	5.0
474	150, 200	1.2, 1.4	+0.7, +1.0	7.6	0.9	1.1	2.3	1.1	0.7	0.3	0.2	0.1	0.5	0.3	0.2	0.0	0.0	0.1	8.3

Table 2. Central rapidity electron channel uncertainties in selected bins. All uncertainties quoted are in units of percent, relative to the measured differential cross section. The uncertainties are separated into those which are bin-to-bin correlated within a single channel (marked "cor") and those which are uncorrelated (marked "unc"). The sources are the uncertainties arising from the data sample size ($\delta^{\rm stat}_{\rm unc}$); the signal MC sample size ($\delta^{\rm sig}_{\rm unc}$); the sizes of the background MC samples ($\delta^{\rm bkg}_{\rm unc}$); the statistical component of the multijet estimation ($\delta^{\rm mj}_{\rm unc}$); the combined correlated (normalisation) component of all background MC samples ($\delta^{\rm bkg}_{\rm cor}$); the multijet estimation ($\delta^{\rm mj}_{\rm cor}$); the electron energy scale ($\delta^{\rm scl}_{\rm cor}$) and resolution ($\delta^{\rm res}_{\rm cor}$); the reconstruction ($\delta^{\rm rec}_{\rm cor}$), identification ($\delta^{\rm id}_{\rm cor}$), and trigger efficiencies ($\delta^{\rm trig}_{\rm cor}$); the electron charge misidentification ($\delta^{\rm qmid}_{\rm cor}$); the K-factors ($\delta^{\rm kfac}_{\rm cor}$); the Z boson $p_{\rm T}$ modelling ($\delta^{\rm zpt}_{\rm cor}$); the PDF variation ($\delta^{\rm pdf}_{\rm cor}$); and the total measurement uncertainty ($\delta^{\rm tot}$). The luminosity uncertainty is not included in these tables.

JHEP12(2017)059

Bin	m_{ee} [GeV]	$\lvert y_{ee}\rvert$	$\cos\theta^*$	$\delta^{\rm stat}_{\rm unc}$ [%]	$\delta^{\rm sig}_{\rm unc}$ [%]	$\delta^{\rm bkg}_{\rm unc}$ [%]	$\delta^{\rm mj}_{\rm unc}$ [%]	$\delta^{\rm bkg}_{\rm cor}$ [%]	$\delta^{\rm mj}_{\rm cor}$ [%]	$\delta^{\rm scl}_{\rm cor}$ [%]	$\delta^{\rm res}_{\rm cor}$ [%]	$\delta^{\rm fscl}_{\rm cor}$ [%]	$\delta^{\rm fres}_{\rm cor}$ [%]	$\delta^{\rm rec}_{\rm cor}$ [%]	$\delta^{\rm id}_{\rm cor}$ [%]	$\delta^{\rm trig}_{\rm cor}$ [%]	$\delta^{\rm iso}_{\rm cor}$ [%]	$\delta^{\rm fid}_{\rm cor}$ [%]	$\delta^{\rm qmid}_{\rm cor}$ [%]	$\delta^{\rm kfac}_{\rm cor}$ [%]	$\delta^{\rm zpt}_{\rm cor}$ [%]	$\delta^{\rm pdf}_{\rm cor}$ [%]	$\delta^{\rm tot}$ [%]
1	66, 80	1.2, 1.6	−1.0, −0.7	6.4	3.0	6.0	4.5	0.9	11.5	0.4	0.6	3.1	2.1	0.2	0.8	0.3	0.0	0.7	0.0	0.0	0.8	0.6	16.0
2	66, 80	1.2, 1.6	−0.7, −0.4	16.4	8.7	8.0	9.9	0.5	11.4	0.5	1.2	5.8	2.5	0.1	0.2	0.1	0.0	0.8	0.0	0.0	0.8	0.3	26.0
3	66, 80	1.2, 1.6	−0.4, 0.0	—	—	—	—	—	—	—	—	—	—	—	—	—	—	—	—	—	—	—	—
4	66, 80	1.2, 1.6	0.0, +0.4	—	—	—	—	—	—	—	—	—	—	—	—	—	—	—	—	—	—	—	—
5	66, 80	1.2, 1.6	+0.4, +0.7	15.7	8.0	6.7	7.9	0.5	10.7	0.9	0.8	3.8	5.5	0.1	0.1	0.1	0.0	0.8	0.0	0.0	1.6	1.4	24.1
6	66, 80	1.2, 1.6	+0.7, +1.0	7.9	3.3	8.8	5.8	1.6	15.3	0.7	0.7	2.3	2.9	0.2	0.8	0.3	0.0	0.7	0.0	0.0	0.9	0.3	20.9
19	66, 80	2.4, 2.8	−1.0, −0.7	3.4	2.2	1.4	2.8	0.3	3.4	2.5	0.7	4.3	5.2	0.2	1.6	0.4	0.1	1.4	0.0	0.0	2.4	0.2	10.1
20	66, 80	2.4, 2.8	−0.7, −0.4	2.2	1.3	0.8	1.6	0.3	1.1	1.2	0.6	3.1	3.9	0.1	0.8	0.2	0.0	1.3	0.0	0.0	0.5	0.1	6.4
21	66, 80	2.4, 2.8	−0.4, 0.0	2.3	1.0	0.8	1.4	0.2	1.5	0.4	0.2	0.9	0.3	0.1	0.5	0.2	0.0	0.8	0.0	0.0	0.1	0.0	3.6
22	66, 80	2.4, 2.8	0.0, +0.4	2.8	1.2	1.5	1.9	0.4	2.0	0.4	0.5	1.3	0.3	0.1	0.5	0.2	0.0	0.7	0.0	0.0	0.3	0.1	4.7
23	66, 80	2.4, 2.8	+0.4, +0.7	2.7	1.6	1.3	2.3	0.4	1.7	1.6	0.2	4.0	6.0	0.1	0.8	0.2	0.0	1.4	0.1	0.0	1.1	0.2	8.8
24	66, 80	2.4, 2.8	+0.7, +1.0	4.2	2.7	3.4	3.7	0.7	5.5	2.8	0.9	4.9	6.5	0.2	1.6	0.4	0.1	1.4	0.0	0.0	3.6	0.3	13.2
73	91, 102	2.0, 2.4	−1.0, −0.7	0.9	0.6	0.2	0.3	0.0	0.8	0.8	0.1	1.9	0.1	0.2	0.8	0.2	0.0	1.2	0.0	0.0	0.8	0.1	2.9
74	91, 102	2.0, 2.4	−0.7, −0.4	0.5	0.3	0.0	0.2	0.0	0.7	0.9	0.1	1.5	0.2	0.0	0.4	0.1	0.0	0.8	0.0	0.0	0.1	0.1	2.1
75	91, 102	2.0, 2.4	−0.4, 0.0	0.7	0.3	0.1	0.4	0.0	0.6	0.6	0.1	1.7	0.1	0.0	0.2	0.1	0.0	0.7	0.0	0.0	0.1	0.0	2.2
76	91, 102	2.0, 2.4	0.0, +0.4	0.6	0.3	0.1	0.4	0.0	0.5	0.5	0.1	1.5	0.1	0.0	0.2	0.1	0.0	0.7	0.0	0.0	0.1	0.1	2.0
77	91, 102	2.0, 2.4	+0.4, +0.7	0.5	0.3	0.1	0.1	0.0	0.5	0.9	0.2	1.3	0.3	0.0	0.4	0.1	0.0	0.8	0.0	0.0	0.2	0.1	2.0
78	91, 102	2.0, 2.4	+0.7, +1.0	0.9	0.5	0.2	0.3	0.0	0.3	0.7	0.2	1.6	0.2	0.2	0.7	0.2	0.0	1.2	0.0	0.0	0.8	0.0	2.6
97	102, 116	1.6, 2.0	−1.0, −0.7	3.8	1.8	2.0	2.9	0.7	4.2	0.6	0.3	2.4	2.2	0.1	0.3	0.1	0.0	0.8	0.0	0.0	1.5	0.1	7.9
98	102, 116	1.6, 2.0	−0.7, −0.4	4.4	2.1	2.0	3.4	0.3	3.6	1.2	0.6	2.1	1.2	0.0	0.2	0.0	0.0	0.7	0.0	0.0	1.5	0.2	8.0
99	102, 116	1.6, 2.0	−0.4, 0.0	—	—	—	—	—	—	—	—	—	—	—	—	—	—	—	—	—	—	—	—
100	102, 116	1.6, 2.0	0.0, +0.4	—	—	—	—	—	—	—	—	—	—	—	—	—	—	—	—	—	—	—	—
101	102, 116	1.6, 2.0	+0.4, +0.7	3.3	1.5	1.6	2.1	0.2	2.2	1.0	0.7	1.7	1.0	0.0	0.2	0.0	0.0	0.7	0.0	0.0	1.1	0.1	5.6
102	102, 116	1.6, 2.0	+0.7, +1.0	2.6	1.4	1.3	1.5	0.3	1.9	0.3	0.1	2.1	1.0	0.1	0.3	0.1	0.0	0.8	0.0	0.0	0.9	0.2	4.9
109	102, 116	2.4, 2.8	−1.0, −0.7	3.7	2.2	2.3	3.4	0.8	6.2	3.3	1.2	6.7	6.6	0.1	0.6	0.1	0.0	1.4	0.0	0.0	3.3	0.3	13.7
110	102, 116	2.4, 2.8	−0.7, −0.4	4.2	2.3	1.0	3.7	0.3	3.3	1.4	1.2	5.5	4.2	0.0	0.2	0.1	0.0	1.2	0.0	0.0	2.0	0.2	10.2
111	102, 116	2.4, 2.8	−0.4, 0.0	3.9	1.9	1.5	4.5	0.2	4.6	0.7	0.9	2.3	1.2	0.1	0.3	0.2	0.0	0.7	0.0	0.0	0.9	0.2	8.5
112	102, 116	2.4, 2.8	0.0, +0.4	3.1	1.5	0.7	2.9	0.1	3.2	0.6	0.4	2.3	1.3	0.1	0.3	0.1	0.0	0.8	0.0	0.0	0.9	0.1	6.3
113	102, 116	2.4, 2.8	+0.4, +0.7	2.7	1.6	1.1	1.7	0.2	1.6	1.2	0.8	4.0	2.1	0.0	0.2	0.1	0.0	1.2	0.0	0.0	1.4	0.2	6.5
114	102, 116	2.4, 2.8	+0.7, +1.0	2.2	1.4	1.3	1.5	0.3	2.4	2.0	0.8	3.3	3.2	0.1	0.6	0.1	0.0	1.3	0.0	0.0	2.2	0.1	7.0
127	116, 150	1.6, 2.0	−1.0, −0.7	8.4	1.7	8.7	7.1	2.9	29.0	0.2	0.4	1.8	1.2	0.0	0.1	0.0	0.0	0.6	0.0	0.0	0.7	0.2	32.5
128	116, 150	1.6, 2.0	−0.7, −0.4	7.6	2.0	4.2	9.0	1.3	8.6	0.6	0.2	0.3	0.5	0.0	0.1	0.0	0.0	0.6	0.0	0.0	0.5	0.2	15.4
129	116, 150	1.6, 2.0	−0.4, 0.0	—	—	—	—	—	—	—	—	—	—	—	—	—	—	—	—	—	—	—	—
130	116, 150	1.6, 2.0	0.0, +0.4	—	—	—	—	—	—	—	—	—	—	—	—	—	—	—	—	—	—	—	—
131	116, 150	1.6, 2.0	+0.4, +0.7	4.4	1.2	3.1	3.8	0.5	3.1	0.2	0.1	0.3	0.2	0.0	0.1	0.0	0.0	0.6	0.0	0.0	0.3	0.1	7.4
132	116, 150	1.6, 2.0	+0.7, +1.0	3.9	0.9	5.5	2.5	1.2	9.8	0.2	0.1	0.9	0.2	0.0	0.1	0.0	0.0	0.7	0.0	0.0	0.5	0.1	12.3
139	116, 150	2.4, 2.8	−1.0, −0.7	16.3	2.9	11.4	14.0	5.4	29.3	1.3	0.5	5.4	1.7	0.1	0.3	0.1	0.0	1.1	0.1	0.0	1.3	0.3	39.1
140	116, 150	2.4, 2.8	−0.7, −0.4	7.5	3.0	7.5	7.3	1.2	10.7	0.2	0.2	1.2	1.4	0.0	0.2	0.1	0.0	0.9	0.0	0.0	1.6	0.3	17.2
141	116, 150	2.4, 2.8	−0.4, 0.0	6.0	1.7	3.8	5.6	0.5	6.8	0.2	0.1	1.8	0.5	0.1	0.4	0.1	0.0	0.6	0.1	0.0	0.9	0.1	11.6
142	116, 150	2.4, 2.8	0.0, +0.4	4.5	1.4	3.1	3.2	0.5	3.4	0.1	0.5	0.8	0.2	0.1	0.4	0.1	0.0	0.6	0.0	0.0	0.5	0.1	7.4
143	116, 150	2.4, 2.8	+0.4, +0.7	3.8	1.4	2.4	2.4	0.4	3.3	0.3	0.3	0.9	0.7	0.0	0.2	0.1	0.0	1.0	0.0	0.0	0.9	0.1	6.5
144	116, 150	2.4, 2.8	+0.7, +1.0	3.3	1.0	1.7	2.0	0.7	3.8	0.7	0.2	1.8	0.6	0.1	0.3	0.1	0.0	1.1	0.0	0.0	0.2	0.1	6.3

Table 3. High rapidity electron channel uncertainties in selected bins. All uncertainties quoted are in units of percent, relative to the measured differential cross section. Bins with blank entries ("−") are those that have been omitted from the measurement due to a lack of expected events. The uncertainties are separated into those which are bin-to-bin correlated within a single channel (marked "cor") and those which are uncorrelated (marked "unc"). The sources are the uncertainties arising from the data sample size ($\delta^{\rm stat}_{\rm unc}$); the signal MC sample size ($\delta^{\rm sig}_{\rm unc}$); the sizes of the background MC samples ($\delta^{\rm bkg}_{\rm unc}$); the statistical component of the multijet estimation ($\delta^{\rm mj}_{\rm unc}$); the combined correlated (normalisation) component of all background MC samples ($\delta^{\rm bkg}_{\rm cor}$); the multijet estimation ($\delta^{\rm mj}_{\rm cor}$); the electron energy scale ($\delta^{\rm scl}_{\rm cor}$) and resolution ($\delta^{\rm res}_{\rm cor}$); the forward electron energy scale ($\delta^{\rm fscl}_{\rm cor}$) and resolution ($\delta^{\rm fres}_{\rm cor}$); the reconstruction ($\delta^{\rm rec}_{\rm cor}$), identification ($\delta^{\rm id}_{\rm cor}$), trigger ($\delta^{\rm trig}_{\rm cor}$), isolation ($\delta^{\rm iso}_{\rm cor}$), and forward identification efficiencies ($\delta^{\rm fid}_{\rm cor}$); the electron charge misidentification ($\delta^{\rm qmid}_{\rm cor}$); the K-factors ($\delta^{\rm kfac}_{\rm cor}$); the Z boson $p_{\rm T}$ modelling ($\delta^{\rm zpt}_{\rm cor}$); the PDF variation ($\delta^{\rm pdf}_{\rm cor}$); and the total measurement uncertainty ($\delta^{\rm tot}$). The luminosity uncertainty is not included in these tables.

JHEP12(2017)059

Bin	$m_{\mu\mu}$ [GeV]	$\lvert y_{\mu\mu}\rvert$	$\cos\theta^*$	$\delta^{\rm stat}_{\rm unc}$ [%]	$\delta^{\rm sig}_{\rm unc}$ [%]	$\delta^{\rm bkg}_{\rm unc}$ [%]	$\delta^{\rm bkg}_{\rm cor}$ [%]	$\delta^{\rm mj}_{\rm cor}$ [%]	$\delta^{\rm scl}_{\rm cor}$ [%]	$\delta^{\rm sag}_{\rm cor}$ [%]	$\delta^{\rm res}_{\rm cor}$ [%]	$\delta^{\rm rec}_{\rm cor}$ [%]	$\delta^{\rm id}_{\rm cor}$ [%]	$\delta^{\rm trig}_{\rm cor}$ [%]	$\delta^{\rm kfac}_{\rm cor}$ [%]	$\delta^{\rm zpt}_{\rm cor}$ [%]	$\delta^{\rm pdf}_{\rm cor}$ [%]	$\delta^{\rm tot}$ [%]
1	46, 66	0.0, 0.2	−1.0, −0.7	5.4	2.0	2.1	1.5	0.5	0.2	0.5	0.6	0.3	0.3	0.7	0.0	0.5	0.3	6.6
2	46, 66	0.0, 0.2	−0.7, −0.4	1.8	0.7	1.1	1.2	0.0	0.0	0.1	0.1	0.2	0.2	0.5	0.2	0.3	0.2	2.7
3	46, 66	0.0, 0.2	−0.4, 0.0	1.5	0.6	0.8	0.9	0.5	0.0	0.1	0.0	0.5	0.4	0.0	0.2	0.4	0.2	2.3
4	46, 66	0.0, 0.2	0.0, +0.4	1.5	0.6	0.9	0.9	0.5	0.0	0.1	0.1	0.5	0.4	0.0	0.2	0.5	0.2	2.3
5	46, 66	0.0, 0.2	+0.4, +0.7	1.9	0.6	1.2	1.2	0.0	0.1	0.1	0.4	0.2	0.2	0.5	0.2	0.3	0.2	2.8
6	46, 66	0.0, 0.2	+0.7, +1.0	5.7	2.0	3.6	1.8	0.5	0.1	1.0	0.1	0.3	0.3	0.8	0.2	0.6	0.8	7.7
79	66, 80	0.2, 0.4	−1.0, −0.7	2.3	1.1	0.5	0.6	0.7	0.1	0.7	0.4	0.2	0.2	0.3	0.0	0.0	0.1	3.0
80	66, 80	0.2, 0.4	−0.7, −0.4	1.3	0.7	0.3	0.4	0.1	0.1	0.2	0.1	0.3	0.3	0.0	0.0	0.0	0.1	1.7
81	66, 80	0.2, 0.4	−0.4, 0.0	1.4	0.7	0.4	0.3	0.2	0.1	0.2	0.2	0.4	0.4	0.0	0.1	0.1	0.3	1.8
82	66, 80	0.2, 0.4	0.0, +0.4	1.4	0.7	0.3	0.3	0.2	0.1	0.1	0.2	0.4	0.4	0.1	0.1	0.1	0.2	1.8
83	66, 80	0.2, 0.4	+0.4, +0.7	1.4	0.7	0.4	0.4	0.1	0.1	0.2	0.2	0.3	0.3	0.0	0.1	0.1	0.1	1.8
84	66, 80	0.2, 0.4	+0.7, +1.0	2.2	1.1	0.4	0.6	0.8	0.2	0.7	0.1	0.2	0.2	0.3	0.0	0.0	0.3	3.0
157	80, 91	0.4, 0.6	−1.0, −0.7	0.4	0.2	0.0	0.0	0.0	0.1	1.0	0.1	0.3	0.3	0.0	0.0	0.0	0.1	1.4
158	80, 91	0.4, 0.6	−0.7, −0.4	0.4	0.2	0.0	0.0	0.0	0.2	0.6	0.1	0.4	0.4	0.1	0.0	0.0	0.0	1.1
159	80, 91	0.4, 0.6	−0.4, 0.0	0.3	0.1	0.0	0.0	0.0	0.2	0.3	0.1	0.3	0.3	0.0	0.0	0.0	0.0	0.9
160	80, 91	0.4, 0.6	0.0, +0.4	0.3	0.1	0.0	0.0	0.0	0.2	0.3	0.1	0.3	0.3	0.0	0.0	0.0	0.0	0.9
161	80, 91	0.4, 0.6	+0.4, +0.7	0.4	0.2	0.0	0.0	0.0	0.2	0.6	0.0	0.4	0.4	0.1	0.0	0.0	0.0	1.1
162	80, 91	0.4, 0.6	+0.7, +1.0	0.4	0.2	0.0	0.0	0.0	0.2	1.1	0.1	0.3	0.3	0.1	0.0	0.1	0.0	1.4
235	91, 102	0.6, 0.8	−1.0, −0.7	0.4	0.2	0.0	0.0	0.0	0.1	0.5	0.0	0.3	0.3	0.1	0.0	0.1	0.0	1.0
236	91, 102	0.6, 0.8	−0.7, −0.4	0.3	0.2	0.0	0.0	0.0	0.1	1.0	0.0	0.4	0.4	0.2	0.0	0.0	0.0	1.3
237	91, 102	0.6, 0.8	−0.4, 0.0	0.3	0.1	0.0	0.0	0.0	0.1	0.3	0.0	0.2	0.2	0.0	0.0	0.0	0.0	0.8
238	91, 102	0.6, 0.8	0.0, +0.4	0.3	0.1	0.0	0.0	0.0	0.2	0.3	0.0	0.3	0.2	0.0	0.0	0.0	0.0	0.8
239	91, 102	0.6, 0.8	+0.4, +0.7	0.3	0.2	0.0	0.0	0.0	0.2	1.0	0.0	0.4	0.4	0.1	0.0	0.0	0.0	1.3
240	91, 102	0.6, 0.8	+0.7, +1.0	0.4	0.2	0.0	0.0	0.0	0.1	0.5	0.0	0.3	0.3	0.1	0.0	0.1	0.1	1.0
313	102, 116	0.8, 1.0	−1.0, −0.7	2.1	1.0	0.1	0.4	0.0	0.2	0.9	1.4	0.4	0.4	0.2	0.0	0.0	0.1	3.0
314	102, 116	0.8, 1.0	−0.7, −0.4	1.8	0.8	0.0	0.2	0.1	0.2	1.8	0.3	0.3	0.3	0.2	0.0	0.0	0.0	2.8
315	102, 116	0.8, 1.0	−0.4, 0.0	1.7	0.7	0.0	0.1	0.0	0.1	0.4	0.6	0.3	0.3	0.1	0.0	0.0	0.0	2.0
316	102, 116	0.8, 1.0	0.0, +0.4	1.6	0.6	0.0	0.1	0.0	0.2	0.4	0.5	0.3	0.3	0.0	0.0	0.0	0.0	2.0
317	102, 116	0.8, 1.0	+0.4, +0.7	1.6	0.7	0.0	0.2	0.1	0.2	2.0	0.8	0.4	0.3	0.1	0.0	0.0	0.1	2.8
318	102, 116	0.8, 1.0	+0.7, +1.0	2.0	0.9	0.1	0.3	0.0	0.2	0.8	1.5	0.4	0.4	0.0	0.0	0.0	0.0	2.7
391	116, 150	1.0, 1.2	−1.0, −0.7	4.1	1.2	0.3	1.3	0.0	0.1	0.5	0.3	0.5	0.5	0.2	0.1	0.0	0.1	4.8
392	116, 150	1.0, 1.2	−0.7, −0.4	2.9	0.7	0.2	0.7	0.1	0.1	0.7	0.4	0.4	0.3	0.2	0.0	0.1	0.1	3.4
393	116, 150	1.0, 1.2	−0.4, 0.0	2.5	0.6	0.1	0.5	0.1	0.1	0.5	0.1	0.3	0.3	0.2	0.0	0.1	0.1	2.8
394	116, 150	1.0, 1.2	0.0, +0.4	2.2	0.6	0.1	0.4	0.0	0.0	0.5	0.0	0.3	0.3	0.1	0.0	0.1	0.1	2.5
395	116, 150	1.0, 1.2	+0.4, +0.7	2.3	0.6	0.2	0.5	0.0	0.0	0.4	0.3	0.3	0.3	0.0	0.0	0.1	0.0	2.6
396	116, 150	1.0, 1.2	+0.7, +1.0	3.2	0.9	0.3	0.7	0.1	0.1	0.8	0.1	0.5	0.5	0.0	0.0	0.0	0.1	3.8
469	150, 200	1.2, 1.4	−1.0, −0.7	11.1	1.5	1.2	2.9	0.1	0.3	2.7	0.5	0.7	0.5	0.2	0.1	0.0	0.1	13.6
470	150, 200	1.2, 1.4	−0.7, −0.4	5.6	0.8	0.5	1.4	0.0	0.1	1.3	0.1	0.5	0.4	0.2	0.0	0.0	0.1	6.2
471	150, 200	1.2, 1.4	−0.4, 0.0	4.6	0.6	0.3	0.9	0.1	0.0	1.0	0.2	0.4	0.4	0.2	0.0	0.0	0.1	5.1
472	150, 200	1.2, 1.4	0.0, +0.4	4.1	0.5	0.2	0.7	0.1	0.0	1.1	0.0	0.4	0.4	0.1	0.0	0.0	0.0	4.5
473	150, 200	1.2, 1.4	+0.4, +0.7	4.0	0.5	0.2	0.8	0.0	0.1	0.8	0.2	0.4	0.4	0.0	0.0	0.0	0.1	4.3
474	150, 200	1.2, 1.4	+0.7, +1.0	6.6	0.9	0.5	1.2	0.1	0.0	1.7	0.0	0.6	0.5	0.0	0.0	0.1	0.1	8.0

Table 4. Central rapidity muon channel uncertainties in selected bins. All uncertainties quoted are in units of percent, relative to the measured differential cross section. The uncertainties are separated into those which are bin-to-bin correlated within a single channel (marked "cor") and those which are uncorrelated (marked "unc"). The sources are the uncertainties arising from the data sample size ($\delta^{\rm stat}_{\rm unc}$); the signal MC sample size ($\delta^{\rm sig}_{\rm unc}$); the sizes of the background MC samples ($\delta^{\rm bkg}_{\rm unc}$); the combined correlated (normalisation) component of all background MC samples ($\delta^{\rm bkg}_{\rm cor}$); the multijet estimation ($\delta^{\rm mj}_{\rm cor}$); the muon momentum scale ($\delta^{\rm scl}_{\rm cor}$); the sagitta bias corrections ($\delta^{\rm sag}_{\rm cor}$); the muon momentum resolution ($\delta^{\rm res}_{\rm cor}$); the reconstruction ($\delta^{\rm rec}_{\rm cor}$), identification ($\delta^{\rm id}_{\rm cor}$), and trigger efficiencies ($\delta^{\rm trig}_{\rm cor}$); the K-factors ($\delta^{\rm kfac}_{\rm cor}$); the Z boson $p_{\rm T}$ modelling ($\delta^{\rm zpt}_{\rm cor}$); the PDF variation ($\delta^{\rm pdf}_{\rm cor}$); and the total measurement uncertainty ($\delta^{\rm tot}$). The luminosity uncertainty is not included in these tables.

JHEP12(2017)059

8 Results

In the two invariant mass bins in the region $80 < m_{\ell\ell} < 102\,\text{GeV}$, the measurement of $\mathrm{d}^3\sigma$ in the central electron channel achieves a total uncertainty (excluding the luminosity contribution) of 1–2% per bin. In the muon channel the precision is better than 1%. In both cases the measurement precision is dominated by the experimental systematic uncertainties, compared to a data statistical uncertainty of about 0.5% per bin in this high-precision region. In the high rapidity electron channel, the precision of the measurement reaches 2–3% per bin, of which the statistical uncertainty is about 0.5%.

The data tables provided in this paper contain compact summaries of the measurement uncertainties; however, complete tables with the full breakdown of all systematic uncertainties and their correlated components are provided in HEPData [71, 72]. These complete tables also include the correction factors used to translate the unfolded measurements from the dressed-level to the Born-level as discussed in section 6.

8.1 Combination of the central rapidity electron and muon channels

The central rapidity electron and muon measurement channels are defined with a common fiducial region given in section 6 and therefore are combined to further reduce the experimental uncertainties. A χ^2-minimisation technique is used to combine the cross sections [73–75]. This method introduces a nuisance parameter for each systematic error source which contributes to the total χ^2. The sources of uncertainty considered are discussed in section 7. Correlated sources of uncertainty which are propagated with the pseudo-experiment or bootstrap resampling methods can be represented in covariance matrix form for each source. The covariance matrices are decomposed into eigenvector representations as input to the χ^2-minimisation function. For each covariance matrix the eigenvectors are sorted by the magnitude of their corresponding eigenvalues. The largest of the eigenvalues are added in order of decreasing value until their sum exceeds a certain fraction of the sum of all eigenvalues, f_{eig}. At which point the correlation information for the eigenvectors whose eigenvalues were not included in the sum is ignored and the eigenvectors are added in quadrature to form a diagonal uncorrelated uncertainty matrix. The resulting numbers of nuisance parameters depends on the complexity of the correlation pattern and on f_{eig}, for which values between 99% and 20% are chosen depending on the source.

This method of decomposition can accurately describe the full covariance matrix, and simultaneously reduce the number of nuisance parameters. The method preserves the total uncertainty and marginally enhances the uncorrelated component of the uncertainty by construction. The original and decomposed covariance matrices are compared and found to agree well such that the combined results are found to be stable in terms of χ^2 and the central values and their uncertainties when f_{eig} is varied around the chosen value in a wide range.

Bin-to-bin correlated sources of uncertainty which are also correlated between the two measurement channels share common nuisance parameters, and are listed in section 7.6. In total, 275 nuisance parameters are used in the procedure. The behaviour of the uncertainties with respect to the combined cross-section values can lead to non-Gaussian

JHEP12(2017)059

distributions of the nuisance parameters. For example, sources related to the selection efficiencies are expected to be proportional to the combined cross-section value, i.e. have multiplicative behaviour; sources related to background subtraction are expected to be independent of the combined cross section and therefore have an additive behaviour. Finally, data statistical sources are expected to be proportional to the square-root of the combined cross section, and have Poisson-like behaviour even after unfolding.

The combination of the central electron and muon channels introduces shifts and constraints to the nuisance parameters. These shifts are propagated to high rapidity electron channel measurement but only have a small impact on this channel since it is dominated by the forward calorimeter uncertainties. The combination of the electron and muon channel cross-section measurements results in a χ^2 per degree of freedom (dof) of 489/451 (p-value of 10%). The pulls of the individual channel measurements to the combined data are found to be Gaussian-distributed about zero with unit RMS. They do not indicate any trends as a function of the kinematic variables. The pulls of the nuisance parameters are similarly found to be Gaussian-distributed about zero with a somewhat larger width of 1.18. Only six nuisance parameters have shifts exceeding three standard deviations, which are sources related to the calibration of the electromagnetic calorimeter, and the source describing the normalisation of the $Z \to \tau\tau$ background MC sample. These particular sources have negligible impact on the measurement.

8.2 Compatibility tests and integrated measurements

In the following subsections, the triple-differential cross sections measured in each of the three channels are compared to one another. The compatibility of the combined data with published ATLAS DY measurements made using the same 2012 dataset is briefly discussed. Moreover, the combined triple-differential cross section is integrated to produce single- and double-differential cross sections which are then compared to theoretical predictions.

8.2.1 Compatibility of the central and high rapidity measurements

The measurements performed in the central electron and muon channels are compared with the high rapidity analysis to test for compatibility. The measurements are made in two different fiducial regions and therefore a common fiducial volume is defined within which the comparison is made. This volume is chosen to be $66 < m_{\ell\ell} < 150\,\text{GeV}$, $p_{\text{T}}^{\ell} > 20\,\text{GeV}$, and no requirement is made on the pseudorapidity of the lepton. The comparison is performed in the overlapping $|y_{\ell\ell}|$ bins of the central and high rapidity analyses.

The corresponding acceptance corrections are obtained from the Powheg simulation for each individual measurement bin. Bins with extrapolation factors smaller than 0.1 are excluded from this test, since they correspond to very restricted regions of phase space. Such regions are subject to large modelling uncertainties, in particular the uncertainty associated with modelling the Z boson transverse momentum. In each bin, the sum of the extrapolation factors for the central and high rapidity channels are found to be close to 80%, indicating that the two sets of measurements cover most of the phase space for $66 < m_{\ell\ell} < 150\,\text{GeV}$ and $p_{\text{T}}^{\ell} > 20\,\text{GeV}$. A second calculation of the extrapolation factors to the full phase space (i.e. $p_{\text{T}}^{\ell} > 0\,\text{GeV}$) has an uncertainty of 1.5%. This is assumed to be

JHEP12(2017)059

strongly anti-correlated between the factors for the central and high rapidity channels since the sum of factors is close to unity. Therefore, an additional 1% anti-correlated uncertainty in the extrapolation factors is used.

The uncertainties arising from electron efficiency corrections are taken to be uncorrelated between the central and high rapidity electron channels since they use different identification criteria and triggers. The multijet uncertainty is also taken to be uncorrelated. The χ^2/dof of the compatibility test is found to be 32/30 (p-value of 37%) for the electron channel and 39/30 (p-value of 13%) for the muon channel.

8.2.2 Compatibility with published data

The cross-section measurements in the central electron and muon channels partially overlap with published DY measurements from ATLAS using the same data set. They are differential measurements of the Z boson transverse momentum spectrum [16] and of the high-mass DY cross section for $m_{\ell\ell} > 116\,\text{GeV}$ [17]. The compatibility of the data presented here with these two published measurements has been tested in identical fiducial regions, separately for the electron and muon channels. The measurements are in good agreement with each other.

The reader is referred to [16] where the most precise measurements of integrated and p_{T}-differential Z cross sections were made in the fiducial region $p_{\text{T}}^{\ell} > 20\,\text{GeV}$ and $|\eta^{\ell}| < 2.4$.

For cross sections differential in $m_{\ell\ell}$ and $|y_{\ell\ell}|$ in the region $m_{\ell\ell} > 116\,\text{GeV}$, see the results presented in reference [17]. These measurements are given in the fiducial region of $p_{\text{T}}^{\ell} > 40, 30\,\text{GeV}$ for leading and subleading leptons, and $|\eta^{\ell}| < 2.5$. Note that the published cross sections include the $\gamma\gamma \to \ell^+\ell^-$ process.

For cross sections measured in the region $m_{\ell\ell} < 116\,\text{GeV}$ and differential in $m_{\ell\ell}$ and $|y_{\ell\ell}|$, the data presented in this paper should be used.

8.2.3 Integrated cross sections

The combined measurements are integrated over the kinematic variables $\cos\theta^*$ and $y_{\ell\ell}$ in order to determine the cross section $\mathrm{d}\sigma/\mathrm{d}m_{\ell\ell}$. Similarly, the integration is performed in $\cos\theta^*$ to determine the cross section $\mathrm{d}^2\sigma/\mathrm{d}m_{\ell\ell}\mathrm{d}|y_{\ell\ell}|$. The integration is firstly performed for the electron and muon channels separately to allow a χ^2-test for compatibility of the two channels. The measurements are simply summed in the e and μ channels for the bins in which both electron and muon measurements are present. Statistical and uncorrelated uncertainties are added in quadrature, whereas correlated systematic uncertainties are propagated linearly. The compatibility tests return $\chi^2/\text{dof} = 12.8/7$ (p-value of 7.7%) for the one-dimensional cross section, and 103/84 (p-value of 7.4%) for the two-dimensional cross section.

The integrated cross sections $\mathrm{d}\sigma/\mathrm{d}m_{\ell\ell}$ and $\mathrm{d}^2\sigma/\mathrm{d}m_{\ell\ell}\mathrm{d}|y_{\ell\ell}|$ are determined from the combined Born-level fiducial triple-differential cross sections. The one-dimensional result is shown in figure 5. The corresponding table of measurements is given in table 5 located in the appendix. The data shows that the combined Born-level fiducial cross section falls by three orders of magnitude in the invariant mass region from the resonant peak to 200 GeV. The data have an uncertainty of about 2%, dominated by the luminosity uncertainty of

JHEP12(2017)059

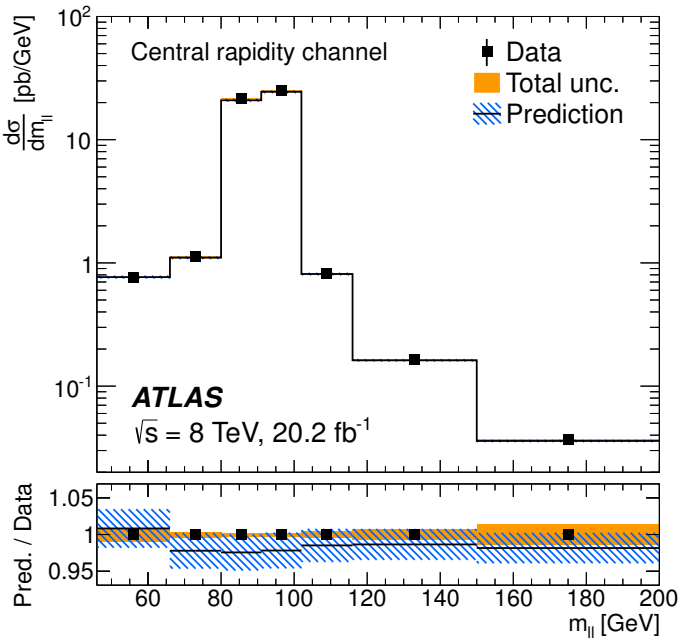

Figure 5. The combined Born-level fiducial cross section $\mathrm{d}\sigma/\mathrm{d}m_{\ell\ell}$. The data are shown as solid markers and the prediction from Powheg including NNLO QCD and NLO EW K-factors is shown as the solid line. The lower panel shows the ratio of prediction to measurement. The inner error bars represent the data statistical uncertainty and the solid band shows the total experimental uncertainty. The contribution to the uncertainty from the luminosity measurement is excluded. The hatched band represents the statistical and PDF uncertainties in the prediction.

1.9%, while uncertainties from the experimental systematic sources can be as low as 0.5% for the peak region. The statistical precision is 0.5% or better, even for the highest invariant mass bin. The fiducial measurements are well predicted by the NLO QCD and parton shower simulation from Powheg partially corrected for NNLO QCD and NLO EW effects, and scattering amplitude coefficients as described in section 3. The uncertainties in the predictions include those arising from the sample size and the PDF variations. No renormalization, factorisation and matching scale variation uncertainties are included although they can be sizeable — as large as 5% for NLO predictions. Except in the lowest mass bin, the predictions underestimate the cross section by about 1–2% (smaller than the luminosity uncertainty), as seen in the lower panel of the figure which shows the ratio of prediction to the measurement.

The two-dimensional Born-level fiducial cross section, $\mathrm{d}^2\sigma/\mathrm{d}m_{\ell\ell}\mathrm{d}|y_{\ell\ell}|$, is illustrated in figure 6 and listed in table 6 of the appendix. In each measured invariant mass bin, the shape of the rapidity distribution shows a plateau at small $|y_{\ell\ell}|$ leading to a broad shoulder followed by a cross section falling to zero at the highest accessible $|y_{\ell\ell}|$. The width of the plateau narrows with increasing $m_{\ell\ell}$. In the two high-precision Z-peak mass bins, the measured cross-section values have a total uncertainty (excluding the common luminosity uncertainty) of 0.4% for $|y_{\ell\ell}| < 1$ rising to 0.7% at $|y_{\ell\ell}| = 2.4$. At high invariant mass, the statistical and experimental uncertainty components contribute equally

JHEP12(2017)059

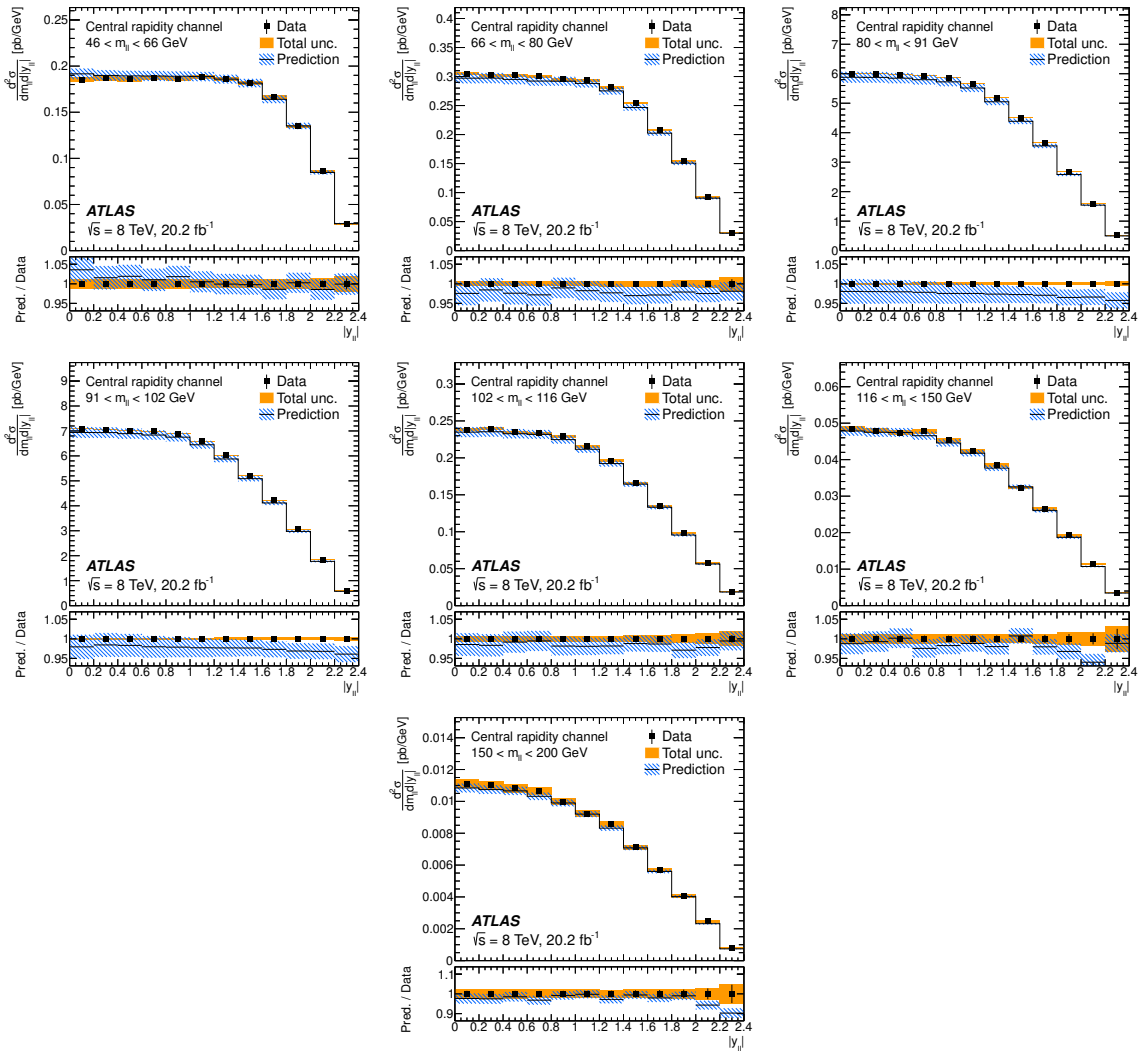

Figure 6. The combined Born-level fiducial cross section $\mathrm{d}^2\sigma/\mathrm{d}m_{\ell\ell}\mathrm{d}|y_{\ell\ell}|$ in the seven invariant mass bins of the central measurements. The data are shown as solid markers and the prediction from Powheg including NNLO QCD and NLO EW K-factors is shown as the solid line. The lower panel shows the ratio of prediction to measurement. The inner error bars represent the data statistical uncertainty and the solid band shows the total experimental uncertainty. The contribution to the uncertainty from the luminosity measurement is excluded. The hatched band represents the statistical and PDF uncertainties in the prediction.

to the total measurement precision in the plateau region, increasing from 0.5% to 1.8%. The theoretical predictions replicate the features in the data well. The lower panel of each figure shows the ratio of the prediction to the measurement. Here, in addition to overall rate difference already observed in the one-dimensional distribution, a small tendency of the data to exceed the predictions at the highest $|y_{\ell\ell}|$ can be seen in some of the mass bins.

JHEP12(2017)059

8.3 Triple-differential cross sections

The combined triple-differential Born-level cross section is shown in figures 7–10. For each invariant mass bin, the data are presented as a function of $|y_{\ell\ell}|$, with each of the six $\cos\theta^*$ regions overlaid in the main panel of the figures. The lower panels show in more detail the ratio of the prediction to the data for each $\cos\theta^*$ bin in turn. The statistical and total, excluding the contribution from the luminosity, uncertainties in the data are shown in the ratio panels.

The accessible range of the $|y_{\ell\ell}|$ distribution is largest for the region close to $\cos\theta^* \simeq 0$, and smallest at the extremes of $\cos\theta^*$. In the lowest invariant mass bin, the cross-section measurements in $\cos\theta^*$ bins with the same absolute value, e.g. bins $-1.0 < \cos\theta^* < -0.7$ and $+0.7 < \cos\theta^* < +1.0$, are consistent with each other at low $|y_{\ell\ell}| \simeq 0$, but exhibit an asymmetry which increases with $|y_{\ell\ell}|$. At large $|y_{\ell\ell}|$, the cross sections for $\cos\theta^* < 0$ are up to 35% larger than the corresponding measurements at $\cos\theta^* > 0$. In the $66 < m_{\ell\ell} < 80\,\text{GeV}$ bin, all cross sections are larger, for large $|\cos\theta^*|$ in particular, due to reduced influence of the fiducial selection on p_{T}^{ℓ}.

The next two invariant mass bins show the peak of the cross section where the asymmetry is smallest. In fact, for $80 < m_{\ell\ell} < 91\,\text{GeV}$ the difference between $\cos\theta^* > 0$ and $\cos\theta^* < 0$ is close to zero. The dramatic improvement in the overall precision of the measurements in this region is also apparent. For the $91 < m_{\ell\ell} < 102\,\text{GeV}$ region, the small asymmetry is observed to change sign, yielding larger cross sections for the $\cos\theta^* < 0$ part of the phase space. This behaviour is expected from the interference effects between the Z and γ^* contributions to the scattering amplitudes. For bins of higher invariant mass the asymmetry increases albeit with larger uncertainties due to the limited statistical precision of the data. The combined measurement is listed in table 7 with its uncertainties.

The predictions describe the data very well, as can be seen from the ratio panels, apart from some bins at large $|y_{\ell\ell}|$ and $|\cos\theta^*|$. These bins correspond to edges of the fiducial acceptance and may be affected by the $p_{\text{T},\ell\ell}$ modelling uncertainties which are not shown for the predictions.

In figures 11–15 the measured triple differential Born-level cross section for the high rapidity electron channel analysis is presented as a function of $\cos\theta^*$. In this channel the region of small $|\cos\theta^*|$ is experimentally accessible only for moderate values of rapidity, i.e. $|y_{\ell\ell}| \simeq 2.0$–$2.8$. Nevertheless the same features of the cross section are observed: the cross sections are largest for the region $m_{\ell\ell} \sim m_Z$; an asymmetry in the $\cos\theta^*$ spectrum is observed with larger cross sections at negative $\cos\theta^*$ for $m_{\ell\ell} < m_Z$, and larger cross sections at positive $\cos\theta^*$ for $m_{\ell\ell} > m_Z$; the magnitude of the asymmetry is smallest for $80 < m_{\ell\ell} < 91\,\text{GeV}$ and increases with $m_{\ell\ell}$. The triple-differential measurement is listed in table 8 with its uncertainties.

JHEP12(2017)059

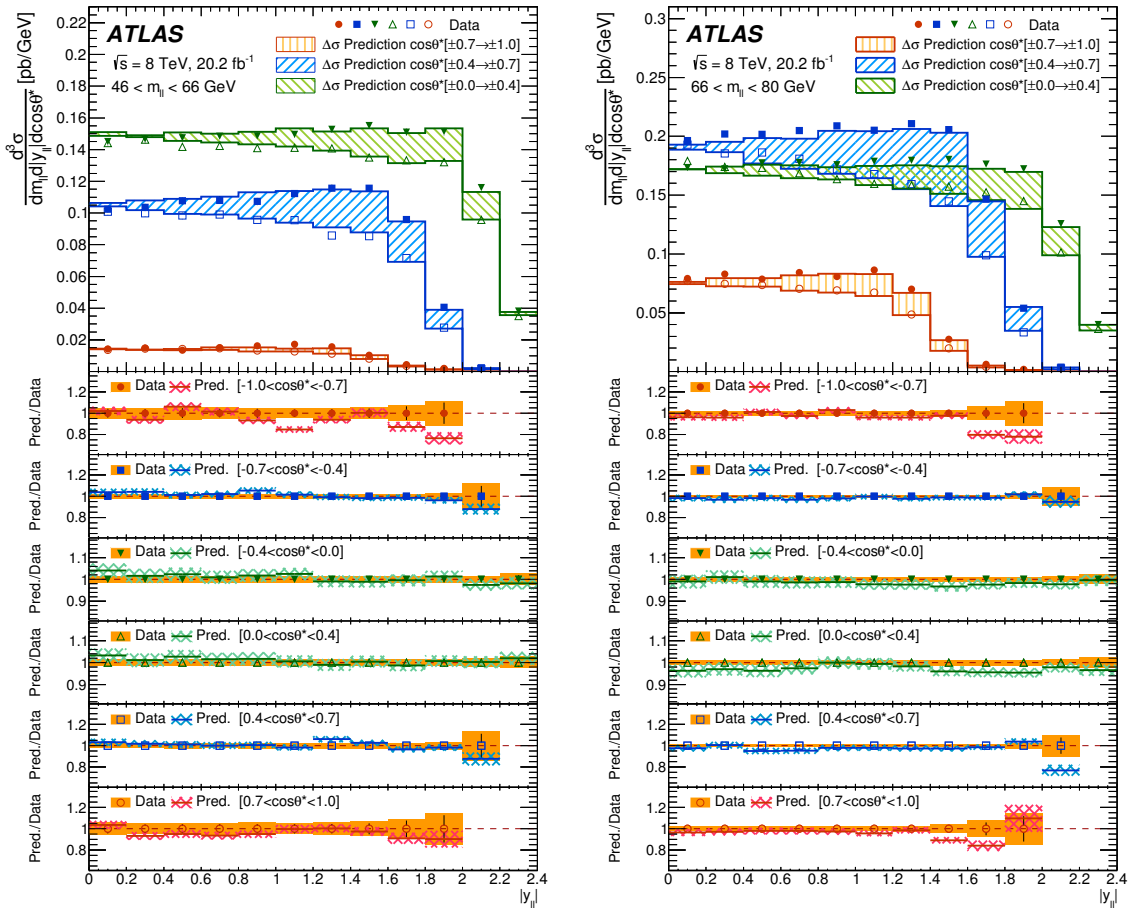

Figure 7. The combined Born-level fiducial cross sections $d^3\sigma$. The kinematic region shown is labelled in each plot. The data are shown as solid ($\cos\theta^* < 0$) and open ($\cos\theta^* > 0$) markers and the prediction from Powheg including NNLO QCD and NLO EW K-factors is shown as the solid line. The difference, $\Delta\sigma$, between the predicted cross sections in the two measurement bins at equal $|\cos\theta^*|$ symmetric around $\cos\theta^* = 0$ is represented by the hatched shading. In each plot, the lower panel shows the ratio of prediction to measurement. The inner error bars represent the statistical uncertainty of the data and the solid band shows the total experimental uncertainty. The contribution to the uncertainty from the luminosity measurement is excluded. The crosshatched band represents the statistical and PDF uncertainties in the prediction.

JHEP12(2017)059

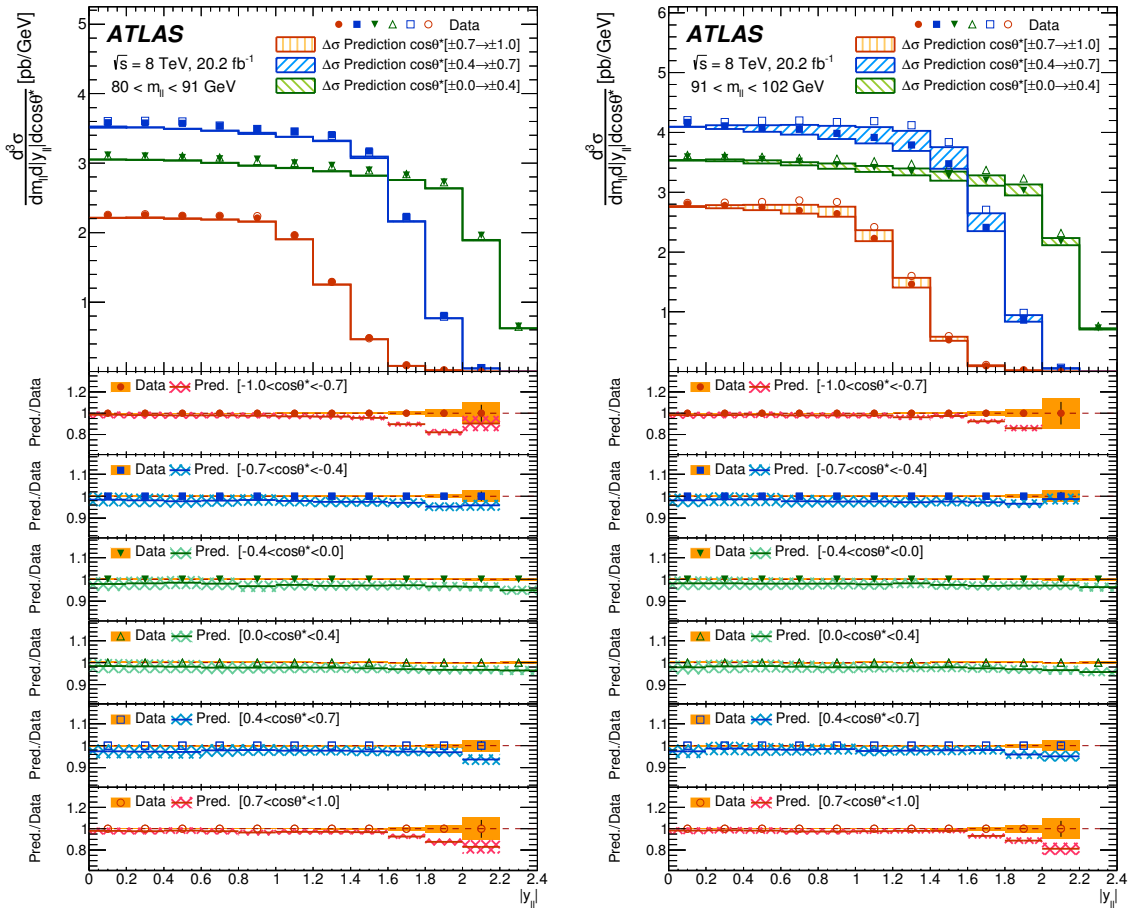

Figure 8. The combined Born-level fiducial cross sections $\mathrm{d}^3\sigma$. The kinematic region shown is labelled in each plot. The data are shown as solid ($\cos\theta^* < 0$) and open ($\cos\theta^* > 0$) markers and the prediction from Powheg including NNLO QCD and NLO EW K-factors is shown as the solid line. The difference, $\Delta\sigma$, between the predicted cross sections in the two measurement bins at equal $|\cos\theta^*|$ symmetric around $\cos\theta^* = 0$ is represented by the hatched shading. In each plot, the lower panel shows the ratio of prediction to measurement. The inner error bars represent the statistical uncertainty of the data and the solid band shows the total experimental uncertainty. The contribution to the uncertainty from the luminosity measurement is excluded. The crosshatched band represents the statistical and PDF uncertainties in the prediction.

JHEP12(2017)059

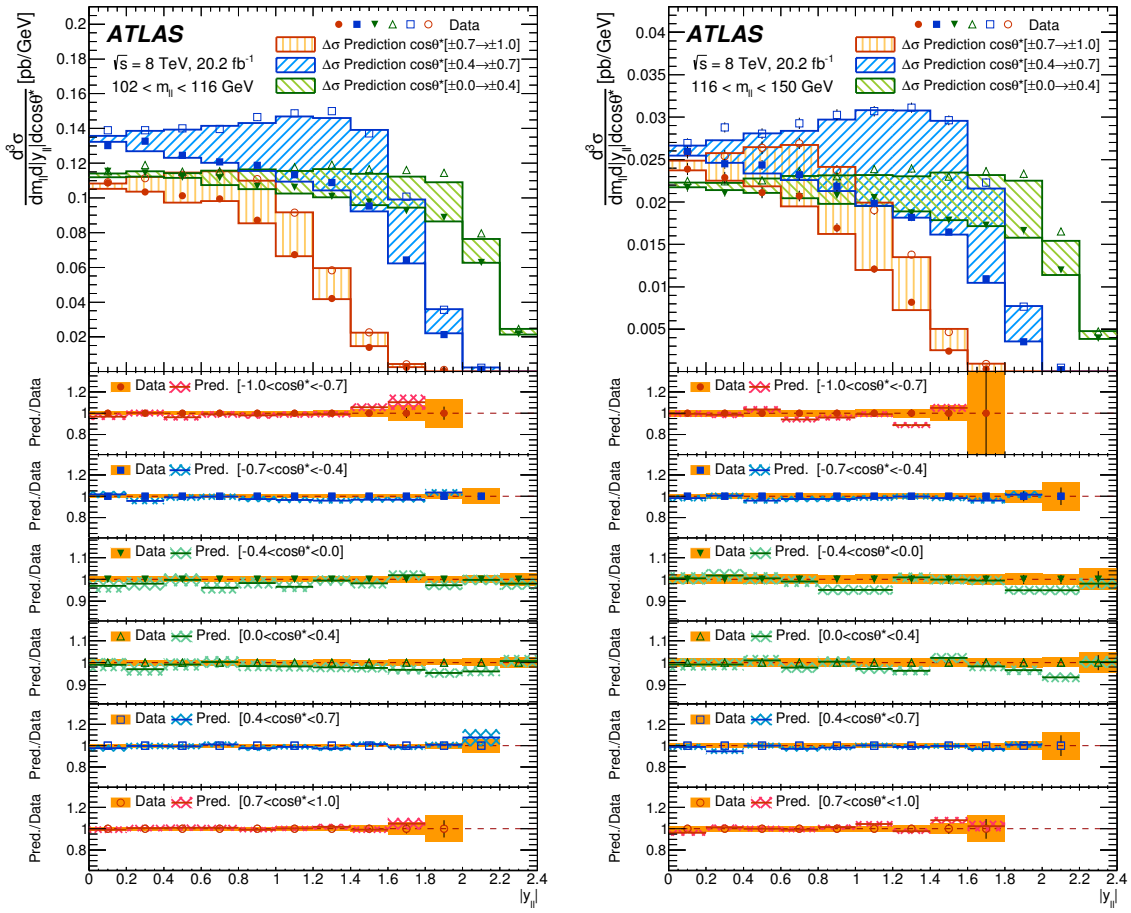

Figure 9. The combined Born-level fiducial cross sections $d^3\sigma$. The kinematic region shown is labelled in each plot. The data are shown as solid ($\cos\theta^* < 0$) and open ($\cos\theta^* > 0$) markers and the prediction from Powheg including NNLO QCD and NLO EW K-factors is shown as the solid line. The difference, $\Delta\sigma$, between the predicted cross sections in the two measurement bins at equal $|\cos\theta^*|$ symmetric around $\cos\theta^* = 0$ is represented by the hatched shading. In each plot, the lower panel shows the ratio of prediction to measurement. The inner error bars represent the statistical uncertainty of the data and the solid band shows the total experimental uncertainty. The contribution to the uncertainty from the luminosity measurement is excluded. The crosshatched band represents the statistical and PDF uncertainties in the prediction.

JHEP12(2017)059

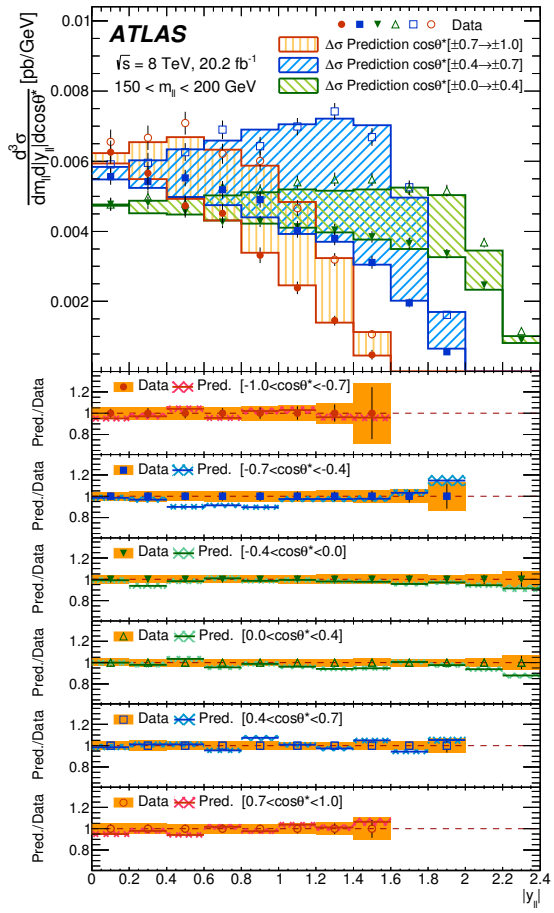

Figure 10. The combined Born-level fiducial cross sections $\mathrm{d}^3\sigma$. The kinematic region shown is labelled in each plot. The data are shown as solid ($\cos\theta^* < 0$) and open ($\cos\theta^* > 0$) markers and the prediction from Powheg including NNLO QCD and NLO EW K-factors is shown as the solid line. The difference, $\Delta\sigma$, between the predicted cross sections in the two measurement bins at equal $|\cos\theta^*|$ symmetric around $\cos\theta^* = 0$ is represented by the hatched shading. In each plot, the lower panel shows the ratio of prediction to measurement. The inner error bars represent the statistical uncertainty of the data and the solid band shows the total experimental uncertainty. The contribution to the uncertainty from the luminosity measurement is excluded. The crosshatched band represents the statistical and PDF uncertainties in the prediction.

JHEP12(2017)059

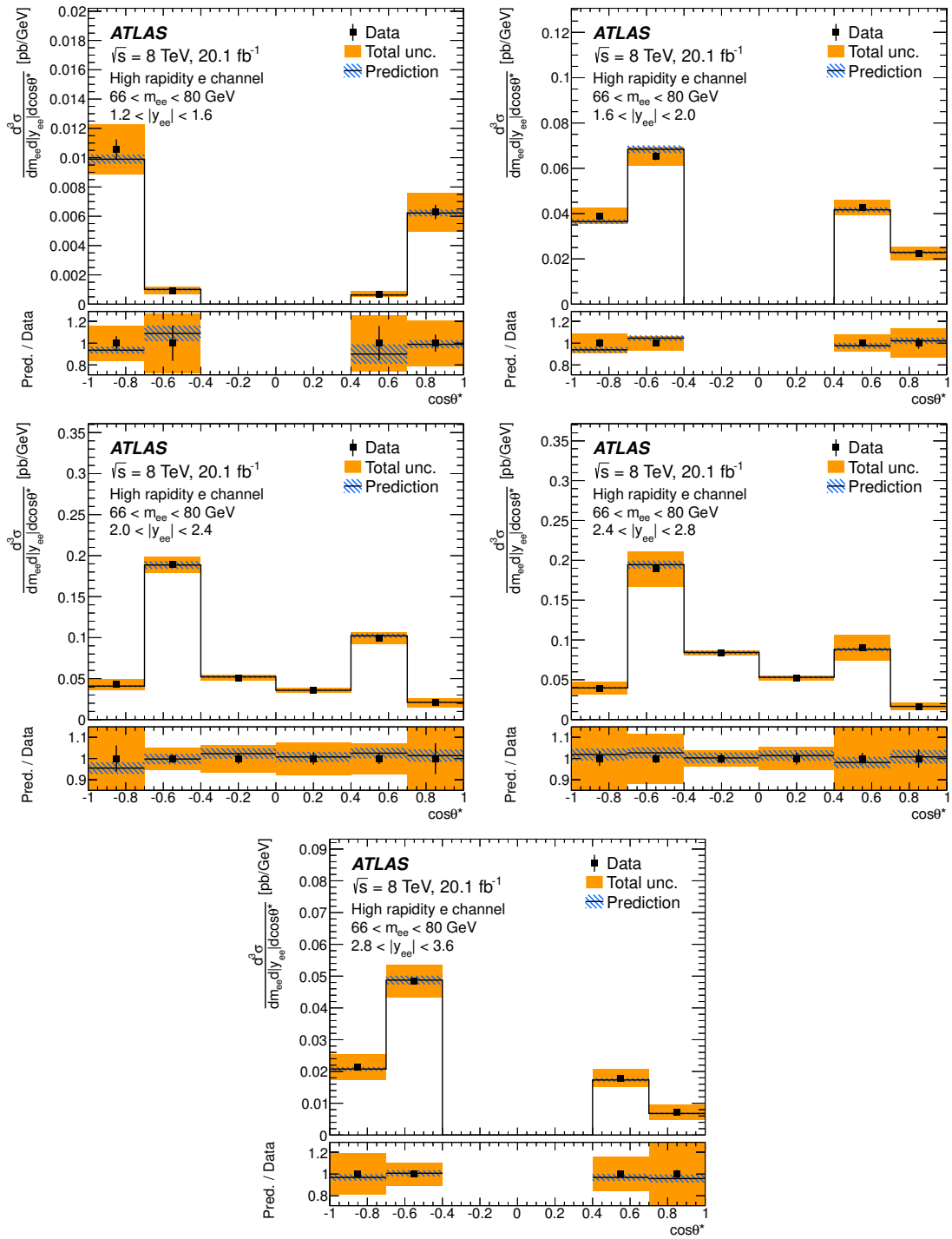

Figure 11. The high rapidity electron channel Born-level fiducial cross section $d^3\sigma$. The kinematic region shown is labelled in each plot. The data are shown as solid markers and the prediction from Powheg including NNLO QCD and NLO EW K-factors is shown as the solid line. In each plot, the lower panel shows the ratio of prediction to measurement. The inner error bars represent the statistical uncertainty of the data and the solid band shows the total experimental uncertainty. The contribution from the uncertainty of the luminosity measurement is excluded. The hatched band represents the statistical and PDF uncertainties in the prediction.

JHEP12(2017)059

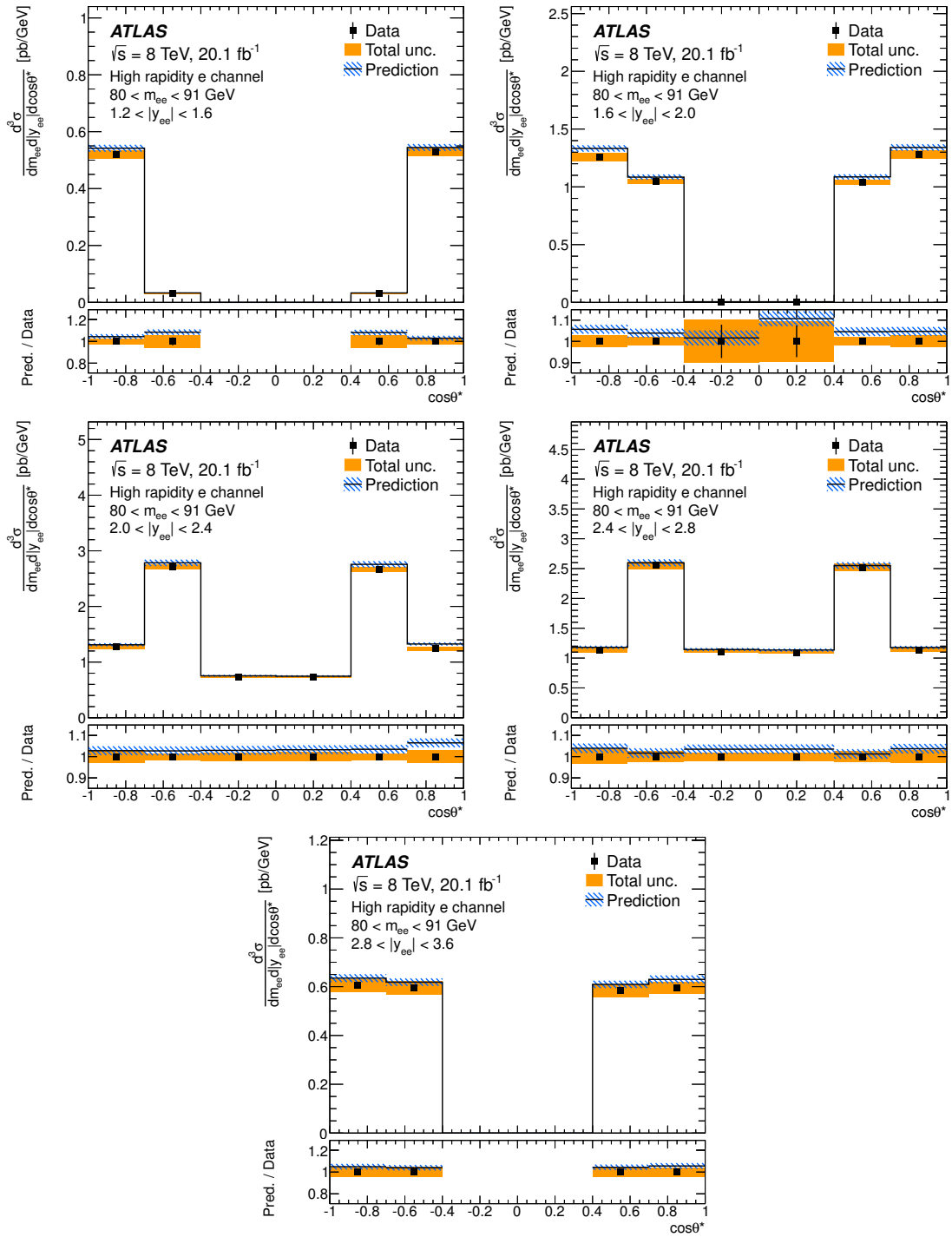

Figure 12. The high rapidity electron channel Born-level fiducial cross section $d^3\sigma$. The kinematic region shown is labelled in each plot. The data are shown as solid markers and the prediction from Powheg including NNLO QCD and NLO EW K-factors is shown as the solid line. In each plot, the lower panel shows the ratio of prediction to measurement. The inner error bars represent the statistical uncertainty of the data and the solid band shows the total experimental uncertainty. The contribution from the uncertainty of the luminosity measurement is excluded. The hatched band represents the statistical and PDF uncertainties in the prediction.

JHEP12(2017)059

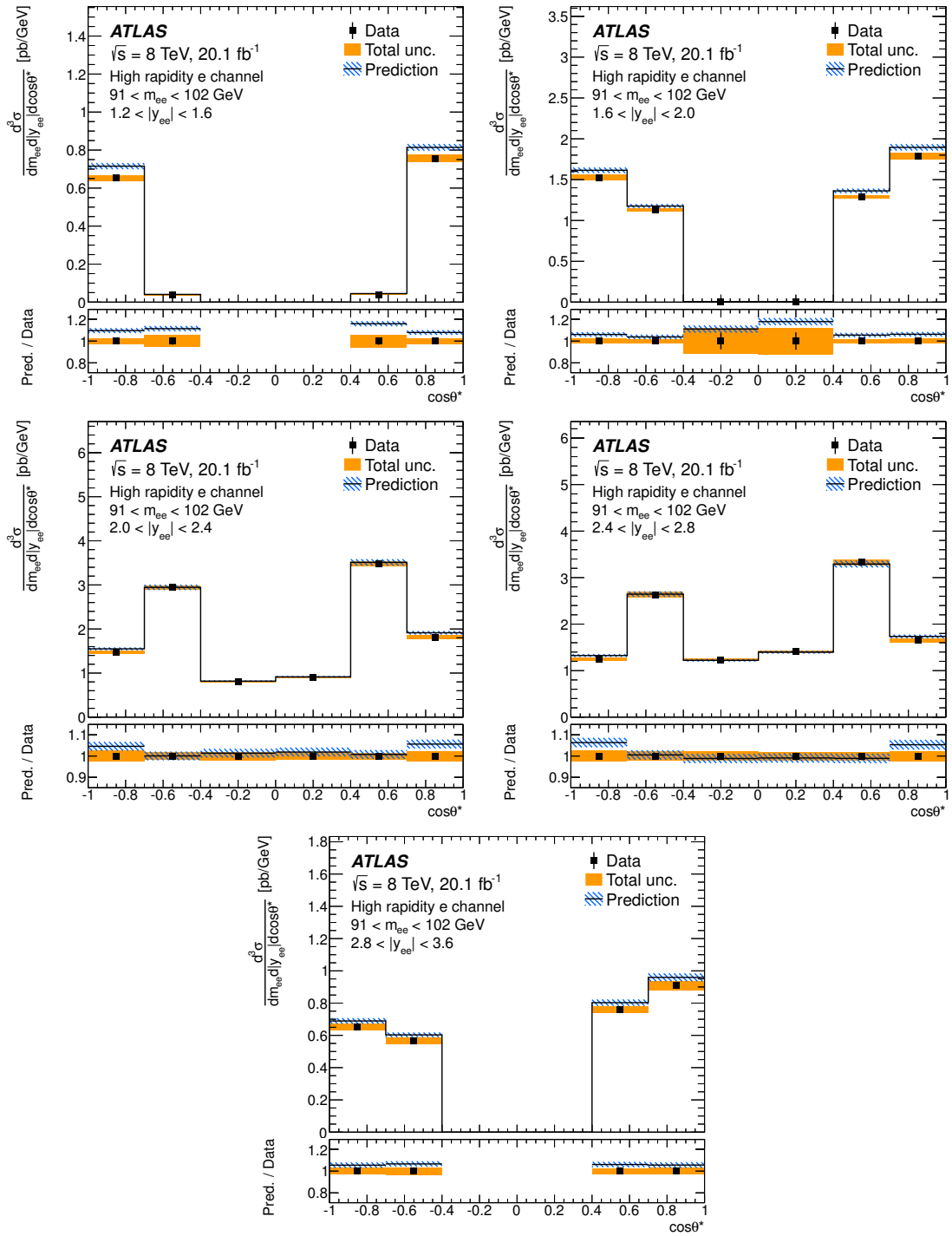

Figure 13. The high rapidity electron channel Born-level fiducial cross section $d^3\sigma$. The kinematic region shown is labelled in each plot. The data are shown as solid markers and the prediction from Powheg including NNLO QCD and NLO EW K-factors is shown as the solid line. In each plot, the lower panel shows the ratio of prediction to measurement. The inner error bars represent the statistical uncertainty of the data and the solid band shows the total experimental uncertainty. The contribution from the uncertainty of the luminosity measurement is excluded. The hatched band represents the statistical and PDF uncertainties in the prediction.

JHEP12(2017)059

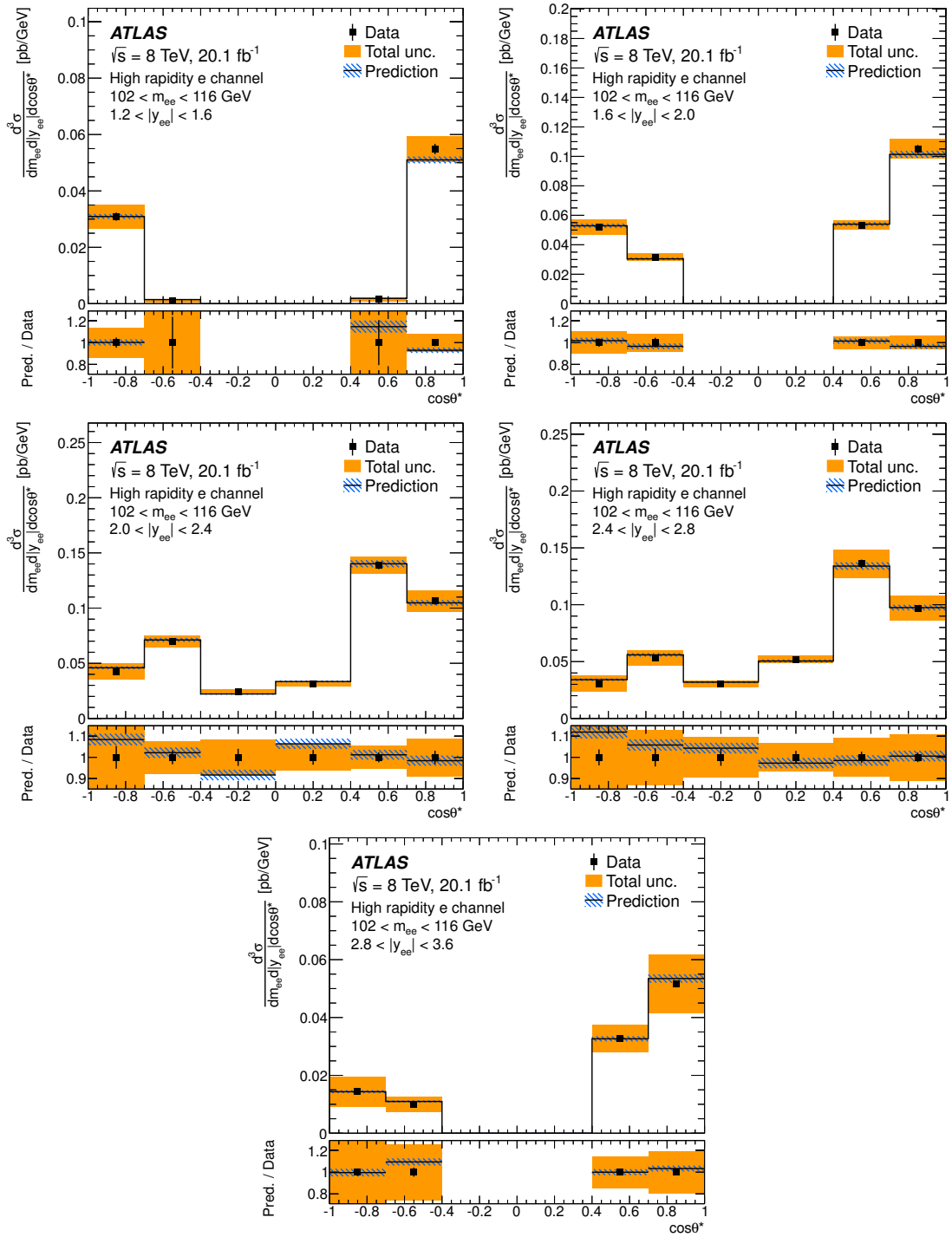

Figure 14. The high rapidity electron channel Born-level fiducial cross section $d^3\sigma$. The kinematic region shown is labelled in each plot. The data are shown as solid markers and the prediction from Powheg including NNLO QCD and NLO EW K-factors is shown as the solid line. In each plot, the lower panel shows the ratio of prediction to measurement. The inner error bars represent the statistical uncertainty of the data and the solid band shows the total experimental uncertainty. The contribution from the uncertainty of the luminosity measurement is excluded. The hatched band represents the statistical and PDF uncertainties in the prediction.

JHEP12(2017)059

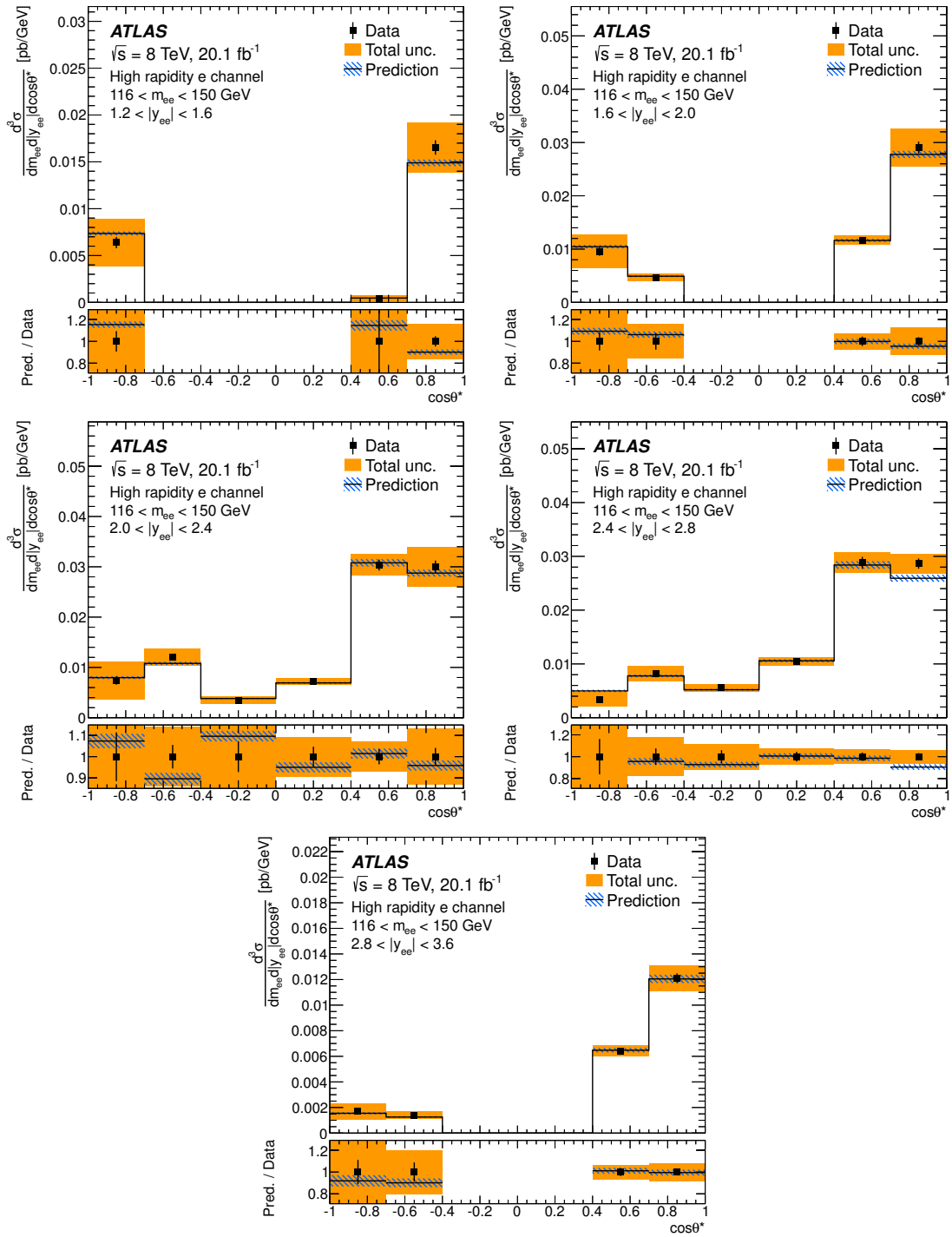

Figure 15. The high rapidity electron channel Born-level fiducial cross section $d^3\sigma$. The kinematic region shown is labelled in each plot. The data are shown as solid markers and the prediction from Powheg including NNLO QCD and NLO EW K-factors is shown as the solid line. In each plot, the lower panel shows the ratio of prediction to measurement. The inner error bars represent the statistical uncertainty of the data and the solid band shows the total experimental uncertainty. The contribution from the uncertainty of the luminosity measurement is excluded. The hatched band represents the statistical and PDF uncertainties in the prediction.

JHEP12(2017)059

8.4 Forward-backward asymmetry

The effect of parity violation in Z boson decays is more clearly visible in the forward-backward asymmetry, A_{FB}, derived from the cross-section measurements of $\mathrm{d}^3\sigma$. The combined Born-level cross sections are used to determine A_{FB} in the region $0 < |y_{\ell\ell}| < 2.4$ by summing the measurement bins for $\cos\theta^* > 0$ and for $\cos\theta^* < 0$ and calculating the asymmetry according to equation (1.3).

The uncorrelated uncertainty in A_{FB} is determined using standard error propagation. The correlated uncertainty is determined for each source in turn by coherently shifting $\mathrm{d}^3\sigma$ by the associated correlated uncertainty and calculating the difference to the nominal value of A_{FB}. Finally, the total uncertainty in A_{FB} is taken as the sum in quadrature of the correlated and uncorrelated components. The uncertainties in A_{FB} are significantly reduced, especially the correlated uncertainties such as the electron energy scale and resolution. The total uncertainty is dominated by the data statistical uncertainty everywhere. An experimental uncertainty of 1×10^{-3} is reached for the combined measurement, and 4×10^{-3} for the high rapidity electron channel measurement. In the high-precision region of $80 < m_{\ell\ell} < 102\,\mathrm{GeV}$ the largest systematic uncertainty contributions are from the MC sample size (which are a factor two smaller than the data statistical uncertainty) and the lepton scale contributions, which are an order of magnitude smaller. At low $m_{\ell\ell}$ the uncorrelated and statistical contributions from the background sources are also of comparable size. Summary tables of these measurements are given in tables 9 and 10 in the appendix.

The measurements of A_{FB} are shown in figure 16 for the combined data. The data are compared to a Born-level prediction from Powheg including K-factors for NNLO QCD and NLO EW corrections. The value of $\sin^2\theta^{\mathrm{eff}}_{\mathrm{lept}}$ used in the simulation is 0.23113 [76]. The measured asymmetry is found to generally increase with $m_{\ell\ell}$ from a negative to a positive asymmetry which is close to zero near $m_{\ell\ell} = m_Z$. The magnitude of A_{FB} is smallest for $|y_{\ell\ell}| = 0$ and increases to a maximum in the region $1.0 < |y_{\ell\ell}| < 2.0$, before decreasing at larger rapidity. This is expected from the effect of dilution and the unknown direction of the incident q on an event-by-event basis. At larger $|y_{\ell\ell}|$, and hence larger x, the influence of the higher-momentum valence u- and d-quarks becomes increasingly apparent through the longitudinal boost in the valence direction. This allows a correct determination of the q direction to be made on average and is well modelled by the Powheg prediction. At even larger $|y_{\ell\ell}|$ in the combined measurements the maximum of $|A_{\mathrm{FB}}|$ decreases again due to the limited acceptance of the detector in $\eta^{e,\mu}$.

The measurements of A_{FB} in the high rapidity electron channel analysis, which is expected to be more sensitive to the asymmetry, are presented in figure 17. Qualitatively, the asymmetry shows behaviour similar to that seen in the combined measurement: the asymmetry increases with m_{ee} and values of $|A_{\mathrm{FB}}|$ reaching 0.7 are observed at the highest $|y_{ee}|$ where the influence of dilution is smallest. As was the case in the combined measurement, the high rapidity A_{FB} measurement is well-described by the Powheg prediction.

JHEP12(2017)059

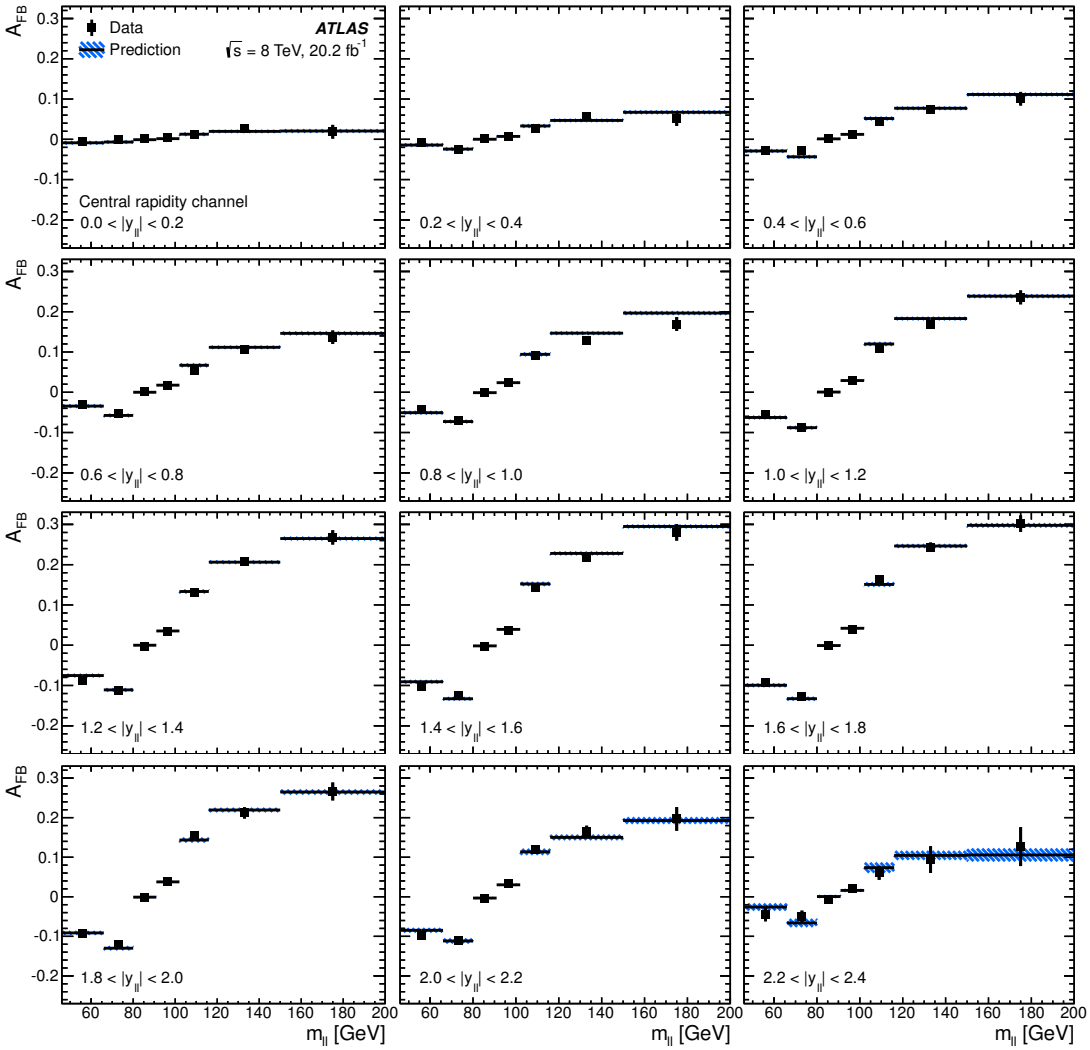

Figure 16. Forward-backward asymmetry, A_{FB}, determined from the combined Born-level fiducial cross section. The kinematic region shown is labelled in each plot. The data are shown as solid markers and the error bars represent the total experimental uncertainty. The prediction from Powheg including NNLO QCD and NLO EW K-factors is shown as the solid line and the hatched band represents the statistical and PDF uncertainties in the prediction.

JHEP12(2017)059

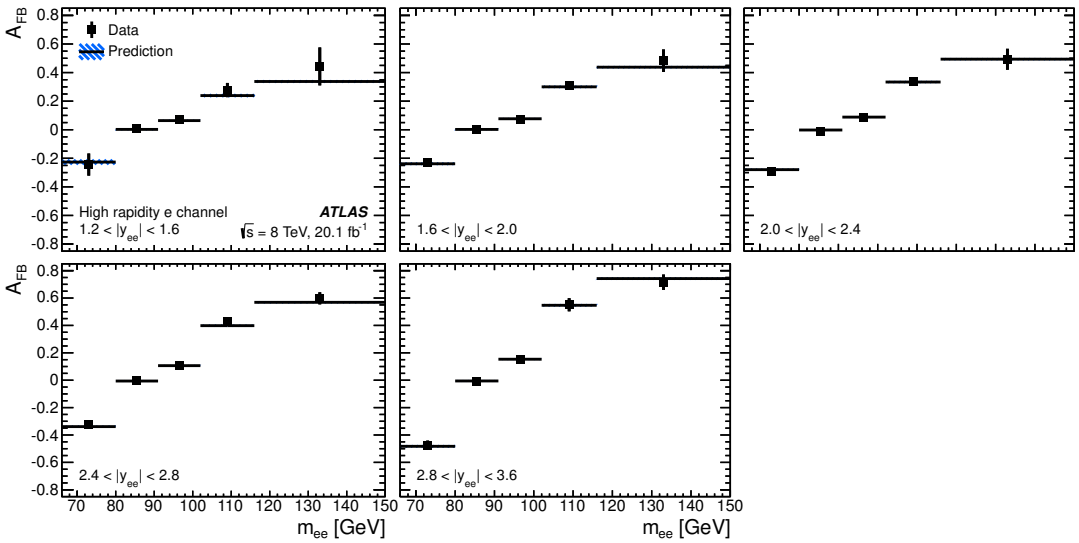

Figure 17. Forward-backward asymmetry, A_{FB}, determined from the high rapidity electron Born-level fiducial cross section. The kinematic region shown is labelled in each plot. The data are shown as solid markers and the error bars represent the total experimental uncertainty. The prediction from Powheg including NNLO QCD and NLO EW K-factors is shown as the solid line and the hatched band represents the statistical and PDF uncertainties in the prediction.

JHEP12(2017)059

9 Conclusion

The triple-differential Drell-Yan production cross section $\mathrm{d}^3\sigma/\mathrm{d}m_{\ell\ell}\mathrm{d}|y_{\ell\ell}|\mathrm{d}\cos\theta^*$ is measured in the range $46 < m_{\ell\ell} < 200\,\mathrm{GeV}$ and $|y_{\ell\ell}| < 2.4$ for electron and muon pairs. The measurements are extended to high rapidity in the electron channel up to $|y_{ee}| = 3.6$ in the mass range $66 < m_{\ell\ell} < 150\,\mathrm{GeV}$. The analysis uses $20.2\,\mathrm{fb}^{-1}$ of pp collision data at $\sqrt{s} = 8$ TeV collected in 2012 by the ATLAS detector at the LHC. The central rapidity measurement channels are combined taking into account the systematic uncertainty correlations. Their combination achieves an experimental precision of better than 0.5%, excluding the overall uncertainty in the luminosity measurement of 1.9%.

The combined cross sections are integrated to produce the single- and double-differential cross sections $\mathrm{d}\sigma/\mathrm{d}m_{\ell\ell}$ and $\mathrm{d}^2\sigma/\mathrm{d}m_{\ell\ell}\mathrm{d}|y_{\ell\ell}|$. The fiducial cross sections are compared to a theoretical prediction calculated using Powheg at NLO with matched leading-logarithm parton showers. The calculation is approximately corrected for NNLO QCD effects and for additional higher-order electroweak effects applied as a function of $m_{\ell\ell}$. The single- and double-differential measurements are well described by the prediction. Having applied corrections to the scattering amplitude coefficients in Powheg the prediction also provides a good description of the triple-differential measurements.

The measured cross sections are used to determine the forward-backward asymmetry A_{FB} as a function of dilepton invariant mass and rapidity. The Powheg predictions enhanced with NNLO QCD and NLO EW K-factors describe the observed behaviour of A_{FB} well.

Acknowledgments

We thank CERN for the very successful operation of the LHC, as well as the support staff from our institutions without whom ATLAS could not be operated efficiently.

We acknowledge the support of ANPCyT, Argentina; YerPhI, Armenia; ARC, Australia; BMWFW and FWF, Austria; ANAS, Azerbaijan; SSTC, Belarus; CNPq and FAPESP, Brazil; NSERC, NRC and CFI, Canada; CERN; CONICYT, Chile; CAS, MOST and NSFC, China; COLCIENCIAS, Colombia; MSMT CR, MPO CR and VSC CR, Czech Republic; DNRF and DNSRC, Denmark; IN2P3-CNRS, CEA-DSM/IRFU, France; SRNSF, Georgia; BMBF, HGF, and MPG, Germany; GSRT, Greece; RGC, Hong Kong SAR, China; ISF, I-CORE and Benoziyo Center, Israel; INFN, Italy; MEXT and JSPS, Japan; CNRST, Morocco; NWO, Netherlands; RCN, Norway; MNiSW and NCN, Poland; FCT, Portugal; MNE/IFA, Romania; MES of Russia and NRC KI, Russian Federation; JINR; MESTD, Serbia; MSSR, Slovakia; ARRS and MIZŠ, Slovenia; DST/NRF, South Africa; MINECO, Spain; SRC and Wallenberg Foundation, Sweden; SERI, SNSF and Cantons of Bern and Geneva, Switzerland; MOST, Taiwan; TAEK, Turkey; STFC, United Kingdom; DOE and NSF, United States of America. In addition, individual groups and members have received support from BCKDF, the Canada Council, CANARIE, CRC, Compute Canada, FQRNT, and the Ontario Innovation Trust, Canada; EPLANET, ERC, ERDF, FP7, Horizon 2020 and Marie Skłodowska-Curie Actions, European Union; In-

JHEP12(2017)059

vestissements d'Avenir Labex and Idex, ANR, Région Auvergne and Fondation Partager le Savoir, France; DFG and AvH Foundation, Germany; Herakleitos, Thales and Aristeia programmes co-financed by EU-ESF and the Greek NSRF; BSF, GIF and Minerva, Israel; BRF, Norway; CERCA Programme Generalitat de Catalunya, Generalitat Valenciana, Spain; the Royal Society and Leverhulme Trust, United Kingdom.

The crucial computing support from all WLCG partners is acknowledged gratefully, in particular from CERN, the ATLAS Tier-1 facilities at TRIUMF (Canada), NDGF (Denmark, Norway, Sweden), CC-IN2P3 (France), KIT/GridKA (Germany), INFN-CNAF (Italy), NL-T1 (Netherlands), PIC (Spain), ASGC (Taiwan), RAL (U.K.) and BNL (U.S.A.), the Tier-2 facilities worldwide and large non-WLCG resource providers. Major contributors of computing resources are listed in ref. [77].

A Data tables

Summary tables of $\mathrm{d}^3\sigma/\mathrm{d}m_{\ell\ell}\mathrm{d}|y_{\ell\ell}|\mathrm{d}\cos\theta^*$ cross sections and A_{FB} are given in this appendix. Tables containing the complete breakdown of systematic uncertainties are available in HEPData [71, 72].

A.1 Integrated cross-section tables

$m_{\ell\ell}$ [GeV]	$\mathrm{d}\sigma/\mathrm{d}m_{\ell\ell}$ [pb/GeV]	δ^{stat} [%]	$\delta^{\mathrm{syst}}_{\mathrm{unc}}$ [%]	$\delta^{\mathrm{syst}}_{\mathrm{cor}}$ [%]	δ^{total} [%]
46, 66	7.61×10^{-1}	0.2	0.1	0.9	0.9
66, 80	1.13	0.1	0.1	0.4	0.4
80, 91	21.4	0.0	0.0	0.2	0.2
91, 102	25.0	0.0	0.0	0.2	0.2
102, 116	8.25×10^{-1}	0.2	0.1	0.4	0.4
116, 150	1.64×10^{-1}	0.3	0.1	0.7	0.7
150, 200	3.66×10^{-2}	0.5	0.2	1.3	1.4

Table 5. The combined Born-level single-differential cross section $\mathrm{d}\sigma/\mathrm{d}m_{\ell\ell}$. The measurements are listed together with the statistical (δ^{stat}), uncorrelated systematic ($\delta^{\mathrm{syst}}_{\mathrm{unc}}$), correlated systematic ($\delta^{\mathrm{syst}}_{\mathrm{cor}}$), and total ($\delta^{\mathrm{total}}$) uncertainties. The luminosity uncertainty of 1.9% is not shown and not included in the overall systematic and total uncertainties.

JHEP12(2017)059

$m_{\ell\ell}$ [GeV]	$\lvert y_{\ell\ell}\rvert$	$d^2\sigma/dm_{\ell\ell}d\lvert y_{\ell\ell}\rvert$ [pb/GeV]	δ^{stat} [%]	δ^{syst}_{unc} [%]	δ^{syst}_{cor} [%]	δ^{total} [%]	m_{ee} [GeV]	$\lvert y_{\ell\ell}\rvert$	$d^2\sigma/dm_{\ell\ell}d\lvert y_{\ell\ell}\rvert$ [pb/GeV]	δ^{stat} [%]	δ^{syst}_{unc} [%]	δ^{syst}_{cor} [%]	δ^{total} [%]
46, 66	0.0, 0.2	1.85×10^{-1}	0.6	0.4	1.0	1.2	46, 66	1.2, 1.4	1.86×10^{-1}	0.6	0.4	0.9	1.1
46, 66	0.2, 0.4	1.87×10^{-1}	0.6	0.5	1.0	1.2	46, 66	1.4, 1.6	1.82×10^{-1}	0.6	0.4	0.9	1.1
46, 66	0.4, 0.6	1.86×10^{-1}	0.6	0.4	0.9	1.2	46, 66	1.6, 1.8	1.66×10^{-1}	0.6	0.5	0.9	1.2
46, 66	0.6, 0.8	1.87×10^{-1}	0.6	0.4	0.9	1.2	46, 66	1.8, 2.0	1.35×10^{-1}	0.7	0.5	0.8	1.2
46, 66	0.8, 1.0	1.86×10^{-1}	0.6	0.4	0.9	1.2	46, 66	2.0, 2.2	8.60×10^{-2}	0.8	0.6	0.8	1.3
46, 66	1.0, 1.2	1.88×10^{-1}	0.6	0.4	0.9	1.1	46, 66	2.2, 2.4	2.93×10^{-2}	1.4	1.1	0.9	2.0
66, 80	0.0, 0.2	3.05×10^{-1}	0.4	0.2	0.4	0.6	66, 80	1.2, 1.4	2.82×10^{-1}	0.4	0.2	0.4	0.6
66, 80	0.2, 0.4	3.02×10^{-1}	0.4	0.2	0.4	0.6	66, 80	1.4, 1.6	2.54×10^{-1}	0.5	0.3	0.4	0.6
66, 80	0.4, 0.6	3.02×10^{-1}	0.4	0.2	0.4	0.6	66, 80	1.6, 1.8	2.08×10^{-1}	0.5	0.3	0.4	0.7
66, 80	0.6, 0.8	3.01×10^{-1}	0.4	0.2	0.4	0.6	66, 80	1.8, 2.0	1.54×10^{-1}	0.6	0.3	0.5	0.8
66, 80	0.8, 1.0	2.95×10^{-1}	0.4	0.2	0.4	0.6	66, 80	2.0, 2.2	9.27×10^{-2}	0.7	0.4	0.6	1.0
66, 80	1.0, 1.2	2.93×10^{-1}	0.4	0.2	0.4	0.6	66, 80	2.2, 2.4	3.05×10^{-2}	1.2	0.7	0.9	1.7
80, 91	0.0, 0.2	6.00	0.1	0.0	0.2	0.2	80, 91	1.2, 1.4	5.19	0.1	0.1	0.2	0.3
80, 91	0.2, 0.4	6.00	0.1	0.0	0.2	0.2	80, 91	1.4, 1.6	4.51	0.1	0.1	0.2	0.3
80, 91	0.4, 0.6	5.97	0.1	0.1	0.2	0.2	80, 91	1.6, 1.8	3.66	0.1	0.1	0.3	0.3
80, 91	0.6, 0.8	5.93	0.1	0.0	0.2	0.3	80, 91	1.8, 2.0	2.67	0.1	0.1	0.3	0.3
80, 91	0.8, 1.0	5.87	0.1	0.1	0.2	0.3	80, 91	2.0, 2.2	1.60	0.2	0.1	0.3	0.4
80, 91	1.0, 1.2	5.66	0.1	0.1	0.2	0.3	80, 91	2.2, 2.4	5.20×10^{-1}	0.3	0.2	0.4	0.5
91, 102	0.0, 0.2	7.08	0.1	0.1	0.2	0.2	91, 102	1.2, 1.4	6.02	0.1	0.0	0.2	0.3
91, 102	0.2, 0.4	7.04	0.1	0.1	0.2	0.2	91, 102	1.4, 1.6	5.21	0.1	0.1	0.2	0.3
91, 102	0.4, 0.6	7.01	0.1	0.1	0.2	0.2	91, 102	1.6, 1.8	4.23	0.1	0.1	0.3	0.3
91, 102	0.6, 0.8	6.98	0.1	0.0	0.2	0.2	91, 102	1.8, 2.0	3.07	0.2	0.1	0.3	0.3
91, 102	0.8, 1.0	6.90	0.1	0.0	0.2	0.2	91, 102	2.0, 2.2	1.83	0.2	0.1	0.3	0.4
91, 102	1.0, 1.2	6.60	0.1	0.1	0.2	0.3	91, 102	2.2, 2.4	5.96×10^{-1}	0.3	0.2	0.4	0.5
102, 116	0.0, 0.2	2.38×10^{-1}	0.5	0.2	0.3	0.7	102, 116	1.2, 1.4	1.96×10^{-1}	0.5	0.3	0.5	0.7
102, 116	0.2, 0.4	2.39×10^{-1}	0.5	0.2	0.4	0.7	102, 116	1.4, 1.6	1.66×10^{-1}	0.5	0.3	0.5	0.8
102, 116	0.4, 0.6	2.35×10^{-1}	0.5	0.2	0.4	0.7	102, 116	1.6, 1.8	1.35×10^{-1}	0.6	0.4	0.7	1.0
102, 116	0.6, 0.8	2.33×10^{-1}	0.5	0.3	0.4	0.7	102, 116	1.8, 2.0	9.84×10^{-2}	0.6	0.4	0.8	1.1
102, 116	0.8, 1.0	2.29×10^{-1}	0.5	0.3	0.4	0.7	102, 116	2.0, 2.2	5.76×10^{-2}	0.7	0.5	1.0	1.3
102, 116	1.0, 1.2	2.16×10^{-1}	0.5	0.3	0.4	0.7	102, 116	2.2, 2.4	1.85×10^{-2}	1.0	0.9	1.3	1.9
116, 150	0.0, 0.2	4.84×10^{-2}	0.8	0.3	0.8	1.2	116, 150	1.2, 1.4	3.84×10^{-2}	0.9	0.4	0.6	1.1
116, 150	0.2, 0.4	4.79×10^{-2}	0.8	0.3	0.8	1.2	116, 150	1.4, 1.6	3.23×10^{-2}	0.9	0.4	0.5	1.1
116, 150	0.4, 0.6	4.74×10^{-2}	0.8	0.3	0.8	1.2	116, 150	1.6, 1.8	2.66×10^{-2}	1.0	0.5	0.5	1.2
116, 150	0.6, 0.8	4.77×10^{-2}	0.8	0.3	0.8	1.2	116, 150	1.8, 2.0	1.93×10^{-2}	1.2	0.7	0.6	1.5
116, 150	0.8, 1.0	4.54×10^{-2}	0.8	0.3	0.7	1.1	116, 150	2.0, 2.2	1.14×10^{-2}	1.4	0.7	0.7	1.7
116, 150	1.0, 1.2	4.23×10^{-2}	0.8	0.4	0.6	1.1	116, 150	2.2, 2.4	3.48×10^{-3}	2.6	1.7	1.2	3.3
150, 200	0.0, 0.2	1.11×10^{-2}	1.6	0.6	1.8	2.4	150, 200	1.2, 1.4	8.56×10^{-3}	1.6	0.6	1.0	2.0
150, 200	0.2, 0.4	1.10×10^{-2}	1.5	0.7	1.8	2.4	150, 200	1.4, 1.6	7.12×10^{-3}	1.8	0.9	0.9	2.2
150, 200	0.4, 0.6	1.08×10^{-2}	1.5	0.6	1.7	2.3	150, 200	1.6, 1.8	5.72×10^{-3}	1.9	0.7	0.8	2.2
150, 200	0.6, 0.8	1.07×10^{-2}	1.5	0.5	1.5	2.2	150, 200	1.8, 2.0	4.06×10^{-3}	2.2	0.7	0.7	2.4
150, 200	0.8, 1.0	9.98×10^{-3}	1.6	0.5	1.3	2.1	150, 200	2.0, 2.2	2.46×10^{-3}	2.8	1.0	0.7	3.0
150, 200	1.0, 1.2	9.22×10^{-3}	1.6	0.6	1.2	2.1	150, 200	2.2, 2.4	8.20×10^{-4}	4.7	1.3	1.0	5.0

Table 6. The combined Born-level double-differential cross section $d^2\sigma/dm_{\ell\ell}d|y_{\ell\ell}|$. The measurements are listed together with the statistical (δ^{stat}), uncorrelated systematic (δ^{syst}_{unc}), correlated systematic (δ^{syst}_{cor}), and total (δ^{total}) uncertainties. The luminosity uncertainty of 1.9% is not shown and not included in the overall systematic and total uncertainties.

JHEP12(2017)059

A.2 Triple-differential cross-section tables

Bin	$m_{\ell\ell}$ [GeV]	$\lvert y_{\ell\ell}\rvert$	$\cos\theta^*$	$d^3\sigma$ [pb/GeV]	δ^{stat} [%]	$\delta^{\text{syst}}_{\text{unc}}$ [%]	$\delta^{\text{syst}}_{\text{cor}}$ [%]	δ^{total} [%]	Bin	$m_{\ell\ell}$ [GeV]	$\lvert y_{\ell\ell}\rvert$	$\cos\theta^*$	$d^3\sigma$ [pb/GeV]	δ^{stat} [%]	$\delta^{\text{syst}}_{\text{unc}}$ [%]	$\delta^{\text{syst}}_{\text{cor}}$ [%]	δ^{total} [%]
1	46, 66	0.0, 0.2	−1.0, −0.7	1.42×10^{-2}	4.0	2.5	1.8	5.1	6	46, 66	0.0, 0.2	+0.7, +1.0	1.37×10^{-2}	4.2	3.4	2.0	5.7
2	46, 66	0.0, 0.2	−0.7, −0.4	1.02×10^{-1}	1.4	1.1	1.2	2.1	5	46, 66	0.0, 0.2	+0.4, +0.7	1.01×10^{-1}	1.4	1.1	1.2	2.1
3	46, 66	0.0, 0.2	−0.4, 0.0	1.45×10^{-1}	1.0	0.8	0.9	1.5	4	46, 66	0.0, 0.2	0.0, +0.4	1.44×10^{-1}	1.0	0.8	0.9	1.6
7	46, 66	0.2, 0.4	−1.0, −0.7	1.48×10^{-2}	3.9	2.1	1.8	4.8	12	46, 66	0.2, 0.4	+0.7, +1.0	1.46×10^{-2}	3.9	1.9	1.8	4.7
8	46, 66	0.2, 0.4	−0.7, −0.4	1.03×10^{-1}	1.4	1.3	1.2	2.2	11	46, 66	0.2, 0.4	+0.4, +0.7	9.99×10^{-2}	1.4	1.1	1.2	2.2
9	46, 66	0.2, 0.4	−0.4, 0.0	1.47×10^{-1}	1.0	0.8	0.9	1.5	10	46, 66	0.2, 0.4	0.0, +0.4	1.46×10^{-1}	1.0	0.9	0.9	1.6
13	46, 66	0.4, 0.6	−1.0, −0.7	1.35×10^{-2}	4.5	3.3	1.9	5.9	18	46, 66	0.4, 0.6	+0.7, +1.0	1.43×10^{-2}	4.2	2.5	1.8	5.2
14	46, 66	0.4, 0.6	−0.7, −0.4	1.08×10^{-1}	1.4	1.1	1.0	2.1	17	46, 66	0.4, 0.6	+0.4, +0.7	9.84×10^{-2}	1.6	1.3	1.2	2.3
15	46, 66	0.4, 0.6	−0.4, 0.0	1.47×10^{-1}	0.9	0.7	0.9	1.5	16	46, 66	0.4, 0.6	0.0, +0.4	1.42×10^{-1}	1.0	0.8	0.9	1.5
19	46, 66	0.6, 0.8	−1.0, −0.7	1.50×10^{-2}	4.0	2.8	1.8	5.2	24	46, 66	0.6, 0.8	+0.7, +1.0	1.46×10^{-2}	4.1	3.0	1.9	5.5
20	46, 66	0.6, 0.8	−0.7, −0.4	1.08×10^{-1}	1.4	1.0	1.1	2.1	23	46, 66	0.6, 0.8	+0.4, +0.7	9.90×10^{-2}	1.5	1.1	1.2	2.2
21	46, 66	0.6, 0.8	−0.4, 0.0	1.48×10^{-1}	0.9	0.7	0.8	1.4	22	46, 66	0.6, 0.8	0.0, +0.4	1.42×10^{-1}	0.9	0.8	0.9	1.5
25	46, 66	0.8, 1.0	−1.0, −0.7	1.63×10^{-2}	4.1	2.7	1.5	5.1	30	46, 66	0.8, 1.0	+0.7, +1.0	1.33×10^{-2}	4.4	3.2	2.0	5.8
26	46, 66	0.8, 1.0	−0.7, −0.4	1.07×10^{-1}	1.5	1.1	1.1	2.1	29	46, 66	0.8, 1.0	+0.4, +0.7	9.57×10^{-2}	1.6	1.1	1.3	2.3
27	46, 66	0.8, 1.0	−0.4, 0.0	1.49×10^{-1}	0.9	0.7	0.8	1.4	28	46, 66	0.8, 1.0	0.0, +0.4	1.41×10^{-1}	1.0	0.8	0.8	1.5
31	46, 66	1.0, 1.2	−1.0, −0.7	1.71×10^{-2}	3.5	2.2	1.4	4.4	36	46, 66	1.0, 1.2	+0.7, +1.0	1.27×10^{-2}	4.2	2.5	1.8	5.2
32	46, 66	1.0, 1.2	−0.7, −0.4	1.12×10^{-1}	1.4	1.0	1.1	2.0	35	46, 66	1.0, 1.2	+0.4, +0.7	9.56×10^{-2}	1.5	1.1	1.2	2.2
33	46, 66	1.0, 1.2	−0.4, 0.0	1.50×10^{-1}	1.0	0.8	0.8	1.5	34	46, 66	1.0, 1.2	0.0, +0.4	1.41×10^{-1}	1.0	0.8	0.8	1.5
37	46, 66	1.2, 1.4	−1.0, −0.7	1.57×10^{-2}	3.8	2.3	1.6	4.7	42	46, 66	1.2, 1.4	+0.7, +1.0	1.13×10^{-2}	4.4	3.3	1.9	5.8
38	46, 66	1.2, 1.4	−0.7, −0.4	1.16×10^{-1}	1.3	0.9	1.0	1.9	41	46, 66	1.2, 1.4	+0.4, +0.7	8.57×10^{-2}	1.6	1.2	1.4	2.4
39	46, 66	1.2, 1.4	−0.4, 0.0	1.53×10^{-1}	1.0	0.7	0.8	1.4	40	46, 66	1.2, 1.4	0.0, +0.4	1.41×10^{-1}	1.0	0.8	0.8	1.5
43	46, 66	1.4, 1.6	−1.0, −0.7	1.04×10^{-2}	4.4	2.4	1.5	5.3	48	46, 66	1.4, 1.6	+0.7, +1.0	8.25×10^{-3}	5.0	3.9	1.7	6.6
44	46, 66	1.4, 1.6	−0.7, −0.4	1.16×10^{-1}	1.3	0.9	0.9	1.8	47	46, 66	1.4, 1.6	+0.4, +0.7	8.55×10^{-2}	1.6	1.3	1.3	2.5
45	46, 66	1.4, 1.6	−0.4, 0.0	1.55×10^{-1}	1.0	0.7	0.7	1.4	46	46, 66	1.4, 1.6	0.0, +0.4	1.35×10^{-1}	1.1	0.8	0.9	1.6
49	46, 66	1.6, 1.8	−1.0, −0.7	4.44×10^{-3}	6.6	3.2	1.8	7.5	54	46, 66	1.6, 1.8	+0.7, +1.0	3.58×10^{-3}	7.8	4.2	2.3	9.1
50	46, 66	1.6, 1.8	−0.7, −0.4	9.59×10^{-2}	1.4	1.0	1.0	2.0	53	46, 66	1.6, 1.8	+0.4, +0.7	7.16×10^{-2}	1.7	1.4	1.3	2.6
51	46, 66	1.6, 1.8	−0.4, 0.0	1.51×10^{-1}	1.0	0.8	0.8	1.5	52	46, 66	1.6, 1.8	0.0, +0.4	1.33×10^{-1}	1.1	0.8	0.9	1.6
55	46, 66	1.8, 2.0	−1.0, −0.7	1.97×10^{-3}	10.0	4.7	2.4	11.4	60	46, 66	1.8, 2.0	+0.7, +1.0	1.38×10^{-3}	12.8	6.6	2.7	14.7
56	46, 66	1.8, 2.0	−0.7, −0.4	4.05×10^{-2}	2.3	1.4	1.0	2.9	59	46, 66	1.8, 2.0	+0.4, +0.7	2.76×10^{-2}	2.8	2.0	1.3	3.6
57	46, 66	1.8, 2.0	−0.4, 0.0	1.51×10^{-1}	1.0	0.8	0.8	1.5	58	46, 66	1.8, 2.0	0.0, +0.4	1.32×10^{-1}	1.1	0.8	0.9	1.6
61	46, 66	2.0, 2.2	−1.0, −0.7	—	—	—	—	—	66	46, 66	2.0, 2.2	+0.7, +1.0	—	—	—	—	—
62	46, 66	2.0, 2.2	−0.7, −0.4	2.48×10^{-3}	9.7	7.1	3.0	12.3	65	46, 66	2.0, 2.2	+0.4, +0.7	1.64×10^{-3}	11.1	6.4	5.2	13.8
63	46, 66	2.0, 2.2	−0.4, 0.0	1.16×10^{-1}	1.1	0.8	0.7	1.6	64	46, 66	2.0, 2.2	0.0, +0.4	9.58×10^{-2}	1.2	1.0	0.9	1.8
67	46, 66	2.2, 2.4	−1.0, −0.7	—	—	—	—	—	72	46, 66	2.2, 2.4	+0.7, +1.0	—	—	—	—	—
68	46, 66	2.2, 2.4	−0.7, −0.4	—	—	—	—	—	71	46, 66	2.2, 2.4	+0.4, +0.7	—	—	—	—	—
69	46, 66	2.2, 2.4	−0.4, 0.0	3.82×10^{-2}	1.9	1.5	0.9	2.6	70	46, 66	2.2, 2.4	0.0, +0.4	3.50×10^{-2}	2.0	1.4	1.0	2.6
73	66, 80	0.0, 0.2	−1.0, −0.7	7.92×10^{-2}	1.6	0.9	0.8	2.0	78	66, 80	0.0, 0.2	+0.7, +1.0	7.70×10^{-2}	1.6	0.9	0.8	2.0
74	66, 80	0.0, 0.2	−0.7, −0.4	1.96×10^{-1}	0.9	0.5	0.4	1.1	77	66, 80	0.0, 0.2	+0.4, +0.7	1.93×10^{-1}	1.0	0.5	0.4	1.1
75	66, 80	0.0, 0.2	−0.4, 0.0	1.74×10^{-1}	0.9	0.6	0.3	1.1	76	66, 80	0.0, 0.2	0.0, +0.4	1.79×10^{-1}	0.9	0.4	0.3	1.0
79	66, 80	0.2, 0.4	−1.0, −0.7	8.29×10^{-2}	1.7	0.9	0.8	2.0	84	66, 80	0.2, 0.4	+0.7, +1.0	7.47×10^{-2}	1.6	0.9	0.8	2.0
80	66, 80	0.2, 0.4	−0.7, −0.4	2.02×10^{-1}	0.9	0.5	0.4	1.1	83	66, 80	0.2, 0.4	+0.4, +0.7	1.85×10^{-1}	1.0	0.5	0.4	1.2
81	66, 80	0.2, 0.4	−0.4, 0.0	1.72×10^{-1}	0.9	0.5	0.3	1.0	82	66, 80	0.2, 0.4	0.0, +0.4	1.74×10^{-1}	0.9	0.5	0.3	1.0
85	66, 80	0.4, 0.6	−1.0, −0.7	7.86×10^{-2}	1.6	0.9	0.9	2.0	90	66, 80	0.4, 0.6	+0.7, +1.0	7.37×10^{-2}	1.7	0.9	0.9	2.1
86	66, 80	0.4, 0.6	−0.7, −0.4	2.02×10^{-1}	1.0	0.5	0.4	1.2	89	66, 80	0.4, 0.6	+0.4, +0.7	1.86×10^{-1}	1.0	0.5	0.4	1.2
87	66, 80	0.4, 0.6	−0.4, 0.0	1.77×10^{-1}	0.8	0.4	0.3	1.0	88	66, 80	0.4, 0.6	0.0, +0.4	1.73×10^{-1}	0.8	0.4	0.3	1.0
91	66, 80	0.6, 0.8	−1.0, −0.7	8.41×10^{-2}	1.6	0.8	0.8	2.0	96	66, 80	0.6, 0.8	+0.7, +1.0	7.03×10^{-2}	1.6	1.0	0.8	2.1
92	66, 80	0.6, 0.8	−0.7, −0.4	2.05×10^{-1}	1.0	0.5	0.4	1.2	95	66, 80	0.6, 0.8	+0.4, +0.7	1.81×10^{-1}	1.0	0.7	0.5	1.3
93	66, 80	0.6, 0.8	−0.4, 0.0	1.78×10^{-1}	0.8	0.4	0.3	1.0	94	66, 80	0.6, 0.8	0.0, +0.4	1.69×10^{-1}	0.9	0.4	0.3	1.0
97	66, 80	0.8, 1.0	−1.0, −0.7	8.08×10^{-2}	1.7	1.0	0.8	2.1	102	66, 80	0.8, 1.0	+0.7, +1.0	6.90×10^{-2}	1.8	1.0	0.9	2.2
98	66, 80	0.8, 1.0	−0.7, −0.4	2.09×10^{-1}	1.0	0.5	0.4	1.2	101	66, 80	0.8, 1.0	+0.4, +0.7	1.72×10^{-1}	1.0	0.6	0.5	1.3
99	66, 80	0.8, 1.0	−0.4, 0.0	1.76×10^{-1}	0.8	0.4	0.3	1.0	100	66, 80	0.8, 1.0	0.0, +0.4	1.63×10^{-1}	0.9	0.5	0.3	1.0
103	66, 80	1.0, 1.2	−1.0, −0.7	8.63×10^{-2}	1.6	0.9	0.7	2.0	108	66, 80	1.0, 1.2	+0.7, +1.0	6.71×10^{-2}	1.7	1.0	0.8	2.1
104	66, 80	1.0, 1.2	−0.7, −0.4	2.05×10^{-1}	0.9	0.5	0.4	1.1	107	66, 80	1.0, 1.2	+0.4, +0.7	1.68×10^{-1}	1.0	0.6	0.5	1.2
105	66, 80	1.0, 1.2	−0.4, 0.0	1.79×10^{-1}	0.9	0.5	0.3	1.0	106	66, 80	1.0, 1.2	0.0, +0.4	1.60×10^{-1}	0.9	0.5	0.4	1.1
109	66, 80	1.2, 1.4	−1.0, −0.7	7.00×10^{-2}	1.6	1.0	0.8	2.1	114	66, 80	1.2, 1.4	+0.7, +1.0	4.86×10^{-2}	1.9	1.0	1.0	2.3
110	66, 80	1.2, 1.4	−0.7, −0.4	2.11×10^{-1}	0.9	0.5	0.4	1.1	113	66, 80	1.2, 1.4	+0.4, +0.7	1.59×10^{-1}	1.0	0.6	0.5	1.2
111	66, 80	1.2, 1.4	−0.4, 0.0	1.79×10^{-1}	0.9	0.5	0.4	1.1	112	66, 80	1.2, 1.4	0.0, +0.4	1.58×10^{-1}	0.9	0.5	0.4	1.2
115	66, 80	1.4, 1.6	−1.0, −0.7	2.74×10^{-2}	2.6	1.5	0.8	3.1	120	66, 80	1.4, 1.6	+0.7, +1.0	1.97×10^{-2}	2.9	2.3	1.1	3.9
116	66, 80	1.4, 1.6	−0.7, −0.4	2.06×10^{-1}	0.9	0.5	0.4	1.1	119	66, 80	1.4, 1.6	+0.4, +0.7	1.45×10^{-1}	1.0	0.6	0.5	1.3
117	66, 80	1.4, 1.6	−0.4, 0.0	1.80×10^{-1}	0.9	0.5	0.4	1.1	118	66, 80	1.4, 1.6	0.0, +0.4	1.57×10^{-1}	0.9	0.5	0.4	1.1
121	66, 80	1.6, 1.8	−1.0, −0.7	6.28×10^{-3}	5.1	3.5	1.8	6.5	126	66, 80	1.6, 1.8	+0.7, +1.0	4.06×10^{-3}	6.1	4.2	1.8	7.7
122	66, 80	1.6, 1.8	−0.7, −0.4	1.47×10^{-1}	1.0	0.6	0.5	1.3	125	66, 80	1.6, 1.8	+0.4, +0.7	9.89×10^{-2}	1.2	0.8	0.6	1.6
123	66, 80	1.6, 1.8	−0.4, 0.0	1.76×10^{-1}	0.9	0.5	0.4	1.1	124	66, 80	1.6, 1.8	0.0, +0.4	1.52×10^{-1}	0.9	0.5	0.5	1.1
127	66, 80	1.8, 2.0	−1.0, −0.7	1.90×10^{-3}	9.4	5.8	3.5	11.6	132	66, 80	1.8, 2.0	+0.7, +1.0	8.82×10^{-4}	11.9	7.4	4.3	14.7
128	66, 80	1.8, 2.0	−0.7, −0.4	5.38×10^{-2}	1.8	1.2	0.9	2.3	131	66, 80	1.8, 2.0	+0.4, +0.7	3.34×10^{-2}	2.1	1.3	1.0	2.7
129	66, 80	1.8, 2.0	−0.4, 0.0	1.72×10^{-1}	0.8	0.5	0.5	1.1	130	66, 80	1.8, 2.0	0.0, +0.4	1.45×10^{-1}	0.9	0.5	0.5	1.2
133	66, 80	2.0, 2.2	−1.0, −0.7	—	—	—	—	—	138	66, 80	2.0, 2.2	+0.7, +1.0	—	—	—	—	—
134	66, 80	2.0, 2.2	−0.7, −0.4	3.68×10^{-3}	6.5	4.8	3.0	8.6	137	66, 80	2.0, 2.2	+0.4, +0.7	2.62×10^{-3}	7.8	5.4	3.9	10.2
135	66, 80	2.0, 2.2	−0.4, 0.0	1.26×10^{-1}	1.0	0.5	0.6	1.3	136	66, 80	2.0, 2.2	0.0, +0.4	1.01×10^{-1}	1.0	0.6	0.7	1.4
139	66, 80	2.2, 2.4	−1.0, −0.7	—	—	—	—	—	144	66, 80	2.2, 2.4	+0.7, +1.0	—	—	—	—	—
140	66, 80	2.2, 2.4	−0.7, −0.4	—	—	—	—	—	143	66, 80	2.2, 2.4	+0.4, +0.7	—	—	—	—	—
141	66, 80	2.2, 2.4	−0.4, 0.0	4.01×10^{-2}	1.6	1.0	1.1	2.2	142	66, 80	2.2, 2.4	0.0, +0.4	3.62×10^{-2}	1.7	1.1	1.1	2.3

JHEP12(2017)059

Bin	$m_{\ell\ell}$ [GeV]	$\lvert y_{\ell\ell}\rvert$	$\cos\theta^*$	$d^3\sigma$ [pb/GeV]	δ^{stat} [%]	$\delta^{\text{syst}}_{\text{unc}}$ [%]	$\delta^{\text{syst}}_{\text{cor}}$ [%]	δ^{total} [%]	Bin	$m_{\ell\ell}$ [GeV]	$\lvert y_{\ell\ell}\rvert$	$\cos\theta^*$	$d^3\sigma$ [pb/GeV]	δ^{stat} [%]	$\delta^{\text{syst}}_{\text{unc}}$ [%]	$\delta^{\text{syst}}_{\text{cor}}$ [%]	δ^{total} [%]
145	91, 102	0.0, 0.2	−1.0, −0.7	2.25	0.3	0.2	0.3	0.5	150	91, 102	0.0, 0.2	+0.7, +1.0	2.26	0.3	0.2	0.3	0.5
146	91, 102	0.0, 0.2	−0.7, −0.4	3.58	0.3	0.1	0.2	0.3	149	91, 102	0.0, 0.2	+0.4, +0.7	3.60	0.3	0.1	0.2	0.3
147	91, 102	0.0, 0.2	−0.4, 0.0	3.12	0.3	0.1	0.2	0.4	148	91, 102	0.0, 0.2	0.0, +0.4	3.10	0.3	0.1	0.2	0.4
151	91, 102	0.2, 0.4	−1.0, −0.7	2.26	0.3	0.2	0.3	0.5	156	91, 102	0.2, 0.4	+0.7, +1.0	2.27	0.3	0.2	0.3	0.5
152	91, 102	0.2, 0.4	−0.7, −0.4	3.58	0.3	0.1	0.2	0.3	155	91, 102	0.2, 0.4	+0.4, +0.7	3.61	0.3	0.1	0.2	0.4
153	91, 102	0.2, 0.4	−0.4, 0.0	3.10	0.3	0.1	0.2	0.4	154	91, 102	0.2, 0.4	0.0, +0.4	3.10	0.2	0.1	0.2	0.4
157	91, 102	0.4, 0.6	−1.0, −0.7	2.24	0.3	0.2	0.3	0.5	162	91, 102	0.4, 0.6	+0.7, +1.0	2.24	0.3	0.2	0.3	0.5
158	91, 102	0.4, 0.6	−0.7, −0.4	3.57	0.3	0.1	0.2	0.4	161	91, 102	0.4, 0.6	+0.4, +0.7	3.60	0.3	0.1	0.2	0.4
159	91, 102	0.4, 0.6	−0.4, 0.0	3.08	0.2	0.1	0.2	0.3	160	91, 102	0.4, 0.6	0.0, +0.4	3.10	0.2	0.1	0.2	0.3
163	91, 102	0.6, 0.8	−1.0, −0.7	2.24	0.3	0.2	0.3	0.5	168	91, 102	0.6, 0.8	+0.7, +1.0	2.24	0.3	0.2	0.3	0.5
164	91, 102	0.6, 0.8	−0.7, −0.4	3.54	0.3	0.1	0.3	0.4	167	91, 102	0.6, 0.8	+0.4, +0.7	3.54	0.3	0.1	0.3	0.4
165	91, 102	0.6, 0.8	−0.4, 0.0	3.06	0.2	0.1	0.2	0.3	166	91, 102	0.6, 0.8	0.0, +0.4	3.08	0.2	0.1	0.2	0.3
169	91, 102	0.8, 1.0	−1.0, −0.7	2.21	0.3	0.2	0.3	0.5	174	91, 102	0.8, 1.0	+0.7, +1.0	2.24	0.3	0.2	0.3	0.5
170	91, 102	0.8, 1.0	−0.7, −0.4	3.50	0.3	0.1	0.3	0.4	173	91, 102	0.8, 1.0	+0.4, +0.7	3.49	0.3	0.1	0.3	0.4
171	91, 102	0.8, 1.0	−0.4, 0.0	3.06	0.2	0.1	0.2	0.3	172	91, 102	0.8, 1.0	0.0, +0.4	3.03	0.2	0.1	0.2	0.3
175	91, 102	1.0, 1.2	−1.0, −0.7	1.96	0.4	0.2	0.3	0.5	180	91, 102	1.0, 1.2	+0.7, +1.0	1.96	0.3	0.2	0.3	0.5
176	91, 102	1.0, 1.2	−0.7, −0.4	3.45	0.3	0.1	0.3	0.4	179	91, 102	1.0, 1.2	+0.4, +0.7	3.46	0.2	0.1	0.3	0.4
177	91, 102	1.0, 1.2	−0.4, 0.0	3.01	0.2	0.1	0.3	0.4	178	91, 102	1.0, 1.2	0.0, +0.4	3.00	0.2	0.1	0.3	0.4
181	91, 102	1.2, 1.4	−1.0, −0.7	1.29	0.4	0.2	0.4	0.6	186	91, 102	1.2, 1.4	+0.7, +1.0	1.29	0.4	0.2	0.4	0.6
182	91, 102	1.2, 1.4	−0.7, −0.4	3.41	0.3	0.1	0.3	0.4	185	91, 102	1.2, 1.4	+0.4, +0.7	3.39	0.2	0.1	0.2	0.4
183	91, 102	1.2, 1.4	−0.4, 0.0	2.97	0.3	0.1	0.3	0.4	184	91, 102	1.2, 1.4	0.0, +0.4	2.95	0.2	0.1	0.3	0.4
187	91, 102	1.4, 1.6	−1.0, −0.7	4.87×10^{-1}	0.7	0.4	0.4	0.8	192	91, 102	1.4, 1.6	+0.7, +1.0	4.80×10^{-1}	0.6	0.4	0.4	0.8
188	91, 102	1.4, 1.6	−0.7, −0.4	3.18	0.2	0.1	0.3	0.4	191	91, 102	1.4, 1.6	+0.4, +0.7	3.16	0.2	0.1	0.3	0.4
189	91, 102	1.4, 1.6	−0.4, 0.0	2.90	0.2	0.1	0.3	0.4	190	91, 102	1.4, 1.6	0.0, +0.4	2.90	0.2	0.1	0.3	0.4
193	91, 102	1.6, 1.8	−1.0, −0.7	9.17×10^{-2}	1.5	0.9	0.5	1.8	198	91, 102	1.6, 1.8	+0.7, +1.0	9.08×10^{-2}	1.5	0.9	0.6	1.8
194	91, 102	1.6, 1.8	−0.7, −0.4	2.24	0.3	0.2	0.3	0.5	197	91, 102	1.6, 1.8	+0.4, +0.7	2.22	0.3	0.2	0.3	0.5
195	91, 102	1.6, 1.8	−0.4, 0.0	2.83	0.2	0.1	0.3	0.4	196	91, 102	1.6, 1.8	0.0, +0.4	2.84	0.2	0.1	0.3	0.4
199	91, 102	1.8, 2.0	−1.0, −0.7	2.11×10^{-2}	2.9	1.9	0.7	3.5	204	91, 102	1.8, 2.0	+0.7, +1.0	2.02×10^{-2}	2.9	1.9	1.1	3.6
200	91, 102	1.8, 2.0	−0.7, −0.4	8.08×10^{-1}	0.5	0.3	0.4	0.7	203	91, 102	1.8, 2.0	+0.4, +0.7	7.92×10^{-1}	0.5	0.3	0.4	0.7
201	91, 102	1.8, 2.0	−0.4, 0.0	2.73	0.2	0.1	0.3	0.4	202	91, 102	1.8, 2.0	0.0, +0.4	2.73	0.2	0.1	0.3	0.4
205	91, 102	2.0, 2.2	−1.0, −0.7	2.53×10^{-3}	7.9	6.1	2.2	10.3	210	91, 102	2.0, 2.2	+0.7, +1.0	2.74×10^{-3}	8.3	5.6	3.4	10.6
206	91, 102	2.0, 2.2	−0.7, −0.4	4.99×10^{-2}	2.1	1.5	0.7	2.7	209	91, 102	2.0, 2.2	+0.4, +0.7	5.03×10^{-2}	2.1	1.5	0.7	2.7
207	91, 102	2.0, 2.2	−0.4, 0.0	1.96	0.3	0.2	0.3	0.5	208	91, 102	2.0, 2.2	0.0, +0.4	1.95	0.3	0.2	0.3	0.5
211	91, 102	2.2, 2.4	−1.0, −0.7	—	—	—	—	—	216	91, 102	2.2, 2.4	+0.7, +1.0	—	—	—	—	—
212	91, 102	2.2, 2.4	−0.7, −0.4	—	—	—	—	—	215	91, 102	2.2, 2.4	+0.4, +0.7	—	—	—	—	—
213	91, 102	2.2, 2.4	−0.4, 0.0	6.54×10^{-1}	0.4	0.3	0.4	0.7	214	91, 102	2.2, 2.4	0.0, +0.4	6.46×10^{-1}	0.4	0.3	0.4	0.7
217	91, 102	0.0, 0.2	−1.0, −0.7	2.80	0.3	0.2	0.3	0.4	222	91, 102	0.0, 0.2	+0.7, +1.0	2.82	0.3	0.2	0.3	0.4
218	91, 102	0.0, 0.2	−0.7, −0.4	4.17	0.2	0.1	0.2	0.3	221	91, 102	0.0, 0.2	+0.4, +0.7	4.21	0.2	0.1	0.2	0.3
219	91, 102	0.0, 0.2	−0.4, 0.0	3.59	0.2	0.1	0.2	0.4	220	91, 102	0.0, 0.2	0.0, +0.4	3.62	0.2	0.1	0.2	0.4
223	91, 102	0.2, 0.4	−1.0, −0.7	2.78	0.3	0.2	0.3	0.4	228	91, 102	0.2, 0.4	+0.7, +1.0	2.83	0.3	0.2	0.3	0.4
224	91, 102	0.2, 0.4	−0.7, −0.4	4.11	0.3	0.1	0.2	0.3	227	91, 102	0.2, 0.4	+0.4, +0.7	4.17	0.2	0.1	0.2	0.3
225	91, 102	0.2, 0.4	−0.4, 0.0	3.58	0.2	0.1	0.2	0.4	226	91, 102	0.2, 0.4	0.0, +0.4	3.61	0.2	0.1	0.2	0.3
229	91, 102	0.4, 0.6	−1.0, −0.7	2.75	0.3	0.2	0.3	0.5	234	91, 102	0.4, 0.6	+0.7, +1.0	2.84	0.3	0.2	0.3	0.5
230	91, 102	0.4, 0.6	−0.7, −0.4	4.07	0.3	0.1	0.2	0.4	233	91, 102	0.4, 0.6	+0.4, +0.7	4.19	0.3	0.1	0.2	0.4
231	91, 102	0.4, 0.6	−0.4, 0.0	3.55	0.2	0.1	0.2	0.3	232	91, 102	0.4, 0.6	0.0, +0.4	3.59	0.2	0.1	0.2	0.3
235	91, 102	0.6, 0.8	−1.0, −0.7	2.70	0.3	0.2	0.3	0.4	240	91, 102	0.6, 0.8	+0.7, +1.0	2.86	0.3	0.1	0.3	0.4
236	91, 102	0.6, 0.8	−0.7, −0.4	4.05	0.3	0.1	0.3	0.4	239	91, 102	0.6, 0.8	+0.4, +0.7	4.20	0.3	0.1	0.3	0.4
237	91, 102	0.6, 0.8	−0.4, 0.0	3.52	0.2	0.1	0.2	0.3	238	91, 102	0.6, 0.8	0.0, +0.4	3.57	0.2	0.1	0.2	0.3
241	91, 102	0.8, 1.0	−1.0, −0.7	2.64	0.3	0.2	0.3	0.5	246	91, 102	0.8, 1.0	+0.7, +1.0	2.83	0.3	0.2	0.3	0.5
242	91, 102	0.8, 1.0	−0.7, −0.4	3.98	0.3	0.1	0.3	0.4	245	91, 102	0.8, 1.0	+0.4, +0.7	4.17	0.3	0.1	0.3	0.4
243	91, 102	0.8, 1.0	−0.4, 0.0	3.46	0.2	0.1	0.2	0.3	244	91, 102	0.8, 1.0	0.0, +0.4	3.56	0.2	0.1	0.2	0.3
247	91, 102	1.0, 1.2	−1.0, −0.7	2.23	0.3	0.2	0.3	0.5	252	91, 102	1.0, 1.2	+0.7, +1.0	2.42	0.3	0.2	0.3	0.5
248	91, 102	1.0, 1.2	−0.7, −0.4	3.91	0.2	0.1	0.3	0.4	251	91, 102	1.0, 1.2	+0.4, +0.7	4.19	0.2	0.1	0.2	0.4
249	91, 102	1.0, 1.2	−0.4, 0.0	3.41	0.2	0.1	0.3	0.4	250	91, 102	1.0, 1.2	0.0, +0.4	3.52	0.2	0.1	0.2	0.4
253	91, 102	1.2, 1.4	−1.0, −0.7	1.46	0.4	0.2	0.3	0.5	258	91, 102	1.2, 1.4	+0.7, +1.0	1.60	0.4	0.2	0.3	0.5
254	91, 102	1.2, 1.4	−0.7, −0.4	3.79	0.3	0.1	0.2	0.4	257	91, 102	1.2, 1.4	+0.4, +0.7	4.12	0.2	0.1	0.2	0.3
255	91, 102	1.2, 1.4	−0.4, 0.0	3.34	0.2	0.1	0.3	0.4	256	91, 102	1.2, 1.4	0.0, +0.4	3.48	0.2	0.1	0.3	0.4
259	91, 102	1.4, 1.6	−1.0, −0.7	5.29×10^{-1}	0.6	0.3	0.4	0.8	264	91, 102	1.4, 1.6	+0.7, +1.0	5.95×10^{-1}	0.6	0.3	0.4	0.8
260	91, 102	1.4, 1.6	−0.7, −0.4	3.48	0.2	0.1	0.3	0.4	263	91, 102	1.4, 1.6	+0.4, +0.7	3.84	0.2	0.1	0.2	0.4
261	91, 102	1.4, 1.6	−0.4, 0.0	3.27	0.2	0.1	0.3	0.4	262	91, 102	1.4, 1.6	0.0, +0.4	3.42	0.2	0.1	0.3	0.4
265	91, 102	1.6, 1.8	−1.0, −0.7	9.80×10^{-2}	1.5	1.0	0.7	1.9	270	91, 102	1.6, 1.8	+0.7, +1.0	1.13×10^{-1}	1.3	0.9	0.6	1.7
266	91, 102	1.6, 1.8	−0.7, −0.4	2.41	0.3	0.1	0.3	0.5	269	91, 102	1.6, 1.8	+0.4, +0.7	2.70	0.3	0.1	0.3	0.4
267	91, 102	1.6, 1.8	−0.4, 0.0	3.20	0.2	0.1	0.3	0.4	268	91, 102	1.6, 1.8	0.0, +0.4	3.37	0.2	0.1	0.3	0.4
271	91, 102	1.8, 2.0	−1.0, −0.7	2.17×10^{-2}	3.0	1.8	0.9	3.7	276	91, 102	1.8, 2.0	+0.7, +1.0	2.36×10^{-2}	2.8	1.7	0.8	3.4
272	91, 102	1.8, 2.0	−0.7, −0.4	8.61×10^{-1}	0.5	0.3	0.5	0.7	275	91, 102	1.8, 2.0	+0.4, +0.7	9.82×10^{-1}	0.5	0.3	0.4	0.7
273	91, 102	1.8, 2.0	−0.4, 0.0	3.03	0.2	0.1	0.3	0.4	274	91, 102	1.8, 2.0	0.0, +0.4	3.23	0.2	0.1	0.3	0.4
277	91, 102	2.0, 2.2	−1.0, −0.7	2.30×10^{-3}	10.6	8.0	5.2	14.3	282	91, 102	2.0, 2.2	+0.7, +1.0	3.47×10^{-3}	7.6	5.2	2.6	9.6
278	91, 102	2.0, 2.2	−0.7, −0.4	5.15×10^{-2}	2.0	1.3	1.0	2.6	281	91, 102	2.0, 2.2	+0.4, +0.7	6.30×10^{-2}	1.9	1.2	1.0	2.5
279	91, 102	2.0, 2.2	−0.4, 0.0	2.17	0.3	0.1	0.3	0.4	280	91, 102	2.0, 2.2	0.0, +0.4	2.32	0.3	0.1	0.3	0.4
283	91, 102	2.2, 2.4	−1.0, −0.7	—	—	—	—	—	288	91, 102	2.2, 2.4	+0.7, +1.0	—	—	—	—	—
284	91, 102	2.2, 2.4	−0.7, −0.4	—	—	—	—	—	287	91, 102	2.2, 2.4	+0.4, +0.7	—	—	—	—	—
285	91, 102	2.2, 2.4	−0.4, 0.0	7.30×10^{-1}	0.4	0.2	0.4	0.7	286	91, 102	2.2, 2.4	0.0, +0.4	7.59×10^{-1}	0.4	0.2	0.4	0.6

JHEP12(2017)059

Bin	$m_{\ell\ell}$ [GeV]	$\lvert y_{\ell\ell}\rvert$	$\cos\theta^*$	$d^3\sigma$ [pb/GeV]	$\delta^{\rm stat}$ [%]	$\delta^{\rm syst}_{\rm unc}$ [%]	$\delta^{\rm syst}_{\rm cor}$ [%]	$\delta^{\rm total}$ [%]	Bin	$m_{\ell\ell}$ [GeV]	$\lvert y_{\ell\ell}\rvert$	$\cos\theta^*$	$d^3\sigma$ [pb/GeV]	$\delta^{\rm stat}$ [%]	$\delta^{\rm syst}_{\rm unc}$ [%]	$\delta^{\rm syst}_{\rm cor}$ [%]	$\delta^{\rm total}$ [%]
289	102, 116	0.0, 0.2	−1.0, −0.7	1.09×10^{-1}	1.4	0.8	0.6	1.7	294	102, 116	0.0, 0.2	+0.7, +1.0	1.09×10^{-1}	1.4	0.8	0.6	1.7
290	102, 116	0.0, 0.2	−0.7, −0.4	1.30×10^{-1}	1.2	0.6	0.4	1.4	293	102, 116	0.0, 0.2	+0.4, +0.7	1.39×10^{-1}	1.2	0.5	0.3	1.4
291	102, 116	0.0, 0.2	−0.4, 0.0	1.15×10^{-1}	1.2	0.5	0.3	1.4	292	102, 116	0.0, 0.2	0.0, +0.4	1.15×10^{-1}	1.2	0.5	0.4	1.4
295	102, 116	0.2, 0.4	−1.0, −0.7	1.03×10^{-1}	1.5	0.8	0.6	1.8	300	102, 116	0.2, 0.4	+0.7, +1.0	1.11×10^{-1}	1.5	0.8	0.6	1.7
296	102, 116	0.2, 0.4	−0.7, −0.4	1.33×10^{-1}	1.2	0.6	0.4	1.4	299	102, 116	0.2, 0.4	+0.4, +0.7	1.39×10^{-1}	1.2	0.5	0.4	1.4
297	102, 116	0.2, 0.4	−0.4, 0.0	1.14×10^{-1}	1.2	0.5	0.4	1.3	298	102, 116	0.2, 0.4	0.0, +0.4	1.19×10^{-1}	1.2	0.5	0.4	1.3
301	102, 116	0.4, 0.6	−1.0, −0.7	1.01×10^{-1}	1.5	0.8	0.6	1.8	306	102, 116	0.4, 0.6	+0.7, +1.0	1.13×10^{-1}	1.4	0.7	0.6	1.7
302	102, 116	0.4, 0.6	−0.7, −0.4	1.25×10^{-1}	1.3	0.7	0.4	1.5	305	102, 116	0.4, 0.6	+0.4, +0.7	1.40×10^{-1}	1.2	0.6	0.4	1.4
303	102, 116	0.4, 0.6	−0.4, 0.0	1.12×10^{-1}	1.1	0.5	0.4	1.3	304	102, 116	0.4, 0.6	0.0, +0.4	1.15×10^{-1}	1.1	0.5	0.3	1.3
307	102, 116	0.6, 0.8	−1.0, −0.7	9.95×10^{-2}	1.4	0.8	0.7	1.8	312	102, 116	0.6, 0.8	+0.7, +1.0	1.14×10^{-1}	1.4	0.7	0.7	1.7
308	102, 116	0.6, 0.8	−0.7, −0.4	1.21×10^{-1}	1.4	0.7	0.5	1.6	311	102, 116	0.6, 0.8	+0.4, +0.7	1.40×10^{-1}	1.3	0.7	0.5	1.6
309	102, 116	0.6, 0.8	−0.4, 0.0	1.12×10^{-1}	1.1	0.5	0.4	1.3	310	102, 116	0.6, 0.8	0.0, +0.4	1.15×10^{-1}	1.1	0.5	0.3	1.3
313	102, 116	0.8, 1.0	−1.0, −0.7	8.72×10^{-2}	1.6	0.9	0.6	1.9	318	102, 116	0.8, 1.0	+0.7, +1.0	1.11×10^{-1}	1.4	0.8	0.6	1.7
314	102, 116	0.8, 1.0	−0.7, −0.4	1.19×10^{-1}	1.3	0.7	0.5	1.6	317	102, 116	0.8, 1.0	+0.4, +0.7	1.47×10^{-1}	1.2	0.6	0.5	1.4
315	102, 116	0.8, 1.0	−0.4, 0.0	1.07×10^{-1}	1.1	0.7	0.4	1.4	316	102, 116	0.8, 1.0	0.0, +0.4	1.18×10^{-1}	1.0	0.5	0.4	1.2
319	102, 116	1.0, 1.2	−1.0, −0.7	6.74×10^{-2}	1.7	1.0	0.7	2.1	324	102, 116	1.0, 1.2	+0.7, +1.0	9.14×10^{-2}	1.5	0.8	0.6	1.8
320	102, 116	1.0, 1.2	−0.7, −0.4	1.13×10^{-1}	1.2	0.7	0.5	1.5	323	102, 116	1.0, 1.2	+0.4, +0.7	1.49×10^{-1}	1.1	0.6	0.5	1.3
321	102, 116	1.0, 1.2	−0.4, 0.0	1.06×10^{-1}	1.1	0.6	0.5	1.4	322	102, 116	1.0, 1.2	0.0, +0.4	1.18×10^{-1}	1.1	0.5	0.5	1.3
325	102, 116	1.2, 1.4	−1.0, −0.7	4.21×10^{-2}	1.9	1.2	1.1	2.5	330	102, 116	1.2, 1.4	+0.7, +1.0	5.84×10^{-2}	1.7	1.0	0.8	2.1
326	102, 116	1.2, 1.4	−0.7, −0.4	1.09×10^{-1}	1.2	0.6	0.6	1.5	329	102, 116	1.2, 1.4	+0.4, +0.7	1.50×10^{-1}	1.0	0.6	0.5	1.3
327	102, 116	1.2, 1.4	−0.4, 0.0	1.01×10^{-1}	1.1	0.6	0.6	1.4	328	102, 116	1.2, 1.4	0.0, +0.4	1.19×10^{-1}	1.1	0.7	0.7	1.5
331	102, 116	1.4, 1.6	−1.0, −0.7	1.39×10^{-2}	2.5	1.9	1.5	3.5	336	102, 116	1.4, 1.6	+0.7, +1.0	2.25×10^{-2}	2.2	1.6	1.5	3.1
332	102, 116	1.4, 1.6	−0.7, −0.4	9.53×10^{-2}	1.2	0.7	0.6	1.5	335	102, 116	1.4, 1.6	+0.4, +0.7	1.37×10^{-1}	1.1	0.6	0.6	1.3
333	102, 116	1.4, 1.6	−0.4, 0.0	9.77×10^{-2}	1.1	0.6	0.7	1.5	334	102, 116	1.4, 1.6	0.0, +0.4	1.17×10^{-1}	1.0	0.6	0.6	1.3
337	102, 116	1.6, 1.8	−1.0, −0.7	2.35×10^{-3}	4.6	4.9	2.8	7.3	342	102, 116	1.6, 1.8	+0.7, +1.0	4.19×10^{-3}	4.2	3.8	2.2	6.1
338	102, 116	1.6, 1.8	−0.7, −0.4	6.43×10^{-2}	1.2	0.9	1.0	1.8	341	102, 116	1.6, 1.8	+0.4, +0.7	1.01×10^{-1}	1.1	0.7	0.9	1.6
339	102, 116	1.6, 1.8	−0.4, 0.0	9.25×10^{-2}	1.1	0.7	1.0	1.6	340	102, 116	1.6, 1.8	0.0, +0.4	1.16×10^{-1}	1.0	0.7	0.8	1.5
343	102, 116	1.8, 2.0	−1.0, −0.7	4.34×10^{-4}	6.1	11.4	3.4	13.4	348	102, 116	1.8, 2.0	+0.7, +1.0	8.65×10^{-4}	8.2	9.1	2.9	12.6
344	102, 116	1.8, 2.0	−0.7, −0.4	2.13×10^{-2}	1.7	1.5	1.6	2.8	347	102, 116	1.8, 2.0	+0.4, +0.7	3.56×10^{-2}	1.5	1.3	1.5	2.5
345	102, 116	1.8, 2.0	−0.4, 0.0	8.89×10^{-2}	1.0	0.6	0.9	1.5	346	102, 116	1.8, 2.0	0.0, +0.4	1.14×10^{-1}	0.9	0.6	0.9	1.4
349	102, 116	2.0, 2.2	−1.0, −0.7	—	—	—	—	—	354	102, 116	2.0, 2.2	+0.7, +1.0	—	—	—	—	—
350	102, 116	2.0, 2.2	−0.7, −0.4	1.39×10^{-3}	3.3	5.6	3.5	7.4	353	102, 116	2.0, 2.2	+0.4, +0.7	2.22×10^{-3}	3.6	4.9	2.2	6.5
351	102, 116	2.0, 2.2	−0.4, 0.0	6.28×10^{-2}	1.0	0.8	1.3	1.8	352	102, 116	2.0, 2.2	0.0, +0.4	7.95×10^{-2}	0.9	0.7	1.1	1.6
355	102, 116	2.2, 2.4	−1.0, −0.7	—	—	—	—	—	360	102, 116	2.2, 2.4	+0.7, +1.0	—	—	—	—	—
356	102, 116	2.2, 2.4	−0.7, −0.4	—	—	—	—	—	359	102, 116	2.2, 2.4	+0.4, +0.7	—	—	—	—	—
357	102, 116	2.2, 2.4	−0.4, 0.0	2.17×10^{-2}	1.4	1.4	1.9	2.7	358	102, 116	2.2, 2.4	0.0, +0.4	2.45×10^{-2}	1.3	1.3	1.6	2.5
361	116, 150	0.0, 0.2	−1.0, −0.7	2.39×10^{-2}	2.4	1.1	1.4	3.0	366	116, 150	0.0, 0.2	+0.7, +1.0	2.59×10^{-2}	2.2	1.0	1.3	2.7
362	116, 150	0.0, 0.2	−0.7, −0.4	2.59×10^{-2}	1.9	0.6	0.8	2.1	365	116, 150	0.0, 0.2	+0.4, +0.7	2.69×10^{-2}	1.9	0.6	0.7	2.1
363	116, 150	0.0, 0.2	−0.4, 0.0	2.16×10^{-2}	1.9	0.9	0.6	2.2	364	116, 150	0.0, 0.2	0.0, +0.4	2.25×10^{-2}	1.8	0.7	0.6	2.0
367	116, 150	0.2, 0.4	−1.0, −0.7	2.29×10^{-2}	2.3	1.2	1.5	3.0	372	116, 150	0.2, 0.4	+0.7, +1.0	2.54×10^{-2}	2.3	1.2	1.3	2.8
368	116, 150	0.2, 0.4	−0.7, −0.4	2.45×10^{-2}	2.1	0.8	0.8	2.4	371	116, 150	0.2, 0.4	+0.4, +0.7	2.88×10^{-2}	1.9	0.6	0.7	2.1
369	116, 150	0.2, 0.4	−0.4, 0.0	2.10×10^{-2}	1.9	0.6	0.7	2.1	370	116, 150	0.2, 0.4	0.0, +0.4	2.25×10^{-2}	1.8	0.5	0.6	2.0
373	116, 150	0.4, 0.6	−1.0, −0.7	2.11×10^{-2}	2.4	1.0	1.6	3.1	378	116, 150	0.4, 0.6	+0.7, +1.0	2.64×10^{-2}	2.3	1.1	1.3	2.8
374	116, 150	0.4, 0.6	−0.7, −0.4	2.44×10^{-2}	2.1	0.7	0.8	2.4	377	116, 150	0.4, 0.6	+0.4, +0.7	2.81×10^{-2}	2.0	0.7	0.7	2.2
375	116, 150	0.4, 0.6	−0.4, 0.0	2.10×10^{-2}	1.8	0.7	0.6	2.0	376	116, 150	0.4, 0.6	0.0, +0.4	2.26×10^{-2}	1.7	0.5	0.6	1.9
379	116, 150	0.6, 0.8	−1.0, −0.7	2.07×10^{-2}	2.4	1.0	1.5	3.0	384	116, 150	0.6, 0.8	+0.7, +1.0	2.69×10^{-2}	2.0	0.8	1.1	2.4
380	116, 150	0.6, 0.8	−0.7, −0.4	2.32×10^{-2}	2.3	0.8	0.9	2.5	383	116, 150	0.6, 0.8	+0.4, +0.7	2.93×10^{-2}	2.0	0.8	0.7	2.3
381	116, 150	0.6, 0.8	−0.4, 0.0	2.06×10^{-2}	1.8	0.6	0.6	2.0	382	116, 150	0.6, 0.8	0.0, +0.4	2.36×10^{-2}	1.7	0.5	0.5	1.9
385	116, 150	0.8, 1.0	−1.0, −0.7	1.69×10^{-2}	2.6	1.2	1.5	3.3	390	116, 150	0.8, 1.0	+0.7, +1.0	2.37×10^{-2}	2.1	0.9	1.1	2.6
386	116, 150	0.8, 1.0	−0.7, −0.4	2.18×10^{-2}	2.3	0.9	0.8	2.6	389	116, 150	0.8, 1.0	+0.4, +0.7	3.03×10^{-2}	1.9	0.7	0.6	2.1
387	116, 150	0.8, 1.0	−0.4, 0.0	2.08×10^{-2}	1.8	0.6	0.6	2.0	388	116, 150	0.8, 1.0	0.0, +0.4	2.30×10^{-2}	1.7	0.6	0.5	1.9
391	116, 150	1.0, 1.2	−1.0, −0.7	1.21×10^{-2}	3.1	1.6	1.3	3.7	396	116, 150	1.0, 1.2	+0.7, +1.0	1.90×10^{-2}	2.4	1.2	1.1	2.9
392	116, 150	1.0, 1.2	−0.7, −0.4	1.99×10^{-2}	2.2	0.9	0.8	2.5	395	116, 150	1.0, 1.2	+0.4, +0.7	3.07×10^{-2}	1.8	0.6	0.6	2.0
393	116, 150	1.0, 1.2	−0.4, 0.0	2.05×10^{-2}	1.9	0.8	0.6	2.1	394	116, 150	1.0, 1.2	0.0, +0.4	2.39×10^{-2}	1.7	0.6	0.6	1.9
397	116, 150	1.2, 1.4	−1.0, −0.7	8.16×10^{-3}	3.6	1.5	1.3	4.1	402	116, 150	1.2, 1.4	+0.7, +1.0	1.38×10^{-2}	2.7	1.0	0.8	3.0
398	116, 150	1.2, 1.4	−0.7, −0.4	1.82×10^{-2}	2.2	1.1	0.8	2.6	401	116, 150	1.2, 1.4	+0.4, +0.7	3.11×10^{-2}	1.7	0.7	0.6	1.9
399	116, 150	1.2, 1.4	−0.4, 0.0	1.87×10^{-2}	2.0	0.8	0.6	2.2	400	116, 150	1.2, 1.4	0.0, +0.4	2.39×10^{-2}	1.8	0.7	0.6	2.0
403	116, 150	1.4, 1.6	−1.0, −0.7	2.40×10^{-3}	6.3	2.9	2.0	7.2	408	116, 150	1.4, 1.6	+0.7, +1.0	4.68×10^{-3}	4.4	2.5	1.2	5.2
404	116, 150	1.4, 1.6	−0.7, −0.4	1.64×10^{-2}	2.2	0.9	0.8	2.6	407	116, 150	1.4, 1.6	+0.4, +0.7	2.96×10^{-2}	1.7	0.7	0.6	1.9
405	116, 150	1.4, 1.6	−0.4, 0.0	1.79×10^{-2}	2.0	0.9	0.7	2.3	406	116, 150	1.4, 1.6	0.0, +0.4	2.30×10^{-2}	1.7	0.8	0.5	2.0
409	116, 150	1.6, 1.8	−1.0, −0.7	3.00×10^{-4}	70.7	18.8	4.6	73.3	414	116, 150	1.6, 1.8	+0.7, +1.0	9.12×10^{-4}	9.2	7.6	2.1	12.2
410	116, 150	1.6, 1.8	−0.7, −0.4	1.09×10^{-2}	2.8	1.2	0.9	3.1	413	116, 150	1.6, 1.8	+0.4, +0.7	2.23×10^{-2}	2.0	0.9	0.7	2.3
411	116, 150	1.6, 1.8	−0.4, 0.0	1.72×10^{-2}	2.0	0.9	0.7	2.3	412	116, 150	1.6, 1.8	0.0, +0.4	2.36×10^{-2}	1.8	0.9	0.6	2.0
415	116, 150	1.8, 2.0	−1.0, −0.7	—	—	—	—	—	420	116, 150	1.8, 2.0	+0.7, +1.0	—	—	—	—	—
416	116, 150	1.8, 2.0	−0.7, −0.4	3.51×10^{-3}	4.7	2.7	1.8	5.7	419	116, 150	1.8, 2.0	+0.4, +0.7	7.66×10^{-3}	3.5	2.0	1.3	4.2
417	116, 150	1.8, 2.0	−0.4, 0.0	1.66×10^{-2}	2.1	1.2	0.8	2.6	418	116, 150	1.8, 2.0	0.0, +0.4	2.33×10^{-2}	1.8	1.0	0.7	2.2
421	116, 150	2.0, 2.2	−1.0, −0.7	—	—	—	—	—	426	116, 150	2.0, 2.2	+0.7, +1.0	—	—	—	—	—
422	116, 150	2.0, 2.2	−0.7, −0.4	2.20×10^{-4}	8.3	8.9	6.0	13.5	425	116, 150	2.0, 2.2	+0.4, +0.7	4.66×10^{-4}	9.7	7.6	3.8	12.9
423	116, 150	2.0, 2.2	−0.4, 0.0	1.20×10^{-2}	2.1	1.0	0.9	2.5	424	116, 150	2.0, 2.2	0.0, +0.4	1.65×10^{-2}	1.9	0.9	0.8	2.2
427	116, 150	2.2, 2.4	−1.0, −0.7	—	—	—	—	—	432	116, 150	2.2, 2.4	+0.7, +1.0	—	—	—	—	—
428	116, 150	2.2, 2.4	−0.7, −0.4	—	—	—	—	—	431	116, 150	2.2, 2.4	+0.4, +0.7	—	—	—	—	—
429	116, 150	2.2, 2.4	−0.4, 0.0	3.94×10^{-3}	3.8	2.5	1.9	4.9	430	116, 150	2.2, 2.4	0.0, +0.4	4.75×10^{-3}	3.5	2.2	1.9	4.5

JHEP12(2017)059

Bin	$m_{\ell\ell}$ [GeV]	$\lvert y_{\ell\ell}\rvert$	$\cos\theta^*$	$d^3\sigma$ [pb/GeV]	δ^{stat} [%]	$\delta^{\text{syst}}_{\text{unc}}$ [%]	$\delta^{\text{syst}}_{\text{cor}}$ [%]	δ^{total} [%]	Bin	$m_{\ell\ell}$ [GeV]	$\lvert y_{\ell\ell}\rvert$	$\cos\theta^*$	$d^3\sigma$ [pb/GeV]	δ^{stat} [%]	$\delta^{\text{syst}}_{\text{unc}}$ [%]	$\delta^{\text{syst}}_{\text{cor}}$ [%]	δ^{total} [%]
433	150, 200	0.0, 0.2	−1.0, −0.7	6.26×10^{-3}	4.2	1.6	2.8	5.3	438	150, 200	0.0, 0.2	+0.7, +1.0	6.55×10^{-3}	4.3	1.7	2.8	5.4
434	150, 200	0.0, 0.2	−0.7, −0.4	5.56×10^{-3}	3.7	1.2	1.6	4.2	437	150, 200	0.0, 0.2	+0.4, +0.7	5.91×10^{-3}	3.6	1.3	1.6	4.1
435	150, 200	0.0, 0.2	−0.4, 0.0	4.77×10^{-3}	3.4	1.3	1.2	3.8	436	150, 200	0.0, 0.2	0.0, +0.4	4.76×10^{-3}	3.5	0.7	1.1	3.7
439	150, 200	0.2, 0.4	−1.0, −0.7	5.66×10^{-3}	4.6	1.7	3.2	5.8	444	150, 200	0.2, 0.4	+0.7, +1.0	6.67×10^{-3}	4.0	2.0	2.7	5.2
440	150, 200	0.2, 0.4	−0.7, −0.4	5.41×10^{-3}	3.9	1.9	1.6	4.7	443	150, 200	0.2, 0.4	+0.4, +0.7	5.96×10^{-3}	3.6	1.9	2.5	4.8
441	150, 200	0.2, 0.4	−0.4, 0.0	4.81×10^{-3}	3.4	0.9	1.2	3.7	442	150, 200	0.2, 0.4	0.0, +0.4	4.97×10^{-3}	3.2	1.0	1.2	3.6
445	150, 200	0.4, 0.6	−1.0, −0.7	4.73×10^{-3}	4.8	2.2	3.3	6.2	450	150, 200	0.4, 0.6	+0.7, +1.0	7.08×10^{-3}	3.7	1.3	2.3	4.6
446	150, 200	0.4, 0.6	−0.7, −0.4	5.52×10^{-3}	3.9	1.0	1.6	4.3	449	150, 200	0.4, 0.6	+0.4, +0.7	6.26×10^{-3}	3.6	1.2	1.4	4.0
447	150, 200	0.4, 0.6	−0.4, 0.0	4.56×10^{-3}	3.4	0.8	1.1	3.7	448	150, 200	0.4, 0.6	0.0, +0.4	4.79×10^{-3}	3.4	1.9	1.1	4.1
451	150, 200	0.6, 0.8	−1.0, −0.7	4.51×10^{-3}	4.7	1.9	3.0	5.9	456	150, 200	0.6, 0.8	+0.7, +1.0	6.21×10^{-3}	3.8	1.3	2.2	4.6
452	150, 200	0.6, 0.8	−0.7, −0.4	5.18×10^{-3}	4.2	1.5	1.7	4.8	455	150, 200	0.6, 0.8	+0.4, +0.7	6.90×10^{-3}	3.5	0.8	1.2	3.8
453	150, 200	0.6, 0.8	−0.4, 0.0	4.26×10^{-3}	3.4	1.2	1.2	3.8	454	150, 200	0.6, 0.8	0.0, +0.4	5.26×10^{-3}	3.1	0.6	1.0	3.3
457	150, 200	0.8, 1.0	−1.0, −0.7	3.32×10^{-3}	5.4	2.3	3.2	6.7	462	150, 200	0.8, 1.0	+0.7, +1.0	6.01×10^{-3}	3.8	1.5	1.8	4.5
458	150, 200	0.8, 1.0	−0.7, −0.4	4.91×10^{-3}	4.3	1.1	1.7	4.8	461	150, 200	0.8, 1.0	+0.4, +0.7	6.43×10^{-3}	3.7	1.3	1.3	4.1
459	150, 200	0.8, 1.0	−0.4, 0.0	4.28×10^{-3}	3.5	0.8	1.1	3.7	460	150, 200	0.8, 1.0	0.0, +0.4	5.18×10^{-3}	3.1	0.7	0.9	3.3
463	150, 200	1.0, 1.2	−1.0, −0.7	2.39×10^{-3}	6.4	2.4	3.0	7.5	468	150, 200	1.0, 1.2	+0.7, +1.0	4.66×10^{-3}	4.2	1.8	1.8	4.9
464	150, 200	1.0, 1.2	−0.7, −0.4	4.03×10^{-3}	4.4	1.7	1.8	5.1	467	150, 200	1.0, 1.2	+0.4, +0.7	6.99×10^{-3}	3.2	1.1	1.0	3.5
465	150, 200	1.0, 1.2	−0.4, 0.0	4.13×10^{-3}	3.7	1.2	1.3	4.1	466	150, 200	1.0, 1.2	0.0, +0.4	5.40×10^{-3}	3.1	1.2	0.9	3.5
469	150, 200	1.2, 1.4	−1.0, −0.7	1.46×10^{-3}	8.1	4.1	2.8	9.5	474	150, 200	1.2, 1.4	+0.7, +1.0	3.19×10^{-3}	5.0	2.4	1.5	5.7
470	150, 200	1.2, 1.4	−0.7, −0.4	3.80×10^{-3}	4.4	2.1	1.8	5.2	473	150, 200	1.2, 1.4	+0.4, +0.7	7.42×10^{-3}	3.0	1.0	0.9	3.3
471	150, 200	1.2, 1.4	−0.4, 0.0	4.04×10^{-3}	3.8	1.3	1.2	4.2	472	150, 200	1.2, 1.4	0.0, +0.4	5.48×10^{-3}	3.3	0.8	0.9	3.5
475	150, 200	1.4, 1.6	−1.0, −0.7	4.78×10^{-4}	24.4	14.5	3.2	28.6	480	150, 200	1.4, 1.6	+0.7, +1.0	1.06×10^{-3}	8.4	5.8	2.2	10.4
476	150, 200	1.4, 1.6	−0.7, −0.4	3.12×10^{-3}	4.9	2.4	2.0	5.9	479	150, 200	1.4, 1.6	+0.4, +0.7	6.69×10^{-3}	3.1	2.0	0.9	3.8
477	150, 200	1.4, 1.6	−0.4, 0.0	3.84×10^{-3}	3.8	1.4	1.2	4.2	478	150, 200	1.4, 1.6	0.0, +0.4	5.48×10^{-3}	3.1	1.1	0.8	3.4
481	150, 200	1.6, 1.8	−1.0, −0.7	—	—	—	—	—	486	150, 200	1.6, 1.8	+0.7, +1.0	—	—	—	—	—
482	150, 200	1.6, 1.8	−0.7, −0.4	1.96×10^{-3}	5.9	2.0	2.0	6.5	485	150, 200	1.6, 1.8	+0.4, +0.7	5.25×10^{-3}	3.5	1.2	0.9	3.8
483	150, 200	1.6, 1.8	−0.4, 0.0	3.65×10^{-3}	3.9	1.6	1.5	4.5	484	150, 200	1.6, 1.8	0.0, +0.4	5.22×10^{-3}	3.2	1.1	0.8	3.5
487	150, 200	1.8, 2.0	−1.0, −0.7	—	—	—	—	—	492	150, 200	1.8, 2.0	+0.7, +1.0	—	—	—	—	—
488	150, 200	1.8, 2.0	−0.7, −0.4	5.67×10^{-4}	11.8	4.8	4.4	13.4	491	150, 200	1.8, 2.0	+0.4, +0.7	1.62×10^{-3}	6.4	1.9	1.6	6.9
489	150, 200	1.8, 2.0	−0.4, 0.0	3.36×10^{-3}	3.8	0.9	1.0	4.0	490	150, 200	1.8, 2.0	0.0, +0.4	5.16×10^{-3}	3.0	0.9	0.7	3.2
493	150, 200	2.0, 2.2	−1.0, −0.7	—	—	—	—	—	498	150, 200	2.0, 2.2	+0.7, +1.0	—	—	—	—	—
494	150, 200	2.0, 2.2	−0.7, −0.4	—	—	—	—	—	497	150, 200	2.0, 2.2	+0.4, +0.7	—	—	—	—	—
495	150, 200	2.0, 2.2	−0.4, 0.0	2.47×10^{-3}	4.4	1.7	1.3	4.9	496	150, 200	2.0, 2.2	0.0, +0.4	3.68×10^{-3}	3.5	1.2	0.8	3.8
499	150, 200	2.2, 2.4	−1.0, −0.7	—	—	—	—	—	504	150, 200	2.2, 2.4	+0.7, +1.0	—	—	—	—	—
500	150, 200	2.2, 2.4	−0.7, −0.4	—	—	—	—	—	503	150, 200	2.2, 2.4	+0.4, +0.7	—	—	—	—	—
501	150, 200	2.2, 2.4	−0.4, 0.0	8.93×10^{-4}	7.0	2.0	1.7	7.5	502	150, 200	2.2, 2.4	0.0, +0.4	1.15×10^{-3}	6.3	1.8	1.3	6.6

Table 7. The combined Born-level triple-differential cross section $d^3\sigma/dm_{\ell\ell}d|y_{\ell\ell}|d\cos\theta^*$. The measurements are listed together with the statistical (δ^{stat}), uncorrelated systematic ($\delta^{\text{syst}}_{\text{unc}}$), correlated systematic ($\delta^{\text{syst}}_{\text{cor}}$), and total ($\delta^{\text{total}}$) uncertainties. The luminosity uncertainty of 1.9% is not shown and not included in the overall systematic and total uncertainties.

JHEP12(2017)059

Bin	m_{ee} [GeV]	$\lvert y_{ee}\rvert$	$\cos\theta^*$	$d^3\sigma$ [pb/GeV]	δ^{stat} [%]	δ^{syst}_{unc} [%]	δ^{syst}_{cor} [%]	δ^{total} [%]	Bin	m_{ee} [GeV]	$\lvert y_{ee}\rvert$	$\cos\theta^*$	$d^3\sigma$ [pb/GeV]	δ^{stat} [%]	δ^{syst}_{unc} [%]	δ^{syst}_{cor} [%]	δ^{total} [%]
1	66, 80	1.2, 1.6	−1.0, −0.7	1.06×10^{-2}	6.4	8.1	12.4	16.1	6	66, 80	1.2, 1.6	+0.7, +1.0	6.29×10^{-3}	7.8	11.0	16.1	21.0
2	66, 80	1.2, 1.6	−0.7, −0.4	9.24×10^{-4}	16.2	15.4	15.3	27.1	5	66, 80	1.2, 1.6	+0.4, +0.7	6.97×10^{-4}	15.7	13.1	15.5	25.7
3	66, 80	1.2, 1.6	−0.4, 0.0	—	—	—	—	—	4	66, 80	1.2, 1.6	0.0, +0.4	—	—	—	—	—
7	66, 80	1.6, 2.0	−1.0, −0.7	3.89×10^{-2}	3.9	3.8	7.0	8.9	12	66, 80	1.6, 2.0	+0.7, +1.0	2.24×10^{-2}	5.1	6.7	10.4	13.3
8	66, 80	1.6, 2.0	−0.7, −0.4	6.54×10^{-2}	2.8	2.6	5.1	6.4	11	66, 80	1.6, 2.0	+0.4, +0.7	4.27×10^{-2}	3.2	3.5	6.1	7.8
9	66, 80	1.6, 2.0	−0.4, 0.0	—	—	—	—	—	10	66, 80	1.6, 2.0	0.0, +0.4	—	—	—	—	—
13	66, 80	2.0, 2.4	−1.0, −0.7	4.28×10^{-2}	6.2	6.6	13.1	16.0	18	66, 80	2.0, 2.4	+0.7, +1.0	2.08×10^{-2}	7.3	8.6	25.4	27.8
14	66, 80	2.0, 2.4	−0.7, −0.4	1.89×10^{-1}	2.0	2.1	4.4	5.2	17	66, 80	2.0, 2.4	+0.4, +0.7	9.97×10^{-2}	2.6	3.4	6.0	7.3
15	66, 80	2.0, 2.4	−0.4, 0.0	5.10×10^{-2}	2.5	2.5	5.4	6.5	16	66, 80	2.0, 2.4	0.0, +0.4	3.55×10^{-2}	2.8	3.2	6.3	7.6
19	66, 80	2.4, 2.8	−1.0, −0.7	3.91×10^{-2}	3.5	3.8	19.5	20.2	24	66, 80	2.4, 2.8	+0.7, +1.0	1.65×10^{-2}	4.3	5.7	26.9	27.9
20	66, 80	2.4, 2.8	−0.7, −0.4	1.89×10^{-1}	2.2	2.2	11.3	11.8	23	66, 80	2.4, 2.8	+0.4, +0.7	8.98×10^{-2}	2.7	3.1	17.5	18.0
21	66, 80	2.4, 2.8	−0.4, 0.0	8.40×10^{-2}	2.3	1.9	2.4	3.8	22	66, 80	2.4, 2.8	0.0, +0.4	5.24×10^{-2}	2.8	2.7	3.9	5.5
25	66, 80	2.8, 3.6	−1.0, −0.7	2.14×10^{-2}	3.0	3.1	18.4	18.9	30	66, 80	2.8, 3.6	+0.7, +1.0	7.09×10^{-3}	3.8	7.4	32.7	33.8
26	66, 80	2.8, 3.6	−0.7, −0.4	4.84×10^{-2}	2.1	1.9	10.3	10.7	29	66, 80	2.8, 3.6	+0.4, +0.7	1.79×10^{-2}	2.8	3.2	15.2	15.7
27	66, 80	2.8, 3.6	−0.4, 0.0	—	—	—	—	—	28	66, 80	2.8, 3.6	0.0, +0.4	—	—	—	—	—
31	80, 91	1.2, 1.6	−1.0, −0.7	5.20×10^{-1}	0.9	0.7	2.4	2.7	36	80, 91	1.2, 1.6	+0.7, +1.0	5.29×10^{-1}	0.9	0.7	2.6	2.8
32	80, 91	1.2, 1.6	−0.7, −0.4	3.07×10^{-2}	3.6	2.6	3.4	5.6	35	80, 91	1.2, 1.6	+0.4, +0.7	3.07×10^{-2}	3.5	2.8	3.6	5.8
33	80, 91	1.2, 1.6	−0.4, 0.0	—	—	—	—	—	34	80, 91	1.2, 1.6	0.0, +0.4	—	—	—	—	—
37	80, 91	1.6, 2.0	−1.0, −0.7	1.26	0.7	0.4	2.7	2.8	42	80, 91	1.6, 2.0	+0.7, +1.0	1.28	0.6	0.4	2.6	2.7
38	80, 91	1.6, 2.0	−0.7, −0.4	1.04	0.7	0.5	1.7	1.9	41	80, 91	1.6, 2.0	+0.4, +0.7	1.04	0.7	0.5	1.7	1.9
39	80, 91	1.6, 2.0	−0.4, 0.0	5.59×10^{-3}	7.9	4.4	4.4	10.0	40	80, 91	1.6, 2.0	0.0, +0.4	5.05×10^{-3}	7.4	4.6	3.5	9.4
43	80, 91	2.0, 2.4	−1.0, −0.7	1.28	0.9	0.8	2.7	2.9	48	80, 91	2.0, 2.4	+0.7, +1.0	1.24	0.9	0.7	2.6	2.9
44	80, 91	2.0, 2.4	−0.7, −0.4	2.71	0.5	0.4	1.4	1.5	47	80, 91	2.0, 2.4	+0.4, +0.7	2.66	0.5	0.4	1.5	1.6
45	80, 91	2.0, 2.4	−0.4, 0.0	7.32×10^{-1}	0.6	0.6	1.8	2.0	46	80, 91	2.0, 2.4	0.0, +0.4	7.23×10^{-1}	0.6	0.6	1.9	2.1
49	80, 91	2.4, 2.8	−1.0, −0.7	1.14	0.7	0.6	3.2	3.4	54	80, 91	2.4, 2.8	+0.7, +1.0	1.14	0.6	0.6	2.7	2.9
50	80, 91	2.4, 2.8	−0.7, −0.4	2.55	0.6	0.5	2.4	2.5	53	80, 91	2.4, 2.8	+0.4, +0.7	2.52	0.6	0.5	2.5	2.6
51	80, 91	2.4, 2.8	−0.4, 0.0	1.10	0.6	0.5	1.7	1.9	52	80, 91	2.4, 2.8	0.0, +0.4	1.10	0.6	0.5	1.7	1.9
55	80, 91	2.8, 3.6	−1.0, −0.7	6.05×10^{-1}	0.6	0.6	4.1	4.2	60	80, 91	2.8, 3.6	+0.7, +1.0	5.97×10^{-1}	0.6	0.6	4.0	4.1
56	80, 91	2.8, 3.6	−0.7, −0.4	5.95×10^{-1}	0.5	0.5	4.6	4.6	59	80, 91	2.8, 3.6	+0.4, +0.7	5.84×10^{-1}	0.5	0.5	4.5	4.5
57	80, 91	2.8, 3.6	−0.4, 0.0	—	—	—	—	—	58	80, 91	2.8, 3.6	0.0, +0.4	—	—	—	—	—
61	91, 102	1.2, 1.6	−1.0, −0.7	6.53×10^{-1}	0.8	0.6	2.2	2.4	66	91, 102	1.2, 1.6	+0.7, +1.0	7.55×10^{-1}	0.8	0.6	2.3	2.5
62	91, 102	1.2, 1.6	−0.7, −0.4	3.64×10^{-2}	3.5	2.8	2.7	5.2	65	91, 102	1.2, 1.6	+0.4, +0.7	3.88×10^{-2}	3.5	3.0	3.2	5.6
63	91, 102	1.2, 1.6	−0.4, 0.0	—	—	—	—	—	64	91, 102	1.2, 1.6	0.0, +0.4	—	—	—	—	—
67	91, 102	1.6, 2.0	−1.0, −0.7	1.52	0.6	0.4	2.2	2.3	72	91, 102	1.6, 2.0	+0.7, +1.0	1.78	0.6	0.4	2.1	2.3
68	91, 102	1.6, 2.0	−0.7, −0.4	1.13	0.7	0.5	1.5	1.7	71	91, 102	1.6, 2.0	+0.4, +0.7	1.29	0.7	0.4	1.4	1.6
69	91, 102	1.6, 2.0	−0.4, 0.0	6.15×10^{-3}	7.6	6.1	6.4	11.6	70	91, 102	1.6, 2.0	0.0, +0.4	5.73×10^{-3}	8.0	6.7	6.3	12.2
73	91, 102	2.0, 2.4	−1.0, −0.7	1.48	0.9	0.7	2.3	2.6	78	91, 102	2.0, 2.4	+0.7, +1.0	1.81	0.8	0.6	2.2	2.4
74	91, 102	2.0, 2.4	−0.7, −0.4	2.94	0.5	0.3	1.6	1.7	77	91, 102	2.0, 2.4	+0.4, +0.7	3.48	0.4	0.3	1.5	1.6
75	91, 102	2.0, 2.4	−0.4, 0.0	8.06×10^{-1}	0.7	0.6	1.6	1.9	76	91, 102	2.0, 2.4	0.0, +0.4	8.97×10^{-1}	0.6	0.6	1.5	1.7
79	91, 102	2.4, 2.8	−1.0, −0.7	1.25	0.7	0.6	2.3	2.5	84	91, 102	2.4, 2.8	+0.7, +1.0	1.65	0.6	0.5	2.3	2.4
80	91, 102	2.4, 2.8	−0.7, −0.4	2.63	0.6	0.5	2.0	2.1	83	91, 102	2.4, 2.8	+0.4, +0.7	3.33	0.5	0.5	1.8	2.0
81	91, 102	2.4, 2.8	−0.4, 0.0	1.24	0.6	1.0	1.7	2.1	82	91, 102	2.4, 2.8	0.0, +0.4	1.41	0.6	0.8	1.5	1.8
85	91, 102	2.8, 3.6	−1.0, −0.7	6.54×10^{-1}	0.6	0.6	3.0	3.1	90	91, 102	2.8, 3.6	+0.7, +1.0	9.09×10^{-1}	0.5	0.6	2.9	3.0
86	91, 102	2.8, 3.6	−0.7, −0.4	5.66×10^{-1}	0.6	0.5	3.3	3.4	89	91, 102	2.8, 3.6	+0.4, +0.7	7.57×10^{-1}	0.5	0.4	2.5	2.6
87	91, 102	2.8, 3.6	−0.4, 0.0	—	—	—	—	—	88	91, 102	2.8, 3.6	0.0, +0.4	—	—	—	—	—
91	102, 116	1.2, 1.6	−1.0, −0.7	3.09×10^{-2}	4.6	6.3	11.4	13.8	96	102, 116	1.2, 1.6	+0.7, +1.0	5.49×10^{-2}	3.3	4.0	6.5	8.3
92	102, 116	1.2, 1.6	−0.7, −0.4	1.06×10^{-3}	23.7	22.9	33.4	46.9	95	102, 116	1.2, 1.6	+0.4, +0.7	1.64×10^{-3}	20.6	29.7	24.2	43.5
93	102, 116	1.2, 1.6	−0.4, 0.0	—	—	—	—	—	94	102, 116	1.2, 1.6	0.0, +0.4	—	—	—	—	—
97	102, 116	1.6, 2.0	−1.0, −0.7	5.20×10^{-2}	3.8	4.0	8.5	10.1	102	102, 116	1.6, 2.0	+0.7, +1.0	1.05×10^{-1}	2.6	2.4	5.0	6.2
98	102, 116	1.6, 2.0	−0.7, −0.4	3.15×10^{-2}	4.4	4.4	4.9	8.0	101	102, 116	1.6, 2.0	+0.4, +0.7	5.32×10^{-2}	3.3	3.0	3.5	5.7
99	102, 116	1.6, 2.0	−0.4, 0.0	—	—	—	—	—	100	102, 116	1.6, 2.0	0.0, +0.4	—	—	—	—	—
103	102, 116	2.0, 2.4	−1.0, −0.7	4.24×10^{-2}	5.3	5.0	15.5	17.1	108	102, 116	2.0, 2.4	+0.7, +1.0	1.06×10^{-1}	3.2	3.1	7.8	9.0
104	102, 116	2.0, 2.4	−0.7, −0.4	6.96×10^{-2}	3.2	3.5	5.9	7.6	107	102, 116	2.0, 2.4	+0.4, +0.7	1.38×10^{-1}	2.4	2.2	4.4	5.4
105	102, 116	2.0, 2.4	−0.4, 0.0	2.42×10^{-2}	4.0	4.4	5.9	8.4	106	102, 116	2.0, 2.4	0.0, +0.4	3.15×10^{-2}	3.5	3.5	4.0	6.3
109	102, 116	2.4, 2.8	−1.0, −0.7	3.05×10^{-2}	3.8	4.6	22.0	22.8	114	102, 116	2.4, 2.8	+0.7, +1.0	9.69×10^{-2}	2.2	2.4	10.5	11.0
110	102, 116	2.4, 2.8	−0.7, −0.4	5.28×10^{-2}	4.3	4.5	11.4	12.9	113	102, 116	2.4, 2.8	+0.4, +0.7	1.36×10^{-1}	2.7	2.6	8.4	9.2
111	102, 116	2.4, 2.8	−0.4, 0.0	3.06×10^{-2}	4.0	5.1	6.9	9.5	112	102, 116	2.4, 2.8	0.0, +0.4	5.19×10^{-2}	3.1	3.3	4.8	6.6
115	102, 116	2.8, 3.6	−1.0, −0.7	1.44×10^{-2}	3.4	3.9	35.9	36.3	120	102, 116	2.8, 3.6	+0.7, +1.0	5.18×10^{-2}	2.0	1.8	19.3	19.4
116	102, 116	2.8, 3.6	−0.7, −0.4	1.00×10^{-2}	4.2	4.6	24.8	25.5	119	102, 116	2.8, 3.6	+0.4, +0.7	3.27×10^{-2}	2.4	2.1	14.2	14.6
117	102, 116	2.8, 3.6	−0.4, 0.0	—	—	—	—	—	118	102, 116	2.8, 3.6	0.0, +0.4	—	—	—	—	—

JHEP12(2017)059

Bin	m_{ee} [GeV]	$\lvert y_{ee}\rvert$	$\cos\theta^*$	$d^3\sigma$ [pb/GeV]	δ^{stat} [%]	$\delta^{\text{syst}}_{\text{unc}}$ [%]	$\delta^{\text{syst}}_{\text{cor}}$ [%]	δ^{total} [%]	Bin	m_{ee} [GeV]	$\lvert y_{ee}\rvert$	$\cos\theta^*$	$d^3\sigma$ [pb/GeV]	δ^{stat} [%]	$\delta^{\text{syst}}_{\text{unc}}$ [%]	$\delta^{\text{syst}}_{\text{cor}}$ [%]	δ^{total} [%]
121	116, 150	1.2, 1.6	−1.0, −0.7	6.38×10^{-3}	9.4	13.8	36.2	39.9	126	116, 150	1.2, 1.6	+0.7, +1.0	1.65×10^{-2}	4.7	5.6	14.4	16.1
122	116, 150	1.2, 1.6	−0.7, −0.4	—	—	—	—	—	125	116, 150	1.2, 1.6	+0.4, +0.7	4.05×10^{-4}	33.3	55.4	43.5	78.0
123	116, 150	1.2, 1.6	−0.4, 0.0	—	—	—	—	—	124	116, 150	1.2, 1.6	0.0, +0.4	—	—	—	—	—
127	116, 150	1.6, 2.0	−1.0, −0.7	9.56×10^{-3}	8.4	11.4	29.7	32.9	132	116, 150	1.6, 2.0	+0.7, +1.0	2.91×10^{-2}	3.9	6.2	9.9	12.3
128	116, 150	1.6, 2.0	−0.7, −0.4	4.62×10^{-3}	7.6	10.1	9.1	15.6	131	116, 150	1.6, 2.0	+0.4, +0.7	1.16×10^{-2}	4.4	5.1	3.3	7.5
129	116, 150	1.6, 2.0	−0.4, 0.0	—	—	—	—	—	130	116, 150	1.6, 2.0	0.0, +0.4	—	—	—	—	—
133	116, 150	2.0, 2.4	−1.0, −0.7	7.42×10^{-3}	11.5	16.3	46.1	50.3	138	116, 150	2.0, 2.4	+0.7, +1.0	3.00×10^{-2}	4.1	5.2	11.3	13.1
134	116, 150	2.0, 2.4	−0.7, −0.4	1.21×10^{-2}	5.5	6.4	11.2	14.0	137	116, 150	2.0, 2.4	+0.4, +0.7	3.03×10^{-2}	3.6	3.8	4.7	7.0
135	116, 150	2.0, 2.4	−0.4, 0.0	3.48×10^{-3}	7.2	12.2	14.1	20.1	136	116, 150	2.0, 2.4	0.0, +0.4	7.29×10^{-3}	4.7	5.9	5.6	9.4
139	116, 150	2.4, 2.8	−1.0, −0.7	3.36×10^{-3}	16.2	18.3	30.4	39.0	144	116, 150	2.4, 2.8	+0.7, +1.0	2.87×10^{-2}	3.3	3.0	4.3	6.2
140	116, 150	2.4, 2.8	−0.7, −0.4	8.13×10^{-3}	7.6	10.9	11.6	17.6	143	116, 150	2.4, 2.8	+0.4, +0.7	2.88×10^{-2}	3.8	3.8	3.9	6.7
141	116, 150	2.4, 2.8	−0.4, 0.0	5.61×10^{-3}	5.9	7.0	7.1	11.6	142	116, 150	2.4, 2.8	0.0, +0.4	1.05×10^{-2}	4.5	4.7	3.8	7.5
145	116, 150	2.8, 3.6	−1.0, −0.7	1.68×10^{-3}	11.1	13.6	32.3	36.8	150	116, 150	2.8, 3.6	+0.7, +1.0	1.21×10^{-2}	3.1	3.6	6.8	8.3
146	116, 150	2.8, 3.6	−0.7, −0.4	1.39×10^{-3}	8.8	11.4	14.1	20.1	149	116, 150	2.8, 3.6	+0.4, +0.7	6.41×10^{-3}	3.7	4.0	3.8	6.6
147	116, 150	2.8, 3.6	−0.4, 0.0	—	—	—	—	—	148	116, 150	2.8, 3.6	0.0, +0.4	—	—	—	—	—

Table 8. The high rapidity electron channel Born-level triple-differential cross section $d^3\sigma/dm_{\ell\ell}d|y_{\ell\ell}|d\cos\theta^*$. The measurements are listed together with the statistical (δ^{stat}), uncorrelated systematic ($\delta^{\text{syst}}_{\text{unc}}$), correlated systematic ($\delta^{\text{syst}}_{\text{cor}}$), and total ($\delta^{\text{total}}$) uncertainties. The luminosity uncertainty of 1.9% is not shown and not included in the overall systematic and total uncertainties.

JHEP12(2017)059

A.3 Forward-backward asymmetry tables

$\lvert y_{\ell\ell}\rvert$	$m_{\ell\ell}$ [GeV]	A_{FB}	Δ^{stat}	$\Delta^{\mathrm{syst}}_{\mathrm{unc}}$	$\Delta^{\mathrm{syst}}_{\mathrm{cor}}$	Δ^{total}	$\lvert y_{\ell\ell}\rvert$	$m_{\ell\ell}$ [GeV]	A_{FB}	Δ^{stat}	$\Delta^{\mathrm{syst}}_{\mathrm{unc}}$	$\Delta^{\mathrm{syst}}_{\mathrm{cor}}$	Δ^{total}
0.0, 0.2	46, 66	-5.97×10^{-3}	5.6×10^{-3}	4.5×10^{-3}	7.2×10^{-4}	7.3×10^{-3}	0.2, 0.4	46, 66	-8.12×10^{-3}	5.7×10^{-3}	4.7×10^{-3}	8.7×10^{-4}	7.4×10^{-3}
0.0, 0.2	66, 80	-2.48×10^{-4}	4.2×10^{-3}	2.3×10^{-3}	7.5×10^{-4}	4.8×10^{-3}	0.2, 0.4	66, 80	-2.61×10^{-2}	4.2×10^{-3}	2.3×10^{-3}	6.7×10^{-4}	4.9×10^{-3}
0.0, 0.2	80, 91	8.26×10^{-4}	1.1×10^{-3}	5.6×10^{-4}	3.5×10^{-4}	1.3×10^{-3}	0.2, 0.4	80, 91	1.85×10^{-3}	1.1×10^{-3}	5.5×10^{-4}	5.5×10^{-4}	1.4×10^{-3}
0.0, 0.2	91, 102	3.78×10^{-3}	1.1×10^{-3}	5.1×10^{-4}	3.2×10^{-4}	1.2×10^{-3}	0.2, 0.4	91, 102	6.49×10^{-3}	1.1×10^{-3}	5.0×10^{-4}	5.1×10^{-4}	1.3×10^{-3}
0.0, 0.2	102, 116	1.29×10^{-2}	5.3×10^{-3}	2.5×10^{-3}	9.1×10^{-4}	5.9×10^{-3}	0.2, 0.4	102, 116	2.59×10^{-2}	5.3×10^{-3}	2.5×10^{-3}	1.1×10^{-3}	5.9×10^{-3}
0.0, 0.2	116, 150	2.60×10^{-2}	8.3×10^{-3}	3.3×10^{-3}	1.3×10^{-3}	9.0×10^{-3}	0.2, 0.4	116, 150	5.69×10^{-2}	8.4×10^{-3}	3.6×10^{-3}	1.5×10^{-3}	9.2×10^{-3}
0.0, 0.2	150, 200	1.88×10^{-2}	1.6×10^{-2}	5.8×10^{-3}	2.9×10^{-3}	1.7×10^{-2}	0.2, 0.4	150, 200	5.11×10^{-2}	1.6×10^{-2}	6.9×10^{-3}	4.2×10^{-3}	1.8×10^{-2}
0.4, 0.6	46, 66	-2.71×10^{-2}	5.9×10^{-3}	4.5×10^{-3}	9.1×10^{-4}	7.5×10^{-3}	0.6, 0.8	46, 66	-2.96×10^{-2}	5.7×10^{-3}	4.3×10^{-3}	9.5×10^{-4}	7.2×10^{-3}
0.4, 0.6	66, 80	-2.76×10^{-2}	4.3×10^{-3}	2.3×10^{-3}	7.6×10^{-4}	4.9×10^{-3}	0.6, 0.8	66, 80	-5.27×10^{-2}	4.4×10^{-3}	2.5×10^{-3}	9.2×10^{-4}	5.1×10^{-3}
0.4, 0.6	80, 91	2.61×10^{-3}	1.1×10^{-3}	5.5×10^{-4}	6.0×10^{-4}	1.4×10^{-3}	0.6, 0.8	80, 91	1.48×10^{-3}	1.1×10^{-3}	5.6×10^{-4}	6.6×10^{-4}	1.4×10^{-3}
0.4, 0.6	91, 102	1.23×10^{-2}	1.1×10^{-3}	5.2×10^{-4}	5.7×10^{-4}	1.3×10^{-3}	0.6, 0.8	91, 102	1.74×10^{-2}	1.1×10^{-3}	5.1×10^{-4}	6.4×10^{-4}	1.4×10^{-3}
0.4, 0.6	102, 116	4.39×10^{-2}	5.2×10^{-3}	2.6×10^{-3}	1.2×10^{-3}	6.0×10^{-3}	0.6, 0.8	102, 116	5.37×10^{-2}	5.2×10^{-3}	2.7×10^{-3}	1.7×10^{-3}	6.1×10^{-3}
0.4, 0.6	116, 150	7.39×10^{-2}	8.5×10^{-3}	3.3×10^{-3}	1.7×10^{-3}	9.3×10^{-3}	0.6, 0.8	116, 150	1.06×10^{-1}	8.3×10^{-3}	3.1×10^{-3}	1.8×10^{-3}	9.1×10^{-3}
0.4, 0.6	150, 200	1.01×10^{-1}	1.6×10^{-2}	5.8×10^{-3}	2.7×10^{-3}	1.7×10^{-2}	0.6, 0.8	150, 200	1.37×10^{-1}	1.6×10^{-2}	5.3×10^{-3}	3.2×10^{-3}	1.7×10^{-2}
0.8, 1.0	46, 66	-4.28×10^{-2}	5.8×10^{-3}	4.4×10^{-3}	8.9×10^{-4}	7.3×10^{-3}	1.0, 1.2	46, 66	-5.60×10^{-2}	5.7×10^{-3}	4.2×10^{-3}	1.2×10^{-3}	7.2×10^{-3}
0.8, 1.0	66, 80	-7.03×10^{-2}	4.4×10^{-3}	2.4×10^{-3}	9.0×10^{-4}	5.1×10^{-3}	1.0, 1.2	66, 80	-8.76×10^{-2}	4.3×10^{-3}	2.4×10^{-3}	9.5×10^{-4}	5.0×10^{-3}
0.8, 1.0	80, 91	-7.42×10^{-5}	1.1×10^{-3}	5.7×10^{-4}	7.5×10^{-4}	1.5×10^{-3}	1.0, 1.2	80, 91	8.90×10^{-5}	1.1×10^{-3}	5.7×10^{-4}	7.8×10^{-4}	1.5×10^{-3}
0.8, 1.0	91, 102	2.33×10^{-2}	1.1×10^{-3}	5.2×10^{-4}	6.9×10^{-4}	1.4×10^{-3}	1.0, 1.2	91, 102	2.88×10^{-2}	1.1×10^{-3}	5.1×10^{-4}	7.4×10^{-4}	1.4×10^{-3}
0.8, 1.0	102, 116	9.15×10^{-2}	5.2×10^{-3}	2.8×10^{-3}	1.6×10^{-3}	6.1×10^{-3}	1.0, 1.2	102, 116	1.10×10^{-1}	5.1×10^{-3}	2.7×10^{-3}	1.7×10^{-3}	6.0×10^{-3}
0.8, 1.0	116, 150	1.28×10^{-1}	8.4×10^{-3}	3.4×10^{-3}	1.8×10^{-3}	9.2×10^{-3}	1.0, 1.2	116, 150	1.68×10^{-1}	8.4×10^{-3}	3.6×10^{-3}	2.0×10^{-3}	9.3×10^{-3}
0.8, 1.0	150, 200	1.69×10^{-1}	1.6×10^{-2}	5.3×10^{-3}	4.0×10^{-3}	1.7×10^{-2}	1.0, 1.2	150, 200	2.36×10^{-1}	1.6×10^{-2}	5.9×10^{-3}	4.2×10^{-3}	1.7×10^{-2}
1.2, 1.4	46, 66	-8.88×10^{-2}	5.7×10^{-3}	4.2×10^{-3}	1.4×10^{-3}	7.2×10^{-3}	1.4, 1.6	46, 66	-1.03×10^{-1}	5.8×10^{-3}	4.3×10^{-3}	1.7×10^{-3}	7.5×10^{-3}
1.2, 1.4	66, 80	-1.14×10^{-1}	4.2×10^{-3}	2.4×10^{-3}	1.1×10^{-3}	5.0×10^{-3}	1.4, 1.6	66, 80	-1.25×10^{-1}	4.4×10^{-3}	2.6×10^{-3}	1.3×10^{-3}	5.3×10^{-3}
1.2, 1.4	80, 91	-2.23×10^{-3}	1.1×10^{-3}	5.7×10^{-4}	8.7×10^{-4}	1.5×10^{-3}	1.4, 1.6	80, 91	-2.59×10^{-3}	1.2×10^{-3}	6.2×10^{-4}	9.2×10^{-4}	1.6×10^{-3}
1.2, 1.4	91, 102	3.38×10^{-2}	1.1×10^{-3}	5.2×10^{-4}	8.5×10^{-4}	1.5×10^{-3}	1.4, 1.6	91, 102	3.77×10^{-2}	1.1×10^{-3}	5.7×10^{-4}	8.9×10^{-4}	1.6×10^{-3}
1.2, 1.4	102, 116	1.30×10^{-1}	5.0×10^{-3}	2.8×10^{-3}	2.0×10^{-3}	6.1×10^{-3}	1.4, 1.6	102, 116	1.44×10^{-1}	5.1×10^{-3}	3.0×10^{-3}	2.2×10^{-3}	6.3×10^{-3}
1.2, 1.4	116, 150	2.09×10^{-1}	8.5×10^{-3}	3.7×10^{-3}	2.6×10^{-3}	9.6×10^{-3}	1.4, 1.6	116, 150	2.19×10^{-1}	8.9×10^{-3}	3.9×10^{-3}	2.8×10^{-3}	1.0×10^{-2}
1.2, 1.4	150, 200	2.68×10^{-1}	1.6×10^{-2}	6.6×10^{-3}	4.3×10^{-3}	1.8×10^{-2}	1.4, 1.6	150, 200	2.80×10^{-1}	1.8×10^{-2}	9.0×10^{-3}	4.5×10^{-3}	2.1×10^{-2}
1.6, 1.8	46, 66	-9.35×10^{-2}	6.1×10^{-3}	4.6×10^{-3}	1.4×10^{-3}	7.8×10^{-3}	1.8, 2.0	46, 66	-9.23×10^{-2}	6.7×10^{-3}	4.9×10^{-3}	1.5×10^{-3}	8.5×10^{-3}
1.6, 1.8	66, 80	-1.26×10^{-1}	4.9×10^{-3}	2.8×10^{-3}	1.5×10^{-3}	5.8×10^{-3}	1.8, 2.0	66, 80	-1.20×10^{-1}	5.6×10^{-3}	3.3×10^{-3}	2.0×10^{-3}	6.8×10^{-3}
1.6, 1.8	80, 91	-7.79×10^{-4}	1.3×10^{-3}	7.0×10^{-4}	1.0×10^{-3}	1.8×10^{-3}	1.8, 2.0	80, 91	-2.65×10^{-3}	1.5×10^{-3}	8.1×10^{-4}	1.1×10^{-3}	2.0×10^{-3}
1.6, 1.8	91, 102	3.96×10^{-2}	1.3×10^{-3}	6.3×10^{-4}	9.6×10^{-4}	1.7×10^{-3}	1.8, 2.0	91, 102	3.97×10^{-2}	1.5×10^{-3}	7.4×10^{-4}	1.1×10^{-3}	2.0×10^{-3}
1.6, 1.8	102, 116	1.63×10^{-1}	5.3×10^{-3}	3.6×10^{-3}	2.8×10^{-3}	7.0×10^{-3}	1.8, 2.0	102, 116	1.54×10^{-1}	5.6×10^{-3}	3.9×10^{-3}	3.5×10^{-3}	7.7×10^{-3}
1.6, 1.8	116, 150	2.43×10^{-1}	1.0×10^{-2}	4.6×10^{-3}	2.6×10^{-3}	1.2×10^{-2}	1.8, 2.0	116, 150	2.12×10^{-1}	1.2×10^{-2}	6.8×10^{-3}	3.9×10^{-3}	1.4×10^{-2}
1.6, 1.8	150, 200	3.02×10^{-1}	1.8×10^{-2}	6.8×10^{-3}	5.6×10^{-3}	2.0×10^{-2}	1.8, 2.0	150, 200	2.66×10^{-1}	2.1×10^{-2}	6.3×10^{-3}	4.2×10^{-3}	2.3×10^{-2}
2.0, 2.2	46, 66	-9.82×10^{-2}	8.3×10^{-3}	6.2×10^{-3}	2.6×10^{-3}	1.1×10^{-2}	2.2, 2.4	46, 66	-4.44×10^{-2}	1.4×10^{-2}	1.1×10^{-2}	3.1×10^{-3}	1.8×10^{-2}
2.0, 2.2	66, 80	-1.10×10^{-1}	6.9×10^{-3}	4.2×10^{-3}	3.0×10^{-3}	8.6×10^{-3}	2.2, 2.4	66, 80	-5.03×10^{-2}	1.2×10^{-2}	7.5×10^{-3}	6.1×10^{-3}	1.5×10^{-2}
2.0, 2.2	80, 91	-3.33×10^{-3}	1.9×10^{-3}	1.1×10^{-3}	1.5×10^{-3}	2.7×10^{-3}	2.2, 2.4	80, 91	-6.44×10^{-3}	3.1×10^{-3}	1.9×10^{-3}	2.1×10^{-3}	4.2×10^{-3}
2.0, 2.2	91, 102	3.33×10^{-2}	1.9×10^{-3}	9.8×10^{-4}	1.5×10^{-3}	2.6×10^{-3}	2.2, 2.4	91, 102	1.99×10^{-2}	3.1×10^{-3}	1.6×10^{-3}	2.3×10^{-3}	4.2×10^{-3}
2.0, 2.2	102, 116	1.20×10^{-1}	6.5×10^{-3}	5.1×10^{-3}	6.3×10^{-3}	1.0×10^{-2}	2.2, 2.4	102, 116	6.06×10^{-2}	9.7×10^{-3}	9.3×10^{-3}	1.2×10^{-2}	1.8×10^{-2}
2.0, 2.2	116, 150	1.64×10^{-1}	1.4×10^{-2}	6.6×10^{-3}	3.9×10^{-3}	1.6×10^{-2}	2.2, 2.4	116, 150	9.40×10^{-2}	2.6×10^{-2}	1.6×10^{-2}	1.5×10^{-2}	3.4×10^{-2}
2.0, 2.2	150, 200	1.97×10^{-1}	2.7×10^{-2}	1.0×10^{-2}	7.7×10^{-3}	3.0×10^{-2}	2.2, 2.4	150, 200	1.27×10^{-1}	4.6×10^{-2}	1.3×10^{-2}	1.0×10^{-2}	4.9×10^{-2}

Table 9. The asymmetry A_{FB} determined from the combined triple-differential cross-section measurements. The measurements are listed together with the statistical (Δ^{stat}), uncorrelated systematic ($\Delta^{\mathrm{syst}}_{\mathrm{unc}}$), correlated systematic ($\Delta^{\mathrm{syst}}_{\mathrm{cor}}$), and total ($\Delta^{\mathrm{total}}$) uncertainties.

JHEP12(2017)059

$\lvert y_{ee}\rvert$	m_{ee} [GeV]	A_{FB}	Δ^{stat}	$\Delta^{\mathrm{syst}}_{\mathrm{unc}}$	$\Delta^{\mathrm{syst}}_{\mathrm{cor}}$	Δ^{total}
1.2, 1.6	66, 80	-2.44×10^{-1}	4.4×10^{-2}	5.9×10^{-2}	2.5×10^{-2}	7.8×10^{-2}
1.2, 1.6	80, 91	8.57×10^{-3}	6.2×10^{-3}	4.6×10^{-3}	3.6×10^{-3}	8.5×10^{-3}
1.2, 1.6	91, 102	7.03×10^{-2}	5.7×10^{-3}	4.1×10^{-3}	4.9×10^{-3}	8.6×10^{-3}
1.2, 1.6	102, 116	2.78×10^{-1}	2.6×10^{-2}	3.4×10^{-2}	2.6×10^{-2}	5.0×10^{-2}
1.2, 1.6	116, 150	4.43×10^{-1}	4.2×10^{-2}	6.0×10^{-2}	1.1×10^{-1}	1.3×10^{-1}
1.6, 2.0	66, 80	-2.32×10^{-1}	1.7×10^{-2}	1.9×10^{-2}	1.1×10^{-2}	2.7×10^{-2}
1.6, 2.0	80, 91	3.08×10^{-3}	3.3×10^{-3}	2.3×10^{-3}	2.5×10^{-3}	4.7×10^{-3}
1.6, 2.0	91, 102	7.30×10^{-2}	3.2×10^{-3}	2.1×10^{-3}	1.8×10^{-3}	4.2×10^{-3}
1.6, 2.0	102, 116	3.09×10^{-1}	1.6×10^{-2}	1.6×10^{-2}	1.3×10^{-2}	2.6×10^{-2}
1.6, 2.0	116, 150	4.83×10^{-1}	2.6×10^{-2}	3.7×10^{-2}	6.5×10^{-2}	7.9×10^{-2}
2.0, 2.4	66, 80	-2.89×10^{-1}	1.2×10^{-2}	1.4×10^{-2}	1.3×10^{-2}	2.3×10^{-2}
2.0, 2.4	80, 91	-9.15×10^{-3}	2.8×10^{-3}	2.1×10^{-3}	1.7×10^{-3}	3.9×10^{-3}
2.0, 2.4	91, 102	8.43×10^{-2}	2.7×10^{-3}	1.9×10^{-3}	2.7×10^{-3}	4.3×10^{-3}
2.0, 2.4	102, 116	3.40×10^{-1}	1.3×10^{-2}	1.3×10^{-2}	1.6×10^{-2}	2.5×10^{-2}
2.0, 2.4	116, 150	4.93×10^{-1}	2.1×10^{-2}	2.7×10^{-2}	6.5×10^{-2}	7.3×10^{-2}
2.4, 2.8	66, 80	-3.26×10^{-1}	1.1×10^{-2}	1.1×10^{-2}	1.7×10^{-2}	2.3×10^{-2}
2.4, 2.8	80, 91	-4.68×10^{-3}	2.6×10^{-3}	2.2×10^{-3}	2.4×10^{-3}	4.2×10^{-3}
2.4, 2.8	91, 102	1.11×10^{-1}	2.6×10^{-3}	2.5×10^{-3}	2.1×10^{-3}	4.1×10^{-3}
2.4, 2.8	102, 116	4.29×10^{-1}	1.2×10^{-2}	1.3×10^{-2}	1.8×10^{-2}	2.6×10^{-2}
2.4, 2.8	116, 150	5.98×10^{-1}	1.8×10^{-2}	2.3×10^{-2}	3.3×10^{-2}	4.4×10^{-2}
2.8, 3.6	66, 80	-4.73×10^{-1}	1.1×10^{-2}	1.4×10^{-2}	2.7×10^{-2}	3.2×10^{-2}
2.8, 3.6	80, 91	-8.07×10^{-3}	2.8×10^{-3}	2.7×10^{-3}	2.3×10^{-3}	4.5×10^{-3}
2.8, 3.6	91, 102	1.55×10^{-1}	2.7×10^{-3}	2.7×10^{-3}	5.0×10^{-3}	6.2×10^{-3}
2.8, 3.6	102, 116	5.51×10^{-1}	1.1×10^{-2}	1.1×10^{-2}	4.5×10^{-2}	4.8×10^{-2}
2.8, 3.6	116, 150	7.15×10^{-1}	1.9×10^{-2}	2.3×10^{-2}	4.8×10^{-2}	5.7×10^{-2}

Table 10. The asymmetry A_{FB} determined from the high rapidity electron channel triple-differential cross-section measurement. The measurement is listed together with the statistical (Δ^{stat}), uncorrelated systematic ($\Delta^{\mathrm{syst}}_{\mathrm{unc}}$), correlated systematic ($\Delta^{\mathrm{syst}}_{\mathrm{cor}}$), and total ($\Delta^{\mathrm{total}}$) uncertainties.

JHEP12(2017)059

Open Access. This article is distributed under the terms of the Creative Commons Attribution License (CC-BY 4.0), which permits any use, distribution and reproduction in any medium, provided the original author(s) and source are credited.

References

[1] S.D. Drell and T.-M. Yan, *Massive Lepton Pair Production in Hadron-Hadron Collisions at High-Energies*, *Phys. Rev. Lett.* **25** (1970) 316 [*Erratum ibid.* **25** (1970) 902] [INSPIRE].

[2] S.D. Drell and T.-M. Yan, *Partons and their Applications at High-Energies*, *Annals Phys.* **66** (1971) 578 [INSPIRE].

[3] SLD Electroweak Group, DELPHI, ALEPH, SLD, SLD Heavy Flavour Group, OPAL, LEP Electroweak Working Group and L3 collaborations, S. Schael et al., *Precision electroweak measurements on the Z resonance*, *Phys. Rept.* **427** (2006) 257 [hep-ex/0509008] [INSPIRE].

[4] ATLAS collaboration, *Measurement of $W^{\pm}$ and Z-boson production cross sections in pp collisions at $\sqrt{s} = 13$ TeV with the ATLAS detector*, *Phys. Lett.* **B 759** (2016) 601 [arXiv:1603.09222] [INSPIRE].

[5] ATLAS collaboration, *Measurements of top-quark pair to Z-boson cross-section ratios at $\sqrt{s} = 13$, 8, 7 TeV with the ATLAS detector*, *JHEP* **02** (2017) 117 [arXiv:1612.03636] [INSPIRE].

[6] CMS collaboration, *Measurement of the Inclusive W and Z Production Cross sections in pp Collisions at $\sqrt{s} = 7$ TeV*, *JHEP* **10** (2011) 132 [arXiv:1107.4789] [INSPIRE].

[7] CMS collaboration, *Measurement of inclusive W and Z boson production cross sections in pp collisions at $\sqrt{s} = 8$ TeV*, *Phys. Rev. Lett.* **112** (2014) 191802 [arXiv:1402.0923] [INSPIRE].

[8] ATLAS collaboration, *Measurement of the inclusive $W^{\pm}$ and Z/gamma cross sections in the electron and muon decay channels in pp collisions at $\sqrt{s} = 7$ TeV with the ATLAS detector*, *Phys. Rev.* **D 85** (2012) 072004 [arXiv:1109.5141] [INSPIRE].

[9] CMS collaboration, *Measurement of the Rapidity and Transverse Momentum Distributions of Z Bosons in pp Collisions at $\sqrt{s} = 7$ TeV*, *Phys. Rev.* **D 85** (2012) 032002 [arXiv:1110.4973] [INSPIRE].

[10] ATLAS collaboration, *Measurement of angular correlations in Drell-Yan lepton pairs to probe Z/gamma* boson transverse momentum at $\sqrt{s} = 7$ TeV with the ATLAS detector*, *Phys. Lett.* **B 720** (2013) 32 [arXiv:1211.6899] [INSPIRE].

[11] ATLAS collaboration, *Measurement of the Z/γ^* boson transverse momentum distribution in pp collisions at $\sqrt{s} = 7$ TeV with the ATLAS detector*, *JHEP* **09** (2014) 145 [arXiv:1406.3660] [INSPIRE].

[12] CMS collaboration, *Measurement of the transverse momentum spectra of weak vector bosons produced in proton-proton collisions at $\sqrt{s} = 8$ TeV*, *JHEP* **02** (2017) 096 [arXiv:1606.05864] [INSPIRE].

[13] ATLAS collaboration, *Measurement of the high-mass Drell-Yan differential cross-section in pp collisions at $\sqrt{s} = 7$ TeV with the ATLAS detector*, *Phys. Lett.* **B 725** (2013) 223 [arXiv:1305.4192] [INSPIRE].

JHEP12(2017)059

[14] ATLAS collaboration, *Measurement of the low-mass Drell-Yan differential cross section at $\sqrt{s} = 7$ TeV using the ATLAS detector*, *JHEP* **06** (2014) 112 [arXiv:1404.1212] [INSPIRE].

[15] CMS collaboration, *Measurement of the Drell-Yan Cross section in pp Collisions at $\sqrt{s} = 7$ TeV*, *JHEP* **10** (2011) 007 [arXiv:1108.0566] [INSPIRE].

[16] ATLAS collaboration, *Measurement of the transverse momentum and ϕ^*_η distributions of Drell-Yan lepton pairs in proton-proton collisions at $\sqrt{s} = 8$ TeV with the ATLAS detector*, *Eur. Phys. J.* **C 76** (2016) 291 [arXiv:1512.02192] [INSPIRE].

[17] ATLAS collaboration, *Measurement of the double-differential high-mass Drell-Yan cross section in pp collisions at $\sqrt{s} = 8$ TeV with the ATLAS detector*, *JHEP* **08** (2016) 009 [arXiv:1606.01736] [INSPIRE].

[18] ATLAS collaboration, *Precision measurement and interpretation of inclusive W^+, W^- and Z/γ^* production cross sections with the ATLAS detector*, *Eur. Phys. J.* **C 77** (2017) 367 [arXiv:1612.03016] [INSPIRE].

[19] CMS collaboration, *Measurement of the Z boson differential cross section in transverse momentum and rapidity in proton-proton collisions at 8 TeV*, *Phys. Lett.* **B 749** (2015) 187 [arXiv:1504.03511] [INSPIRE].

[20] CMS collaboration, *Measurements of differential and double-differential Drell-Yan cross sections in proton-proton collisions at 8 TeV*, *Eur. Phys. J.* **C 75** (2015) 147 [arXiv:1412.1115] [INSPIRE].

[21] CMS collaboration, *Measurement of the differential and double-differential Drell-Yan cross sections in proton-proton collisions at $\sqrt{s} = 7$ TeV*, *JHEP* **12** (2013) 030 [arXiv:1310.7291] [INSPIRE].

[22] ATLAS collaboration, *Measurement of the angular coefficients in Z-boson events using electron and muon pairs from data taken at $\sqrt{s} = 8$ TeV with the ATLAS detector*, *JHEP* **08** (2016) 159 [arXiv:1606.00689] [INSPIRE].

[23] CMS collaboration, *Angular coefficients of Z bosons produced in pp collisions at $\sqrt{s} = 8$ TeV and decaying to $\mu^+\mu^-$ as a function of transverse momentum and rapidity*, *Phys. Lett.* **B 750** (2015) 154 [arXiv:1504.03512] [INSPIRE].

[24] ATLAS collaboration, *Measurement of the forward-backward asymmetry of electron and muon pair-production in pp collisions at $\sqrt{s} = 7$ TeV with the ATLAS detector*, *JHEP* **09** (2015) 049 [arXiv:1503.03709] [INSPIRE].

[25] CMS collaboration, *Forward-backward asymmetry of Drell-Yan lepton pairs in pp collisions at $\sqrt{s} = 7$ TeV*, *Phys. Lett.* **B 718** (2013) 752 [arXiv:1207.3973] [INSPIRE].

[26] J.C. Collins and D.E. Soper, *Angular Distribution of Dileptons in High-Energy Hadron Collisions*, *Phys. Rev.* **D 16** (1977) 2219 [INSPIRE].

[27] ATLAS collaboration, *The ATLAS Experiment at the CERN Large Hadron Collider*, 2008 *JINST* **3** S08003 [INSPIRE].

[28] ATLAS collaboration, *Performance of the ATLAS Trigger System in 2010*, *Eur. Phys. J.* **C 72** (2012) 1849 [arXiv:1110.1530] [INSPIRE].

[29] P. Nason, *A new method for combining NLO QCD with shower Monte Carlo algorithms*, *JHEP* **11** (2004) 040 [hep-ph/0409146] [INSPIRE].

JHEP12(2017)059

[30] S. Frixione, P. Nason and C. Oleari, *Matching NLO QCD computations with Parton Shower simulations: the POWHEG method*, *JHEP* **11** (2007) 070 [arXiv:0709.2092] [INSPIRE].

[31] S. Alioli, P. Nason, C. Oleari and E. Re, *NLO vector-boson production matched with shower in POWHEG*, *JHEP* **07** (2008) 060 [arXiv:0805.4802] [INSPIRE].

[32] S. Alioli, P. Nason, C. Oleari and E. Re, *A general framework for implementing NLO calculations in shower Monte Carlo programs: the POWHEG BOX*, *JHEP* **06** (2010) 043 [arXiv:1002.2581] [INSPIRE].

[33] H.-L. Lai et al., *New parton distributions for collider physics*, *Phys. Rev.* **D 82** (2010) 074024 [arXiv:1007.2241] [INSPIRE].

[34] T. Sjöstrand, S. Mrenna and P.Z. Skands, *A Brief Introduction to PYTHIA 8.1*, *Comput. Phys. Commun.* **178** (2008) 852 [arXiv:0710.3820] [INSPIRE].

[35] K. Melnikov and F. Petriello, *Electroweak gauge boson production at hadron colliders through* $\mathcal{O}(\alpha_s^2)$, *Phys. Rev.* **D 74** (2006) 114017 [hep-ph/0609070] [INSPIRE].

[36] R. Gavin, Y. Li, F. Petriello and S. Quackenbush, *FEWZ 2.0: A code for hadronic Z production at next-to-next-to-leading order*, *Comput. Phys. Commun.* **182** (2011) 2388 [arXiv:1011.3540] [INSPIRE].

[37] Y. Li and F. Petriello, *Combining QCD and electroweak corrections to dilepton production in FEWZ*, *Phys. Rev.* **D 86** (2012) 094034 [arXiv:1208.5967] [INSPIRE].

[38] A.D. Martin, W.J. Stirling, R.S. Thorne and G. Watt, *Parton distributions for the LHC*, *Eur. Phys. J.* **C 63** (2009) 189 [arXiv:0901.0002] [INSPIRE].

[39] W.F.L. Hollik, *Radiative Corrections in the Standard Model and their Role for Precision Tests of the Electroweak Theory*, *Fortsch. Phys.* **38** (1990) 165 [INSPIRE].

[40] S. Catani, L. Cieri, G. Ferrera, D. de Florian and M. Grazzini, *Vector boson production at hadron colliders: a fully exclusive QCD calculation at NNLO*, *Phys. Rev. Lett.* **103** (2009) 082001 [arXiv:0903.2120] [INSPIRE].

[41] A.D. Martin, R.G. Roberts, W.J. Stirling and R.S. Thorne, *Parton distributions incorporating QED contributions*, *Eur. Phys. J.* **C 39** (2005) 155 [hep-ph/0411040] [INSPIRE].

[42] D. Bardin et al., *SANC integrator in the progress: QCD and EW contributions*, *JETP Lett.* **96** (2012) 285 [arXiv:1207.4400] [INSPIRE].

[43] S.G. Bondarenko and A.A. Sapronov, *NLO EW and QCD proton-proton cross section calculations with mcsanc-v1.01*, *Comput. Phys. Commun.* **184** (2013) 2343 [arXiv:1301.3687] [INSPIRE].

[44] T. Sjöstrand, S. Mrenna and P.Z. Skands, *PYTHIA 6.4 Physics and Manual*, *JHEP* **05** (2006) 026 [hep-ph/0603175] [INSPIRE].

[45] M. Cacciari, M. Czakon, M. Mangano, A. Mitov and P. Nason, *Top-pair production at hadron colliders with next-to-next-to-leading logarithmic soft-gluon resummation*, *Phys. Lett.* **B 710** (2012) 612 [arXiv:1111.5869] [INSPIRE].

[46] P. Bärnreuther, M. Czakon and A. Mitov, *Percent Level Precision Physics at the Tevatron: First Genuine NNLO QCD Corrections to* $q\bar{q} \to t\bar{t} + X$, *Phys. Rev. Lett.* **109** (2012) 132001 [arXiv:1204.5201] [INSPIRE].

JHEP12(2017)059

[47] M. Czakon and A. Mitov, *NNLO corrections to top-pair production at hadron colliders: the all-fermionic scattering channels*, *JHEP* **12** (2012) 054 [arXiv:1207.0236] [INSPIRE].

[48] M. Czakon and A. Mitov, *NNLO corrections to top pair production at hadron colliders: the quark-gluon reaction*, *JHEP* **01** (2013) 080 [arXiv:1210.6832] [INSPIRE].

[49] M. Czakon, P. Fiedler and A. Mitov, *Total Top-Quark Pair-Production Cross section at Hadron Colliders Through* $O(\alpha_S^4)$, *Phys. Rev. Lett.* **110** (2013) 252004 [arXiv:1303.6254] [INSPIRE].

[50] M. Czakon and A. Mitov, *Top++: A Program for the Calculation of the Top-Pair Cross-Section at Hadron Colliders*, *Comput. Phys. Commun.* **185** (2014) 2930 [arXiv:1112.5675] [INSPIRE].

[51] J. Pumplin, D.R. Stump, J. Huston, H.L. Lai, P.M. Nadolsky and W.K. Tung, *New generation of parton distributions with uncertainties from global QCD analysis*, *JHEP* **07** (2002) 012 [hep-ph/0201195] [INSPIRE].

[52] J.M. Campbell and R.K. Ellis, *An update on vector boson pair production at hadron colliders*, *Phys. Rev.* **D 60** (1999) 113006 [hep-ph/9905386] [INSPIRE].

[53] J.M. Campbell, R.K. Ellis and C. Williams, *Vector boson pair production at the LHC*, *JHEP* **07** (2011) 018 [arXiv:1105.0020] [INSPIRE].

[54] P. Golonka and Z. Was, *PHOTOS Monte Carlo: A precision tool for QED corrections in Z and W decays*, *Eur. Phys. J.* **C 45** (2006) 97 [hep-ph/0506026] [INSPIRE].

[55] ATLAS collaboration, *The ATLAS Simulation Infrastructure*, *Eur. Phys. J.* **C 70** (2010) 823 [arXiv:1005.4568] [INSPIRE].

[56] GEANT4 collaboration, S. Agostinelli et al., *GEANT4: A simulation toolkit*, *Nucl. Instrum. Meth.* **A 506** (2003) 250 [INSPIRE].

[57] ATLAS collaboration, *Electron and photon energy calibration with the ATLAS detector using LHC Run 1 data*, *Eur. Phys. J.* **C 74** (2014) 3071 [arXiv:1407.5063] [INSPIRE].

[58] ATLAS collaboration, *Electron reconstruction and identification efficiency measurements with the ATLAS detector using the 2011 LHC proton-proton collision data*, *Eur. Phys. J.* **C 74** (2014) 2941 [arXiv:1404.2240] [INSPIRE].

[59] ATLAS collaboration, *Electron efficiency measurements with the ATLAS detector using 2012 LHC proton-proton collision data*, *Eur. Phys. J.* **C 77** (2017) 195 [arXiv:1612.01456] [INSPIRE].

[60] ATLAS collaboration, *Measurement of the muon reconstruction performance of the ATLAS detector using 2011 and 2012 LHC proton-proton collision data*, *Eur. Phys. J.* **C 74** (2014) 3130 [arXiv:1407.3935] [INSPIRE].

[61] ATLAS collaboration, *Performance of the ATLAS muon trigger in pp collisions at* $\sqrt{s} = 8$ *TeV*, *Eur. Phys. J.* **C 75** (2015) 120 [arXiv:1408.3179] [INSPIRE].

[62] ATLAS collaboration, *Summary of ATLAS Pythia 8 tunes*, ATL-PHYS-PUB-2012-003 (2012).

[63] R. Corke and T. Sjöstrand, *Interleaved Parton Showers and Tuning Prospects*, *JHEP* **03** (2011) 032 [arXiv:1011.1759] [INSPIRE].

[64] ATLAS collaboration, *New ATLAS event generator tunes to 2010 data*, ATL-PHYS-PUB-2011-008 (2011).

JHEP12(2017)059

[65] ATLAS collaboration, *Measurement of the W-boson mass in pp collisions at $\sqrt{s} = 7$ TeV with the ATLAS detector*, arXiv:1701.07240 [INSPIRE].

[66] G. D'Agostini, *A multidimensional unfolding method based on Bayes' theorem*, *Nucl. Instrum. Meth.* **A 362** (1995) 487 [INSPIRE].

[67] B. Efron, *Bootstrap methods: Another look at the jackknife*, *Ann. Statist.* **7** (1979) 1.

[68] ATLAS collaboration, *Electron efficiency measurements with the ATLAS detector using the 2012 LHC proton-proton collision data*, ATLAS-CONF-2014-032 (2014).

[69] M. Botje et al., *The PDF4LHC Working Group Interim Recommendations*, arXiv:1101.0538 [INSPIRE].

[70] ATLAS collaboration, *Luminosity determination in pp collisions at $\sqrt{s} = 8$ TeV using the ATLAS detector at the LHC*, *Eur. Phys. J.* **C 76** (2016) 653 [arXiv:1608.03953] [INSPIRE].

[71] *The durham high energy physics database*, https://www.hepdata.net.

[72] E. Maguire, L. Heinrich and G. Watt, *HEPData: a repository for high energy physics data*, arXiv:1704.05473 [INSPIRE].

[73] A. Glazov, *Averaging of DIS cross section data*, *AIP Conf. Proc.* **792** (2005) 237 [INSPIRE].

[74] H1 collaboration, F.D. Aaron et al., *Measurement of the Inclusive ep Scattering Cross section at Low Q^2 and x at HERA*, *Eur. Phys. J.* **C 63** (2009) 625 [arXiv:0904.0929] [INSPIRE].

[75] ZEUS and H1 collaborations, F.D. Aaron et al., *Combined Measurement and QCD Analysis of the Inclusive e+- p Scattering Cross sections at HERA*, *JHEP* **01** (2010) 109 [arXiv:0911.0884] [INSPIRE].

[76] Particle Data Group collaboration, C. Patrignani et al., *Review of Particle Physics*, *Chin. Phys.* **C 40** (2016) 100001 [INSPIRE].

[77] ATLAS collaboration, *ATLAS Computing Acknowledgements 2016-2017*, ATL-GEN-PUB-2016-002 (2016).

JHEP12(2017)059

The ATLAS collaboration

M. Aaboud[137d], G. Aad[88], B. Abbott[115], O. Abdinov[12,*], B. Abeloos[119], S.H. Abidi[161], O.S. AbouZeid[139], N.L. Abraham[151], H. Abramowicz[155], H. Abreu[154], R. Abreu[118], Y. Abulaiti[148a,148b], B.S. Acharya[167a,167b,a], S. Adachi[157], L. Adamczyk[41a], J. Adelman[110], M. Adersberger[102], T. Adye[133], A.A. Affolder[139], Y. Afik[154], T. Agatonovic-Jovin[14], C. Agheorghiesei[28c], J.A. Aguilar-Saavedra[128a,128f], S.P. Ahlen[24], F. Ahmadov[68,b], G. Aielli[135a,135b], S. Akatsuka[71], H. Akerstedt[148a,148b], T.P.A. Åkesson[84], E. Akilli[52], A.V. Akimov[98], G.L. Alberghi[22a,22b], J. Albert[172], P. Albicocco[50], M.J. Alconada Verzini[74], S.C. Alderweireldt[108], M. Aleksa[32], I.N. Aleksandrov[68], C. Alexa[28b], G. Alexander[155], T. Alexopoulos[10], M. Alhroob[115], B. Ali[130], M. Aliev[76a,76b], G. Alimonti[94a], J. Alison[33], S.P. Alkire[38], B.M.M. Allbrooke[151], B.W. Allen[118], P.P. Allport[19], A. Aloisio[106a,106b], A. Alonso[39], F. Alonso[74], C. Alpigiani[140], A.A. Alshehri[56], M.I. Alstaty[88], B. Alvarez Gonzalez[32], D. Álvarez Piqueras[170], M.G. Alviggi[106a,106b], B.T. Amadio[16], Y. Amaral Coutinho[26a], C. Amelung[25], D. Amidei[92], S.P. Amor Dos Santos[128a,128c], S. Amoroso[32], G. Amundsen[25], C. Anastopoulos[141], L.S. Ancu[52], N. Andari[19], T. Andeen[11], C.F. Anders[60b], J.K. Anders[77], K.J. Anderson[33], A. Andreazza[94a,94b], V. Andrei[60a], S. Angelidakis[37], I. Angelozzi[109], A. Angerami[38], A.V. Anisenkov[111,c], N. Anjos[13], A. Annovi[126a,126b], C. Antel[60a], M. Antonelli[50], A. Antonov[100,*], D.J. Antrim[166], F. Anulli[134a], M. Aoki[69], L. Aperio Bella[32], G. Arabidze[93], Y. Arai[69], J.P. Araque[128a], V. Araujo Ferraz[26a], A.T.H. Arce[48], R.E. Ardell[80], F.A. Arduh[74], J-F. Arguin[97], S. Argyropoulos[66], M. Arik[20a], A.J. Armbruster[32], L.J. Armitage[79], O. Arnaez[161], H. Arnold[51], M. Arratia[30], O. Arslan[23], A. Artamonov[99,*], G. Artoni[122], S. Artz[86], S. Asai[157], N. Asbah[45], A. Ashkenazi[155], L. Asquith[151], K. Assamagan[27], R. Astalos[146a], M. Atkinson[169], N.B. Atlay[143], K. Augsten[130], G. Avolio[32], B. Axen[16], M.K. Ayoub[35a], G. Azuelos[97,d], A.E. Baas[60a], M.J. Baca[19], H. Bachacou[138], K. Bachas[76a,76b], M. Backes[122], P. Bagnaia[134a,134b], M. Bahmani[42], H. Bahrasemani[144], J.T. Baines[133], M. Bajic[39], O.K. Baker[179], P.J. Bakker[109], E.M. Baldin[111,c], P. Balek[175], F. Balli[138], W.K. Balunas[124], E. Banas[42], A. Bandyopadhyay[23], Sw. Banerjee[176,e], A.A.E. Bannoura[178], L. Barak[155], E.L. Barberio[91], D. Barberis[53a,53b], M. Barbero[88], T. Barillari[103], M-S Barisits[32], J.T. Barkeloo[118], T. Barklow[145], N. Barlow[30], S.L. Barnes[36c], B.M. Barnett[133], R.M. Barnett[16], Z. Barnovska-Blenessy[36a], A. Baroncelli[136a], G. Barone[25], A.J. Barr[122], L. Barranco Navarro[170], F. Barreiro[85], J. Barreiro Guimarães da Costa[35a], R. Bartoldus[145], A.E. Barton[75], P. Bartos[146a], A. Basalaev[125], A. Bassalat[119,f], R.L. Bates[56], S.J. Batista[161], J.R. Batley[30], M. Battaglia[139], M. Bauce[134a,134b], F. Bauer[138], H.S. Bawa[145,g], J.B. Beacham[113], M.D. Beattie[75], T. Beau[83], P.H. Beauchemin[165], P. Bechtle[23], H.P. Beck[18,h], H.C. Beck[57], K. Becker[122], M. Becker[86], C. Becot[112], A.J. Beddall[20e], A. Beddall[20b], V.A. Bednyakov[68], M. Bedognetti[109], C.P. Bee[150], T.A. Beermann[32], M. Begalli[26a], M. Begel[27], J.K. Behr[45], A.S. Bell[81], G. Bella[155], L. Bellagamba[22a], A. Bellerive[31], M. Bellomo[154], K. Belotskiy[100], O. Beltramello[32], N.L. Belyaev[100], O. Benary[155,*], D. Benchekroun[137a], M. Bender[102], N. Benekos[10], Y. Benhammou[155], E. Benhar Noccioli[179], J. Benitez[66], D.P. Benjamin[48], M. Benoit[52], J.R. Bensinger[25], S. Bentvelsen[109], L. Beresford[122], M. Beretta[50], D. Berge[109], E. Bergeaas Kuutmann[168], N. Berger[5], J. Beringer[16], S. Berlendis[58], N.R. Bernard[89], G. Bernardi[83], C. Bernius[145], F.U. Bernlochner[23], T. Berry[80], P. Berta[86], C. Bertella[35a], G. Bertoli[148a,148b], I.A. Bertram[75], C. Bertsche[45], D. Bertsche[115], G.J. Besjes[39], O. Bessidskaia Bylund[148a,148b], M. Bessner[45], N. Besson[138], A. Bethani[87], S. Bethke[103], A.J. Bevan[79], J. Beyer[103], R.M. Bianchi[127], O. Biebel[102], D. Biedermann[17], R. Bielski[87], K. Bierwagen[86], N.V. Biesuz[126a,126b], M. Biglietti[136a], T.R.V. Billoud[97], H. Bilokon[50], M. Bindi[57], A. Bingul[20b], C. Bini[134a,134b], S. Biondi[22a,22b], T. Bisanz[57], C. Bittrich[47], D.M. Bjergaard[48], J.E. Black[145], K.M. Black[24], R.E. Blair[6], T. Blazek[146a], I. Bloch[45], C. Blocker[25], A. Blue[56],

JHEP12(2017)059

W. Blum[86,*], U. Blumenschein[79], S. Blunier[34a], G.J. Bobbink[109], V.S. Bobrovnikov[111,c], S.S. Bocchetta[84], A. Bocci[48], C. Bock[102], M. Boehler[51], D. Boerner[178], D. Bogavac[102], A.G. Bogdanchikov[111], C. Bohm[148a], V. Boisvert[80], P. Bokan[168,i], T. Bold[41a], A.S. Boldyrev[101], A.E. Bolz[60b], M. Bomben[83], M. Bona[79], M. Boonekamp[138], A. Borisov[132], G. Borissov[75], J. Bortfeldt[32], D. Bortoletto[122], V. Bortolotto[62a,62b,62c], D. Boscherini[22a], M. Bosman[13], J.D. Bossio Sola[29], J. Boudreau[127], J. Bouffard[2], E.V. Bouhova-Thacker[75], D. Boumediene[37], C. Bourdarios[119], S.K. Boutle[56], A. Boveia[113], J. Boyd[32], I.R. Boyko[68], A.J. Bozson[80], J. Bracinik[19], A. Brandt[8], G. Brandt[57], O. Brandt[60a], F. Braren[45], U. Bratzler[158], B. Brau[89], J.E. Brau[118], W.D. Breaden Madden[56], K. Brendlinger[45], A.J. Brennan[91], L. Brenner[109], R. Brenner[168], S. Bressler[175], D.L. Briglin[19], T.M. Bristow[49], D. Britton[56], D. Britzger[45], F.M. Brochu[30], I. Brock[23], R. Brock[93], G. Brooijmans[38], T. Brooks[80], W.K. Brooks[34b], J. Brosamer[16], E. Brost[110], J.H Broughton[19], P.A. Bruckman de Renstrom[42], D. Bruncko[146b], A. Bruni[22a], G. Bruni[22a], L.S. Bruni[109], S. Bruno[135a,135b], BH Brunt[30], M. Bruschi[22a], N. Bruscino[127], P. Bryant[33], L. Bryngemark[45], T. Buanes[15], Q. Buat[144], P. Buchholz[143], A.G. Buckley[56], I.A. Budagov[68], F. Buehrer[51], M.K. Bugge[121], O. Bulekov[100], D. Bullock[8], T.J. Burch[110], S. Burdin[77], C.D. Burgard[51], A.M. Burger[5], B. Burghgrave[110], K. Burka[42], S. Burke[133], I. Burmeister[46], J.T.P. Burr[122], E. Busato[37], D. Büscher[51], V. Büscher[86], P. Bussey[56], J.M. Butler[24], C.M. Buttar[56], J.M. Butterworth[81], P. Butti[32], W. Buttinger[27], A. Buzatu[153], A.R. Buzykaev[111,c], S. Cabrera Urbán[170], D. Caforio[130], H. Cai[169], V.M. Cairo[40a,40b], O. Cakir[4a], N. Calace[52], P. Calafiura[16], A. Calandri[88], G. Calderini[83], P. Calfayan[64], G. Callea[40a,40b], L.P. Caloba[26a], S. Calvente Lopez[85], D. Calvet[37], S. Calvet[37], T.P. Calvet[88], R. Camacho Toro[33], S. Camarda[32], P. Camarri[135a,135b], D. Cameron[121], R. Caminal Armadans[169], C. Camincher[58], S. Campana[32], M. Campanelli[81], A. Camplani[94a,94b], A. Campoverde[143], V. Canale[106a,106b], M. Cano Bret[36c], J. Cantero[116], T. Cao[155], M.D.M. Capeans Garrido[32], I. Caprini[28b], M. Caprini[28b], M. Capua[40a,40b], R.M. Carbone[38], R. Cardarelli[135a], F. Cardillo[51], I. Carli[131], T. Carli[32], G. Carlino[106a], B.T. Carlson[127], L. Carminati[94a,94b], R.M.D. Carney[148a,148b], S. Caron[108], E. Carquin[34b], S. Carrá[94a,94b], G.D. Carrillo-Montoya[32], D. Casadei[19], M.P. Casado[13,j], M. Casolino[13], D.W. Casper[166], R. Castelijn[109], V. Castillo Gimenez[170], N.F. Castro[128a,k], A. Catinaccio[32], J.R. Catmore[121], A. Cattai[32], J. Caudron[23], V. Cavaliere[169], E. Cavallaro[13], D. Cavalli[94a], M. Cavalli-Sforza[13], V. Cavasinni[126a,126b], E. Celebi[20d], F. Ceradini[136a,136b], L. Cerda Alberich[170], A.S. Cerqueira[26b], A. Cerri[151], L. Cerrito[135a,135b], F. Cerutti[16], A. Cervelli[22a,22b], S.A. Cetin[20d], A. Chafaq[137a], D. Chakraborty[110], S.K. Chan[59], W.S. Chan[109], Y.L. Chan[62a], P. Chang[169], J.D. Chapman[30], D.G. Charlton[19], C.C. Chau[31], C.A. Chavez Barajas[151], S. Che[113], S. Cheatham[167a,167c], A. Chegwidden[93], S. Chekanov[6], S.V. Chekulaev[163a], G.A. Chelkov[68,l], M.A. Chelstowska[32], C. Chen[36a], C. Chen[67], H. Chen[27], J. Chen[36a], S. Chen[35b], S. Chen[157], X. Chen[35c,m], Y. Chen[70], H.C. Cheng[92], H.J. Cheng[35a], A. Cheplakov[68], E. Cheremushkina[132], R. Cherkaoui El Moursli[137e], E. Cheu[7], K. Cheung[63], L. Chevalier[138], V. Chiarella[50], G. Chiarelli[126a,126b], G. Chiodini[76a], A.S. Chisholm[32], A. Chitan[28b], Y.H. Chiu[172], M.V. Chizhov[68], K. Choi[64], A.R. Chomont[37], S. Chouridou[156], Y.S. Chow[62a], V. Christodoulou[81], M.C. Chu[62a], J. Chudoba[129], A.J. Chuinard[90], J.J. Chwastowski[42], L. Chytka[117], A.K. Ciftci[4a], D. Cinca[46], V. Cindro[78], I.A. Cioara[23], A. Ciocio[16], F. Cirotto[106a,106b], Z.H. Citron[175], M. Citterio[94a], M. Ciubancan[28b], A. Clark[52], B.L. Clark[59], M.R. Clark[38], P.J. Clark[49], R.N. Clarke[16], C. Clement[148a,148b], Y. Coadou[88], M. Cobal[167a,167c], A. Coccaro[52], J. Cochran[67], L. Colasurdo[108], B. Cole[38], A.P. Colijn[109], J. Collot[58], T. Colombo[166], P. Conde Muiño[128a,128b], E. Coniavitis[51], S.H. Connell[147b], I.A. Connelly[87], S. Constantinescu[28b], G. Conti[32], F. Conventi[106a,n], M. Cooke[16], A.M. Cooper-Sarkar[122], F. Cormier[171], K.J.R. Cormier[161], M. Corradi[134a,134b], F. Corriveau[90,o], A. Cortes-Gonzalez[32], G. Costa[94a], M.J. Costa[170], D. Costanzo[141], G. Cottin[30],

JHEP12(2017)059

G. Cowan[80], B.E. Cox[87], K. Cranmer[112], S.J. Crawley[56], R.A. Creager[124], G. Cree[31], S. Crépé-Renaudin[58], F. Crescioli[83], W.A. Cribbs[148a,148b], M. Cristinziani[23], V. Croft[112], G. Crosetti[40a,40b], A. Cueto[85], T. Cuhadar Donszelmann[141], A.R. Cukierman[145], J. Cummings[179], M. Curatolo[50], J. Cúth[86], S. Czekierda[42], P. Czodrowski[32], G. D'amen[22a,22b], S. D'Auria[56], L. D'eramo[83], M. D'Onofrio[77], M.J. Da Cunha Sargedas De Sousa[128a,128b], C. Da Via[87], W. Dabrowski[41a], T. Dado[146a], T. Dai[92], O. Dale[15], F. Dallaire[97], C. Dallapiccola[89], M. Dam[39], J.R. Dandoy[124], M.F. Daneri[29], N.P. Dang[176], A.C. Daniells[19], N.S. Dann[87], M. Danninger[171], M. Dano Hoffmann[138], V. Dao[150], G. Darbo[53a], S. Darmora[8], J. Dassoulas[3], A. Dattagupta[118], T. Daubney[45], W. Davey[23], C. David[45], T. Davidek[131], D.R. Davis[48], P. Davison[81], E. Dawe[91], I. Dawson[141], K. De[8], R. de Asmundis[106a], A. De Benedetti[115], S. De Castro[22a,22b], S. De Cecco[83], N. De Groot[108], P. de Jong[109], H. De la Torre[93], F. De Lorenzi[67], A. De Maria[57], D. De Pedis[134a], A. De Salvo[134a], U. De Sanctis[135a,135b], A. De Santo[151], K. De Vasconcelos Corga[88], J.B. De Vivie De Regie[119], R. Debbe[27], C. Debenedetti[139], D.V. Dedovich[68], N. Dehghanian[3], I. Deigaard[109], M. Del Gaudio[40a,40b], J. Del Peso[85], D. Delgove[119], F. Deliot[138], C.M. Delitzsch[7], A. Dell'Acqua[32], L. Dell'Asta[24], M. Dell'Orso[126a,126b], M. Della Pietra[106a,106b], D. della Volpe[52], M. Delmastro[5], C. Delporte[119], P.A. Delsart[58], D.A. DeMarco[161], S. Demers[179], M. Demichev[68], A. Demilly[83], S.P. Denisov[132], D. Denysiuk[138], D. Derendarz[42], J.E. Derkaoui[137d], F. Derue[83], P. Dervan[77], K. Desch[23], C. Deterre[45], K. Dette[161], M.R. Devesa[29], P.O. Deviveiros[32], A. Dewhurst[133], S. Dhaliwal[25], F.A. Di Bello[52], A. Di Ciaccio[135a,135b], L. Di Ciaccio[5], W.K. Di Clemente[124], C. Di Donato[106a,106b], A. Di Girolamo[32], B. Di Girolamo[32], B. Di Micco[136a,136b], R. Di Nardo[32], K.F. Di Petrillo[59], A. Di Simone[51], R. Di Sipio[161], D. Di Valentino[31], C. Diaconu[88], M. Diamond[161], F.A. Dias[39], M.A. Diaz[34a], E.B. Diehl[92], J. Dietrich[17], S. Díez Cornell[45], A. Dimitrievska[14], J. Dingfelder[23], P. Dita[28b], S. Dita[28b], F. Dittus[32], F. Djama[88], T. Djobava[54b], J.I. Djuvsland[60a], M.A.B. do Vale[26c], D. Dobos[32], M. Dobre[28b], D. Dodsworth[25], C. Doglioni[84], J. Dolejsi[131], Z. Dolezal[131], M. Donadelli[26d], S. Donati[126a,126b], P. Dondero[123a,123b], J. Donini[37], J. Dopke[133], A. Doria[106a], M.T. Dova[74], A.T. Doyle[56], E. Drechsler[57], M. Dris[10], Y. Du[36b], J. Duarte-Campderros[155], A. Dubreuil[52], E. Duchovni[175], G. Duckeck[102], A. Ducourthial[83], O.A. Ducu[97,p], D. Duda[109], A. Dudarev[32], A.Chr. Dudder[86], E.M. Duffield[16], L. Duflot[119], M. Dührssen[32], C. Dulsen[178], M. Dumancic[175], A.E. Dumitriu[28b], A.K. Duncan[56], M. Dunford[60a], A. Duperrin[88], H. Duran Yildiz[4a], M. Düren[55], A. Durglishvili[54b], D. Duschinger[47], B. Dutta[45], D. Duvnjak[1], M. Dyndal[45], B.S. Dziedzic[42], C. Eckardt[45], K.M. Ecker[103], R.C. Edgar[92], T. Eifert[32], G. Eigen[15], K. Einsweiler[16], T. Ekelof[168], M. El Kacimi[137c], R. El Kosseifi[88], V. Ellajosyula[88], M. Ellert[168], S. Elles[5], F. Ellinghaus[178], A.A. Elliot[172], N. Ellis[32], J. Elmsheuser[27], M. Elsing[32], D. Emeliyanov[133], Y. Enari[157], O.C. Endner[86], J.S. Ennis[173], M.B. Epland[48], J. Erdmann[46], A. Ereditato[18], M. Ernst[27], S. Errede[169], M. Escalier[119], C. Escobar[170], B. Esposito[50], O. Estrada Pastor[170], A.I. Etienvre[138], E. Etzion[155], H. Evans[64], A. Ezhilov[125], M. Ezzi[137e], F. Fabbri[22a,22b], L. Fabbri[22a,22b], V. Fabiani[108], G. Facini[81], R.M. Fakhrutdinov[132], S. Falciano[134a], R.J. Falla[81], J. Faltova[32], Y. Fang[35a], M. Fanti[94a,94b], A. Farbin[8], A. Farilla[136a], C. Farina[127], E.M. Farina[123a,123b], T. Farooque[93], S. Farrell[16], S.M. Farrington[173], P. Farthouat[32], F. Fassi[137e], P. Fassnacht[32], D. Fassouliotis[9], M. Faucci Giannelli[49], A. Favareto[53a,53b], W.J. Fawcett[122], L. Fayard[119], O.L. Fedin[125,q], W. Fedorko[171], S. Feigl[121], L. Feligioni[88], C. Feng[36b], E.J. Feng[32], M.J. Fenton[56], A.B. Fenyuk[132], L. Feremenga[8], P. Fernandez Martinez[170], S. Fernandez Perez[13], J. Ferrando[45], A. Ferrari[168], P. Ferrari[109], R. Ferrari[123a], D.E. Ferreira de Lima[60b], A. Ferrer[170], D. Ferrere[52], C. Ferretti[92], F. Fiedler[86], A. Filipčič[78], M. Filipuzzi[45], F. Filthaut[108], M. Fincke-Keeler[172], K.D. Finelli[152], M.C.N. Fiolhais[128a,128c,r], L. Fiorini[170], A. Fischer[2], C. Fischer[13], J. Fischer[178], W.C. Fisher[93], N. Flaschel[45], I. Fleck[143], P. Fleischmann[92], R.R.M. Fletcher[124], T. Flick[178], B.M. Flierl[102],

JHEP12(2017)059

L.R. Flores Castillo[62a], M.J. Flowerdew[103], G.T. Forcolin[87], A. Formica[138], F.A. Förster[13], A. Forti[87], A.G. Foster[19], D. Fournier[119], H. Fox[75], S. Fracchia[141], P. Francavilla[83], M. Franchini[22a,22b], S. Franchino[60a], D. Francis[32], L. Franconi[121], M. Franklin[59], M. Frate[166], M. Fraternali[123a,123b], D. Freeborn[81], S.M. Fressard-Batraneanu[32], B. Freund[97], D. Froidevaux[32], J.A. Frost[122], C. Fukunaga[158], T. Fusayasu[104], J. Fuster[170], O. Gabizon[154], A. Gabrielli[22a,22b], A. Gabrielli[16], G.P. Gach[41a], S. Gadatsch[32], S. Gadomski[80], G. Gagliardi[53a,53b], L.G. Gagnon[97], C. Galea[108], B. Galhardo[128a,128c], E.J. Gallas[122], B.J. Gallop[133], P. Gallus[130], G. Galster[39], K.K. Gan[113], S. Ganguly[37], Y. Gao[77], Y.S. Gao[145,g], F.M. Garay Walls[34a], C. García[170], J.E. García Navarro[170], J.A. García Pascual[35a], M. Garcia-Sciveres[16], R.W. Gardner[33], N. Garelli[145], V. Garonne[121], A. Gascon Bravo[45], K. Gasnikova[45], C. Gatti[50], A. Gaudiello[53a,53b], G. Gaudio[123a], I.L. Gavrilenko[98], C. Gay[171], G. Gaycken[23], E.N. Gazis[10], C.N.P. Gee[133], J. Geisen[57], M. Geisen[86], M.P. Geisler[60a], K. Gellerstedt[148a,148b], C. Gemme[53a], M.H. Genest[58], C. Geng[92], S. Gentile[134a,134b], C. Gentsos[156], S. George[80], D. Gerbaudo[13], G. Geßner[46], S. Ghasemi[143], M. Ghneimat[23], B. Giacobbe[22a], S. Giagu[134a,134b], N. Giangiacomi[22a,22b], P. Giannetti[126a,126b], S.M. Gibson[80], M. Gignac[171], M. Gilchriese[16], D. Gillberg[31], G. Gilles[178], D.M. Gingrich[3,d], M.P. Giordani[167a,167c], F.M. Giorgi[22a], P.F. Giraud[138], P. Giromini[59], G. Giugliarelli[167a,167c], D. Giugni[94a], F. Giuli[122], C. Giuliani[103], M. Giulini[60b], B.K. Gjelsten[121], S. Gkaitatzis[156], I. Gkialas[9,s], E.L. Gkougkousis[13], P. Gkountoumis[10], L.K. Gladilin[101], C. Glasman[85], J. Glatzer[13], P.C.F. Glaysher[45], A. Glazov[45], M. Goblirsch-Kolb[25], J. Godlewski[42], S. Goldfarb[91], T. Golling[52], D. Golubkov[132], A. Gomes[128a,128b,128d], R. Gonçalo[128a], R. Goncalves Gama[26a], J. Goncalves Pinto Firmino Da Costa[138], G. Gonella[51], L. Gonella[19], A. Gongadze[68], S. González de la Hoz[170], S. Gonzalez-Sevilla[52], L. Goossens[32], P.A. Gorbounov[99], H.A. Gordon[27], I. Gorelov[107], B. Gorini[32], E. Gorini[76a,76b], A. Gorišek[78], A.T. Goshaw[48], C. Gössling[46], M.I. Gostkin[68], C.A. Gottardo[23], C.R. Goudet[119], D. Goujdami[137c], A.G. Goussiou[140], N. Govender[147b,t], E. Gozani[154], I. Grabowska-Bold[41a], P.O.J. Gradin[168], J. Gramling[166], E. Gramstad[121], S. Grancagnolo[17], V. Gratchev[125], P.M. Gravila[28f], C. Gray[56], H.M. Gray[16], Z.D. Greenwood[82,u], C. Grefe[23], K. Gregersen[81], I.M. Gregor[45], P. Grenier[145], K. Grevtsov[5], J. Griffiths[8], A.A. Grillo[139], K. Grimm[75], S. Grinstein[13,v], Ph. Gris[37], J.-F. Grivaz[119], S. Groh[86], E. Gross[175], J. Grosse-Knetter[57], G.C. Grossi[82], Z.J. Grout[81], A. Grummer[107], L. Guan[92], W. Guan[176], J. Guenther[32], F. Guescini[163a], D. Guest[166], O. Gueta[155], B. Gui[113], E. Guido[53a,53b], T. Guillemin[5], S. Guindon[32], U. Gul[56], C. Gumpert[32], J. Guo[36c], W. Guo[92], Y. Guo[36a], R. Gupta[43], S. Gupta[122], S. Gurbuz[20a], G. Gustavino[115], B.J. Gutelman[154], P. Gutierrez[115], N.G. Gutierrez Ortiz[81], C. Gutschow[81], C. Guyot[138], M.P. Guzik[41a], C. Gwenlan[122], C.B. Gwilliam[77], A. Haas[112], C. Haber[16], H.K. Hadavand[8], N. Haddad[137e], A. Hadef[88], S. Hageböck[23], M. Hagihara[164], H. Hakobyan[180,*], M. Haleem[45], J. Haley[116], G. Halladjian[93], G.D. Hallewell[88], K. Hamacher[178], P. Hamal[117], K. Hamano[172], A. Hamilton[147a], G.N. Hamity[141], P.G. Hamnett[45], L. Han[36a], S. Han[35a], K. Hanagaki[69,w], K. Hanawa[157], M. Hance[139], B. Haney[124], P. Hanke[60a], J.B. Hansen[39], J.D. Hansen[39], M.C. Hansen[23], P.H. Hansen[39], K. Hara[164], A.S. Hard[176], T. Harenberg[178], F. Hariri[119], S. Harkusha[95], P.F. Harrison[173], N.M. Hartmann[102], Y. Hasegawa[142], A. Hasib[49], S. Hassani[138], S. Haug[18], R. Hauser[93], L. Hauswald[47], L.B. Havener[38], M. Havranek[130], C.M. Hawkes[19], R.J. Hawkings[32], D. Hayakawa[159], D. Hayden[93], C.P. Hays[122], J.M. Hays[79], H.S. Hayward[77], S.J. Haywood[133], S.J. Head[19], T. Heck[86], V. Hedberg[84], L. Heelan[8], S. Heer[23], K.K. Heidegger[51], S. Heim[45], T. Heim[16], B. Heinemann[45,x], J.J. Heinrich[102], L. Heinrich[112], C. Heinz[55], J. Hejbal[129], L. Helary[32], A. Held[171], S. Hellman[148a,148b], C. Helsens[32], R.C.W. Henderson[75], Y. Heng[176], S. Henkelmann[171], A.M. Henriques Correia[32], S. Henrot-Versille[119], G.H. Herbert[17], H. Herde[25], V. Herget[177], Y. Hernández Jiménez[147c], H. Herr[86], G. Herten[51], R. Hertenberger[102], L. Hervas[32], T.C. Herwig[124], G.G. Hesketh[81], N.P. Hessey[163a], J.W. Hetherly[43], S. Higashino[69],

JHEP12(2017)059

E. Higón-Rodriguez[170], K. Hildebrand[33], E. Hill[172], J.C. Hill[30], K.H. Hiller[45], S.J. Hillier[19], M. Hils[47], I. Hinchliffe[16], M. Hirose[51], D. Hirschbuehl[178], B. Hiti[78], O. Hladik[129], X. Hoad[49], J. Hobbs[150], N. Hod[163a], M.C. Hodgkinson[141], P. Hodgson[141], A. Hoecker[32], M.R. Hoeferkamp[107], F. Hoenig[102], D. Hohn[23], T.R. Holmes[33], M. Homann[46], S. Honda[164], T. Honda[69], T.M. Hong[127], B.H. Hooberman[169], W.H. Hopkins[118], Y. Horii[105], A.J. Horton[144], J-Y. Hostachy[58], A. Hostiuc[140], S. Hou[153], A. Hoummada[137a], J. Howarth[87], J. Hoya[74], M. Hrabovsky[117], J. Hrdinka[32], I. Hristova[17], J. Hrivnac[119], T. Hryn'ova[5], A. Hrynevich[96], P.J. Hsu[63], S.-C. Hsu[140], Q. Hu[36a], S. Hu[36c], Y. Huang[35a], Z. Hubacek[130], F. Hubaut[88], F. Huegging[23], T.B. Huffman[122], E.W. Hughes[38], G. Hughes[75], M. Huhtinen[32], R.F.H. Hunter[31], P. Huo[150], N. Huseynov[68,b], J. Huston[93], J. Huth[59], R. Hyneman[92], G. Iacobucci[52], G. Iakovidis[27], I. Ibragimov[143], L. Iconomidou-Fayard[119], Z. Idrissi[137e], P. Iengo[32], O. Igonkina[109,y], T. Iizawa[174], Y. Ikegami[69], M. Ikeno[69], Y. Ilchenko[11,z], D. Iliadis[156], N. Ilic[145], F. Iltzsche[47], G. Introzzi[123a,123b], P. Ioannou[9,*], M. Iodice[136a], K. Iordanidou[38], V. Ippolito[59], M.F. Isacson[168], N. Ishijima[120], M. Ishino[157], M. Ishitsuka[159], C. Issever[122], S. Istin[20a], F. Ito[164], J.M. Iturbe Ponce[62a], R. Iuppa[162a,162b], H. Iwasaki[69], J.M. Izen[44], V. Izzo[106a], S. Jabbar[3], P. Jackson[1], R.M. Jacobs[23], V. Jain[2], K.B. Jakobi[86], K. Jakobs[51], S. Jakobsen[65], T. Jakoubek[129], D.O. Jamin[116], D.K. Jana[82], R. Jansky[52], J. Janssen[23], M. Janus[57], P.A. Janus[41a], G. Jarlskog[84], N. Javadov[68,b], T. Javůrek[51], M. Javurkova[51], F. Jeanneau[138], L. Jeanty[16], J. Jejelava[54a,aa], A. Jelinskas[173], P. Jenni[51,ab], C. Jeske[173], S. Jézéquel[5], H. Ji[176], J. Jia[150], H. Jiang[67], Y. Jiang[36a], Z. Jiang[145], S. Jiggins[81], J. Jimenez Pena[170], S. Jin[35a], A. Jinaru[28b], O. Jinnouchi[159], H. Jivan[147c], P. Johansson[141], K.A. Johns[7], C.A. Johnson[64], W.J. Johnson[140], K. Jon-And[148a,148b], R.W.L. Jones[75], S.D. Jones[151], S. Jones[7], T.J. Jones[77], J. Jongmanns[60a], P.M. Jorge[128a,128b], J. Jovicevic[163a], X. Ju[176], A. Juste Rozas[13,v], M.K. Köhler[175], A. Kaczmarska[42], M. Kado[119], H. Kagan[113], M. Kagan[145], S.J. Kahn[88], T. Kaji[174], E. Kajomovitz[154], C.W. Kalderon[84], A. Kaluza[86], S. Kama[43], A. Kamenshchikov[132], N. Kanaya[157], L. Kanjir[78], V.A. Kantserov[100], J. Kanzaki[69], B. Kaplan[112], L.S. Kaplan[176], D. Kar[147c], K. Karakostas[10], N. Karastathis[10], M.J. Kareem[163b], E. Karentzos[10], S.N. Karpov[68], Z.M. Karpova[68], K. Karthik[112], V. Kartvelishvili[75], A.N. Karyukhin[132], K. Kasahara[164], L. Kashif[176], R.D. Kass[113], A. Kastanas[149], Y. Kataoka[157], C. Kato[157], A. Katre[52], J. Katzy[45], K. Kawade[70], K. Kawagoe[73], T. Kawamoto[157], G. Kawamura[57], E.F. Kay[77], V.F. Kazanin[111,c], R. Keeler[172], R. Kehoe[43], J.S. Keller[31], E. Kellermann[84], J.J. Kempster[80], J Kendrick[19], H. Keoshkerian[161], O. Kepka[129], B.P. Kerševan[78], S. Kersten[178], R.A. Keyes[90], M. Khader[169], F. Khalil-zada[12], A. Khanov[116], A.G. Kharlamov[111,c], T. Kharlamova[111,c], A. Khodinov[160], T.J. Khoo[52], V. Khovanskiy[99,*], E. Khramov[68], J. Khubua[54b,ac], S. Kido[70], C.R. Kilby[80], H.Y. Kim[8], S.H. Kim[164], Y.K. Kim[33], N. Kimura[156], O.M. Kind[17], B.T. King[77], D. Kirchmeier[47], J. Kirk[133], A.E. Kiryunin[103], T. Kishimoto[157], D. Kisielewska[41a], V. Kitali[45], O. Kivernyk[5], E. Kladiva[146b], T. Klapdor-Kleingrothaus[51], M.H. Klein[92], M. Klein[77], U. Klein[77], K. Kleinknecht[86], P. Klimek[110], A. Klimentov[27], R. Klingenberg[46], T. Klingl[23], T. Klioutchnikova[32], E.-E. Kluge[60a], P. Kluit[109], S. Kluth[103], E. Kneringer[65], E.B.F.G. Knoops[88], A. Knue[103], A. Kobayashi[157], D. Kobayashi[73], T. Kobayashi[157], M. Kobel[47], M. Kocian[145], P. Kodys[131], T. Koffas[31], E. Koffeman[109], N.M. Köhler[103], T. Koi[145], M. Kolb[60b], I. Koletsou[5], A.A. Komar[98,*], T. Kondo[69], N. Kondrashova[36c], K. Köneke[51], A.C. König[108], T. Kono[69,ad], R. Konoplich[112,ae], N. Konstantinidis[81], R. Kopeliansky[64], S. Koperny[41a], A.K. Kopp[51], K. Korcyl[42], K. Kordas[156], A. Korn[81], A.A. Korol[111,c], I. Korolkov[13], E.V. Korolkova[141], O. Kortner[103], S. Kortner[103], T. Kosek[131], V.V. Kostyukhin[23], A. Kotwal[48], A. Koulouris[10], A. Kourkoumeli-Charalampidi[123a,123b], C. Kourkoumelis[9], E. Kourlitis[141], V. Kouskoura[27], A.B. Kowalewska[42], R. Kowalewski[172], T.Z. Kowalski[41a], C. Kozakai[157], W. Kozanecki[138], A.S. Kozhin[132], V.A. Kramarenko[101], G. Kramberger[78], D. Krasnopevtsev[100], M.W. Krasny[83],

JHEP12(2017)059

A. Krasznahorkay[32], D. Krauss[103], J.A. Kremer[41a], J. Kretzschmar[77], K. Kreutzfeldt[55], P. Krieger[161], K. Krizka[16], K. Kroeninger[46], H. Kroha[103], J. Kroll[129], J. Kroll[124], J. Kroseberg[23], J. Krstic[14], U. Kruchonak[68], H. Krüger[23], N. Krumnack[67], M.C. Kruse[48], T. Kubota[91], H. Kucuk[81], S. Kuday[4b], J.T. Kuechler[178], S. Kuehn[32], A. Kugel[60a], F. Kuger[177], T. Kuhl[45], V. Kukhtin[68], R. Kukla[88], Y. Kulchitsky[95], S. Kuleshov[34b], Y.P. Kulinich[169], M. Kuna[134a,134b], T. Kunigo[71], A. Kupco[129], T. Kupfer[46], O. Kuprash[155], H. Kurashige[70], L.L. Kurchaninov[163a], Y.A. Kurochkin[95], M.G. Kurth[35a], E.S. Kuwertz[172], M. Kuze[159], J. Kvita[117], T. Kwan[172], D. Kyriazopoulos[141], A. La Rosa[103], J.L. La Rosa Navarro[26d], L. La Rotonda[40a,40b], F. La Ruffa[40a,40b], C. Lacasta[170], F. Lacava[134a,134b], J. Lacey[45], D.P.J. Lack[87], H. Lacker[17], D. Lacour[83], E. Ladygin[68], R. Lafaye[5], B. Laforge[83], T. Lagouri[179], S. Lai[57], S. Lammers[64], W. Lampl[7], E. Lançon[27], U. Landgraf[51], M.P.J. Landon[79], M.C. Lanfermann[52], V.S. Lang[45], J.C. Lange[13], R.J. Langenberg[32], A.J. Lankford[166], F. Lanni[27], K. Lantzsch[23], A. Lanza[123a], A. Lapertosa[53a,53b], S. Laplace[83], J.F. Laporte[138], T. Lari[94a], F. Lasagni Manghi[22a,22b], M. Lassnig[32], T.S. Lau[62a], P. Laurelli[50], W. Lavrijsen[16], A.T. Law[139], P. Laycock[77], T. Lazovich[59], M. Lazzaroni[94a,94b], B. Le[91], O. Le Dortz[83], E. Le Guirriec[88], E.P. Le Quilleuc[138], M. LeBlanc[172], T. LeCompte[6], F. Ledroit-Guillon[58], C.A. Lee[27], G.R. Lee[34a], S.C. Lee[153], L. Lee[59], B. Lefebvre[90], G. Lefebvre[83], M. Lefebvre[172], F. Legger[102], C. Leggett[16], G. Lehmann Miotto[32], X. Lei[7], W.A. Leight[45], M.A.L. Leite[26d], R. Leitner[131], D. Lellouch[175], B. Lemmer[57], K.J.C. Leney[81], T. Lenz[23], B. Lenzi[32], R. Leone[7], S. Leone[126a,126b], C. Leonidopoulos[49], G. Lerner[151], C. Leroy[97], R. Les[161], A.A.J. Lesage[138], C.G. Lester[30], M. Levchenko[125], J. Levêque[5], D. Levin[92], L.J. Levinson[175], M. Levy[19], D. Lewis[79], B. Li[36a,af], Changqiao Li[36a], H. Li[150], L. Li[36c], Q. Li[35a], Q. Li[36a], S. Li[48], X. Li[36c], Y. Li[143], Z. Liang[35a], B. Liberti[135a], A. Liblong[161], K. Lie[62c], J. Liebal[23], W. Liebig[15], A. Limosani[152], K. Lin[93], S.C. Lin[182], T.H. Lin[86], R.A. Linck[64], B.E. Lindquist[150], A.E. Lionti[52], E. Lipeles[124], A. Lipniacka[15], M. Lisovyi[60b], T.M. Liss[169,ag], A. Lister[171], A.M. Litke[139], B. Liu[67], H. Liu[92], H. Liu[27], J.K.K. Liu[122], J. Liu[36b], J.B. Liu[36a], K. Liu[88], L. Liu[169], M. Liu[36a], Y.L. Liu[36a], Y. Liu[36a], M. Livan[123a,123b], A. Lleres[58], J. Llorente Merino[35a], S.L. Lloyd[79], C.Y. Lo[62b], F. Lo Sterzo[43], E.M. Lobodzinska[45], P. Loch[7], F.K. Loebinger[87], A. Loesle[51], K.M. Loew[25], T. Lohse[17], K. Lohwasser[141], M. Lokajicek[129], B.A. Long[24], J.D. Long[169], R.E. Long[75], L. Longo[76a,76b], K.A. Looper[113], J.A. Lopez[34b], I. Lopez Paz[13], A. Lopez Solis[83], J. Lorenz[102], N. Lorenzo Martinez[5], M. Losada[21], P.J. Lösel[102], X. Lou[35a], A. Lounis[119], J. Love[6], P.A. Love[75], H. Lu[62a], N. Lu[92], Y.J. Lu[63], H.J. Lubatti[140], C. Luci[134a,134b], A. Lucotte[58], C. Luedtke[51], F. Luehring[64], W. Lukas[65], L. Luminari[134a], O. Lundberg[148a,148b], B. Lund-Jensen[149], M.S. Lutz[89], P.M. Luzi[83], D. Lynn[27], R. Lysak[129], E. Lytken[84], F. Lyu[35a], V. Lyubushkin[68], H. Ma[27], L.L. Ma[36b], Y. Ma[36b], G. Maccarrone[50], A. Macchiolo[103], C.M. Macdonald[141], B. Maček[78], J. Machado Miguens[124,128b], D. Madaffari[170], R. Madar[37], W.F. Mader[47], A. Madsen[45], N. Madysa[47], J. Maeda[70], S. Maeland[15], T. Maeno[27], A.S. Maevskiy[101], V. Magerl[51], C. Maiani[119], C. Maidantchik[26a], T. Maier[102], A. Maio[128a,128b,128d], O. Majersky[146a], S. Majewski[118], Y. Makida[69], N. Makovec[119], B. Malaescu[83], Pa. Malecki[42], V.P. Maleev[125], F. Malek[58], U. Mallik[66], D. Malon[6], C. Malone[30], S. Maltezos[10], S. Malyukov[32], J. Mamuzic[170], G. Mancini[50], I. Mandić[78], J. Maneira[128a,128b], L. Manhaes de Andrade Filho[26b], J. Manjarres Ramos[47], K.H. Mankinen[84], A. Mann[102], A. Manousos[32], B. Mansoulie[138], J.D. Mansour[35a], R. Mantifel[90], M. Mantoani[57], S. Manzoni[94a,94b], L. Mapelli[32], G. Marceca[29], L. March[52], L. Marchese[122], G. Marchiori[83], M. Marcisovsky[129], C.A. Marin Tobon[32], M. Marjanovic[37], D.E. Marley[92], F. Marroquim[26a], S.P. Marsden[87], Z. Marshall[16], M.U.F Martensson[168], S. Marti-Garcia[170], C.B. Martin[113], T.A. Martin[173], V.J. Martin[49], B. Martin dit Latour[15], M. Martinez[13,v], V.I. Martinez Outschoorn[169], S. Martin-Haugh[133], V.S. Martoiu[28b], A.C. Martyniuk[81], A. Marzin[32], L. Masetti[86], T. Mashimo[157], R. Mashinistov[98],

JHEP12(2017)059

J. Masik[87], A.L. Maslennikov[111,c], L.H. Mason[91], L. Massa[135a,135b], P. Mastrandrea[5], A. Mastroberardino[40a,40b], T. Masubuchi[157], P. Mättig[178], J. Maurer[28b], S.J. Maxfield[77], D.A. Maximov[111,c], R. Mazini[153], I. Maznas[156], S.M. Mazza[94a,94b], N.C. Mc Fadden[107], G. Mc Goldrick[161], S.P. Mc Kee[92], A. McCarn[92], R.L. McCarthy[150], T.G. McCarthy[103], L.I. McClymont[81], E.F. McDonald[91], J.A. Mcfayden[32], G. Mchedlidze[57], S.J. McMahon[133], P.C. McNamara[91], C.J. McNicol[173], R.A. McPherson[172,o], S. Meehan[140], T.J. Megy[51], S. Mehlhase[102], A. Mehta[77], T. Meideck[58], K. Meier[60a], B. Meirose[44], D. Melini[170,ah], B.R. Mellado Garcia[147c], J.D. Mellenthin[57], M. Melo[146a], F. Meloni[18], A. Melzer[23], S.B. Menary[87], L. Meng[77], X.T. Meng[92], A. Mengarelli[22a,22b], S. Menke[103], E. Meoni[40a,40b], S. Mergelmeyer[17], C. Merlassino[18], P. Mermod[52], L. Merola[106a,106b], C. Meroni[94a], F.S. Merritt[33], A. Messina[134a,134b], J. Metcalfe[6], A.S. Mete[166], C. Meyer[124], J-P. Meyer[138], J. Meyer[109], H. Meyer Zu Theenhausen[60a], F. Miano[151], R.P. Middleton[133], S. Miglioranzi[53a,53b], L. Mijović[49], G. Mikenberg[175], M. Mikestikova[129], M. Mikuž[78], M. Milesi[91], A. Milic[161], D.A. Millar[79], D.W. Miller[33], C. Mills[49], A. Milov[175], D.A. Milstead[148a,148b], A.A. Minaenko[132], Y. Minami[157], I.A. Minashvili[54b], A.I. Mincer[112], B. Mindur[41a], M. Mineev[68], Y. Minegishi[157], Y. Ming[176], L.M. Mir[13], A. Mirto[76a,76b], K.P. Mistry[124], T. Mitani[174], J. Mitrevski[102], V.A. Mitsou[170], A. Miucci[18], P.S. Miyagawa[141], A. Mizukami[69], J.U. Mjörnmark[84], T. Mkrtchyan[180], M. Mlynarikova[131], T. Moa[148a,148b], K. Mochizuki[97], P. Mogg[51], S. Mohapatra[38], S. Molander[148a,148b], R. Moles-Valls[23], M.C. Mondragon[93], K. Mönig[45], J. Monk[39], E. Monnier[88], A. Montalbano[150], J. Montejo Berlingen[32], F. Monticelli[74], S. Monzani[94a,94b], R.W. Moore[3], N. Morange[119], D. Moreno[21], M. Moreno Llácer[32], P. Morettini[53a], S. Morgenstern[32], D. Mori[144], T. Mori[157], M. Morii[59], M. Morinaga[174], V. Morisbak[121], A.K. Morley[32], G. Mornacchi[32], J.D. Morris[79], L. Morvaj[150], P. Moschovakos[10], M. Mosidze[54b], H.J. Moss[141], J. Moss[145,ai], K. Motohashi[159], R. Mount[145], E. Mountricha[27], E.J.W. Moyse[89], S. Muanza[88], F. Mueller[103], J. Mueller[127], R.S.P. Mueller[102], D. Muenstermann[75], P. Mullen[56], G.A. Mullier[18], F.J. Munoz Sanchez[87], W.J. Murray[173,133], H. Musheghyan[32], M. Muškinja[78], A.G. Myagkov[132,aj], M. Myska[130], B.P. Nachman[16], O. Nackenhorst[52], K. Nagai[122], R. Nagai[69,ad], K. Nagano[69], Y. Nagasaka[61], K. Nagata[164], M. Nagel[51], E. Nagy[88], A.M. Nairz[32], Y. Nakahama[105], K. Nakamura[69], T. Nakamura[157], I. Nakano[114], R.F. Naranjo Garcia[45], R. Narayan[11], D.I. Narrias Villar[60a], I. Naryshkin[125], T. Naumann[45], G. Navarro[21], R. Nayyar[7], H.A. Neal[92], P.Yu. Nechaeva[98], T.J. Neep[138], A. Negri[123a,123b], M. Negrini[22a], S. Nektarijevic[108], C. Nellist[57], A. Nelson[166], M.E. Nelson[122], S. Nemecek[129], P. Nemethy[112], M. Nessi[32,ak], M.S. Neubauer[169], M. Neumann[178], P.R. Newman[19], T.Y. Ng[62c], T. Nguyen Manh[97], R.B. Nickerson[122], R. Nicolaidou[138], J. Nielsen[139], N. Nikiforou[11], V. Nikolaenko[132,aj], I. Nikolic-Audit[83], K. Nikolopoulos[19], J.K. Nilsen[121], P. Nilsson[27], Y. Ninomiya[157], A. Nisati[134a], N. Nishu[36c], R. Nisius[103], I. Nitsche[46], T. Nitta[174], T. Nobe[157], Y. Noguchi[71], M. Nomachi[120], I. Nomidis[31], M.A. Nomura[27], T. Nooney[79], M. Nordberg[32], N. Norjoharuddeen[122], O. Novgorodova[47], M. Nozaki[69], L. Nozka[117], K. Ntekas[166], E. Nurse[81], F. Nuti[91], K. O'connor[25], D.C. O'Neil[144], A.A. O'Rourke[45], V. O'Shea[56], F.G. Oakham[31,d], H. Oberlack[103], T. Obermann[23], J. Ocariz[83], A. Ochi[70], I. Ochoa[38], J.P. Ochoa-Ricoux[34a], S. Oda[73], S. Odaka[69], A. Oh[87], S.H. Oh[48], C.C. Ohm[149], H. Ohman[168], H. Oide[53a,53b], H. Okawa[164], Y. Okumura[157], T. Okuyama[69], A. Olariu[28b], L.F. Oleiro Seabra[128a], S.A. Olivares Pino[34a], D. Oliveira Damazio[27], A. Olszewski[42], J. Olszowska[42], A. Onofre[128a,128e], K. Onogi[105], P.U.E. Onyisi[11,z], H. Oppen[121], M.J. Oreglia[33], Y. Oren[155], D. Orestano[136a,136b], N. Orlando[62b], R.S. Orr[161], B. Osculati[53a,53b,*], R. Ospanov[36a], G. Otero y Garzon[29], H. Otono[73], M. Ouchrif[137d], F. Ould-Saada[121], A. Ouraou[138], K.P. Oussoren[109], Q. Ouyang[35a], M. Owen[56], R.E. Owen[19], V.E. Ozcan[20a], N. Ozturk[8], K. Pachal[144], A. Pacheco Pages[13], L. Pacheco Rodriguez[138], C. Padilla Aranda[13], S. Pagan Griso[16], M. Paganini[179], F. Paige[27], G. Palacino[64], S. Palazzo[40a,40b], S. Palestini[32],

JHEP12(2017)059

M. Palka[41b], D. Pallin[37], E.St. Panagiotopoulou[10], I. Panagoulias[10], C.E. Pandini[52], J.G. Panduro Vazquez[80], P. Pani[32], S. Panitkin[27], D. Pantea[28b], L. Paolozzi[52], Th.D. Papadopoulou[10], K. Papageorgiou[9,s], A. Paramonov[6], D. Paredes Hernandez[179], A.J. Parker[75], M.A. Parker[30], K.A. Parker[45], F. Parodi[53a,53b], J.A. Parsons[38], U. Parzefall[51], V.R. Pascuzzi[161], J.M. Pasner[139], E. Pasqualucci[134a], S. Passaggio[53a], Fr. Pastore[80], S. Pataraia[86], J.R. Pater[87], T. Pauly[32], B. Pearson[103], S. Pedraza Lopez[170], R. Pedro[128a,128b], S.V. Peleganchuk[111,c], O. Penc[129], C. Peng[35a], H. Peng[36a], J. Penwell[64], B.S. Peralva[26b], M.M. Perego[138], D.V. Perepelitsa[27], F. Peri[17], L. Perini[94a,94b], H. Pernegger[32], S. Perrella[106a,106b], R. Peschke[45], V.D. Peshekhonov[68,*], K. Peters[45], R.F.Y. Peters[87], B.A. Petersen[32], T.C. Petersen[39], E. Petit[58], A. Petridis[1], C. Petridou[156], P. Petroff[119], E. Petrolo[134a], M. Petrov[122], F. Petrucci[136a,136b], N.E. Pettersson[89], A. Peyaud[138], R. Pezoa[34b], F.H. Phillips[93], P.W. Phillips[133], G. Piacquadio[150], E. Pianori[173], A. Picazio[89], E. Piccaro[79], M.A. Pickering[122], R. Piegaia[29], J.E. Pilcher[33], A.D. Pilkington[87], M. Pinamonti[135a,135b], J.L. Pinfold[3], H. Pirumov[45], M. Pitt[175], L. Plazak[146a], M.-A. Pleier[27], V. Pleskot[86], E. Plotnikova[68], D. Pluth[67], P. Podberezko[111], R. Poettgen[84], R. Poggi[123a,123b], L. Poggioli[119], I. Pogrebnyak[93], D. Pohl[23], I. Pokharel[57], G. Polesello[123a], A. Poley[45], A. Policicchio[40a,40b], R. Polifka[32], A. Polini[22a], C.S. Pollard[56], V. Polychronakos[27], K. Pommès[32], D. Ponomarenko[100], L. Pontecorvo[134a], G.A. Popeneciu[28d], D.M. Portillo Quintero[83], S. Pospisil[130], K. Potamianos[45], I.N. Potrap[68], C.J. Potter[30], H. Potti[11], T. Poulsen[84], J. Poveda[32], M.E. Pozo Astigarraga[32], P. Pralavorio[88], A. Pranko[16], S. Prell[67], D. Price[87], M. Primavera[76a], S. Prince[90], N. Proklova[100], K. Prokofiev[62c], F. Prokoshin[34b], S. Protopopescu[27], J. Proudfoot[6], M. Przybycien[41a], A. Puri[169], P. Puzo[119], J. Qian[92], G. Qin[56], Y. Qin[87], A. Quadt[57], M. Queitsch-Maitland[45], D. Quilty[56], S. Raddum[121], V. Radeka[27], V. Radescu[122], S.K. Radhakrishnan[150], P. Radloff[118], P. Rados[91], F. Ragusa[94a,94b], G. Rahal[181], J.A. Raine[87], S. Rajagopalan[27], C. Rangel-Smith[168], T. Rashid[119], S. Raspopov[5], M.G. Ratti[94a,94b], D.M. Rauch[45], F. Rauscher[102], S. Rave[86], I. Ravinovich[175], J.H. Rawling[87], M. Raymond[32], A.L. Read[121], N.P. Readioff[58], M. Reale[76a,76b], D.M. Rebuzzi[123a,123b], A. Redelbach[177], G. Redlinger[27], R. Reece[139], R.G. Reed[147c], K. Reeves[44], L. Rehnisch[17], J. Reichert[124], A. Reiss[86], C. Rembser[32], H. Ren[35a], M. Rescigno[134a], S. Resconi[94a], E.D. Resseguie[124], S. Rettie[171], E. Reynolds[19], O.L. Rezanova[111,c], P. Reznicek[131], R. Rezvani[97], R. Richter[103], S. Richter[81], E. Richter-Was[41b], O. Ricken[23], M. Ridel[83], P. Rieck[103], C.J. Riegel[178], J. Rieger[57], O. Rifki[115], M. Rijssenbeek[150], A. Rimoldi[123a,123b], M. Rimoldi[18], L. Rinaldi[22a], G. Ripellino[149], B. Ristić[32], E. Ritsch[32], I. Riu[13], F. Rizatdinova[116], E. Rizvi[79], C. Rizzi[13], R.T. Roberts[87], S.H. Robertson[90,o], A. Robichaud-Veronneau[90], D. Robinson[30], J.E.M. Robinson[45], A. Robson[56], E. Rocco[86], C. Roda[126a,126b], Y. Rodina[88,al], S. Rodriguez Bosca[170], A. Rodriguez Perez[13], D. Rodriguez Rodriguez[170], S. Roe[32], C.S. Rogan[59], O. Røhne[121], J. Roloff[59], A. Romaniouk[100], M. Romano[22a,22b], S.M. Romano Saez[37], E. Romero Adam[170], N. Rompotis[77], M. Ronzani[51], L. Roos[83], S. Rosati[134a], K. Rosbach[51], P. Rose[139], N.-A. Rosien[57], E. Rossi[106a,106b], L.P. Rossi[53a], J.H.N. Rosten[30], R. Rosten[140], M. Rotaru[28b], J. Rothberg[140], D. Rousseau[119], A. Rozanov[88], Y. Rozen[154], X. Ruan[147c], F. Rubbo[145], F. Rühr[51], A. Ruiz-Martinez[31], Z. Rurikova[51], N.A. Rusakovich[68], H.L. Russell[90], J.P. Rutherfoord[7], N. Ruthmann[32], Y.F. Ryabov[125], M. Rybar[169], G. Rybkin[119], S. Ryu[6], A. Ryzhov[132], G.F. Rzehorz[57], A.F. Saavedra[152], G. Sabato[109], S. Sacerdoti[29], H.F-W. Sadrozinski[139], R. Sadykov[68], F. Safai Tehrani[134a], P. Saha[110], M. Sahinsoy[60a], M. Saimpert[45], M. Saito[157], T. Saito[157], H. Sakamoto[157], Y. Sakurai[174], G. Salamanna[136a,136b], J.E. Salazar Loyola[34b], D. Salek[109], P.H. Sales De Bruin[168], D. Salihagic[103], A. Salnikov[145], J. Salt[170], D. Salvatore[40a,40b], F. Salvatore[151], A. Salvucci[62a,62b,62c], A. Salzburger[32], D. Sammel[51], D. Sampsonidis[156], D. Sampsonidou[156], J. Sánchez[170], V. Sanchez Martinez[170], A. Sanchez Pineda[167a,167c], H. Sandaker[121], R.L. Sandbach[79], C.O. Sander[45], M. Sandhoff[178],

JHEP12(2017)059

C. Sandoval[21], D.P.C. Sankey[133], M. Sannino[53a,53b], Y. Sano[105], A. Sansoni[50], C. Santoni[37], H. Santos[128a], I. Santoyo Castillo[151], A. Sapronov[68], J.G. Saraiva[128a,128d], B. Sarrazin[23], O. Sasaki[69], K. Sato[164], E. Sauvan[5], G. Savage[80], P. Savard[161,d], N. Savic[103], C. Sawyer[133], L. Sawyer[82,u], J. Saxon[33], C. Sbarra[22a], A. Sbrizzi[22a,22b], T. Scanlon[81], D.A. Scannicchio[166], J. Schaarschmidt[140], P. Schacht[103], B.M. Schachtner[102], D. Schaefer[33], L. Schaefer[124], R. Schaefer[45], J. Schaeffer[86], S. Schaepe[23], S. Schaetzel[60b], U. Schäfer[86], A.C. Schaffer[119], D. Schaile[102], R.D. Schamberger[150], V.A. Schegelsky[125], D. Scheirich[131], M. Schernau[166], C. Schiavi[53a,53b], S. Schier[139], L.K. Schildgen[23], C. Schillo[51], M. Schioppa[40a,40b], S. Schlenker[32], K.R. Schmidt-Sommerfeld[103], K. Schmieden[32], C. Schmitt[86], S. Schmitt[45], S. Schmitz[86], U. Schnoor[51], L. Schoeffel[138], A. Schoening[60b], B.D. Schoenrock[93], E. Schopf[23], M. Schott[86], J.F.P. Schouwenberg[108], J. Schovancova[32], S. Schramm[52], N. Schuh[86], A. Schulte[86], M.J. Schultens[23], H.-C. Schultz-Coulon[60a], H. Schulz[17], M. Schumacher[51], B.A. Schumm[139], Ph. Schune[138], A. Schwartzman[145], T.A. Schwarz[92], H. Schweiger[87], Ph. Schwemling[138], R. Schwienhorst[93], J. Schwindling[138], A. Sciandra[23], G. Sciolla[25], M. Scornajenghi[40a,40b], F. Scuri[126a,126b], F. Scutti[91], J. Searcy[92], P. Seema[23], S.C. Seidel[107], A. Seiden[139], J.M. Seixas[26a], G. Sekhniaidze[106a], K. Sekhon[92], S.J. Sekula[43], N. Semprini-Cesari[22a,22b], S. Senkin[37], C. Serfon[121], L. Serin[119], L. Serkin[167a,167b], M. Sessa[136a,136b], R. Seuster[172], H. Severini[115], T. Sfiligoj[78], F. Sforza[165], A. Sfyrla[52], E. Shabalina[57], N.W. Shaikh[148a,148b], L.Y. Shan[35a], R. Shang[169], J.T. Shank[24], M. Shapiro[16], P.B. Shatalov[99], K. Shaw[167a,167b], S.M. Shaw[87], A. Shcherbakova[148a,148b], C.Y. Shehu[151], Y. Shen[115], N. Sherafati[31], P. Sherwood[81], L. Shi[153,am], S. Shimizu[70], C.O. Shimmin[179], M. Shimojima[104], I.P.J. Shipsey[122], S. Shirabe[73], M. Shiyakova[68,an], J. Shlomi[175], A. Shmeleva[98], D. Shoaleh Saadi[97], M.J. Shochet[33], S. Shojaii[94a,94b], D.R. Shope[115], S. Shrestha[113], E. Shulga[100], M.A. Shupe[7], P. Sicho[129], A.M. Sickles[169], P.E. Sidebo[149], E. Sideras Haddad[147c], O. Sidiropoulou[177], A. Sidoti[22a,22b], F. Siegert[47], Dj. Sijacki[14], J. Silva[128a,128d], S.B. Silverstein[148a], V. Simak[130], Lj. Simic[68], S. Simion[119], E. Simioni[86], B. Simmons[81], M. Simon[86], P. Sinervo[161], N.B. Sinev[118], M. Sioli[22a,22b], G. Siragusa[177], I. Siral[92], S.Yu. Sivoklokov[101], J. Sjölin[148a,148b], M.B. Skinner[75], P. Skubic[115], M. Slater[19], T. Slavicek[130], M. Slawinska[42], K. Sliwa[165], R. Slovak[131], V. Smakhtin[175], B.H. Smart[5], J. Smiesko[146a], N. Smirnov[100], S.Yu. Smirnov[100], Y. Smirnov[100], L.N. Smirnova[101,ao], O. Smirnova[84], J.W. Smith[57], M.N.K. Smith[38], R.W. Smith[38], M. Smizanska[75], K. Smolek[130], A.A. Snesarev[98], I.M. Snyder[118], S. Snyder[27], R. Sobie[172,o], F. Socher[47], A. Soffer[155], A. Søgaard[49], D.A. Soh[153], G. Sokhrannyi[78], C.A. Solans Sanchez[32], M. Solar[130], E.Yu. Soldatov[100], U. Soldevila[170], A.A. Solodkov[132], A. Soloshenko[68], O.V. Solovyanov[132], V. Solovyev[125], P. Sommer[51], H. Son[165], A. Sopczak[130], D. Sosa[60b], C.L. Sotiropoulou[126a,126b], S. Sottocornola[123a,123b], R. Soualah[167a,167c], A.M. Soukharev[111,c], D. South[45], B.C. Sowden[80], S. Spagnolo[76a,76b], M. Spalla[126a,126b], M. Spangenberg[173], F. Spanò[80], D. Sperlich[17], F. Spettel[103], T.M. Spieker[60a], R. Spighi[22a], G. Spigo[32], L.A. Spiller[91], M. Spousta[131], R.D. St. Denis[56,*], A. Stabile[94a], R. Stamen[60a], S. Stamm[17], E. Stanecka[42], R.W. Stanek[6], C. Stanescu[136a], M.M. Stanitzki[45], B.S. Stapf[109], S. Stapnes[121], E.A. Starchenko[132], G.H. Stark[33], J. Stark[58], S.H Stark[39], P. Staroba[129], P. Starovoitov[60a], S. Stärz[32], R. Staszewski[42], M. Stegler[45], P. Steinberg[27], B. Stelzer[144], H.J. Stelzer[32], O. Stelzer-Chilton[163a], H. Stenzel[55], G.A. Stewart[56], M.C. Stockton[118], M. Stoebe[90], G. Stoicea[28b], P. Stolte[57], S. Stonjek[103], A.R. Stradling[8], A. Straessner[47], M.E. Stramaglia[18], J. Strandberg[149], S. Strandberg[148a,148b], M. Strauss[115], P. Strizenec[146b], R. Ströhmer[177], D.M. Strom[118], R. Stroynowski[43], A. Strubig[49], S.A. Stucci[27], B. Stugu[15], N.A. Styles[45], D. Su[145], J. Su[127], S. Suchek[60a], Y. Sugaya[120], M. Suk[130], V.V. Sulin[98], DMS Sultan[162a,162b], S. Sultansoy[4c], T. Sumida[71], S. Sun[59], X. Sun[3], K. Suruliz[151], C.J.E. Suster[152], M.R. Sutton[151], S. Suzuki[69], M. Svatos[129], M. Swiatlowski[33], S.P. Swift[2], I. Sykora[146a], T. Sykora[131], D. Ta[51],

JHEP12(2017)059

K. Tackmann[45], J. Taenzer[155], A. Taffard[166], R. Tafirout[163a], E. Tahirovic[79], N. Taiblum[155], H. Takai[27], R. Takashima[72], E.H. Takasugi[103], K. Takeda[70], T. Takeshita[142], Y. Takubo[69], M. Talby[88], A.A. Talyshev[111,c], J. Tanaka[157], M. Tanaka[159], R. Tanaka[119], S. Tanaka[69], R. Tanioka[70], B.B. Tannenwald[113], S. Tapia Araya[34b], S. Tapprogge[86], S. Tarem[154], G.F. Tartarelli[94a], P. Tas[131], M. Tasevsky[129], T. Tashiro[71], E. Tassi[40a,40b], A. Tavares Delgado[128a,128b], Y. Tayalati[137e], A.C. Taylor[107], A.J. Taylor[49], G.N. Taylor[91], P.T.E. Taylor[91], W. Taylor[163b], P. Teixeira-Dias[80], D. Temple[144], H. Ten Kate[32], P.K. Teng[153], J.J. Teoh[120], F. Tepel[178], S. Terada[69], K. Terashi[157], J. Terron[85], S. Terzo[13], M. Testa[50], R.J. Teuscher[161,o], T. Theveneaux-Pelzer[88], F. Thiele[39], J.P. Thomas[19], J. Thomas-Wilsker[80], P.D. Thompson[19], A.S. Thompson[56], L.A. Thomsen[179], E. Thomson[124], Y. Tian[38], M.J. Tibbetts[16], R.E. Ticse Torres[88], V.O. Tikhomirov[98,ap], Yu.A. Tikhonov[111,c], S. Timoshenko[100], P. Tipton[179], S. Tisserant[88], K. Todome[159], S. Todorova-Nova[5], S. Todt[47], J. Tojo[73], S. Tokár[146a], K. Tokushuku[69], E. Tolley[59], L. Tomlinson[87], M. Tomoto[105], L. Tompkins[145,aq], K. Toms[107], B. Tong[59], P. Tornambe[51], E. Torrence[118], H. Torres[47], E. Torró Pastor[140], J. Toth[88,ar], F. Touchard[88], D.R. Tovey[141], C.J. Treado[112], T. Trefzger[177], F. Tresoldi[151], A. Tricoli[27], I.M. Trigger[163a], S. Trincaz-Duvoid[83], M.F. Tripiana[13], W. Trischuk[161], B. Trocmé[58], A. Trofymov[45], C. Troncon[94a], M. Trottier-McDonald[16], M. Trovatelli[172], L. Truong[147b], M. Trzebinski[42], A. Trzupek[42], K.W. Tsang[62a], J.C-L. Tseng[122], P.V. Tsiareshka[95], G. Tsipolitis[10], N. Tsirintanis[9], S. Tsiskaridze[13], V. Tsiskaridze[51], E.G. Tskhadadze[54a], I.I. Tsukerman[99], V. Tsulaia[16], S. Tsuno[69], D. Tsybychev[150], Y. Tu[62b], A. Tudorache[28b], V. Tudorache[28b], T.T. Tulbure[28a], A.N. Tuna[59], S. Turchikhin[68], D. Turgeman[175], I. Turk Cakir[4b,as], R. Turra[94a], P.M. Tuts[38], G. Ucchielli[22a,22b], I. Ueda[69], M. Ughetto[148a,148b], F. Ukegawa[164], G. Unal[32], A. Undrus[27], G. Unel[166], F.C. Ungaro[91], Y. Unno[69], K. Uno[157], C. Unverdorben[102], J. Urban[146b], P. Urquijo[91], P. Urrejola[86], G. Usai[8], J. Usui[69], L. Vacavant[88], V. Vacek[130], B. Vachon[90], K.O.H. Vadla[121], A. Vaidya[81], C. Valderanis[102], E. Valdes Santurio[148a,148b], M. Valente[52], S. Valentinetti[22a,22b], A. Valero[170], L. Valéry[13], S. Valkar[131], A. Vallier[5], J.A. Valls Ferrer[170], W. Van Den Wollenberg[109], H. van der Graaf[109], P. van Gemmeren[6], J. Van Nieuwkoop[144], I. van Vulpen[109], M.C. van Woerden[109], M. Vanadia[135a,135b], W. Vandelli[32], A. Vaniachine[160], P. Vankov[109], G. Vardanyan[180], R. Vari[134a], E.W. Varnes[7], C. Varni[53a,53b], T. Varol[43], D. Varouchas[119], A. Vartapetian[8], K.E. Varvell[152], J.G. Vasquez[179], G.A. Vasquez[34b], F. Vazeille[37], D. Vazquez Furelos[13], T. Vazquez Schroeder[90], J. Veatch[57], V. Veeraraghavan[7], L.M. Veloce[161], F. Veloso[128a,128c], S. Veneziano[134a], A. Ventura[76a,76b], M. Venturi[172], N. Venturi[32], A. Venturini[25], V. Vercesi[123a], M. Verducci[136a,136b], W. Verkerke[109], A.T. Vermeulen[109], J.C. Vermeulen[109], M.C. Vetterli[144,d], N. Viaux Maira[34b], O. Viazlo[84], I. Vichou[169,*], T. Vickey[141], O.E. Vickey Boeriu[141], G.H.A. Viehhauser[122], S. Viel[16], L. Vigani[122], M. Villa[22a,22b], M. Villaplana Perez[94a,94b], E. Vilucchi[50], M.G. Vincter[31], V.B. Vinogradov[68], A. Vishwakarma[45], C. Vittori[22a,22b], I. Vivarelli[151], S. Vlachos[10], M. Vogel[178], P. Vokac[130], G. Volpi[13], H. von der Schmitt[103], E. von Toerne[23], V. Vorobel[131], K. Vorobev[100], M. Vos[170], R. Voss[32], J.H. Vossebeld[77], N. Vranjes[14], M. Vranjes Milosavljevic[14], V. Vrba[130], M. Vreeswijk[109], R. Vuillermet[32], I. Vukotic[33], P. Wagner[23], W. Wagner[178], J. Wagner-Kuhr[102], H. Wahlberg[74], S. Wahrmund[47], J. Walder[75], R. Walker[102], W. Walkowiak[143], V. Wallangen[148a,148b], C. Wang[35b], C. Wang[36b,at], F. Wang[176], H. Wang[16], H. Wang[3], J. Wang[45], J. Wang[152], Q. Wang[115], R.-J. Wang[83], R. Wang[6], S.M. Wang[153], T. Wang[38], W. Wang[153,au], W. Wang[36a,av], Z. Wang[36c], C. Wanotayaroj[45], A. Warburton[90], C.P. Ward[30], D.R. Wardrope[81], A. Washbrook[49], P.M. Watkins[19], A.T. Watson[19], M.F. Watson[19], G. Watts[140], S. Watts[87], B.M. Waugh[81], A.F. Webb[11], S. Webb[86], M.S. Weber[18], S.M. Weber[60a], S.W. Weber[177], S.A. Weber[31], J.S. Webster[6], A.R. Weidberg[122], B. Weinert[64], J. Weingarten[57], M. Weirich[86],

JHEP12(2017)059

C. Weiser[51], H. Weits[109], P.S. Wells[32], T. Wenaus[27], T. Wengler[32], S. Wenig[32], N. Wermes[23], M.D. Werner[67], P. Werner[32], M. Wessels[60a], T.D. Weston[18], K. Whalen[118], N.L. Whallon[140], A.M. Wharton[75], A.S. White[92], A. White[8], M.J. White[1], R. White[34b], D. Whiteson[166], B.W. Whitmore[75], F.J. Wickens[133], W. Wiedenmann[176], M. Wielers[133], C. Wiglesworth[39], L.A.M. Wiik-Fuchs[51], A. Wildauer[103], F. Wilk[87], H.G. Wilkens[32], H.H. Williams[124], S. Williams[109], C. Willis[93], S. Willocq[89], J.A. Wilson[19], I. Wingerter-Seez[5], E. Winkels[151], F. Winklmeier[118], O.J. Winston[151], B.T. Winter[23], M. Wittgen[145], M. Wobisch[82,u], T.M.H. Wolf[109], R. Wolff[88], M.W. Wolter[42], H. Wolters[128a,128c], V.W.S. Wong[171], N.L. Woods[139], S.D. Worm[19], B.K. Wosiek[42], J. Wotschack[32], K.W. Wozniak[42], M. Wu[33], S.L. Wu[176], X. Wu[52], Y. Wu[92], T.R. Wyatt[87], B.M. Wynne[49], S. Xella[39], Z. Xi[92], L. Xia[35c], D. Xu[35a], L. Xu[27], T. Xu[138], B. Yabsley[152], S. Yacoob[147a], D. Yamaguchi[159], Y. Yamaguchi[159], A. Yamamoto[69], S. Yamamoto[157], T. Yamanaka[157], F. Yamane[70], M. Yamatani[157], Y. Yamazaki[70], Z. Yan[24], H. Yang[36c], H. Yang[16], Y. Yang[153], Z. Yang[15], W-M. Yao[16], Y.C. Yap[45], Y. Yasu[69], E. Yatsenko[5], K.H. Yau Wong[23], J. Ye[43], S. Ye[27], I. Yeletskikh[68], E. Yigitbasi[24], E. Yildirim[86], K. Yorita[174], K. Yoshihara[124], C. Young[145], C.J.S. Young[32], J. Yu[8], J. Yu[67], S.P.Y. Yuen[23], I. Yusuff[30,aw], B. Zabinski[42], G. Zacharis[10], R. Zaidan[13], A.M. Zaitsev[132,aj], N. Zakharchuk[45], J. Zalieckas[15], A. Zaman[150], S. Zambito[59], D. Zanzi[91], C. Zeitnitz[178], G. Zemaityte[122], A. Zemla[41a], J.C. Zeng[169], Q. Zeng[145], O. Zenin[132], T. Ženiš[146a], D. Zerwas[119], D. Zhang[36b], D. Zhang[92], F. Zhang[176], G. Zhang[36a,av], H. Zhang[119], J. Zhang[6], L. Zhang[51], L. Zhang[36a], M. Zhang[169], P. Zhang[35b], R. Zhang[23], R. Zhang[36a,at], X. Zhang[36b], Y. Zhang[35a], Z. Zhang[119], X. Zhao[43], Y. Zhao[36b,ax], Z. Zhao[36a], A. Zhemchugov[68], B. Zhou[92], C. Zhou[176], L. Zhou[43], M. Zhou[35a], M. Zhou[150], N. Zhou[35c], C.G. Zhu[36b], H. Zhu[35a], J. Zhu[92], Y. Zhu[36a], X. Zhuang[35a], K. Zhukov[98], A. Zibell[177], D. Zieminska[64], N.I. Zimine[68], C. Zimmermann[86], S. Zimmermann[51], Z. Zinonos[103], M. Zinser[86], M. Ziolkowski[143], L. Živković[14], G. Zobernig[176], A. Zoccoli[22a,22b], R. Zou[33], M. zur Nedden[17], L. Zwalinski[32].

[1] *Department of Physics, University of Adelaide, Adelaide, Australia*
[2] *Physics Department, SUNY Albany, Albany NY, United States of America*
[3] *Department of Physics, University of Alberta, Edmonton AB, Canada*
[4] [(a)] *Department of Physics, Ankara University, Ankara;* [(b)] *Istanbul Aydin University, Istanbul;* [(c)] *Division of Physics, TOBB University of Economics and Technology, Ankara, Turkey*
[5] *LAPP, CNRS/IN2P3 and Université Savoie Mont Blanc, Annecy-le-Vieux, France*
[6] *High Energy Physics Division, Argonne National Laboratory, Argonne IL, United States of America*
[7] *Department of Physics, University of Arizona, Tucson AZ, United States of America*
[8] *Department of Physics, The University of Texas at Arlington, Arlington TX, United States of America*
[9] *Physics Department, National and Kapodistrian University of Athens, Athens, Greece*
[10] *Physics Department, National Technical University of Athens, Zografou, Greece*
[11] *Department of Physics, The University of Texas at Austin, Austin TX, United States of America*
[12] *Institute of Physics, Azerbaijan Academy of Sciences, Baku, Azerbaijan*
[13] *Institut de Física d'Altes Energies (IFAE), The Barcelona Institute of Science and Technology, Barcelona, Spain*
[14] *Institute of Physics, University of Belgrade, Belgrade, Serbia*
[15] *Department for Physics and Technology, University of Bergen, Bergen, Norway*
[16] *Physics Division, Lawrence Berkeley National Laboratory and University of California, Berkeley CA, United States of America*
[17] *Department of Physics, Humboldt University, Berlin, Germany*
[18] *Albert Einstein Center for Fundamental Physics and Laboratory for High Energy Physics, University of Bern, Bern, Switzerland*
[19] *School of Physics and Astronomy, University of Birmingham, Birmingham, United Kingdom*

JHEP12(2017)059

[20] [(a)] *Department of Physics, Bogazici University, Istanbul;* [(b)] *Department of Physics Engineering, Gaziantep University, Gaziantep;* [(d)] *Istanbul Bilgi University, Faculty of Engineering and Natural Sciences, Istanbul;* [(e)] *Bahcesehir University, Faculty of Engineering and Natural Sciences, Istanbul, Turkey*
[21] *Centro de Investigaciones, Universidad Antonio Narino, Bogota, Colombia*
[22] [(a)] *INFN Sezione di Bologna;* [(b)] *Dipartimento di Fisica e Astronomia, Università di Bologna, Bologna, Italy*
[23] *Physikalisches Institut, University of Bonn, Bonn, Germany*
[24] *Department of Physics, Boston University, Boston MA, United States of America*
[25] *Department of Physics, Brandeis University, Waltham MA, United States of America*
[26] [(a)] *Universidade Federal do Rio De Janeiro COPPE/EE/IF, Rio de Janeiro;* [(b)] *Electrical Circuits Department, Federal University of Juiz de Fora (UFJF), Juiz de Fora;* [(c)] *Federal University of Sao Joao del Rei (UFSJ), Sao Joao del Rei;* [(d)] *Instituto de Fisica, Universidade de Sao Paulo, Sao Paulo, Brazil*
[27] *Physics Department, Brookhaven National Laboratory, Upton NY, United States of America*
[28] [(a)] *Transilvania University of Brasov, Brasov;* [(b)] *Horia Hulubei National Institute of Physics and Nuclear Engineering, Bucharest;* [(c)] *Department of Physics, Alexandru Ioan Cuza University of Iasi, Iasi;* [(d)] *National Institute for Research and Development of Isotopic and Molecular Technologies, Physics Department, Cluj Napoca;* [(e)] *University Politehnica Bucharest, Bucharest;* [(f)] *West University in Timisoara, Timisoara, Romania*
[29] *Departamento de Física, Universidad de Buenos Aires, Buenos Aires, Argentina*
[30] *Cavendish Laboratory, University of Cambridge, Cambridge, United Kingdom*
[31] *Department of Physics, Carleton University, Ottawa ON, Canada*
[32] *CERN, Geneva, Switzerland*
[33] *Enrico Fermi Institute, University of Chicago, Chicago IL, United States of America*
[34] [(a)] *Departamento de Física, Pontificia Universidad Católica de Chile, Santiago;* [(b)] *Departamento de Física, Universidad Técnica Federico Santa María, Valparaíso, Chile*
[35] [(a)] *Institute of High Energy Physics, Chinese Academy of Sciences, Beijing;* [(b)] *Department of Physics, Nanjing University, Jiangsu;* [(c)] *Physics Department, Tsinghua University, Beijing 100084, China*
[36] [(a)] *Department of Modern Physics and State Key Laboratory of Particle Detection and Electronics, University of Science and Technology of China, Anhui;* [(b)] *School of Physics, Shandong University, Shandong;* [(c)] *Department of Physics and Astronomy, Key Laboratory for Particle Physics, Astrophysics and Cosmology, Ministry of Education; Shanghai Key Laboratory for Particle Physics and Cosmology, Shanghai Jiao Tong University, Shanghai(also at PKU-CHEP), China*
[37] *Université Clermont Auvergne, CNRS/IN2P3, LPC, Clermont-Ferrand, France*
[38] *Nevis Laboratory, Columbia University, Irvington NY, United States of America*
[39] *Niels Bohr Institute, University of Copenhagen, Kobenhavn, Denmark*
[40] [(a)] *INFN Gruppo Collegato di Cosenza, Laboratori Nazionali di Frascati;* [(b)] *Dipartimento di Fisica, Università della Calabria, Rende, Italy*
[41] [(a)] *AGH University of Science and Technology, Faculty of Physics and Applied Computer Science, Krakow;* [(b)] *Marian Smoluchowski Institute of Physics, Jagiellonian University, Krakow, Poland*
[42] *Institute of Nuclear Physics Polish Academy of Sciences, Krakow, Poland*
[43] *Physics Department, Southern Methodist University, Dallas TX, United States of America*
[44] *Physics Department, University of Texas at Dallas, Richardson TX, United States of America*
[45] *DESY, Hamburg and Zeuthen, Germany*
[46] *Lehrstuhl für Experimentelle Physik IV, Technische Universität Dortmund, Dortmund, Germany*
[47] *Institut für Kern- und Teilchenphysik, Technische Universität Dresden, Dresden, Germany*
[48] *Department of Physics, Duke University, Durham NC, United States of America*
[49] *SUPA - School of Physics and Astronomy, University of Edinburgh, Edinburgh, United Kingdom*
[50] *INFN e Laboratori Nazionali di Frascati, Frascati, Italy*
[51] *Fakultät für Mathematik und Physik, Albert-Ludwigs-Universität, Freiburg, Germany*

JHEP12(2017)059

[52] Departement de Physique Nucleaire et Corpusculaire, Université de Genève, Geneva, Switzerland
[53] [(a)] INFN Sezione di Genova; [(b)] Dipartimento di Fisica, Università di Genova, Genova, Italy
[54] [(a)] E. Andronikashvili Institute of Physics, Iv. Javakhishvili Tbilisi State University, Tbilisi; [(b)] High Energy Physics Institute, Tbilisi State University, Tbilisi, Georgia
[55] II Physikalisches Institut, Justus-Liebig-Universität Giessen, Giessen, Germany
[56] SUPA - School of Physics and Astronomy, University of Glasgow, Glasgow, United Kingdom
[57] II Physikalisches Institut, Georg-August-Universität, Göttingen, Germany
[58] Laboratoire de Physique Subatomique et de Cosmologie, Université Grenoble-Alpes, CNRS/IN2P3, Grenoble, France
[59] Laboratory for Particle Physics and Cosmology, Harvard University, Cambridge MA, United States of America
[60] [(a)] Kirchhoff-Institut für Physik, Ruprecht-Karls-Universität Heidelberg, Heidelberg; [(b)] Physikalisches Institut, Ruprecht-Karls-Universität Heidelberg, Heidelberg, Germany
[61] Faculty of Applied Information Science, Hiroshima Institute of Technology, Hiroshima, Japan
[62] [(a)] Department of Physics, The Chinese University of Hong Kong, Shatin, N.T., Hong Kong; [(b)] Department of Physics, The University of Hong Kong, Hong Kong; [(c)] Department of Physics and Institute for Advanced Study, The Hong Kong University of Science and Technology, Clear Water Bay, Kowloon, Hong Kong, China
[63] Department of Physics, National Tsing Hua University, Taiwan, Taiwan
[64] Department of Physics, Indiana University, Bloomington IN, United States of America
[65] Institut für Astro- und Teilchenphysik, Leopold-Franzens-Universität, Innsbruck, Austria
[66] University of Iowa, Iowa City IA, United States of America
[67] Department of Physics and Astronomy, Iowa State University, Ames IA, United States of America
[68] Joint Institute for Nuclear Research, JINR Dubna, Dubna, Russia
[69] KEK, High Energy Accelerator Research Organization, Tsukuba, Japan
[70] Graduate School of Science, Kobe University, Kobe, Japan
[71] Faculty of Science, Kyoto University, Kyoto, Japan
[72] Kyoto University of Education, Kyoto, Japan
[73] Research Center for Advanced Particle Physics and Department of Physics, Kyushu University, Fukuoka, Japan
[74] Instituto de Física La Plata, Universidad Nacional de La Plata and CONICET, La Plata, Argentina
[75] Physics Department, Lancaster University, Lancaster, United Kingdom
[76] [(a)] INFN Sezione di Lecce; [(b)] Dipartimento di Matematica e Fisica, Università del Salento, Lecce, Italy
[77] Oliver Lodge Laboratory, University of Liverpool, Liverpool, United Kingdom
[78] Department of Experimental Particle Physics, Jožef Stefan Institute and Department of Physics, University of Ljubljana, Ljubljana, Slovenia
[79] School of Physics and Astronomy, Queen Mary University of London, London, United Kingdom
[80] Department of Physics, Royal Holloway University of London, Surrey, United Kingdom
[81] Department of Physics and Astronomy, University College London, London, United Kingdom
[82] Louisiana Tech University, Ruston LA, United States of America
[83] Laboratoire de Physique Nucléaire et de Hautes Energies, UPMC and Université Paris-Diderot and CNRS/IN2P3, Paris, France
[84] Fysiska institutionen, Lunds universitet, Lund, Sweden
[85] Departamento de Fisica Teorica C-15, Universidad Autonoma de Madrid, Madrid, Spain
[86] Institut für Physik, Universität Mainz, Mainz, Germany
[87] School of Physics and Astronomy, University of Manchester, Manchester, United Kingdom
[88] CPPM, Aix-Marseille Université and CNRS/IN2P3, Marseille, France
[89] Department of Physics, University of Massachusetts, Amherst MA, United States of America
[90] Department of Physics, McGill University, Montreal QC, Canada
[91] School of Physics, University of Melbourne, Victoria, Australia
[92] Department of Physics, The University of Michigan, Ann Arbor MI, United States of America

JHEP12(2017)059

[93] *Department of Physics and Astronomy, Michigan State University, East Lansing MI, United States of America*
[94] [(a)] *INFN Sezione di Milano;* [(b)] *Dipartimento di Fisica, Università di Milano, Milano, Italy*
[95] *B.I. Stepanov Institute of Physics, National Academy of Sciences of Belarus, Minsk, Republic of Belarus*
[96] *Research Institute for Nuclear Problems of Byelorussian State University, Minsk, Republic of Belarus*
[97] *Group of Particle Physics, University of Montreal, Montreal QC, Canada*
[98] *P.N. Lebedev Physical Institute of the Russian Academy of Sciences, Moscow, Russia*
[99] *Institute for Theoretical and Experimental Physics (ITEP), Moscow, Russia*
[100] *National Research Nuclear University MEPhI, Moscow, Russia*
[101] *D.V. Skobeltsyn Institute of Nuclear Physics, M.V. Lomonosov Moscow State University, Moscow, Russia*
[102] *Fakultät für Physik, Ludwig-Maximilians-Universität München, München, Germany*
[103] *Max-Planck-Institut für Physik (Werner-Heisenberg-Institut), München, Germany*
[104] *Nagasaki Institute of Applied Science, Nagasaki, Japan*
[105] *Graduate School of Science and Kobayashi-Maskawa Institute, Nagoya University, Nagoya, Japan*
[106] [(a)] *INFN Sezione di Napoli;* [(b)] *Dipartimento di Fisica, Università di Napoli, Napoli, Italy*
[107] *Department of Physics and Astronomy, University of New Mexico, Albuquerque NM, United States of America*
[108] *Institute for Mathematics, Astrophysics and Particle Physics, Radboud University Nijmegen/Nikhef, Nijmegen, Netherlands*
[109] *Nikhef National Institute for Subatomic Physics and University of Amsterdam, Amsterdam, Netherlands*
[110] *Department of Physics, Northern Illinois University, DeKalb IL, United States of America*
[111] *Budker Institute of Nuclear Physics, SB RAS, Novosibirsk, Russia*
[112] *Department of Physics, New York University, New York NY, United States of America*
[113] *Ohio State University, Columbus OH, United States of America*
[114] *Faculty of Science, Okayama University, Okayama, Japan*
[115] *Homer L. Dodge Department of Physics and Astronomy, University of Oklahoma, Norman OK, United States of America*
[116] *Department of Physics, Oklahoma State University, Stillwater OK, United States of America*
[117] *Palacký University, RCPTM, Olomouc, Czech Republic*
[118] *Center for High Energy Physics, University of Oregon, Eugene OR, United States of America*
[119] *LAL, Univ. Paris-Sud, CNRS/IN2P3, Université Paris-Saclay, Orsay, France*
[120] *Graduate School of Science, Osaka University, Osaka, Japan*
[121] *Department of Physics, University of Oslo, Oslo, Norway*
[122] *Department of Physics, Oxford University, Oxford, United Kingdom*
[123] [(a)] *INFN Sezione di Pavia;* [(b)] *Dipartimento di Fisica, Università di Pavia, Pavia, Italy*
[124] *Department of Physics, University of Pennsylvania, Philadelphia PA, United States of America*
[125] *National Research Centre "Kurchatov Institute" B.P.Konstantinov Petersburg Nuclear Physics Institute, St. Petersburg, Russia*
[126] [(a)] *INFN Sezione di Pisa;* [(b)] *Dipartimento di Fisica E. Fermi, Università di Pisa, Pisa, Italy*
[127] *Department of Physics and Astronomy, University of Pittsburgh, Pittsburgh PA, United States of America*
[128] [(a)] *Laboratório de Instrumentação e Física Experimental de Partículas - LIP, Lisboa;* [(b)] *Faculdade de Ciências, Universidade de Lisboa, Lisboa;* [(c)] *Department of Physics, University of Coimbra, Coimbra;* [(d)] *Centro de Física Nuclear da Universidade de Lisboa, Lisboa;* [(e)] *Departamento de Fisica, Universidade do Minho, Braga;* [(f)] *Departamento de Fisica Teorica y del Cosmos, Universidad de Granada, Granada;* [(g)] *Dep Fisica and CEFITEC of Faculdade de Ciencias e Tecnologia, Universidade Nova de Lisboa, Caparica, Portugal*
[129] *Institute of Physics, Academy of Sciences of the Czech Republic, Praha, Czech Republic*

JHEP12(2017)059

[130] *Czech Technical University in Prague, Praha, Czech Republic*
[131] *Charles University, Faculty of Mathematics and Physics, Prague, Czech Republic*
[132] *State Research Center Institute for High Energy Physics (Protvino), NRC KI, Russia*
[133] *Particle Physics Department, Rutherford Appleton Laboratory, Didcot, United Kingdom*
[134] [(a)] *INFN Sezione di Roma;* [(b)] *Dipartimento di Fisica, Sapienza Università di Roma, Roma, Italy*
[135] [(a)] *INFN Sezione di Roma Tor Vergata;* [(b)] *Dipartimento di Fisica, Università di Roma Tor Vergata, Roma, Italy*
[136] [(a)] *INFN Sezione di Roma Tre;* [(b)] *Dipartimento di Matematica e Fisica, Università Roma Tre, Roma, Italy*
[137] [(a)] *Faculté des Sciences Ain Chock, Réseau Universitaire de Physique des Hautes Energies - Université Hassan II, Casablanca;* [(b)] *Centre National de l'Energie des Sciences Techniques Nucleaires, Rabat;* [(c)] *Faculté des Sciences Semlalia, Université Cadi Ayyad, LPHEA-Marrakech;* [(d)] *Faculté des Sciences, Université Mohamed Premier and LPTPM, Oujda;* [(e)] *Faculté des sciences, Université Mohammed V, Rabat, Morocco*
[138] *DSM/IRFU (Institut de Recherches sur les Lois Fondamentales de l'Univers), CEA Saclay (Commissariat à l'Energie Atomique et aux Energies Alternatives), Gif-sur-Yvette, France*
[139] *Santa Cruz Institute for Particle Physics, University of California Santa Cruz, Santa Cruz CA, United States of America*
[140] *Department of Physics, University of Washington, Seattle WA, United States of America*
[141] *Department of Physics and Astronomy, University of Sheffield, Sheffield, United Kingdom*
[142] *Department of Physics, Shinshu University, Nagano, Japan*
[143] *Department Physik, Universität Siegen, Siegen, Germany*
[144] *Department of Physics, Simon Fraser University, Burnaby BC, Canada*
[145] *SLAC National Accelerator Laboratory, Stanford CA, United States of America*
[146] [(a)] *Faculty of Mathematics, Physics & Informatics, Comenius University, Bratislava;* [(b)] *Department of Subnuclear Physics, Institute of Experimental Physics of the Slovak Academy of Sciences, Kosice, Slovak Republic*
[147] [(a)] *Department of Physics, University of Cape Town, Cape Town;* [(b)] *Department of Physics, University of Johannesburg, Johannesburg;* [(c)] *School of Physics, University of the Witwatersrand, Johannesburg, South Africa*
[148] [(a)] *Department of Physics, Stockholm University;* [(b)] *The Oskar Klein Centre, Stockholm, Sweden*
[149] *Physics Department, Royal Institute of Technology, Stockholm, Sweden*
[150] *Departments of Physics & Astronomy and Chemistry, Stony Brook University, Stony Brook NY, United States of America*
[151] *Department of Physics and Astronomy, University of Sussex, Brighton, United Kingdom*
[152] *School of Physics, University of Sydney, Sydney, Australia*
[153] *Institute of Physics, Academia Sinica, Taipei, Taiwan*
[154] *Department of Physics, Technion: Israel Institute of Technology, Haifa, Israel*
[155] *Raymond and Beverly Sackler School of Physics and Astronomy, Tel Aviv University, Tel Aviv, Israel*
[156] *Department of Physics, Aristotle University of Thessaloniki, Thessaloniki, Greece*
[157] *International Center for Elementary Particle Physics and Department of Physics, The University of Tokyo, Tokyo, Japan*
[158] *Graduate School of Science and Technology, Tokyo Metropolitan University, Tokyo, Japan*
[159] *Department of Physics, Tokyo Institute of Technology, Tokyo, Japan*
[160] *Tomsk State University, Tomsk, Russia*
[161] *Department of Physics, University of Toronto, Toronto ON, Canada*
[162] [(a)] *INFN-TIFPA;* [(b)] *University of Trento, Trento, Italy*
[163] [(a)] *TRIUMF, Vancouver BC;* [(b)] *Department of Physics and Astronomy, York University, Toronto ON, Canada*
[164] *Faculty of Pure and Applied Sciences, and Center for Integrated Research in Fundamental Science and Engineering, University of Tsukuba, Tsukuba, Japan*

JHEP12(2017)059

[165] Department of Physics and Astronomy, Tufts University, Medford MA, United States of America
[166] Department of Physics and Astronomy, University of California Irvine, Irvine CA, United States of America
[167] [(a)] INFN Gruppo Collegato di Udine, Sezione di Trieste, Udine; [(b)] ICTP, Trieste; [(c)] Dipartimento di Chimica, Fisica e Ambiente, Università di Udine, Udine, Italy
[168] Department of Physics and Astronomy, University of Uppsala, Uppsala, Sweden
[169] Department of Physics, University of Illinois, Urbana IL, United States of America
[170] Instituto de Fisica Corpuscular (IFIC), Centro Mixto Universidad de Valencia - CSIC, Spain
[171] Department of Physics, University of British Columbia, Vancouver BC, Canada
[172] Department of Physics and Astronomy, University of Victoria, Victoria BC, Canada
[173] Department of Physics, University of Warwick, Coventry, United Kingdom
[174] Waseda University, Tokyo, Japan
[175] Department of Particle Physics, The Weizmann Institute of Science, Rehovot, Israel
[176] Department of Physics, University of Wisconsin, Madison WI, United States of America
[177] Fakultät für Physik und Astronomie, Julius-Maximilians-Universität, Würzburg, Germany
[178] Fakultät für Mathematik und Naturwissenschaften, Fachgruppe Physik, Bergische Universität Wuppertal, Wuppertal, Germany
[179] Department of Physics, Yale University, New Haven CT, United States of America
[180] Yerevan Physics Institute, Yerevan, Armenia
[181] Centre de Calcul de l'Institut National de Physique Nucléaire et de Physique des Particules (IN2P3), Villeurbanne, France
[182] Academia Sinica Grid Computing, Institute of Physics, Academia Sinica, Taipei, Taiwan

[a] Also at Department of Physics, King's College London, London, United Kingdom
[b] Also at Institute of Physics, Azerbaijan Academy of Sciences, Baku, Azerbaijan
[c] Also at Novosibirsk State University, Novosibirsk, Russia
[d] Also at TRIUMF, Vancouver BC, Canada
[e] Also at Department of Physics & Astronomy, University of Louisville, Louisville, KY, United States of America
[f] Also at Physics Department, An-Najah National University, Nablus, Palestine
[g] Also at Department of Physics, California State University, Fresno CA, United States of America
[h] Also at Department of Physics, University of Fribourg, Fribourg, Switzerland
[i] Also at II Physikalisches Institut, Georg-August-Universität, Göttingen, Germany
[j] Also at Departament de Fisica de la Universitat Autonoma de Barcelona, Barcelona, Spain
[k] Also at Departamento de Fisica e Astronomia, Faculdade de Ciencias, Universidade do Porto, Portugal
[l] Also at Tomsk State University, Tomsk, and Moscow Institute of Physics and Technology State University, Dolgoprudny, Russia
[m] Also at The Collaborative Innovation Center of Quantum Matter (CICQM), Beijing, China
[n] Also at Universita di Napoli Parthenope, Napoli, Italy
[o] Also at Institute of Particle Physics (IPP), Canada
[p] Also at Horia Hulubei National Institute of Physics and Nuclear Engineering, Bucharest, Romania
[q] Also at Department of Physics, St. Petersburg State Polytechnical University, St. Petersburg, Russia
[r] Also at Borough of Manhattan Community College, City University of New York, New York City, United States of America
[s] Also at Department of Financial and Management Engineering, University of the Aegean, Chios, Greece
[t] Also at Centre for High Performance Computing, CSIR Campus, Rosebank, Cape Town, South Africa
[u] Also at Louisiana Tech University, Ruston LA, United States of America
[v] Also at Institucio Catalana de Recerca i Estudis Avancats, ICREA, Barcelona, Spain

JHEP12(2017)059

[w] Also at Graduate School of Science, Osaka University, Osaka, Japan
[x] Also at Fakultät für Mathematik und Physik, Albert-Ludwigs-Universität, Freiburg, Germany
[y] Also at Institute for Mathematics, Astrophysics and Particle Physics, Radboud University Nijmegen/Nikhef, Nijmegen, Netherlands
[z] Also at Department of Physics, The University of Texas at Austin, Austin TX, United States of America
[aa] Also at Institute of Theoretical Physics, Ilia State University, Tbilisi, Georgia
[ab] Also at CERN, Geneva, Switzerland
[ac] Also at Georgian Technical University (GTU),Tbilisi, Georgia
[ad] Also at Ochadai Academic Production, Ochanomizu University, Tokyo, Japan
[ae] Also at Manhattan College, New York NY, United States of America
[af] Also at Department of Physics, The University of Michigan, Ann Arbor MI, United States of America
[ag] Also at The City College of New York, New York NY, United States of America
[ah] Also at Departamento de Fisica Teorica y del Cosmos, Universidad de Granada, Granada, Portugal
[ai] Also at Department of Physics, California State University, Sacramento CA, United States of America
[aj] Also at Moscow Institute of Physics and Technology State University, Dolgoprudny, Russia
[ak] Also at Departement de Physique Nucleaire et Corpusculaire, Université de Genève, Geneva, Switzerland
[al] Also at Institut de Física d'Altes Energies (IFAE), The Barcelona Institute of Science and Technology, Barcelona, Spain
[am] Also at School of Physics, Sun Yat-sen University, Guangzhou, China
[an] Also at Institute for Nuclear Research and Nuclear Energy (INRNE) of the Bulgarian Academy of Sciences, Sofia, Bulgaria
[ao] Also at Faculty of Physics, M.V.Lomonosov Moscow State University, Moscow, Russia
[ap] Also at National Research Nuclear University MEPhI, Moscow, Russia
[aq] Also at Department of Physics, Stanford University, Stanford CA, United States of America
[ar] Also at Institute for Particle and Nuclear Physics, Wigner Research Centre for Physics, Budapest, Hungary
[as] Also at Giresun University, Faculty of Engineering, Turkey
[at] Also at CPPM, Aix-Marseille Université and CNRS/IN2P3, Marseille, France
[au] Also at Department of Physics, Nanjing University, Jiangsu, China
[av] Also at Institute of Physics, Academia Sinica, Taipei, Taiwan
[aw] Also at University of Malaya, Department of Physics, Kuala Lumpur, Malaysia
[ax] Also at LAL, Univ. Paris-Sud, CNRS/IN2P3, Université Paris-Saclay, Orsay, France
[*] Deceased

JHEP12(2017)059